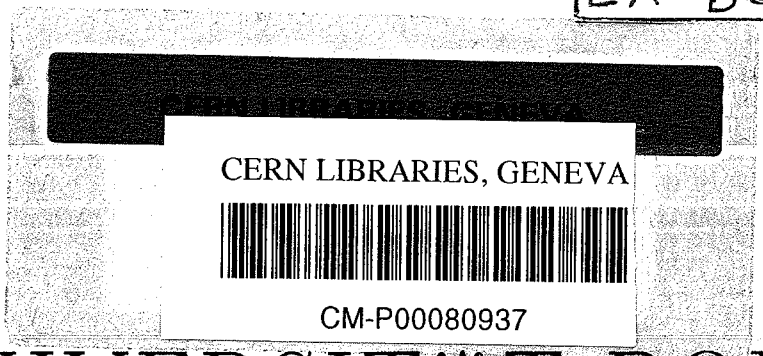



# UNIVERSITÄT BONN
## Physikalisches Institut


# A Precision Measurement of the $Z^0$ - Line Shape

Bernd Schmitt

**Abstract:**
A precise measurement of the cross section of the process $e^+e^- \rightarrow hadrons$ at energies around the $Z^0$-resonance is performed. The aim is to achieve a systematic error of 0.1%. Data recorded with the OPAL detector at LEP during the years 1990 to 1994 are used. To achieve a small systematic luminosity error the OPAL detector was upgraded with a new luminosity monitor. The new luminosity detector, the luminosity measurement, and the selection of multi hadronic events is described in detail. The measured hadronic cross sections together with the leptonic cross sections are used to determine the mass and the width of the $Z^0$-boson. The partial widths are used for a precision test of the Standard Model.


Post address:
Nussallee 12
D-53115 Bonn
Germany

BONN-IR-96-01
Bonn University
January 1996
ISSN-0172-8741

UNIVERSITÄT BONN
Physikalisches Institut

# A Precision Measurement of the $Z^0$-Line Shape

von
Bernd Schmitt

Dieser Forschungsbericht wurde als Doktorarbeit von der mathematisch - naturwissenschaftlichen Fakultät der Universität Bonn angenommen.

| | |
|---|---|
| Angenommen am: | 23. Januar 1996 |
| Referent: | Prof. Dr. N. Wermes |
| Koreferent: | Prof. Dr. E. Hilger |

# Table of Contents

# Chapter 1

# Introduction

The Standard Model is the basis of our understanding of the elementary particles and the forces between them. It has six quarks and six leptons as fundamental particles and describes two kinds of interactions, the electroweak interaction which acts on all particles (quarks and leptons), and the strong interaction which only acts on quarks. The forces between the elementary particles (the fermions) are described by the exchange of gauge particles (the gauge bosons). For the electroweak interaction these bosons are the massless photon, the massive charged bosons $W^{\pm}$, and the massive neutral boson $Z^0$. For the strong interaction there are 8 gluons.

The Standard Model (SM) does not make predictions of the strength of the interactions or the masses of the fermions and gauge bosons but it gives relations between these parameters. A set of free parameters are for example the masses of the fermions, three coupling constants (one for the strong interaction and two for the electroweak interaction), the mixing angle between the mass eigenstates and the eigenstates of the electroweak interaction, and the mass of the $Z^0$ and the Higgs boson. The two electroweak coupling constants and the fermion masses (the uncertainties in the quark masses with the exception of the mass of the top quark $M_{top}$ are not relevant for this analysis) are known from earlier experiments to high accuracy.

The most fundamental parameters measured at LEP are the mass, $M_Z$, and width, $\Gamma_Z$, of the $Z^0$ boson. LEP was built to measure $M_Z$ and $\Gamma_Z$ with high accuracy and it still is (in the 1995 energy scan) one of it's main tasks.

Figure 1.1 shows the measured cross section as a function of the center of mass energy. $M_Z$ is measured by fitting the calculated shape of the cross section (the line shape) to the measured cross sections at different center of mass energies. In lowest order the cross sections depend only on $\alpha$, the electromagnetic coupling constant, $G_F$, the Fermi constant, and $M_Z$. The lowest order predictions have to be modified by higher order corrections (known as radiative corrections) to reach the experimental accuracy. These higher order corrections cause dependencies on less well known parameters like the mass of the top quark or the mass of the Higgs boson.

The Standard Model predicts, after a measurement of $M_Z$, quantities like the $Z^0$ partial widths. Measurements of the partial widths therefore allow a test of the Standard Model. Since the partial widths depend through radiative corrections on the less well known parameters $M_{top}$

and $M_{Higgs}$, it is advantageous to look at quantities which have a reduced sensitivity to these parameters. One of these quantities is the ratio of the $Z^0$ invisible width, $\Gamma_{inv}$ (reflecting $Z^0 \rightarrow \nu\bar{\nu}$ in the SM), to the leptonic width, $\Gamma_{lept}$. In the ratio $\frac{\Gamma_{inv}}{\Gamma_{lept}}$ universal corrections cancel. It is, therefore, almost independent of $M_{top}$ and $M_{Higgs}$ and allows a precision test of the Standard Model. A measurement of $\frac{\Gamma_{inv}}{\Gamma_{lept}}$ significantly different from the Standard Model prediction would be a strong hint for "new physics".

The accuracy of the calculated cross sections is better than 0.1% and the statistics available (see table 1.1) also allows a measurement of the cross section with high statistical accuracy. The cross section is determined using the relation

$$\sigma = \frac{N_{sel} - N_{back}}{\epsilon \int Ldt}$$

where $N_{sel}$ is the number of selected events (i.e. $Z^0 \rightarrow hadrons$) and $N_{back}$ is the number of background events. $\epsilon$ is the efficiency of the selection and $\int Ldt$ is the integrated luminosity. The main experimental errors for the cross section measurement are the systematic error of the selection efficiency and the error of the luminosity measurement. The cross section measurement of the process $Z^0 \rightarrow leptons$ is mainly limited by statistics.

| year | 89 - 90 | 91 | 92 | 93 | 94 |
|---|---|---|---|---|---|
| $N_{had}$ | 140000 | 314000 | 733000 | 646000 | 1542000 |

Table 1.1: *Number of events for the process $Z^0 \rightarrow$ hadron collected with the OPAL detector at LEP.*

At the end of 1992 the luminosity measurement of OPAL was systematics limited at 0.41% without the possibility for an improvement to match the statistics available until the end of LEP I. OPAL therefore decided to install a new luminosity detector, the silicon tungsten calorimeter (SiW), capable to measure the luminosity with an accuracy of 0.1%. The error on the efficiency of the selection $Z^0 \rightarrow hadrons$ (multi hadron selection) at the end of 1992 was 0.2%. It had to be improved as well. The goal is to reduce the systematic error of the cross section from $\frac{\Delta\sigma}{\sigma} = 0.43\%$ to $\frac{\Delta\sigma}{\sigma} = 0.1\%$. Before 1993 the uncertainty in the LEP energy was the dominant error for the determination of $M_Z$. During 1993 the uncertainty in the LEP energy has been largely reduced by frequent calibrations of the LEP energy, allowing a precise determination of $M_Z$. The measurement of $\frac{\Gamma_{inv}}{\Gamma_{lept}}$ profits most from the improved luminosity determination allowing a more stringent test of the Standard Model.

The work presented here concentrates on the two main components of the cross section measurement, the new luminosity determination and the improved multi hadron selection. The results of these analyses are then used to obtain an improved measurement of $M_Z$ and $\Gamma_Z$ and a test of the Standard Model using $\frac{\Gamma_{inv}}{\Gamma_{lept}}$.

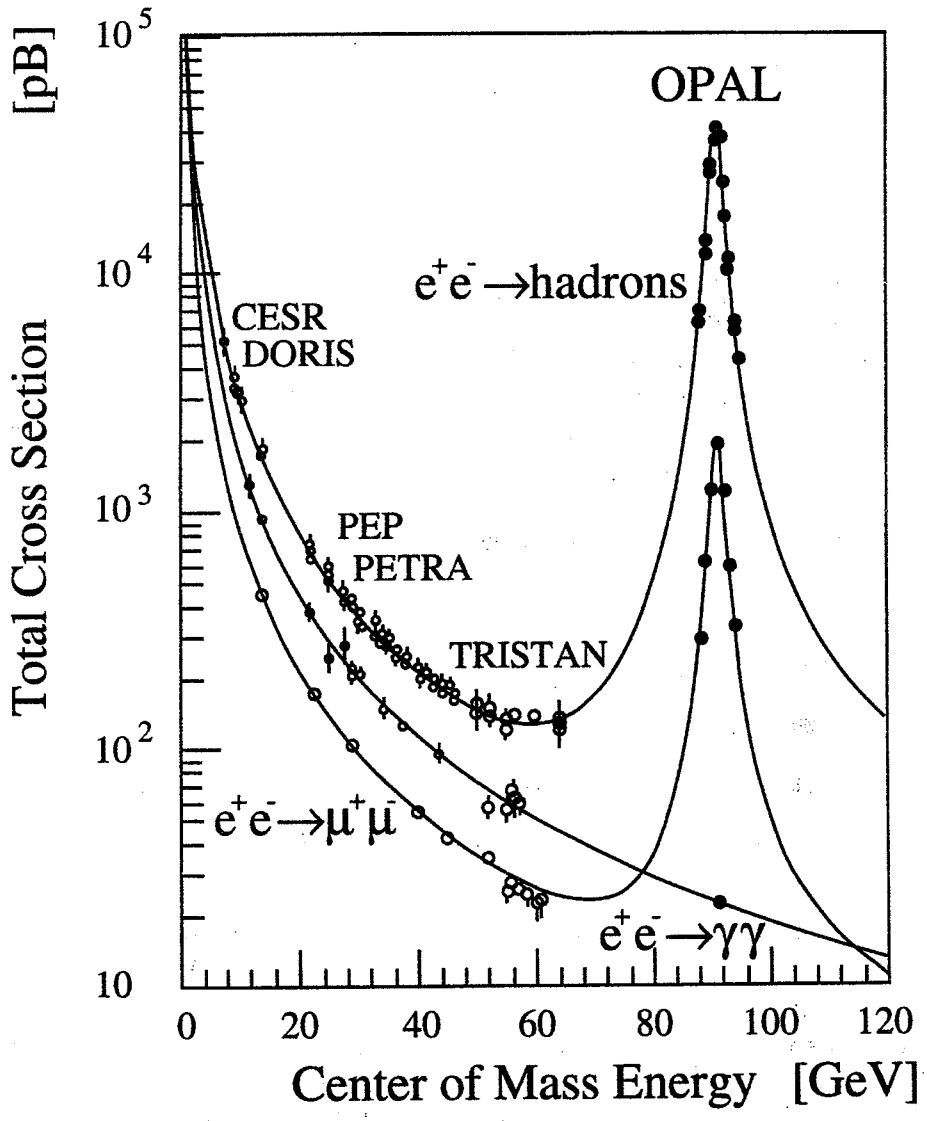


Figure 1.1: *Cross section for $e^+e^-$ annihilation as a function of the center of mass energy. Shown are the hadronic, muonic and two photon cross sections.*

# Chapter 2

# The Standard Model

Today matter is thought to be composed of fundamental spin-$\frac{1}{2}$ particles, the fermions. The fermions can be arranged in families such that each family consists of 8 particles, two leptons and two quarks and the corresponding anti-particles. Three such families exist; the main difference between them are the masses of the particles. Under the assumption that no neutrino with a mass of more than 45 GeV exists, the four LEP experiments proved, that exactly three such families exist.

The forces between particles are mediated by exchange particles (gauge bosons). The known forces are:

- gravitation: the gauge boson is the graviton with spin 2
- the weak interaction: the gauge bosons are $W^+$, $W^-$ and $Z^0$ with spin 1
- the electromagnetic interaction: the gauge boson is the photon with spin 1
- the strong interaction: the gauge bosons are the gluons with spin 1

The charged leptons take part in the first three interactions, the neutral leptons in the first two and the quarks in all four. The strong interaction is described by Quantum Chromo Dynamics (QCD). The electromagnetic and weak interaction are combined in the so called Standard Model of the electroweak interaction. Usually the electroweak theory together with the theory of the strong interaction is refered to as "the Standard Model". Detailled discussions of the Standard Model can be found elsewhere, for example in [1]. In the following the aspects of the Standard Model relevant for this analysis are described.

## 2.1 The Standard Model

### 2.1.1 The Electroweak Interaction

The phenomenological basis of the electroweak sector of the Standard Model is the following:

- The fermions can be grouped in families obeying a SU(2)×U(1) symmetry, i.e. the fermions exist as left handed doublets and right handed singlets. The individual fermions are characterized by the quantum numbers weak isospin I, its third component $I_3$ and the weak hypercharge Y.

| | | | $I$ | $I_3$ | $Y$ |
|---|---|---|---|---|---|
| $\begin{pmatrix} \nu_{e_L} \\ e_L \end{pmatrix}$ | $\begin{pmatrix} \nu_{\mu_L} \\ \mu_L \end{pmatrix}$ | $\begin{pmatrix} \nu_{\tau_L} \\ \tau_L \end{pmatrix}$ | 1/2<br>1/2 | 1/2<br>−1/2 | −1/2<br>−1/2 |
| $e_R$ | $\mu_R$ | $\tau_R$ | 0 | 0 | −1 |
| $\begin{pmatrix} u_L \\ d'_L \end{pmatrix}$ | $\begin{pmatrix} c_L \\ s'_L \end{pmatrix}$ | $\begin{pmatrix} t_L \\ b'_L \end{pmatrix}$ | 1/2<br>1/2 | 1/2<br>−1/2 | 1/6<br>1/6 |
| $u_R$ | $c_R$ | $t_R$ | 0 | 0 | 2/3 |
| $d_R$ | $s_R$ | $b_R$ | 0 | 0 | −1/3 |

The neutrinos only exist as massless left-handed particles. The quarks $d'$, $s'$, $b'$ are linear combinations of the mass eigenstates $d$, $s$, $b$. This is described by the Kobayashi–Maskawa matrix $V$.

$$\begin{pmatrix} d' \\ s' \\ b' \end{pmatrix} = \begin{pmatrix} V_{ud} & V_{us} & V_{ub} \\ V_{cd} & V_{cs} & V_{cb} \\ V_{td} & V_{ts} & V_{tb} \end{pmatrix} \begin{pmatrix} d \\ s \\ b \end{pmatrix}$$

- The electric charge is given by the Gell-Mann–Nishijima relation,

$$Q = I_3 + Y.$$

- The exchange particles of the electroweak interaction are the particles $W^{\pm}$, $Z^0$ and $\gamma$.

This structure can be described in the framework of a gauge invariant quantum field theory of the combined electromagnetic and weak interaction. The SU(2)×U(1) symmetry group is the group of transformations under which the lagrange density is 'locally' gauge invariant.

The SU(2)×U(1) symmetry has an associated triplet field $W_\mu^{1,2,3}$ and a singlet field $B_\mu$. The four physical gauge bosons are obtained as linear combinations.

$$\begin{aligned} W_\mu^{\pm} &= \frac{1}{\sqrt{2}} \left( W_\mu^1 \mp W_\mu^2 \right) \\ Z_\mu &= \cos\theta_W \, W_\mu^3 - \sin\theta_W \, B_\mu \\ A_\mu &= \sin\theta_W \, W_\mu^3 + \cos\theta_W \, B_\mu \end{aligned}$$

In the pure SU(2)×U(1) symmetry the gauge bosons are massles. The symmetry is spontaneously broken by the Higgs mechanism, by which the $W^{\pm}$ and $Z^0$ bosons obtain their masses. The masses of the physical bosons are obtained from the couplings $g_2$ (SU(2)) and $g_1$ (U(1)) and the vacuum expectation value of the Higgs field $v = 2\mu/\sqrt{\lambda}$ ($\mu$ and $\lambda$ are parameters of the Higgs–potential)

$$M_W = \frac{1}{2} g_2 \, v \; ; \quad M_Z = \frac{1}{2} \sqrt{g_1^2 + g_2^2} \, v \; ; \quad M_\gamma = 0$$

The weak mixing anlge, the Weinberg angle, can be expressed as

$$\cos\theta_W = \frac{g_2}{\sqrt{g_1^2 + g_2^2}} = \frac{M_W}{M_Z}$$

For the interpretation of the measurements it is appropriate to chose instead of $g_1$, $g_2$, $\lambda$, $\mu$ another set of independent parameters which are more directly accessible to measurements

$$e,\ G_F,\ M_Z,\ M_H.$$

$G_F$ is the Fermi constant, $e$ is the elementary charge and $M_{Higgs}$ is the mass of the Higgs boson. This results in the following relations

$$e = \frac{g_1\, g_2}{\sqrt{g_1^2 + g_2^2}}\ ; \quad M_Z = \left(\frac{\pi\,\alpha}{\sqrt{2}\,G_F}\right)^{\frac{1}{2}} \frac{1}{\sin\theta_W \cos\theta_W}\ ; \quad M_H = \sqrt{2}\,\mu.$$

### 2.1.2 The Strong Interaction

In correspondance to the electric charge in Quantum Electrodynamics (QED) the concept of colour was developped in Quantum Chromo Dynamics (QCD). But while in QED there is only one electric charge and one exchange particle, the photon, there are three colours and eight gluons in QCD. The gluons themselves carry colour and can therefore interact with each other. The structure of QCD can be derived from the SU(3) colour symmetry group. Since the gluons are massless the fields associated to the symmetry group directly correspond to the physical fields. The only free parameter is the strong coupling constant $\alpha_s$.

The energy dependence of the strong coupling constant is different from that in QED. The force between the quarks increases with their distance. It is therefore impossible to detect free quarks (confinement). On the other hand the coupling decreases with decreasing distance which allows the QCD to be treated as perturbation theory at high momentum transfers.

## 2.2 The Process $e^+e^- \to f\bar{f}$

The reaction $e^+e^- \to f\bar{f}$ ($f\bar{f} \neq e^+e^-$) is described in lowest order in the Standard Model by the two diagrams shown in figure 2.1.

The matrix element $\mathcal{M}$ of the process can be calculated as

$$\begin{aligned}\mathcal{M} &= \frac{e\sqrt{4\pi}}{q^2}\left[\bar{u}(3)\gamma^\mu v(4)\right]\left[\bar{v}(2)\gamma_\mu u(1)\right] + \\ &\frac{e\sqrt{4\pi}}{4\,(q^2 - M_Z^2)}\left[\bar{u}(3)\gamma^\mu\left(g_V^f - g_A^f\gamma^5\right)v(4)\right]\left(g_{\mu\nu} - \frac{q_\mu q_\nu}{M_Z^2}\right)\left[\bar{v}(2)\gamma^\nu\left(g_V^e - g_A^e\gamma^5\right)u(1)\right]\end{aligned} \tag{2.1}$$

The vector– and axial-vector couplings ($g_V^f$, $g_A^f$) are given by:

$$g_V^f = I_3^f - 2\,Q_f \sin^2\theta_W \tag{2.2}$$

$$g_A^f = I_3^f \tag{2.3}$$

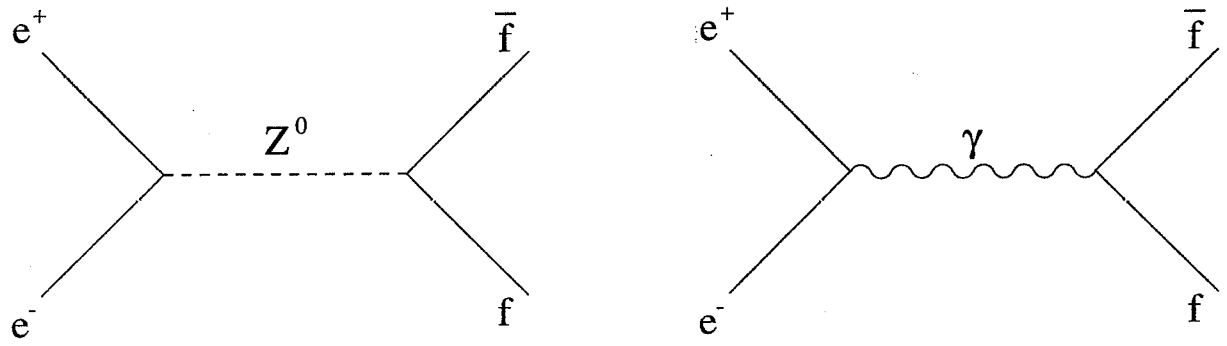


Figure 2.1: *Lowest order diagrams for the process* $e^+e^- \to f\bar{f}$.

where $I_3^f$ is the third component of the weak isospin of the fermion $f$ and $Q_f$ its charge. The first term in equation 2.1 describes the $\gamma$-exchange and the second term the $Z^0$-exchange.

After averaging over the spin of the incoming electrons and summing over the spins of the outgoing particles this results in a cross section, neglecting the fermion masses, of:

$$\begin{aligned} \sigma_{ew}^{ff}(s) &= \\ (\gamma\text{-exchange}) \quad & \frac{4\pi}{3}\frac{\alpha^2 N_c^f}{s} Q_e^2 Q_f^2 \\ (\gamma\text{–}Z^0 \text{ interference}) + & \frac{2\sqrt{2}}{3}\frac{\alpha G_F M_Z^2 N_c^f}{s} Q_e Q_f g_V^e g_V^f \,\mathrm{Re}\,(\chi(s)) \\ (Z^0\text{-exchange}) + & \frac{G_F^2 M_Z^4 N_c^f}{6\pi s}\left((g_V^e)^2+(g_A^e)^2\right)\left((g_V^f)^2+(g_A^f)^2\right)|\chi(s)|^2 \end{aligned} \tag{2.4}$$

The cross section has contributions from $\gamma$-exchange, $Z^0$-exchange and $\gamma - Z$-interference. The QCD colour factor, $N_c^f$, is 1 for leptons and 3 for quarks, $\alpha$ is the electromagnetic coupling constant and $G_F$ the Fermi constant. The propagator term $\chi(s)$ is given by:

$$\chi(s) = \frac{s}{s - M_Z^2 + iM_Z\Gamma_Z} \tag{2.5}$$

where $\Gamma_Z$ is the total width of the $Z^0$. Equation 2.4 describes the process $e^+e^- \to f\bar{f}$ in lowest order, the Born Approximation. In this approximation the processes are completely determined by the variables $\alpha$, $G_F$ and $M_Z$.

The accuracy of the experimental determination of the cross section is higher than that of the lowest order calculation. Therefore higher order corrections have to be taken into account. This is described in detail in chapter 8.1.

For the process $e^+e^- \to e^+e^-$ (Bhabha scattering) two additional diagrams (t-channel $\gamma$ exchange) have to be taken into account (see figure 2.2).

At small angles this process is dominated by the two QED processes where only $\gamma$-exchange takes place. The small angle Bhabha scattering is used as reference interaction for the luminosity measurement (see chapter 5).

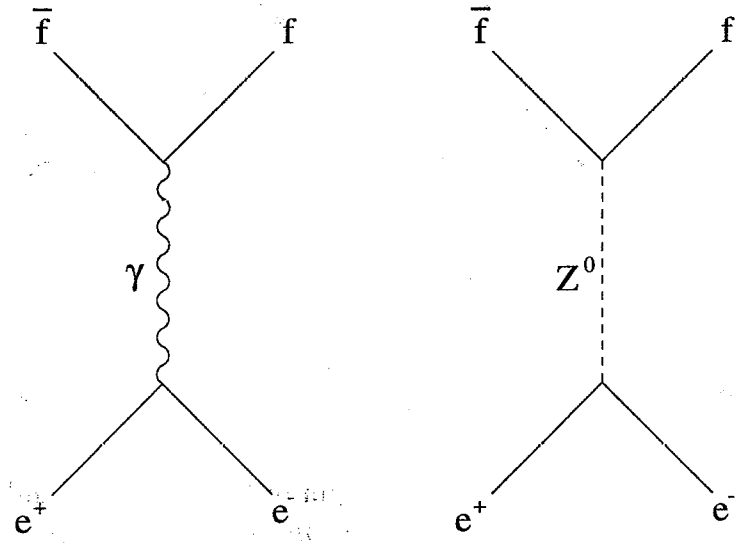


Figure 2.2: *Additional diagrams for the process* $e^+e^- \to e^+e^-$.

The calculation of the lowest order QED diagrams results in:

$$\frac{d\sigma}{d\Omega} = \frac{\alpha^2}{s}\left[\frac{1}{4}\cdot\frac{1+\cos^4\vartheta/2}{\sin^4\vartheta/2} + \frac{1}{8}\left(1+\cos^2\vartheta\right) - \frac{1}{2}\cdot\frac{\cos^4\vartheta/2}{\sin^2\vartheta/2}\right] \tag{2.6}$$

Here also higher order diagrams have to be taken into account to match the experimental accuracy.

A detailed description of the relevant processes can be found in the *CERN-Reports 'Z Physics at LEP'*. The calculation of the cross sections can be found in [5], the higher order corrections in [6] and the Bhabha scattering in [7].

## 2.3 Determination of Electroweak Parameters

The line shape parameters $M_Z$, $\Gamma_Z$ and the partial widths are determined by fitting the calculated shape of the cross section to the measured cross sections. This requires the cross sections to be measured at different energy points, i.e. an energy scan. For the analysis presented here data from 1991 to 1994 is used. This period includes two energy scans, one in 1991 at 7 energy points ranging $\pm$ 3 GeV around the $Z^0$-pole, the other scan was in 1993 at 3 energy points (at the $Z^0$ mass and roughly at $\pm$2 GeV). In 1992 and 1994 LEP was running at the $Z^0$-pole. The number of events used for the cross section measurements is shown in table 2.1 for the years 1991 to 1994.

| year | 1991 | 1992 | 1993 | 1994 |
|---|---|---|---|---|
| number of hadrons | 314000 | 733000 | 646000 | 1524000 |
| number of leptons | 37000 | 58000 | 82000 | 184000 |

Table 2.1: *Number of events used for the cross section measurements in the different years.*

The parametrization of the cross section is described in detail in chapter 8.1. The cross section is calculated using the program ZFITTER [34]. ZFITTER does not include the t-channel contribution of the process $e^+e^- \to e^+e^-$. The Bhabha event generator ALIBABA [20] is usually used to add the cross sections of the $\gamma$-exchange and the $\gamma - Z$-interference to the s-channel cross section calculated with ZFITTER. These contributions have a precision of 0.5% [20]. Since the Bhabha channel does not contribute much to the precision on Standard Model parameters once lepton universality is assumed the Bhabha channel is not included in this analysis.

For this analysis the cross section for the process $e^+e^- \to hadrons$ is measured using the data collected in 1993 and 1994. For the years 1991 and 1992 the published cross sections reported in [8]-[9] are included in the line shape fits.

# Chapter 3

# LEP and the OPAL Detector

OPAL (**O**mni **P**urpose **A**pparatus for **L**EP) is one of the four detectors at the LEP storage ring. In this chapter a brief description of LEP is given and then the OPAL detector is described in more detail.

## 3.1 LEP

The electron-positron storage ring LEP (**L**arge **E**lectron **P**ositron Collider) is an accelerator at the European Center for Nuclear Research, CERN, located near Geneva. The storage ring (see figure 3.2) is placed in a tunnel 100 m underground.

In the first phase, LEP I, which started 1989 and ended in 1995 LEP has been operated at center of mass energies near the $Z^0$ resonance, i.e. between 88.2 and 94.3 GeV. LEP has four interaction points with the detectors ALEPH, DELPHI, L3 and OPAL. Since 1989 each experiment registered about $4 \cdot 10^6$ $Z^0$ decays. Besides the measurement of electroweak parameters, like the mass $M_Z$ and width $\Gamma_Z$ of the $Z^0$ boson, many other physics analyses like searches for new particles, $\tau$-physics, B-physics, $\gamma\gamma$-physics or QCD-studies have been performed. In the next phase of LEP, LEP II, which begins in 1996, LEP is equipped with new superconducting cavities which allow to achieve center of mass energies up to 200 GeV. This will make it possible to create the charged gauge bosons $W^+W^-$ in pairs. The main physical interests are the measurement of the mass of the $W^{\pm}$-pairs, the three gauge boson couplings and the search for the Higgs boson.

Of special interest for the determination of $M_Z$ is the energy calibration of LEP I. This is described in the next chapter.

### 3.1.1 The Energy Calibration of LEP

Until 1992 the measurement of $M_Z$ at LEP was limited by the LEP energy calibration. For the 1993 energy scan the method of resonant depolarization, introduced at the end of 1991, was

used throughout the entire scan. The procedure used for the calibration of the 1993 energy scan is described in detail in [23].

The electrons in LEP naturally polarize vertically due to the emission of synchroton radiation. This polarization reaches 10-20% during physics runs. The number of spin precessions per revolution $\nu_s$ depends on the beam energy. By applying an oscillating weak horizontal magnetic field the electrons can be depolarized. A depolarizing resonance occurs if the depolarizing field is in phase with the spin precession thus allowing a determination of $\nu_s$ and the beam energy. The accuracy of the energy determination with this method is better than 1 MeV.

In 1993, LEP was running at three energy points, at peak energy - 2 GeV, peak energy and peak + 2 GeV, where the peak energy corresponds to the energy of the $Z^0$-pole, $M_Z$. These energy points are called peak−2, peak and peak+2. Out of the 38 fills at peak−2 and 31 fills at peak+2 13 and 11 fills, respectively, were calibrated at the end of physics runs. From the on-peak fills only one was calibrated. Since the calibrations of the LEP energy are totally uncorrelated to changes in the energy, the calibration runs sample the LEP energy in an unbiased way. Their mean is therefore an unbiased estimate of the average LEP energy. The statistical error of the mean energy at each energy point can be obtained by their rms and the number of calibrations at this point. The statistical error at the off-peak points would be about 4 MeV. This error is large compared to the precision required. It can be reduced if sources of variation are identified and related to monitored quantities.

Changes in the LEP energy occur due to variations of the integrated bending field seen by the beam particles along their trajectory. These variations are caused by either changes in the dimensions of the ring or by changes in the magnetic field itself. Changes in the dimensions of the ring are induced in the time scale of a day by earth tides. The motion of the moon and the sun induces tides in the earth. These tides change the circumference of the LEP ring. This has an effect of up to 20 MeV for large tides. The energy variation caused by the tides were measured by several dedicated experiments [25]. Figure 3.1 shows the observed energy variation due to the tides and the model used to describe this effect. The agreement is impressive. The changes in the integrated magnetic field are monitored by measuring the currents of the magnets, their temperature and the magnetic field in a reference magnet, which is connected in series with the LEP magnets but mounted outside the LEP tunnel. The variations in the center of mass energy caused by changes in these quantities are in the range of 10 MeV.

The typical time variation of the LEP energy is of the order of 1 MeV per hour. Since the LEP experiments have slightly different efficiencies and luminosities within a fill, the LEP energy is calculated in 15 minutes intervals in each interaction point for every fill. The energy of LEP is described by a model taking the above monitored quantities and the tides into account. The LEP calibrations again sample this model in an unbiased way and the rms variation of the deviation between the calibrations and the model gives a measurement of the unmodelled effects including any possible non-reproducibility of the LEP settings. Taking additional systematic errors like uncertainties in the measurement of the average beam energy using resonant depolarization or an uncertainty of the energy difference between the electron and positron beam into account, errors of about 2 MeV for the off-peak points and 5.5 MeV for the peak point are achieved.

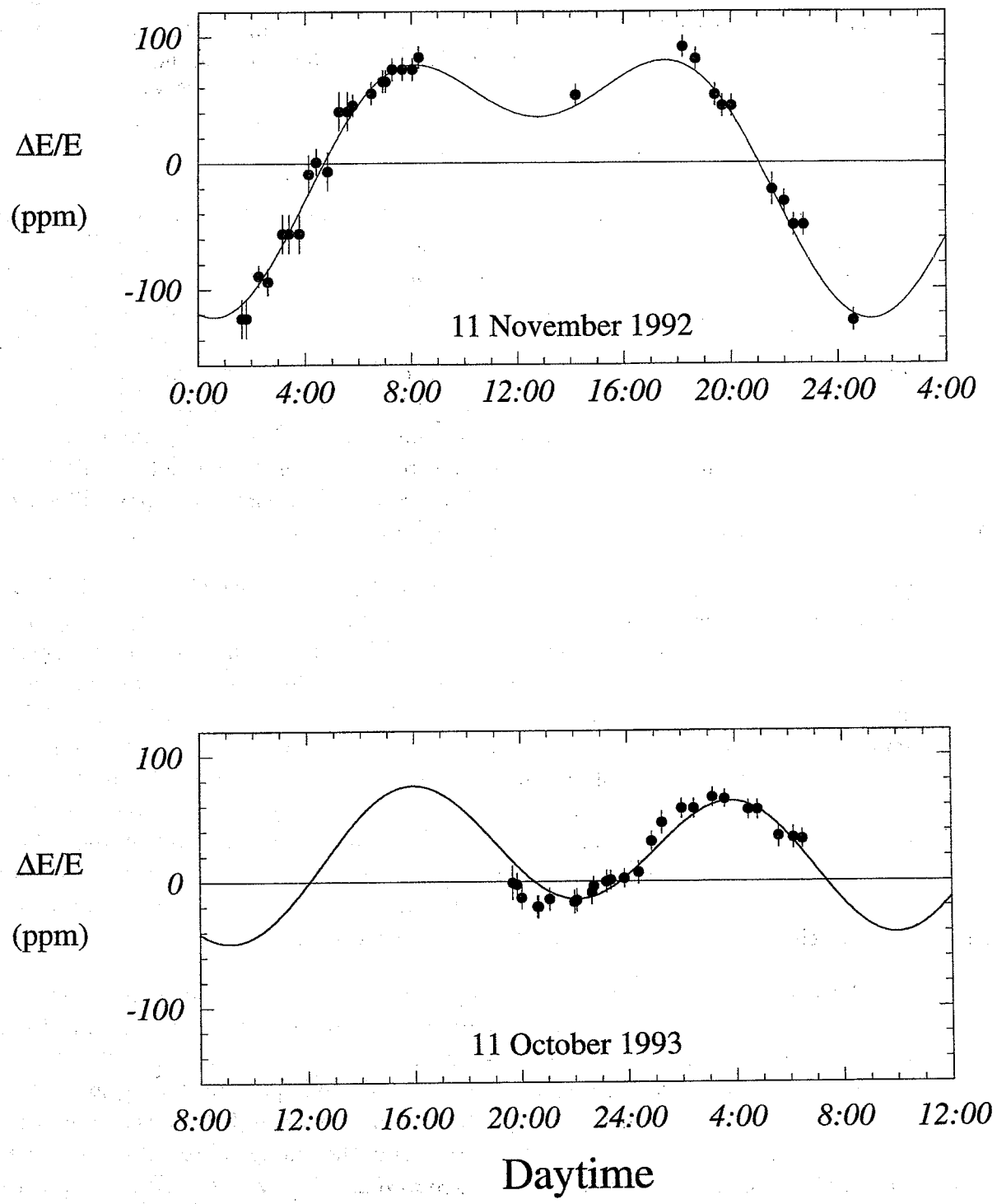


Figure 3.1: *The variation of the beam energy induced by the tides. The model and the measured values agree well.*

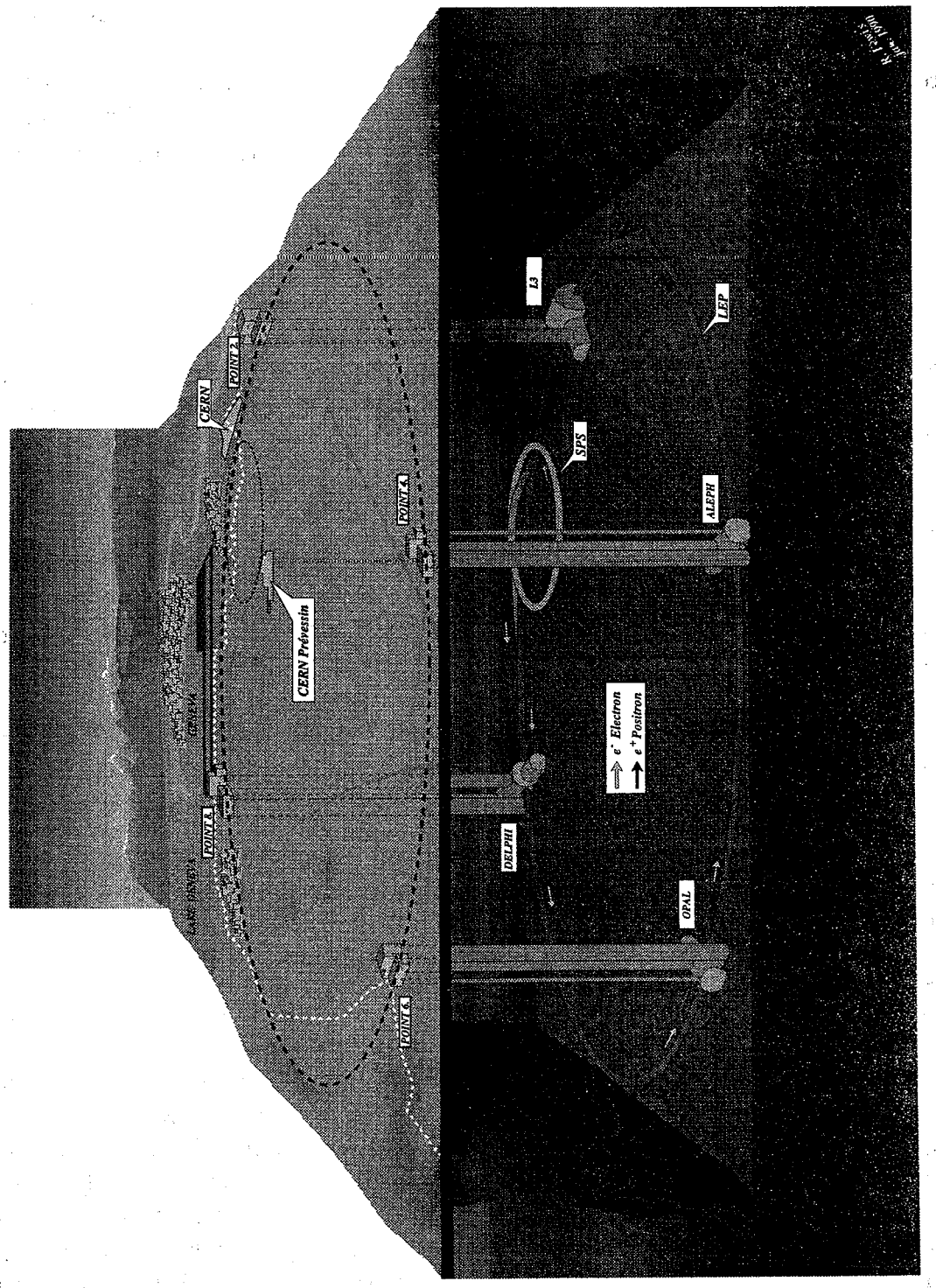


Figure 3.2: *The LEP ring.*

## 3.2 The OPAL Detector

The purpose of the OPAL detector is to measure the energy and momentum of charged and neutral particles produced in $e^+e^-$ collisions. A large angular coverage is important in order to detect all the particles produced in the reaction. The OPAL detector is explained in detail in reference [2]. Figure 3.4 shows the entire detector and figure 3.5 shows a cut perpendicular (r-$\phi$ plane) and parallel (z-direction) to the beam pipe. The detector can be devided into the central detector which consists of tracking devices, the calorimeters, and the muon system.

### 3.2.1 The Central Detector

The central detector is placed within the magnetic field of a coil. Its main task is to measure the direction and momentum of charged particles. In addition it can be used for particle identification using the specific energy loss. It contains several subdetectors (from the inside to the outside):

- **silicon microvertex detector SI**
  The innermost component of OPAL is a microvertex detector. In 1991 and 1992 the detector consisted of two layers of single sided microstrip detectors each layer allowing a determination of the $\phi$-coordinate. From 1993 onwards, each layer consisted of an assembly of two microstrip detectors mounted back-to-back. Each layer now allows a measurement of z and $\phi$. The angular region covered is $|\cos\vartheta| < 0.75$, where $\vartheta$ is the polar angle with respect to the beam pipe (z-axis). The intrinsic resolution of the microstrip detectors is 5 $\mu m$. Its main task is the precise reconstruction of decay vertices.

- **vertex chamber CV**
  The vertex chamber is a small cylindrical gas drift chamber with a length of 1 m, an inner radius of 8.8 cm and a diameter of 47 cm. The resolution in z is about 700 $\mu m$, and in the r-$\phi$ plane 55 $\mu m$.

- **jet chamber CJ**
  The main component of the central detector is the cylindrical jet chamber. It has a length of approximately 4 m, an inner radius of 25 cm and a diameter of 3.7 m. The jet chamber is devided into 24 sectors in $\phi$ each containing 159 sense wires parallel to the beam. The position reconstruction in r-$\phi$ has a resolution of 135 $\mu m$. In the z direction the position is reconstructed by charge division allowing a resolution of about 6 cm per wire. For tracks with a "CJ endpoint", i.e. tracks which leave CJ in the endcap region ($|\cos\vartheta| > 0.72$), the known radius of the outermost hit wire can be used to constrain the z-coordinate. This allows to measure the z-coordinate an order of magnitude better. Requiring at least a hit in 20 sense wires the angular acceptance is $|\cos\vartheta| < 0.96$. With a magnetic field of 0.435 Tesla the momentum resolution without multiple scattering is

$$\frac{\Delta p}{p} \approx 0.12\% \cdot p. \tag{3.1}$$

  For a track with 45 GeV this is about 9%.

- **z-chambers CZ**
  In order to improve the z measurement of tracks which leave the jet chamber radially the cylindrical part of the jet chamber is surrounded by z-chambers. The z chambers are devided into 24 sectors in $\phi$. Each sector has a length of 4.5 m, a width of 50 cm and a thickness of 5.9 cm. The sense wires are located in the $\phi$-direction, perpendicular to the beam pipe (z-direction). Their resolution in z is 300 $\mu m$ and in r-$\phi$ 1.5 cm.

  Combining all tracking detectors a $\vartheta$ resolution, measured with muon pairs, of better than 1.2 mrad is achieved.

The entire central detector is located in an aluminum pressure vessel. Outside the pressure vessel is the coil followed by the calorimeters.

### 3.2.2 The Calorimeter Region of the OPAL Detector

The main purpose of the calorimeters is to measure the energy of the particles. The segmentation of the calorimeters is used to reconstruct the position of the incident particles. The calorimeter region consists of the following parts (from inside to outside):

- **time of flight system TOF**
  The time of flight system covers the cylindrical part of the central detector in an angular region of $|\cos\vartheta| < 0.82$. It consists of 160 scintillating counters. They are mounted at a radius of 2.35 m. The time of flight system is used to identify cosmic events and it allows, together with the measured momentum of the jet chamber, to determine the mass of charged particles. The mean time resolution is 280 ps.

- **electromagnetic calorimeter ECAL**
  The electromagnetic calorimeter consists of two parts, the cylindrical part covering a region of $|\cos\vartheta| < 0.82$, and two endcap calorimeters covering a region of $0.81 < |\cos\vartheta| < 0.98$. The cylindrical part (EB) consists of 9440 lead glass blocks, each having a frontface of $10 \times 10\ cm^2$, and are 37 cm deep which corresponds to 24.6 radiation lengths. The lead glass blocks are directed towards the interaction point (pointing geometry). The two endcap calorimeters (EE) each consist of 1132 leadglass blocks. They do not have pointing geometry but are instead parallel to the beam pipe (see figure 3.5). The main purpose of the electromagnetic calorimeter is to measure the energy of photons and electrons ($e^{\pm}$). These particles lose in general all their energy in the electromagnetic calorimeter. The intrinsic energy resolution is

  $$\frac{\Delta E}{E} \approx \frac{5\%}{\sqrt{E}} + 3\%$$

  which is 4% for 45 GeV electrons. Because the particles have to transfer approximately 2 radiation lengths of material (pressure vessel and coil) before they reach the calorimeter the shower usually starts in front of the calorimeter. A presampler detector is therefore mounted in front of ECAL to measure the amount of preshowering and to give the possibility to correct for the energy loss caused by the preshowering. The energy resolution

without correction is [26]:

$$\frac{\Delta E}{E} \approx \frac{16\%}{\sqrt{E}} + 1.5\% \quad \text{for EB and}$$
$$\frac{\Delta E}{E} \approx \frac{22\%}{\sqrt{E}} + 1.8\% \quad \text{for FE.}$$

Hadrons, usually, leave just a small amount of energy by ionisation in the electromagnetic calorimeter. Occasionally they have a hadronic interaction depositing an energy up to their real energy. The average energy loss of hadrons in the calorimeter is about one third of their actual energy.
The granularity of the electromagnetic calorimeter also allows the reconstruction of the shower position.

- **hadron calorimeter HCAL**
  The hadron calorimeter consists of a cylindrical part in the region $|\cos\vartheta| \leq 0.81$, two endcap calorimeters ($0.81 < |\cos\vartheta| < 0.91$) and two poletip calorimeters ($0.91 < |\cos\vartheta| < 0.99$). Each part consists of alternating parts of iron and active layers. The iron used to initiate the hadronic shower also serves as the return joke of the magnet. The active layers are streamer tubes and wire chambers. The energy resolution of the hadron calorimeter is
  $$\frac{\Delta E}{E} \approx \frac{120\%}{\sqrt{E}}$$
  The hadron calorimeter is used to measure the energy and position of hadronic particles and to identify muons.

### 3.2.3 The Muon System

Muons lose energy only by ionisation. They therefore pass the hadron calorimeter without interaction if they have an energy of more than 3 GeV. All other particles (besides neutrinos) get absorbed. In order to detect the muons muon chambers are placed outside the hadron calorimeter. In the cylindrical region ($|\cos\vartheta| < 0.68$) the muon chambers consist of 4 layers of drift chambers. The two endcap parts cover a region up to $|\cos\vartheta| < 0.985$ and consist of streamer tubes.

### 3.2.4 The Forward Detectors

There are two different types of forward detectors: the "old" forward detector **FD** and the "new" (since 1993) silicon tungsten calorimeter **SiW**. FD was used for the luminosity measurement until 1992. After 1992 the SiW detector is used for the luminosity measurement. FD is in addition used for the selection of multi hadronic events.

The structure of FD is shown in figure 3.3. The two detector assemblies are placed around the beam pipe at a distance to the interaction point of 2.5 m. The region covered is 47 mrad

$< \vartheta <$ 120 mrad. FD is a lead scintillator sandwich calorimeter with 35 layers. The calorimeter is devided into two parts, the presampler (4 radiation lengths) and the main calorimeter (20 radiation lengths). Between the two parts are 3 layers of tube chambers for the position reconstruction. The energy resolution for electrons is

$$\frac{\Delta E}{E} \approx \frac{17\%}{\sqrt{E}}$$

which is about 3% for 45 GeV electrons.
The main calorimeter is devided into 16 $\phi$-segments. The scintillators are read out at the inner and outer edge allowing a coarse position reconstruction. The components for the precise position reconstruction of the electromagnetic showers are 3 drift chambers in front of the calorimeter and the 3 layers of proportional tube chambers between the presampler and main part of the calorimeter.

The SiW detector is described in detail in chapter 4.

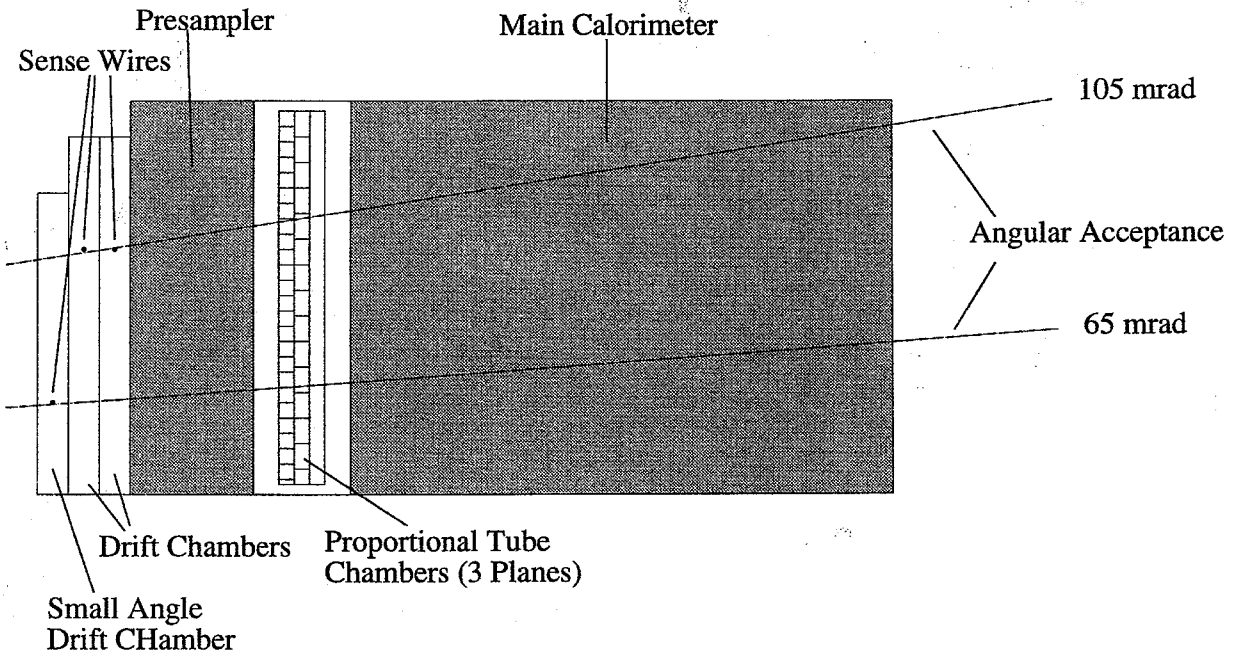


Figure 3.3: *The forward detector before 1993 (FD).*

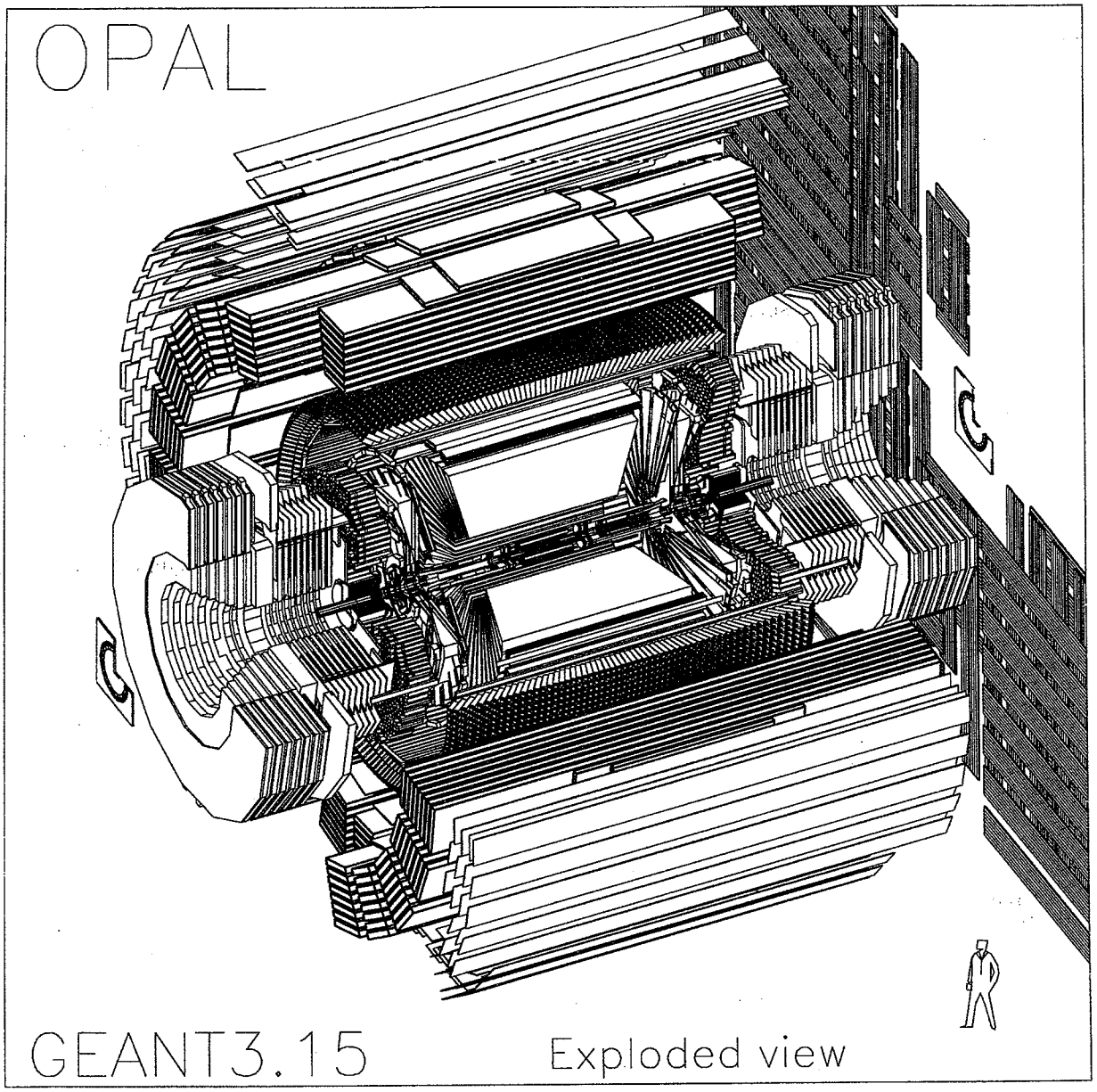


Figure 3.4: *The OPAL detector.*

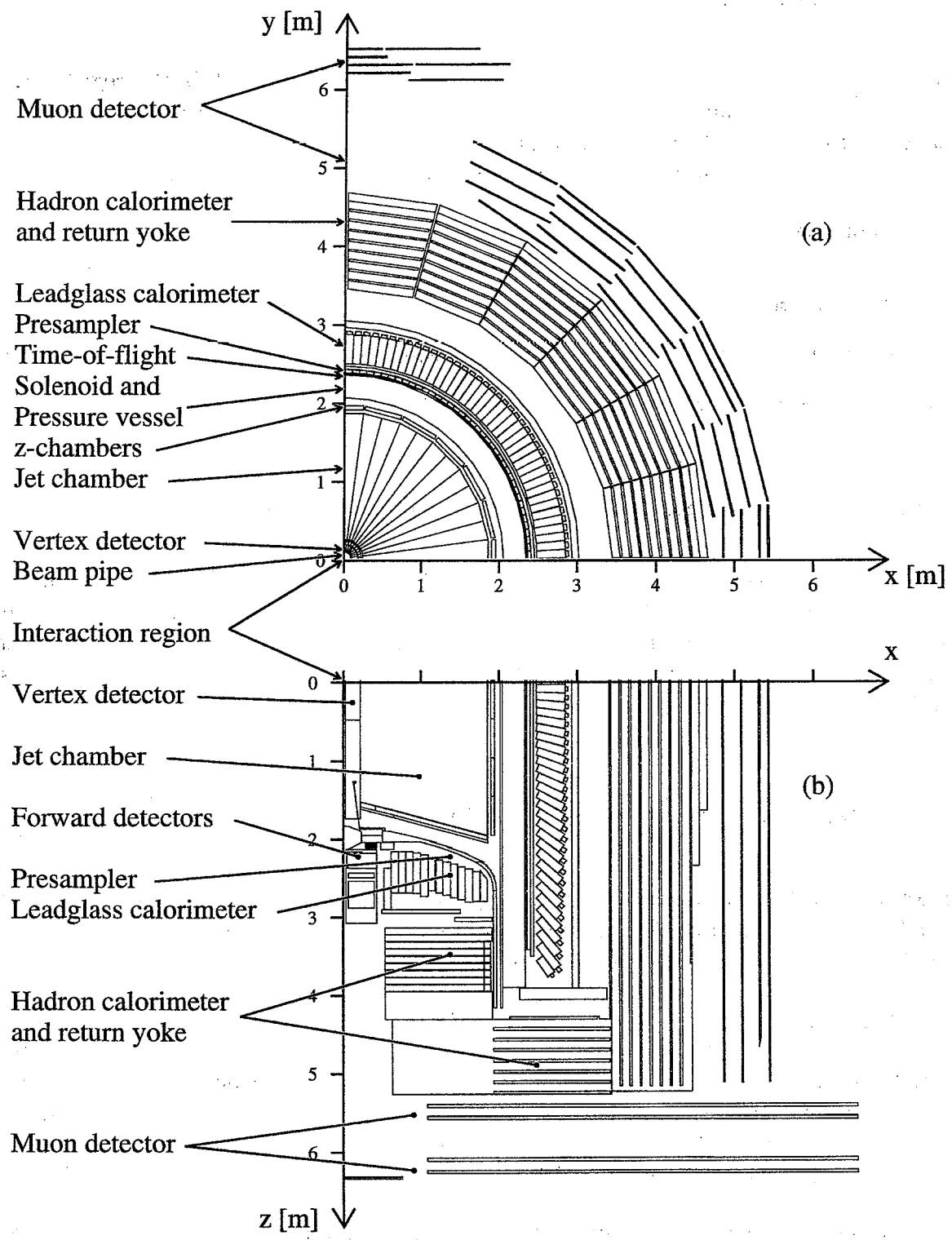


Figure 3.5: *Cut through a quadrant of the OPAL detector pependicular (a) and parallel (b) to the beam pipe.*

## 3.3 The Trigger System

The trigger system initiates the readout of the detectors. Its main task is the registration of all real $e^+e^-$ events. Furthermore it should suppress background events from cosmic radiation or reactions of the beam with remaining atoms from the gas in the beam pipe. At LEP this is easy to accomplish. The reactions have a clear signature and the background is small.

The components of the trigger are:

- the track trigger based on signals from the vertex detector and the jet chamber.
- the energy trigger, which uses the energy deposited in the electromagnetic calorimeter
- the muon trigger, derived from the muon chambers
- the multiplicity trigger, based on the time of flight counters
- the two luminosity triggers obtained from FD and the SiW calorimeter

The individual trigger signals are combined and compared to trigger conditions which are adjusted to the event topologies. The events interesting for the line shape analysis usually fulfill several trigger conditions. Since the individual trigger signals explained above are independent it is possible to determine the trigger efficiency. The trigger efficiency for the events discussed here, multihadron and luminosity events, is very close to 100% with a negligible error.

## 3.4 Monte Carlo Event Simulation

An important tool for the data analyses in high energy physics is the simulation of physics events called the Monte Carlo generation of events (MC). Monte Carlo events are used, for example, for determining selection efficiencies and backgrounds through simulation.

The generation of Monte Carlo events consists of two parts the event generator which generates production and decay of particles, and the detector simulation characterizing the response of the detector to these particles. For OPAL the program package GOPAL [3] was developed for simulating the detector response to particles. It contains a detailed description of the detector components (of both the active and passive parts) and uses the GEANT package [4] to simulate the interaction of particles with the detector material.

Among others an event generator relevant for the analysis of $e^+e^- \rightarrow hadrons$ is the JETSET Monte Carlo [15]. The process $e^+e^- \rightarrow hadrons$ can be devided into 4 parts (see figure 3.6).

- **Pase I**
  In the first phase $e^+$ and $e^-$ annihilate to a $Z^0$ (dominant process) or a photon. The $Z^0$ or $\gamma$ decays to a $q\bar{q}$ pair. This process is calculable within the Standard Model to a very high accuracy (see chapters 2 and 8.1).

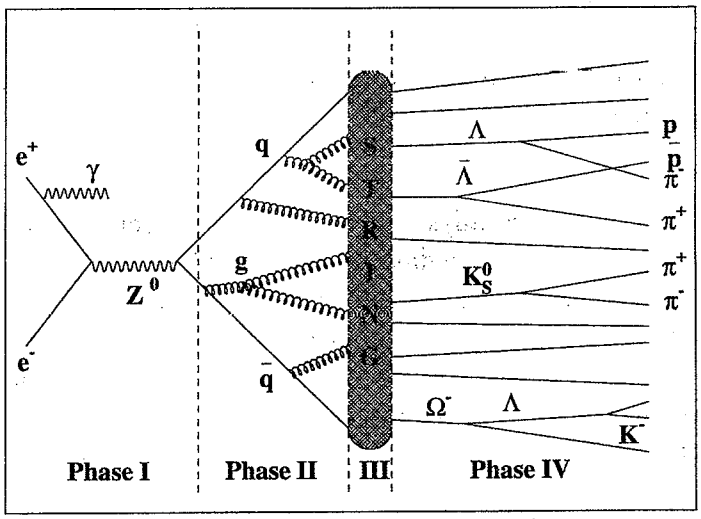


Figure 3.6: *Phases of the process* $e^+e^- \rightarrow$ *hadrons.*

- **Pase II**
  The two quarks move away from the interaction point and radiate gluons. The gluons can convert to further $q\bar{q}$ pairs or generate more gluon pairs. Phase II can be calculated with perturbation theory in QCD as long as the strong coupling constant $\alpha_s$ is small. The coupling constant $\alpha_s$ depends on the momentum transfer $q^2$ of the partons, in leading order

$$\alpha_s(q^2) = \frac{4\pi}{\left(11 - \frac{2}{3}N_f\right) ln\left(\frac{q^2}{\Lambda^2_{QCD}}\right)} \tag{3.2}$$

  where $N_f$ is the number of active quark flavours (here five) and $\Lambda_{QCD}$ is the QCD scaling parameter. In the limit $q^2 \rightarrow \infty$, $\alpha_S$ becomes small $\alpha_s \rightarrow 0$. At small energies ($q^2 \rightarrow 0$) $\alpha_s$ increases and the perturbation theory does not converge. A cut-off parameter $Q_0$ is therefore implemented in JETSET at which the parton shower stops. $Q_0$ is the invariant mass below which partons do not radiate gluons, usually 1 GeV.

- **Pase III**
  In phase III $q^2$ has decreased and thus $\alpha_s$ is large and the processes can no longer be calculated in perturbation theory. Therefore, phenomenological models motivated by QCD are used. The model used by JETSET is the so called "string model". It is based on the assumption that the potential between two quarks is proportional to their distance. A colour tube is formed between two quarks which fly apart. This is called a string. The energy of the string increases until there is enough energy to produce a $q\bar{q}$ pair which breaks the string into two pieces. If it has enough energy each string can form another $q\bar{q}$ pair. The transition from the string to hadrons is called hadronisation. This process is described by empirical fragmentation functions. The description of the entire

fragmentation process has many parameters ($\mathcal{O}(200)$). Here, one parameter of particular interest is $\sigma_q$. It determines the transverse momentum spectrum with respect to the string axis of the hadrons generated during hadronisation.

- **Pase IV**
  The hadrons decay to the particles visible in the detector. Decay tables determined from measurements are used.

The parameters of JETSET are adjusted such that the generated events most resembles data [17]. The variables used to compare data and Monte Carlo are the particle multiplicity and global event shape variables like thrust or sphericity. The parameters can only be determined with a limited accuracy. The parameters which are of particular interest for the selection of multi hadron events are $\Lambda_{QCD}$ which influences the rate of three and four jet events, $Q_0$ which affects the particle multiplicity, and $\sigma_q$ which controls the width of the jets. Uncertainties in these parameters affect the determination of the selection efficiency.

Another event generator for the process $e^+e^- \rightarrow \textit{hadrons}$ is HERWIG [16]. Instead of the string fragmentation in phase III it uses cluster "fragmentation". At the end of phase II neighbouring $q\bar{q}$ pairs are combined to clusters which isotropically decay to hadrons or to two clusters if the cluster energy is too big. Herwig is here used as a cross check to determine the selection efficiency of multi hadron events.

# Chapter 4

# The SiW-Detector

In 1993 a new forward detector for the luminosity measurement, the Silicon-Tungsten Detector, was installed in OPAL. The main requirements for the new luminosity monitor of OPAL is a high geometrical accuracy on the inner boundary to better than 25 $\mu m$ (see chapter 5). A second requirement, due to the limited space available for the installation, is compactness. This almost necessarily leads to the utilization of semiconductor detectors. Their production process is intrinsically accurate to a few microns ($\sim 3\mu m$). The silicon wafers can be very well aligned in the overall detector assembly and, using tungsten as absorber material, a compact calorimeter can be built. This chapter describes the new Silicon-Tungsten-Calorimeter (SiW) of OPAL used for the luminosity measurement.

## 4.1 Mechanics

The Silicon-Tungsten luminosity detector (SiW) consists of two calorimeters each encircling the beam pipe at a distance of 2389 mm on either side of the interaction point. Each calorimeter weights about 100 kg, has an inner radius of 57.5 mm, an outer radius of 370 mm and a total depth of 170 mm. Figure 4.1 shows one calorimeter. Each calorimeter consists of two "C" shaped half detectors. Each "C" is made of an alternating stack of 18 tungsten plates and 19 layers of silicon detectors. The first layer (seen from the interaction point) is an active layer. The next 14 layers are each a layer of tungsten, 1 radiation length (1 $X_0$) thick, followed by a layer of silicon detectors. The last four layers are four layers of tungsten, 2 $X_0$ thick, again followed by an active layer. Figure 4.2 shows a cut through the detector. Electromagnetic showers, initiated by 45 GeV electrons, are almost entirely contained within the 22 radiation lengths represented in total by the tungsten layers.

Each of the 19 layers in the stack consists of a precision machined tungsten half disk glued at the inner radius of a 2 mm thick aluminum support plate. The support plate carries also 8 silicon detectors mounted on top of the tungsten and a semi-circular motherboard (see figure 4.3). The tungsten is only missing in the last layer as it is not followed by an active layer. Mechanically the 19 layers are aligned, and kept in place, by two 15 mm precision dowels which penetrate the entire stack including the aluminum front and rear plates. Spacers are mounted at the inner

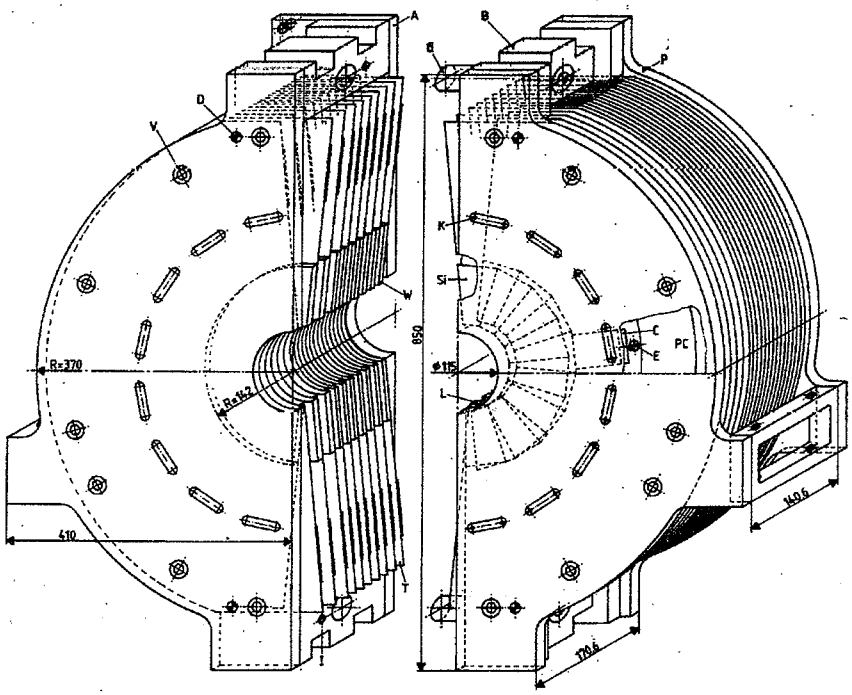


Figure 4.1: *The SiW detector.*

and outer radii of each layer to limit distortions out of the z-plane. The z-position is further constraint by clamps on the cooling pipes which ensures adequate thermal conductivity. Each calorimeter "C" is penetrated by 16 3mm water cooling pipes at a radius of 220 mm which is as close as possible to the front end electronics, the source of the 170 W generated during operation. A flow of 3 l/min of 16° C water per calorimeter maintains the average of 21.5 ± 0.2° C during operation. The two half calorimeters are aligned with respect to each other by two massive brass dowels. They have to ensure that no silicon detectors are damaged during the closing procedure.

## 4.2 Silicon Detectors

Each half layer of the calorimeter contains 8 overlapping silicon wafers. The wafers overlap to ensure that there is no dead region between the silicon detectors (see figure 4.4). The clearance between the wafers is 300 $\mu m$. Every second layer is rotated by 11.25° (half the silicon wafer width) to minimize possible systematic effects in the overlap region.

The wafers are low conductivity n-silicon, 310.8 ± 1.5 $\mu m$ thick. To contact the n material of the bulk the back side entirely consists of a $n^+$ implant contacted by an evaporated gold layer. The front side is devided in two columns, 11.25° wide, in azimuthal angle and in 32 radial pads each 2.5 mm wide (see figure 4.5).

The pads consist of a $p^+$ implant to form a diode structure with the n-silicon of the bulk.

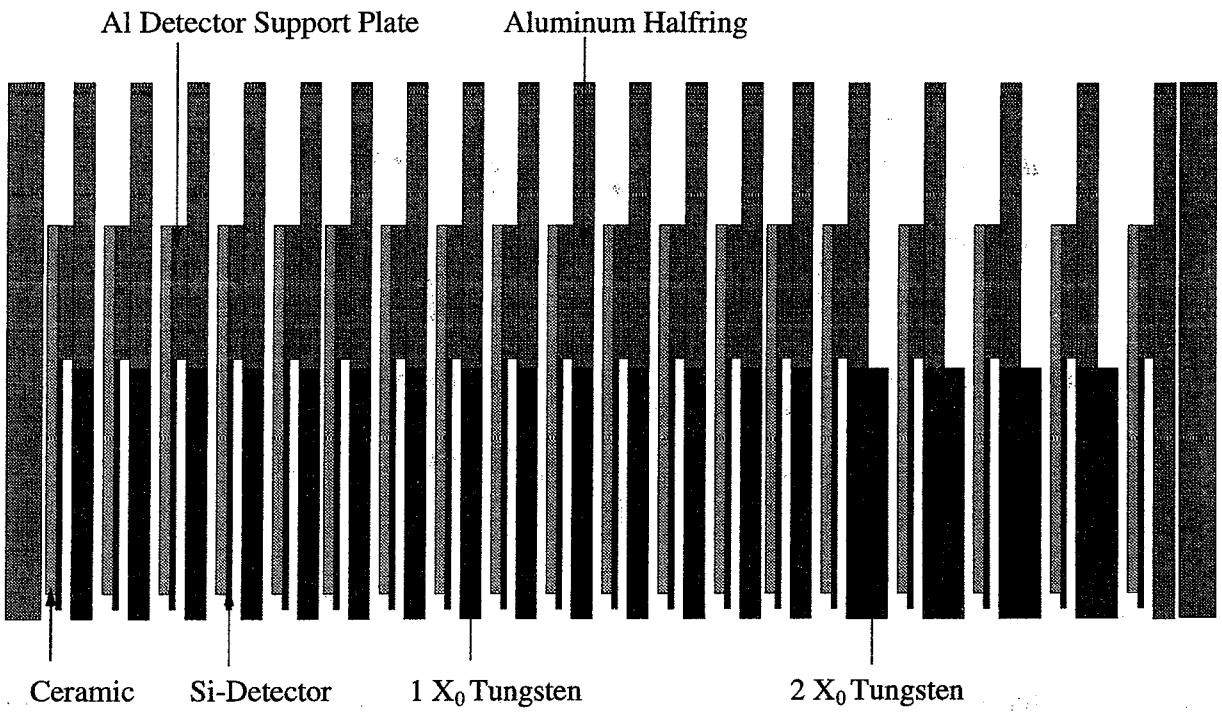


Figure 4.2: *Cut through the SiW detector. The first layer (layer 1) is the left most layer. Layer 19 is the rightmost layer. The electrons enter the detector from the left.*

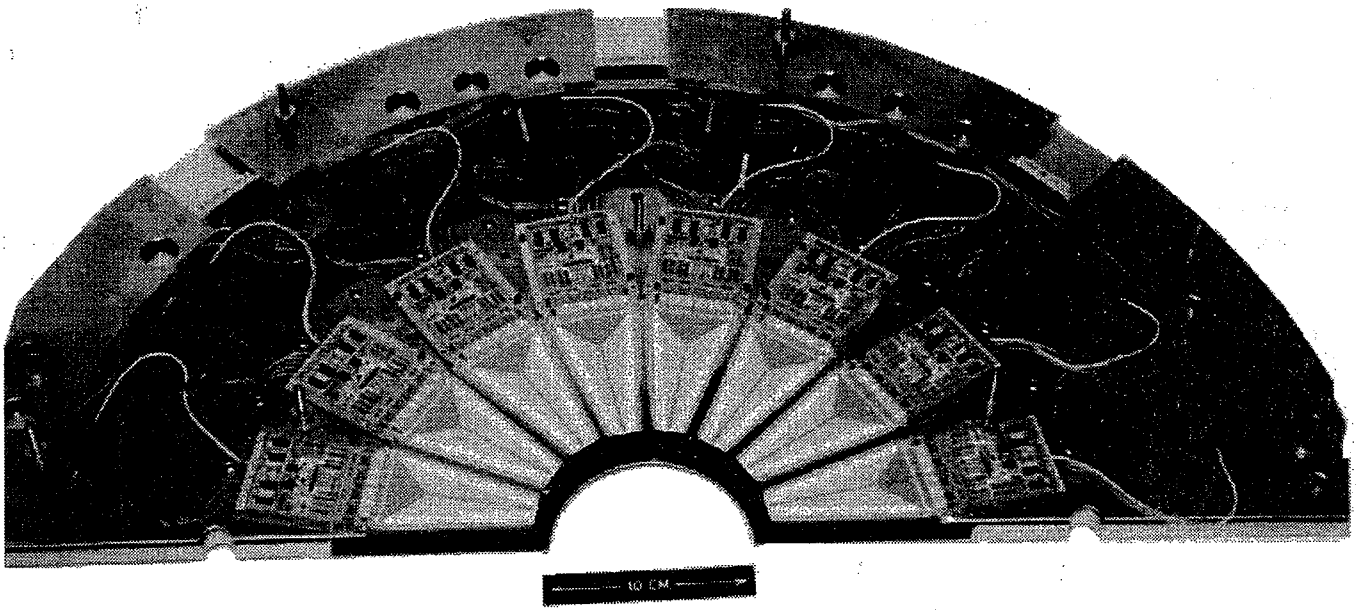

Figure 4.3: *A half layer equipped with 8 detector ceramics and the motherboard.*

A guard ring structure ($p^+$ implant) is implanted on the front surface of the wafer just outside the diode implants to control the potential outside the active area of the wafer. All $p^+$ implants are covered with a layer of aluminium. A protection layer of polymide is applied on the entire front face except on a window of 2×5 mm on each pad which is used to contact the pads by ultrasonic wire bonding with an aluminum wire.

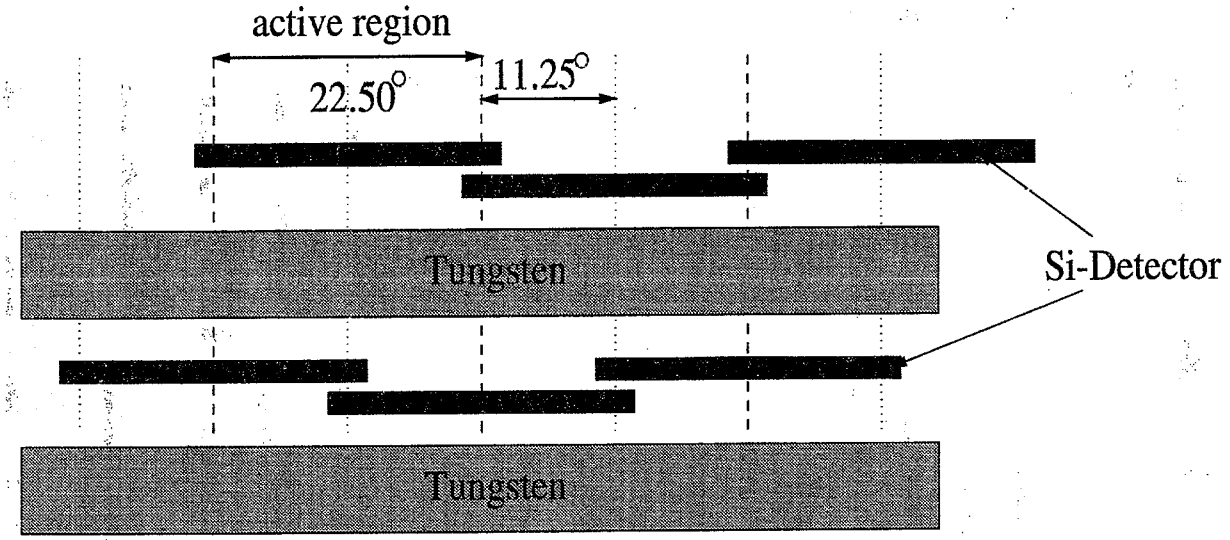


Figure 4.4: *Cut trough a half layer, overlapping and rotation of the silicon detectors.*

Before installation, each wafer was tested to determine the leakage current of every pad and the depletion voltage. The depletion voltage is the bias voltage at which the depleted region of the diode structure in the n-bulk completely extends from the front face to the back side. The leakage current is the current which flows when the detector is biased (the diode structures are reverse biased). The depletion voltage ranges from 60 to 70 V with an average of 62 V. Therefore a bias voltage of 80 V is chosen to ensure full depletion of all wafers. The leakage current at 80 V is about 0.7 nA/pad. It has to be $< 100$ nA/pad to ensure the front end amplifiers to operate within specifications.

The implant side of the silicon detector is glued to a thick film hybrid ceramic which carries the front end electronics. After experimenting with several different techniques a procedure was found such that the leakage current did not increase after gluing. In standard detector setups the silicon detectors are glued to the support structure on the back side where it has no implants. The technique used here has the advantage of a very compact detector ceramic structure which fits well between the tungsten plates.

Figure 4.6 shows a wafer ceramic assembly.

## 4.3 Readout Electronics

The total number of read-out channels is $64 \times 16 \times 19 \times 2 = 38912$ (pads/detector $\times$ detectors/layer $\times$ number of layers/calorimeter $\times$ number of calorimeters). This large number of channels is read out by the help of multiplexer chips which are mounted on the detector ceramics. This chip, the OPAL AMPLEX chip, is essentially the AMPLEX-SICAL chip [11] with slight modifications in the input protection circuit. The AMPLEX-SICAL itself is an upgrade of the UA2 AMPLEX [12], designed for the Si preshower detector of UA2. The AMPLEX reads 16 input channels and multiplexes them to a single output line. Figure 4.7 schematically shows the AMPLEX chip. It contains circuitry to amplify, shape and hold the signals from the

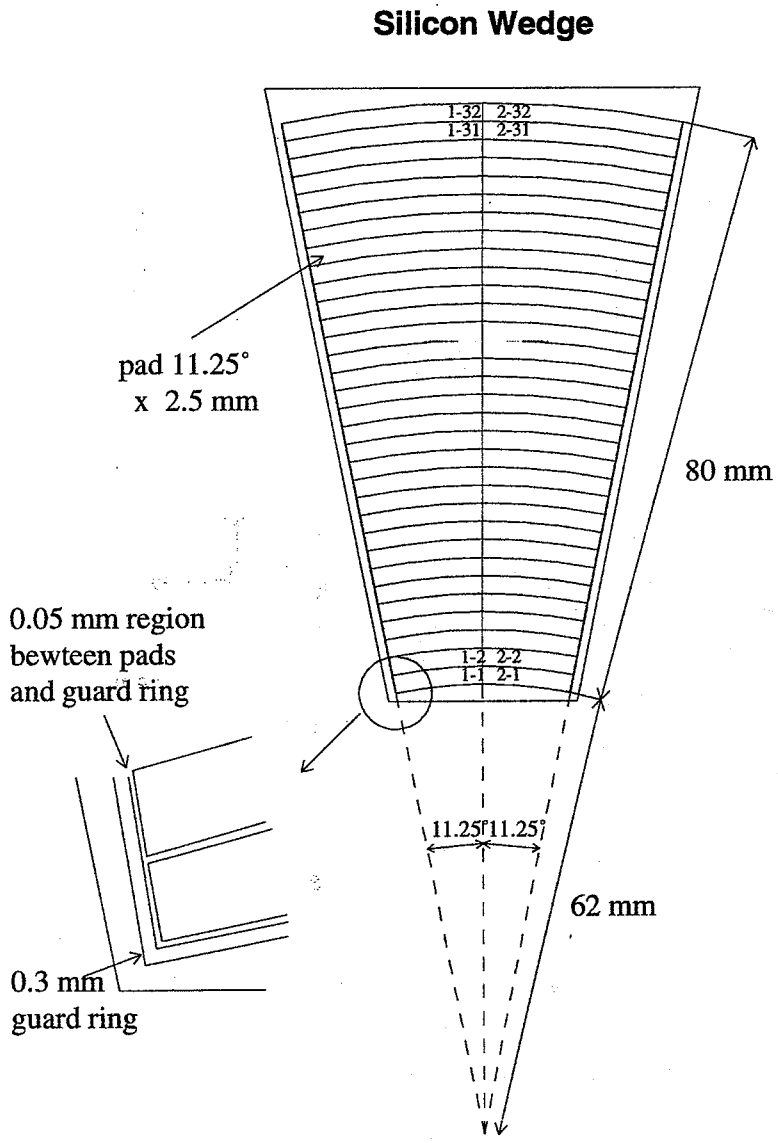


Figure 4.5: *Schematic of a silicon wafer.*

silicon detector. It has also the possibility to calibrate the internal gain of the AMPLEX by applying a constant voltage to the calibration input and putting this voltage sequentially onto the 16 inputs. This is done by using the calibration shift register. To initiate a readout of the AMPLEX a hold signal has to be applied to the T/H (track and hold) line, so that the signals of the shaper circuit are stored on the hold capacitor $C_h$. The voltages on the hold capacitors are then read out by connecting them sequentially to a single output line through the switches SWB1 to SWB16. These switches are transistors which are turned on under control of the readout shift register. To generate the trigger signal all 16 input channels are connected to the

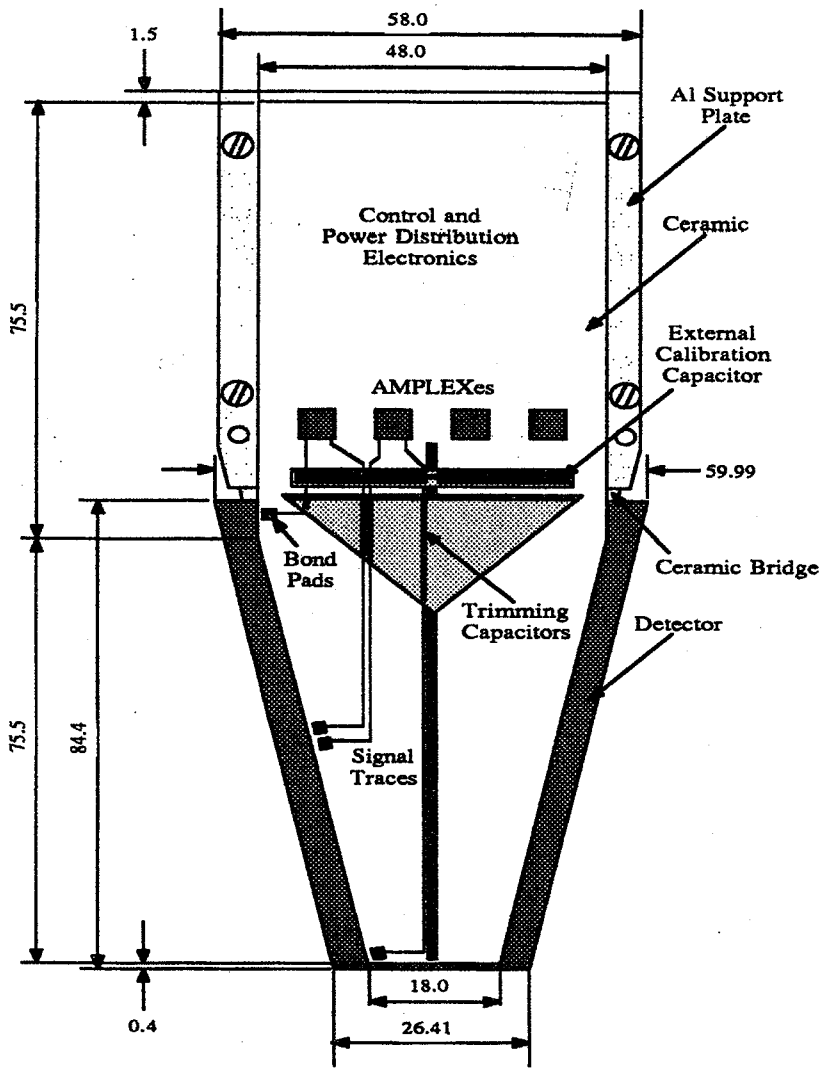


Figure 4.6: *Schematic of a wafer ceramic assembly.*

output and the switches SWC for the hold capacitor are switched on to allow the voltage on $C_h$ to follow the input signal (tracking mode). This generates a fast average of the 16 input lines which is used for the trigger. The AMPLEX chip is optimized for calorimetric measurements. It has a large dynamic range of $\sim$ 1-1000 MIPS, where one MIP (minimum ionizing particle) liberates about 23500 electrons in a 300 $\mu m$ thick silicon wafer. The range of the signals in the calorimeter ranges from 1 to $\sim$600 MIPS.

To read out an entire wafer (64 pads) 4 AMPLEX chips are required. They are glued

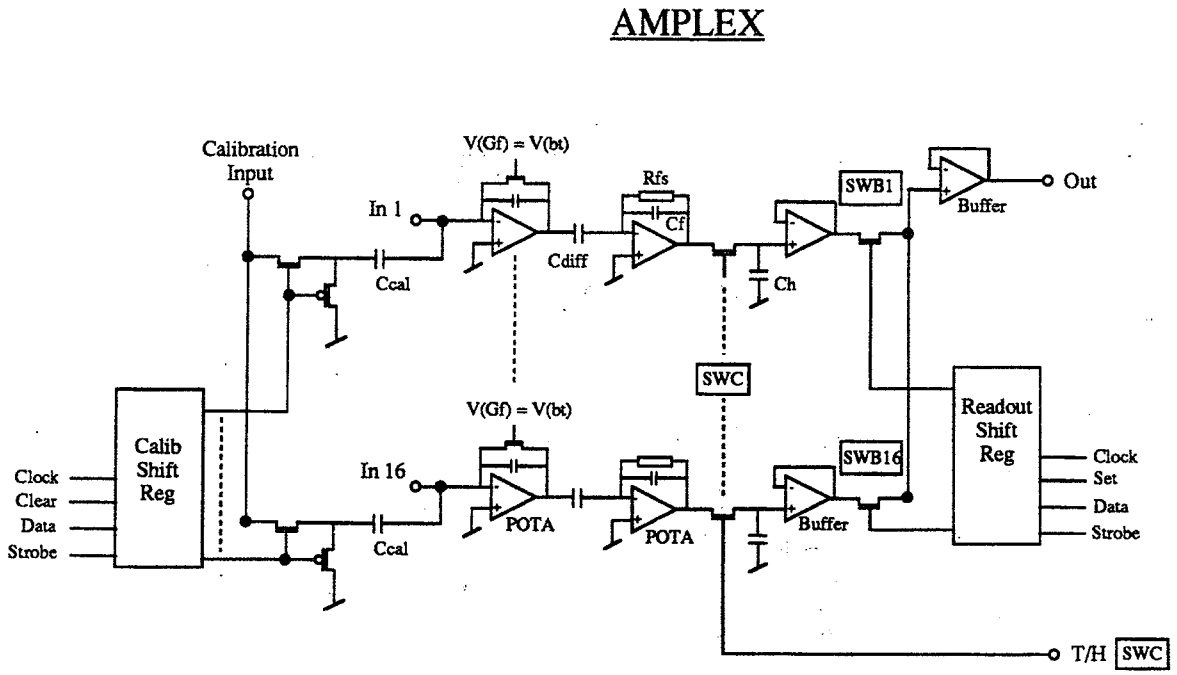


Figure 4.7: *Schematic of an AMPLEX chip.*

on the thick film ceramic which in turn is glued on the silicon wafer. Each of the 64 pads on the wafer is connected, with wire bonding, to individual traces on the ceramic leading to the AMPLEX input. Trimming capacitors are included into each trace to compensate for the different capacitance of the pads due to the varying pad sizes. Figure 4.6 shows the detector ceramic with the 4 AMPLEX chips. Figure 4.8 shows a schematic diagram of the electronics on the ceramic. Further included on the ceramic is a four-to-one multiplexing of the four AMPLEX outputs to a single output line, as well as circuitry for calibration, for providing stabilized bias and to generate the control signals using the control signals received from the SEQUENCER module. Each of the 8 thick film ceramics on a half-layer is connected to a half circular motherboard mounted on the aluminum half-layer. This motherboard distributes the signals obtained from the external modules to the single ceramics and combines the output lines of the ceramics.

## 4.4 Readout and Control System

The control of the AMPLEX chips and their readout is accomplished using two VME-sytem based custom build modules, the DIGITIZER and the SEQUENCER. The readout and control system is designed to run independently of other VME processes. One DIGITIZER has inputs for 32 silicon wafers (2048 channels). It is built around a 14-bit analog to digital converter, ADC, with 2 $\mu s$ conversion time. The DIGITIZER also provides 32 fold multiplexing of the

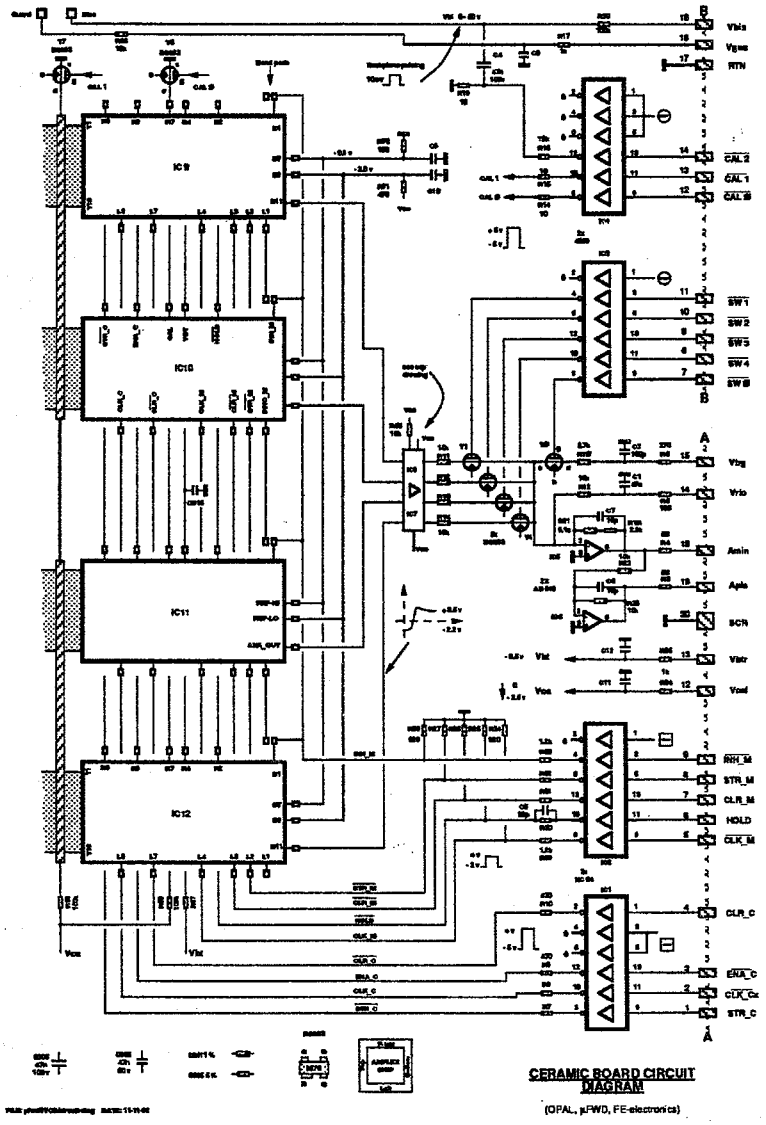


Figure 4.8: *Schematic diagram of the detector ceramic.*

input signals and the capability of analog gain and pedestal correction on a channel by channel basis. It contains double-buffered dual-port memory for data storage and a VME interface.

The master controller of the readout process is the SEQUENCER. It controlls the DIGITIZERs via a custom VME bus, sends timing and control signals to the AMPLEX chips and notifies the CPU when event digitization is complete. The CPU, a Motorola MVME 167, then reads the digitized signals from the memory of the DIGITIZERs.
At the beginning of each read out cycle the AMPLEX chips are set to track mode. The hold

signal is applied 300 ns after the beam crossing signal which is provided by LEP. When the trigger initiates a readout the SEQUENCER sends the control signals to the AMPLEXes and the DIGITIZERs. Ten DIGITIZERs for each calorimeter convert in parallel the input signals. The entire readout time is 3.5 ms. If the trigger does not initiate a readout cycle the hold signal is reset.

## 4.5 The Trigger of the SiW-Detector

The trigger of the SiW-detector is designed to be 100% efficient for Bhabha events which are used for the luminosity measurement. It is, therefore, adapted to the topology of Bhabha events, i.e. the signals in the two calorimeters are back-to-back and have almost beam energy. The analogue averages of the signals from the four AMPLEX chips on a ceramic are used to generate the trigger signal. The average of 9 even and 9 odd layers are summed such that the average of all ceramics which are mounted behind each other at the same $\phi$-segment form tower signals. Since each layer consists of 16 detector ceramics there are two sets of 16 tower signals, one from the even layers and one from the odd layers. For both calorimeters these two sets overlap by half a silicon wafer segment (see figure 4.4). The tower sums are then used to form the following trigger signals:

- **SWSEG**
  SWSEG requires more than 15 GeV deposited in back-to-back towers. This aimes at detecting back-to-back Bhabha events.

- **SWHILO**
  SWHILO requires more than 5 GeV on one side in coincidence with more than 35 GeV on the other side without the back-to-back requirement. This trigger is formed to have a second trigger, independent from SWSEG, to be able to determine the trigger efficiency and to establish a trigger for highly radiative Bhabha events.

- **SWSEGA**
  This trigger imposes the SWSEG requirement on the current event and on an event recorded 8 bunch crossings before. It is used to determine the rate of accidental coincidences of off-momentum electrons faking a Bhabha event.

# Chapter 5

# The Luminosity Measurement

## 5.1 Introduction

The luminosity is needed in order to measure cross sections. The rate $\dot{N}_X$ of interactions of type $X$ can be expressed as

$$\dot{N}_X = \sigma_X \cdot L \tag{5.1}$$

where $\sigma_X$ is the cross section of the relevant interaction. $L$, the luminosity, is a machine parameter, it defines the number of collisions per $cm^2$ and second. In a storage ring, like LEP, the luminosity is

$$L = \frac{N_{e^+} N_{e^-} N_{bunch} c}{A \cdot l} \tag{5.2}$$

Where $N_{e^+,e^-}$ is the average number of electrons or positrons per bunch and $N_{bunch}$ is the number of bunches which come into collision, $l$ is the length of the ring and A is the collision area. At LEP energies the velocity of the electrons is practically c. These parameters can not be measured with sufficient precision, and, therefore, the luminosity is determined by means of a reference interaction, the small angle Bhabha scattering, using equation 5.1.

$$L = \frac{\dot{N}_{Bhabha}}{\sigma_{Bhabha}} \tag{5.3}$$

Bhabha scattered events, $\dot{N}_{Bhabha}$, are counted in a well defined angular region (fiducial volume) and normalized to the calculated cross section $\sigma_{Bhabha}$. The calculated cross section

$$\sigma_{Bhabha} = \int \frac{d\sigma(e^+e^- \to e^+e^-)}{d\Omega} d\Omega \tag{5.4}$$

is usually not obtained by a simple geometrical integration but it is determined using a Bhabha event generator and detector simulation to take the event selection cuts into account.

At small angles Bhabha scattering is dominated by pure t-channel $\gamma$-exchange and is therefore calculable with a very high accuracy. At LEP it is the only reaction which has comparable statistics to multi hadronic events (about a factor of 2 more than $e^+e^- \to$ hadrons depending on the angular region). It is therefore the ideal reference process to measure cross sections. The

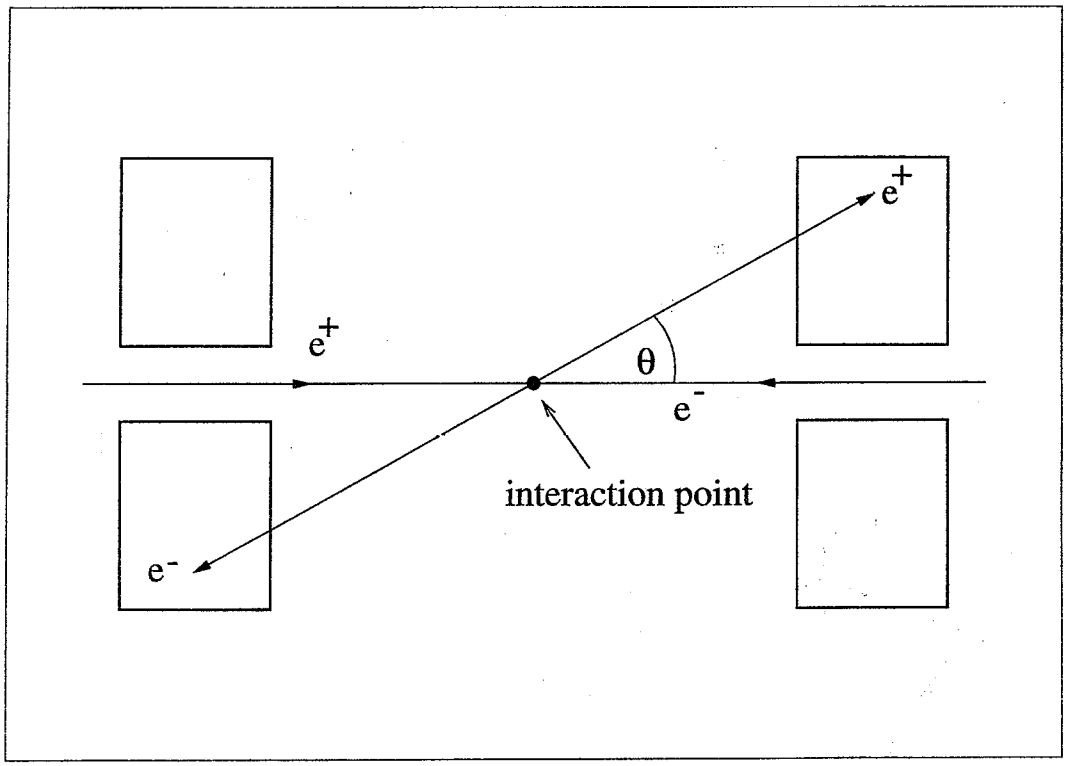


Figure 5.1: *Bhabha scattering.*

Bhabha scattered electrons have a clear signature: they are back-to-back and possess beam energy (see figure 5.1).

Using the two lowest order QED diagrams one obtains for the differential cross section (see chapter 2):

$$\frac{d\sigma}{d\Omega} = \frac{\alpha^2}{s}\left[\frac{1}{4}\cdot\frac{1+\cos^4\frac{\vartheta}{2}}{\sin^4\frac{\vartheta}{2}} + \frac{1}{8}\left(1+\cos^2\vartheta\right) - \frac{1}{2}\cdot\frac{\cos^4\frac{\vartheta}{2}}{\sin^2\frac{\vartheta}{2}}\right] \tag{5.5}$$

At small angles this behaves as:

$$\frac{d\sigma}{d\vartheta} \approx \frac{1}{\vartheta^3} \tag{5.6}$$

Due to the very steep behaviour of $d\sigma/d\vartheta$ (formula 5.6) one of the main problems for a precision measurement is the knowledge of the absolute coordinate of the inner acceptance boundary. This was the main limitation for the luminosity measurements before 1993.

To demonstrate the development in the luminosity measurement fig. 5.2 shows the luminosity monitor of the TASSO experiment at PETRA (1979-1985). It consisted on each side of four single detector assemblies. Each of these assemblies has two acceptance defining scintillation counters (counter A and C) in front of the lead glass blocks of the forward detector. Bhabha events were required to have two coincidences of the counters A and C on diagonally opposit sides. The energy deposited in the forward detector had to be at least 3 GeV. This detector allowed a luminosity measurement with a systematic error of 3-5% [10]. The "old" OPAL forward detector (FD) (see section 3.2.4), as an example of the next generation luminosity detectors, was experimentally systematics limited at 0.41% [9]. The new SiW luminosity detector of OPAL is designed to achieve an experimental systematic error of 0.1%.

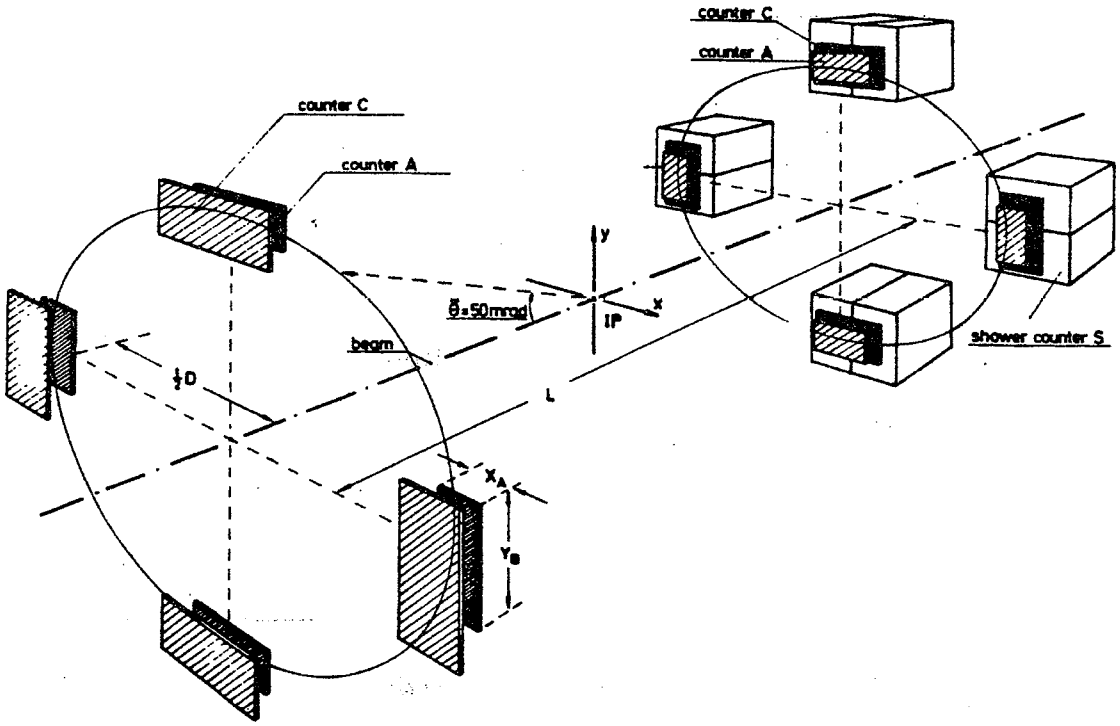


Figure 5.2: *The luminosity detector of the Tasso experiment.*

## 5.2 Geometrical Sources of Systematic Errors

Because of the $1/\vartheta^3$ behaviour of the differential cross section and its integration over the acceptance region the main sources for systematic errors arise from the definition of the acceptance boundaries. In the following the error in the luminosity due to different uncertainties in the detector geometry is discussed. The derivation of the formulae can be found in appendix A.1. The relevant variables are defined in figure 5.3.

- **Uncertainty in the inner edge of the acceptance boundary**

  Any offset $\Delta R_{inner}$ in the inner edge of the acceptance boundary will influence the luminosity as:

  $$\frac{\Delta L}{L} = 2\frac{\Delta R_{inner}}{R_{inner}} \frac{1}{1-\left(\frac{R_{inner}}{R_{outer}}\right)^2} = \frac{\Delta R_{inner}}{25\ \mu m} \cdot 10^{-3} \tag{5.7}$$

  Where $R_{inner}$ and $R_{outer}$ are the radii of the inner and outer acceptance boundaries of the SiW detector.

  An uncertainty in the inner edge of the acceptance boundary of only 25 $\mu m$ would already cause a systematic error on the luminosity measurement of $10^{-3}$.

- **Uncertainty in the outer edge of the acceptance boundary**

  The outer acceptance boundary is less critical:

$$\frac{\Delta L}{L} = \frac{\Delta R_{outer}}{110\ \mu m} \cdot 10^{-3} \tag{5.8}$$

- **Uncertainty in the distance between the two calorimeters**

  An uncertainty $\Delta Z$ in the half-distance of the two calorimeters would influence the luminosity as:

$$\frac{\Delta L}{L} = 2\frac{\Delta Z}{Z} = \frac{\Delta Z}{1.23\ mm} \cdot 10^{-3} \tag{5.9}$$

- **Vertical displacement of one calorimeter**

  A vertical displacement $\Delta S$ of one detector or a displacement of the beam with respect to the nominal beam line results in a second order effect on the luminosity.

$$\frac{\Delta L}{L} = 2\left(\frac{\Delta S}{R_{inner}}\right)^2 = \frac{\Delta s^2}{2.96\ mm^2} \cdot 10^{-3} \tag{5.10}$$

From the above relations it is clear that the key to a luminosity measurement with a systematic error of less than $10^{-3}$ is the knowledge of the inner edge of the acceptance boundary to better than 25 $\mu m$. Other geometrical effects cause a much smaller error in the luminosity. This, on one hand, requires a detector which can be produced with a very high geometrical accuracy and stability, and, on the other hand, since possible biases in the coordinate reconstruction have to be added to the geometrical uncertainty, an essentially bias-free coordinate reconstruction.

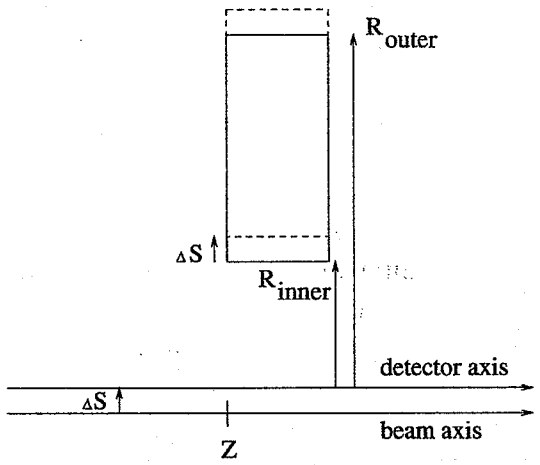


Figure 5.3: *Definition of the geometry of the fiducial volume.*

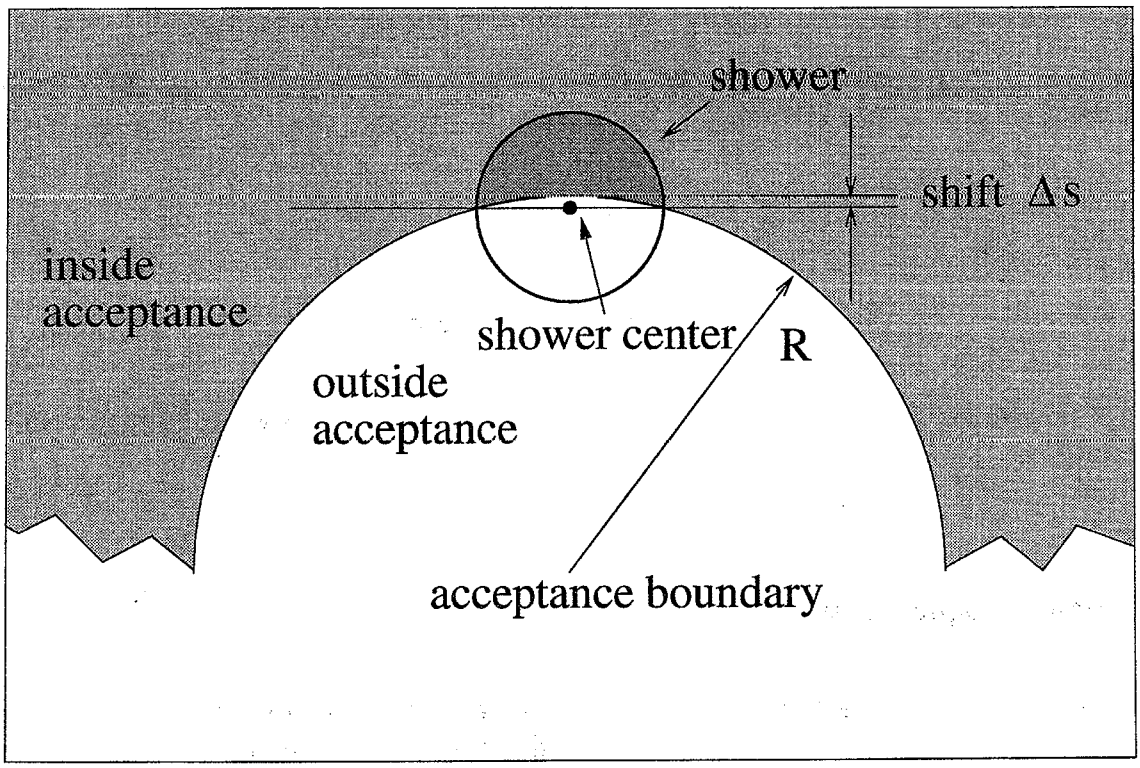


Figure 5.4: *Geometric effect of the $r-\phi$-geometry: the shower center is still outside the acceptance region when already 50% of the energy is inside.*

## 5.3 Analysis Strategy

For the luminosity measurement it would in principal be sufficient to count all Bhabha events inside a given acceptance region. The round shape ($r-\phi$ geometry) of the SiW-detector, however, causes the shower center (which is on average the true position of the incoming electron) to be outside the acceptance region when the shower is reconstructed at the acceptance boundary, i.e. when 50% of the energy is already inside. This is illustrated in figure 5.4. A simple counter which counts all events with at least 50% of the energy inside the acceptance region would, therefore, have an effective inner acceptance boundary not at the geometrical acceptance boundary R but at a radius which is reduced by the shift $\Delta s$, $R+\Delta s$,($\Delta s < 0$). The shift was measured in a testbeam as explained in the next chapter.

The shift $\Delta s_{shower}$ for an individual shower depends on the shower width and, therefore, the average shift $\Delta s$ depends on fluctuations of the showers and the amount of material in front of the detector. A detector simulation would have to correctly account for the amount and geometrical distribution of material in front of the detector and the fluctuations of the showers in order to have the same average shift as measured in data. One part of the material in front of the detector are the cables of the microvertex detector. They have a rather undefined geometrical position which slightly changes from year to year. Furthermore, the modelling of the widths of showers and their fluctuations is a notorious problem for detector simulations. Any uncertainty in the difference of the shift between data and Monte Carlo simulation directly translates (through formula 5.7) to a systematic error of the luminosity measurement. The decision was therefore made not to use a detector simulation to extract the cross section for

the luminosity selection but to directly use generated four vectors of a Bhabha event generator. The acceptance defining selection cuts on the radial coordinate R are made directly on the coordinate of the four vectors. For the energy cut a parametrization obtained from data is used.

Other reasons like an acollinearity cut or a cut on the average R-position on both sides, make it desirable to have a full coordinate reconstruction. Since any bias, like the shift $\Delta s$, in the coordinate reconstruction is not taken into account by the detector simulation this requires a bias free coordinate reconstruction. The coordinate reconstruction is, therefore, the most important issue of the luminosity determination (see chapter 5.5).

The analysis strategy, adopted here, is quite different from the luminosity measurements done by the other LEP experiments (they all use Monte Carlo detector simulations). It has the advantage that all errors and especially the most important uncertainty in the absolute coordinate of the inner acceptance boundary are transparently related to direct measurements.

## 5.4 The SiW Testbeam Measurement of the Shift $\Delta s$

In the summer of 1992 a testbeam run with a SiW-prototype detector was carried out. One of the main goals was to measure the bias $\Delta s$ introduced by the geometrical effect as explained above. The setup of the testbeam is shown in figure 5.5. More details about the testbeam can be found in [13]. The SiW detector was identical to the one installed in OPAL with the exception that only the layers after 4, 6 and 8 radiation lengths were equipped with silicon detectors. The beam was centered at the pad boundary between pad 9 and 10, which corresponds to a radius of 82.5 mm. The other components were a scintillator trigger system, delay wire chambers, and microstrip detectors to measure the trajectory of the incoming particles. The method to measure the bias is as follows: the radius at which an incident particle hits the detector is extrapolated into the SiW detector with the help of the delay wire chambers and microstrip detectors. This coordinate has offsets with respect to the r-$\phi$ coordinates of the SiW detector. The coordinate R (in the microstrip system) of the pad boundary between pad row 9 and 10 is measured with muons. Since muons do not shower in the SiW calorimeter they hit just one pad in R, either pad 9 or pad 10. The extrapolated radii are entered into two separate histograms depending on whether they hit pad 9 or pad 10. The probability for a hit in pad 9 or 10 can be obtained by deviding bin by bin the two corresponding histograms by the sum of both histograms. The resulting histograms give for each bin in R the probability for a hit in pad 9 or pad 10, respectively. The pad boundary can then be defined as the value $R_\mu$ of R where the probability for a hit in pad 9 (or pad 10) is 50%. The radius at which the probability is 50% is determined by fitting a fermi-dirac function to the histogram. This is a bias free determination of the pad boundary. Similarly, the coordinate $R_e$ of the pad boundary determined with electrons can be defined as the value of R where the probabilities to have the maximum energy deposited in either pad 9 or pad 10 are the same (both 50%). The extrapolated radii for electrons are entered into two separate histograms, into the first one if the maximum deposited energy is in pad 9 and in the second one if it is in pad 10. Then the same procedure for determining $R_e$ as for the muons is applied to the electron histograms.

The shift $\Delta s$ in the coordinate due the r-$\phi$ geometry of the detector can be determined

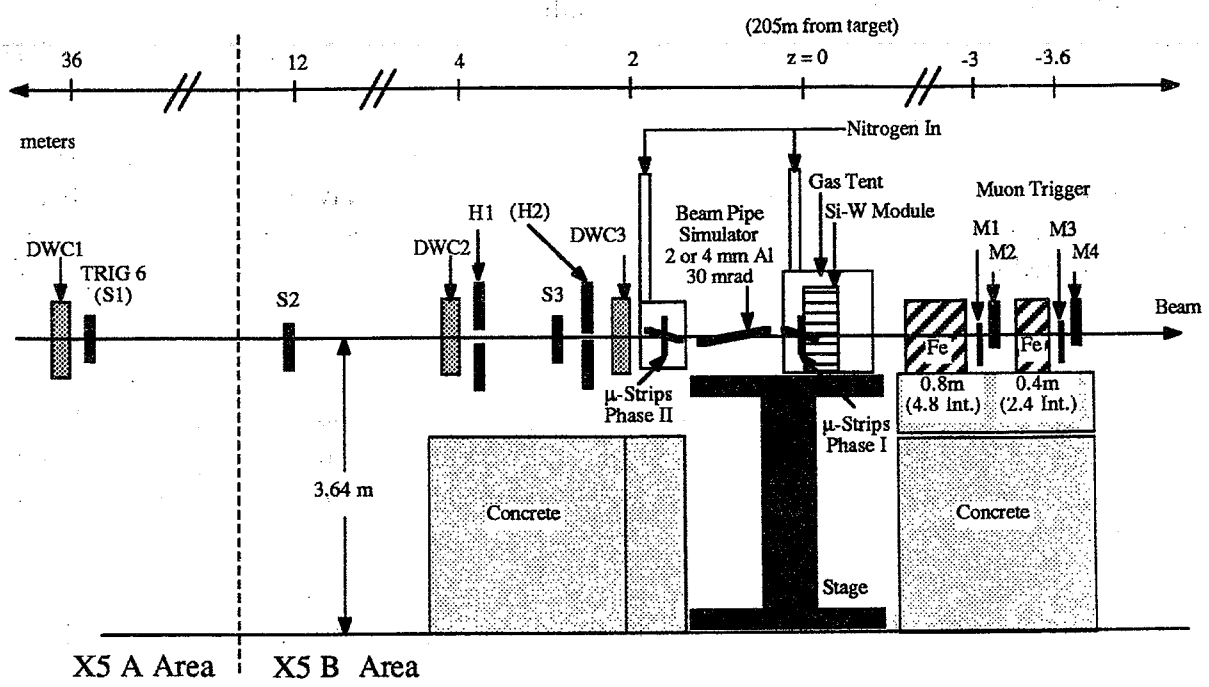


Si-W Test-Beam Layout

Figure 5.5: *Setup of the SiW testbeam. The trajectory of the incoming particle was measured with delay wire chambers (DWC's) and the microstrip detectors (μ-strips). For the measurements discussed here only the runs with the microstrip detectors installed at the front face of the SiW detector were used (Phase I). For other measurements the microstrip detectors were installed 2 meters in front of the SiW detector. The trigger system consisted of several scintillation counters. Electron events were triggered by a coincidence of S1, S2 and S3, no hit in the veto counters H1 and H2 and the muon counters M1 to M4. Muon events were required to have a coincidence in S1, S2 and S3, no hit in H1 and H2, and hits in M1 to M4.*

as $\Delta s = R_e - R_\mu$. The average result of this procedure for the three layers of the testbeam is $\Delta s = -8 \pm 6\ \mu m$. The error was determined by using different testbeam runs and using uncertainties of 1% for the energy calibration of the SiW detector. Figure 5.6 shows, as an example, the probability histograms for a hit in pad 10 for an electron and a muon run. Also shown is the function used to determine the radius with 50% probability.

This means that, on average, the shower center of electron showers in SiW is 8 $\mu m$ below the true geometrical pad boundary when the shower deposits an equal amount of energy in the two pads above and below the pad boundary, i.e. when the shower is reconstructed at the pad boundary. This knowledge is very important for the luminosity determination, since it allows

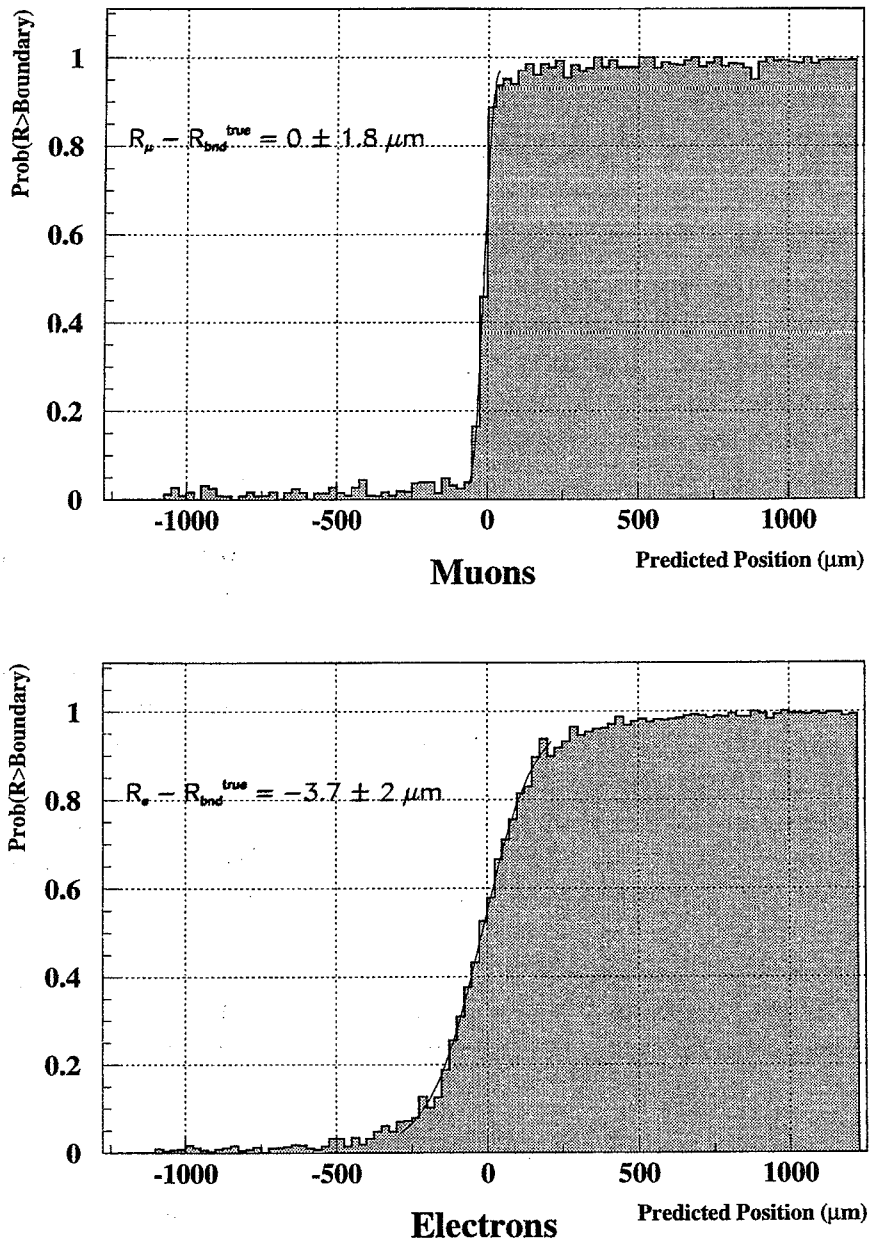


Figure 5.6: *Probability distribution for a hit in pad 10 for a muon and an electron run. The predicted position is $R - R_\mu$, and the offset in $R$ is chosen such that $R_\mu$ and the true pad boundary $R_{bnd}^{true}$ are the same.*

to directly measure biases in a SiW based coordinate reconstruction at pad boundaries. The coordinate reconstruction in SiW for the luminosity measurement, as explained in the next chapter, heavily relies on this testbeam measurement.

## 5.5 The SiW Coordinate Reconstruction

After having studied the geometrical effects of the electromagnetic showers at pad boundaries this section describes the full reconstruction of the R- and $\phi$-coordinate of the showered electrons in the SiW-detector. As already explained in sections 5.2 and 5.3 the reconstruction of the R-coordinate is, besides the geometrical accuracy of the SiW-detector, the most important aspect of the luminosity measurement.

The reconstruction of the R-coordinate is done in several steps. In the first step a coordinate is reconstructed in each of the layers 2 to 10. This coordinates are not bias free. They have to be individually linearized. The linearized coordinates are projected to layer 7 and are combined to a coordinate $\bar{R}$. This combined coordinate is again not bias free and also has to be linearized. In the last step it is veryfied that the combined linearized coordinate does not have an offset at the pad boundary where the inner acceptance cut is made. In the following these steps are explained in more detail.

Since the acceptance defining radial position cuts of the luminosity measurement are placed at pad boundaries a requirement for the position reconstruction algorithm is that it does not move the reconstructed coordinate across pad boundaries. If a shower deposits an equal amount of energy in the pads above and below a certain pad boundary the reconstructed coordinate has to be at the pad boundary and if the shower deposits more energy above the boundary the reconstructed radius has to be larger. The pad boundaries are therefore symmetry points of the coordinate reconstruction. A further symmetry point is the pad center. If a shower deposits an equal amount of energy in the two pads below and above a given pad the shower has to be reconstructed at the center of that pad. This symmetry is spoiled by the geometric effects as explained in the last section. The coordinate has to be corrected for these effects.

The reconstruction of the R-coordinate is based on a function with the above symmetry points. As input the pulse heights of the pad ($\text{pad}_2$) with the most energy ($E_2$) and its two neighbours in R are used in each layer. An intermediate coordinate $Y^0$ in units of half a pad width is calculated as

$$Y^0 = \frac{E_1 - E_3}{2E_2 - E_1 - E_3}$$

where $E_2$ is the energy of the central pad and $E_1$ and $E_3$ are the energies of the two neighbours. $E_1$ is the energy of the neighbour at the larger radius and $E_3$ at the smaller. Figure 5.7 schematically shows the pulse heights of the pads and the coordinate $Y^0$ at the three symmetry points.

In the region between the symmetry points, i.e. between the pad boundaries and pad centers, the variable $Y^0$ is not a linear function of the true position of the incoming electron. It has to be linearized. The deviation from the true position is up to 500 $\mu m$ and depends sensitively ($\pm 100$ $\mu m$) on the width of the shower. Therefore a measure, $W^0$, for the width of the shower has to be used to linearize $Y^0$. The apparent width $W^0$ is calculated (for details see appendix A.2) and $Y^0$ is linearized as a function of $W^0$. The mean of the $W^0$ distribution in each layer is a linear function of the amount of material (in radiation lengths) which the electron passed. The linearization is therefore automatically adjusted in all layers to showers which start late in the detector or to showers which start early in the material in front of the detector.

The linearized coordinate is calculated in the layers 2 to 10 and projected to the reference layer 7. These coordinates are then averaged to the combined coordinate $\bar{R}$. The distribution of $\bar{R}$ is shown in figure 5.8. This radial coordinate is not bias free as evidenced by the structure visible in each of the plots. The structure corresponds to a residual non-linearity of up to 40 $\mu m$ and a periodicity given by the radial pad pitch. The structure is due to the different resolutions of the layers which are combined. The shower center in these layers is at different positions in R, and the resolution is higher at the pad boundary than at the pad center. The resolution of the combined coordinate, which is not a critical parameter for the luminosity measurement, is approximately 220 $\mu m$.

The underlying distribution of the Bhabha events of figure 5.8 is smooth and varies approximately as $\frac{1}{R^3}$. A function $R(\bar{R})$ can be derived such that the distribution of the average radius is smooth. This smoothed distribution of events is shown in figure 5.9. It now obeyes the underlying distribution of events, but there might still be an offset in the coordinate. To remove this possible bias the coordinate has to be "anchored".

This is done with a similar procedure as the one used for the testbeam (see chapter 5.4). From the testbeam it is known that the pad boundary, measured by requiring that the maximum deposited energy is below or above a certain pad boundary, is $8\pm6$ $\mu m$ below the physical pad boundary. Figure 5.10 shows the R distribution of events which have a maximum deposited energy in pad row 6 or below and 7 or above. The pad boundary is clearly visible. Since the pad boundary, $R_{pad}^{true}$, is a symmetry point of the detector the tails in R with $R < R_{pad}^{true}$ for a maximum deposited energy in pad 7 and for $R > R_{pad}^{true}$ for a maximum deposited energy in pad 6 are identical. It is therefore possible to measure the coordinate $R_{pad}$ of the pad boundary between pad 6 and pad 7 in the $R(\bar{R}) = R$ coordinate system by defining $R_{pad}$ as the value of R where the number of events with a radius larger than $R_{pad}$ equals the number of events with a maximum deposited energy in pad 7 or above. This is equivalent to the procedure used in the testbeam. The offset in the coordinate R and the shift $\Delta s$ is then subtracted such that the coordiante $R = R_{pad}$ is equal to the real physical pad boundary:

$$R_{pad} = R_{pad}^{true} - \Delta s$$

The measurement of the bias in R typically has a statistical uncertainty of about 2 $\mu m$, which is small compared to the $\pm6$ $\mu m$ uncertainty of the testbeam measurement of the shift $\Delta s$. The asymmetry in the tails introduced by the $1/R^3$ distribution of the Bhabha events is small. A numerical calulation shows that the $1/R^3$ distribution changes the pad boundary determined with this procedure by less than 1 $\mu m$.

The reconstruction of the $\phi$-coordinate is not critical. It is done as follows. All pads, within a $\phi$ segment, used to form a cluster are first added in each layer and then the $\phi$ segments of all layers are added. This results in an energy for 2 or 3 summed $\phi$ segments depending on the width of the shower. For an electron shower with 3 $\phi$-segments the same function $Y^0$ as for the R reconstruction is used and linearized in order to get the reconstructed $\phi$ coordinate. For a shower with 2 $\phi$ segments the energy weighted $\phi$ is calculated and the resulting coordinate is linearized. For both $\phi$-reconstructions no anchoring is performed.

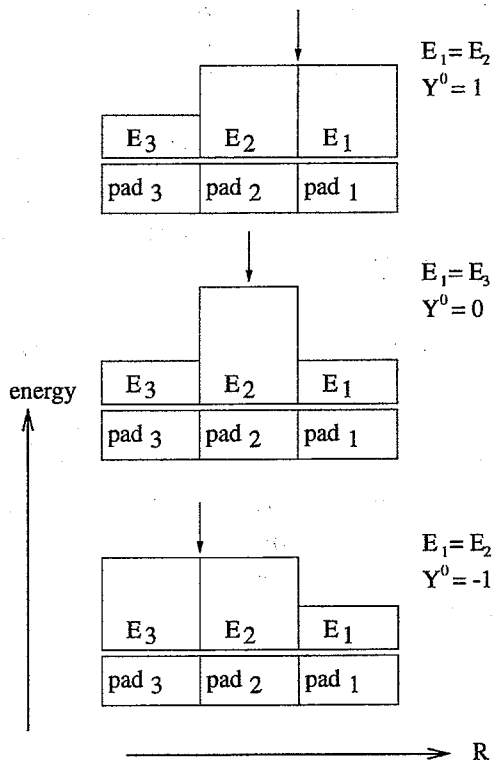


Figure 5.7: *The coordinate $Y^0$ at the three symmetry points. The arrows indicate the position of the incomming electron.*

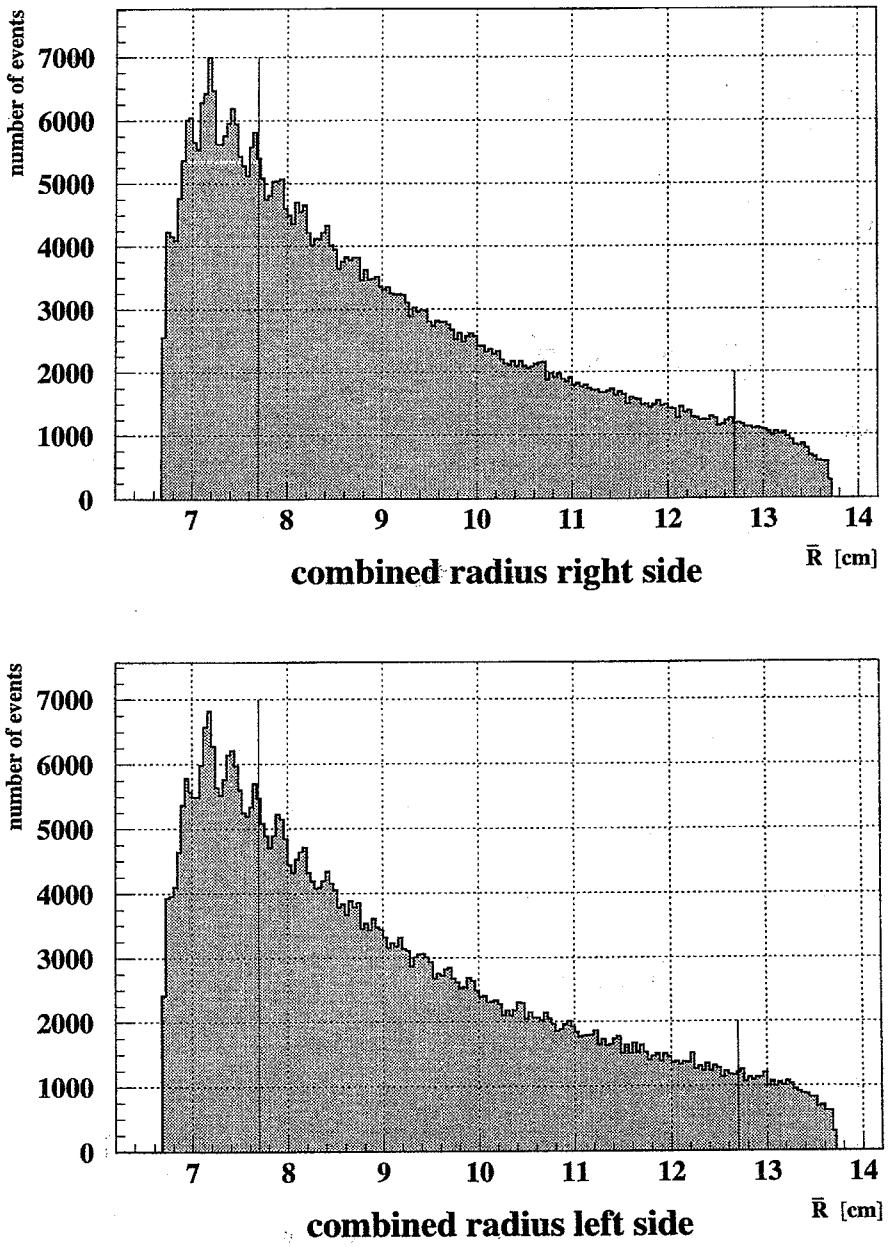


Figure 5.8: *Distribution of the coordinate $\bar{R}$. The positions of the radial acceptance cuts of the luminosity measurement are indicated by straight lines.*

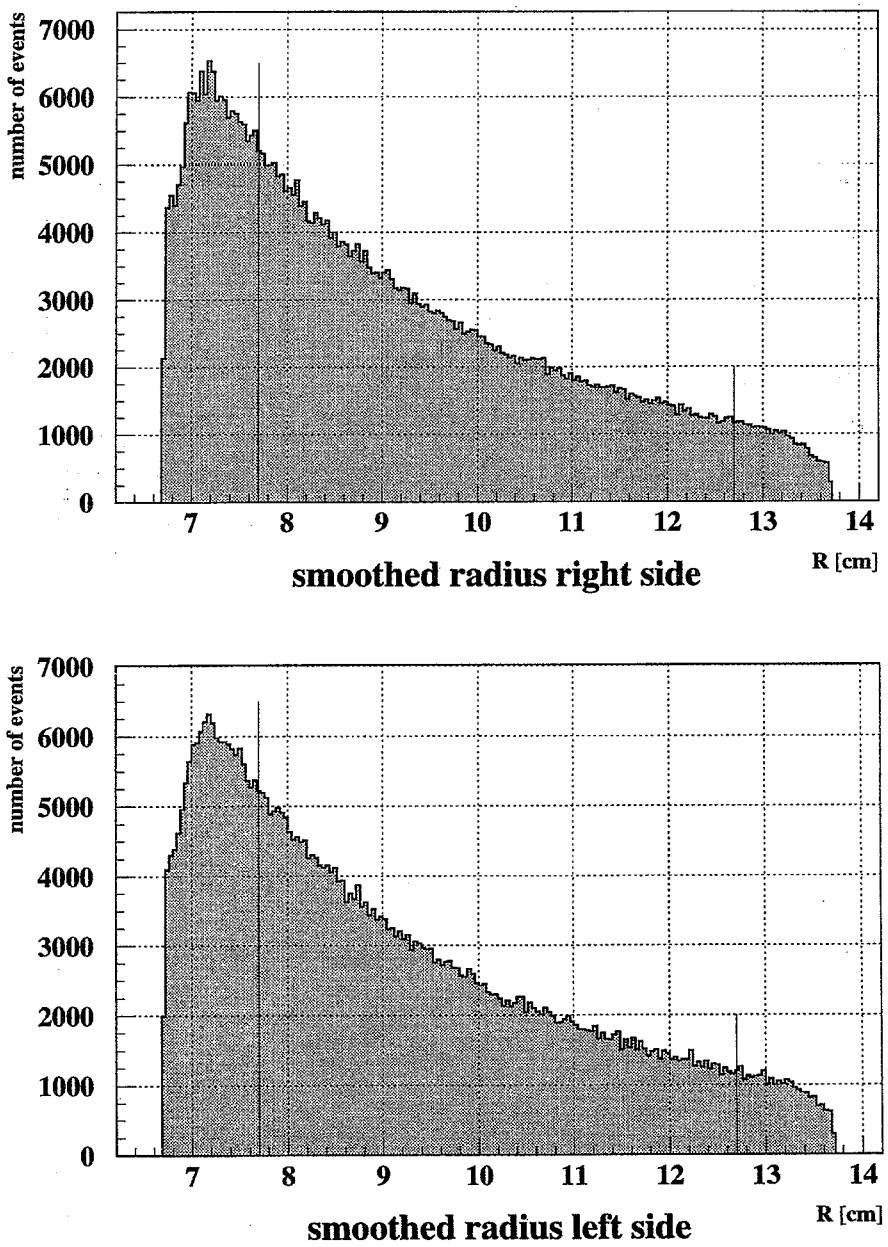


Figure 5.9: *Distribution of the smoothed coordinate R. The positions of the radial cuts are indicated by straight lines.*

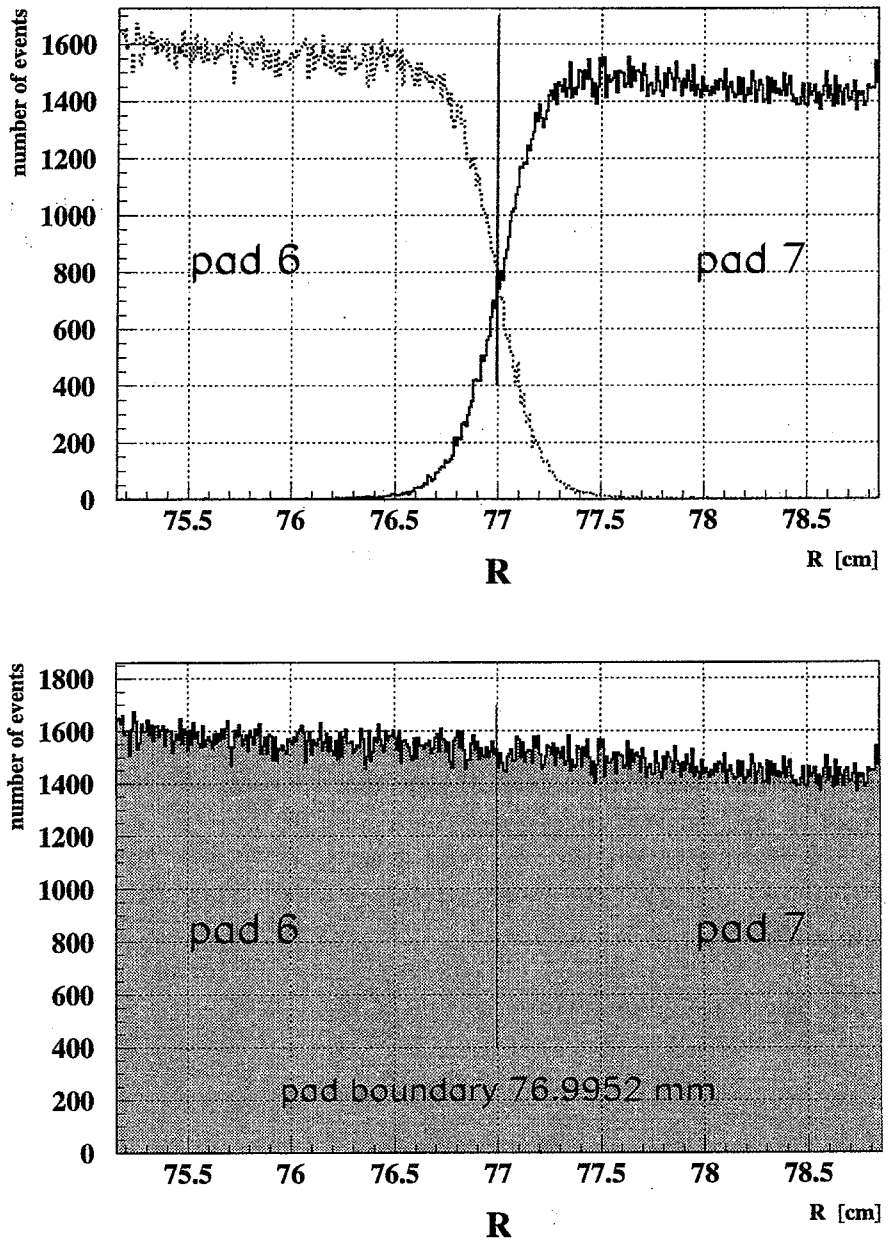


Figure 5.10: *The "anchoring" procedure. The upper histogram shows the distribution of the smoothed coordinate R for events which deposit most of their energy in pad 6 (dotted) and for events which deposit most of their energy in pad 7 (solid line). The number of events in the tails of the two histograms on the right and left side of the pad boundary (indicated by the line) are identical. The lower histogram shows the ditribution for a hit in pad 6 or 7. The lines indicate the determined pad boundary. The pad boundary is determined by moving the pad boundary in the lower histogram from the right to the left until the number of events on the right side of the pad boundary is equal to the number of events in the histogram for a hit in pad 7, i.e. the solid histogram in the upper plot.*

## 5.6 Selection Cuts

The event selection cuts can be classified into "isolation" on one hand or acceptance defining, or "definition" cuts on the other. The isolation cuts define a fiducial set of events which lie within the good acceptance of both calorimeters and are essentially background free. The definition cuts then select subsets of events from within the fiducial sample. These cuts define the inner edge of the acceptance and, therefore, affect most the systematic error of the measurement.

The isolation cuts consist of requirements imposed on the radial and azimuthal coordinates of the highest energy cluster in each of the right and left calorimeters, $R_R, \phi_R$ and $R_L, \phi_L$ and the total energy measured in each of the two calorimeters, $E_R$ and $E_L$.

- Safety Zone Cut $\quad 67\,mm < R_R(R_L) < 137\,mm$
- Minimum Energy Cut $\quad E_R(E_L) > 0.5 \cdot E_{beam}$
- Average Energy Cut $\quad (E_R + E_L)/2 > 0.75 \cdot E_{beam}$
- Acoplanarity Cut $\quad |\phi_R - \phi_L| < 200\,mrad$
- Acollinearity Cut $\quad |R_R - R_L| < 25\,mm$

The cuts on the cluster energy are made relative to the beam energy, to avoid a dependence of the acceptance on $\sqrt{s}$. The acollinearity cut is introduced to reduce the sensitivity of the acceptance to details of the energy response of the calorimeters. This is described in detail in section 5.7.4. Figure 5.11 shows the energy measured in the left calorimeter versus the energy measured in the right calorimeter. All cuts except the energy cuts have been applied. Figure 5.12 shows the energy on the left versus the energy on the right side for the events which fail due to the acollinearity cut.

The definition cuts then distinguish three classes of events:

- SWitA $\quad 77\,mm < \frac{R_R+R_L}{2} < 127\,mm$
- SWitR $\quad 77\,mm < R_R < 127\,mm$
- SWitL $\quad 77\,mm < R_L < 127\,mm$

SWitA events are defined in terms of the average of the radial position of the clusters whereas SWitR and SWitL events are defined in terms of the radial position of the clusters in the right or left calorimeter respectively.

Based on these event selection criteria two measures of luminosity are formed:

$$L_A = \frac{N_{SWitA}}{\sigma_A}$$
$$L_{RL} = \frac{1}{2}\left(\frac{N_{SWitR}}{\sigma_R} + \frac{N_{SWitL}}{\sigma_L}\right)$$

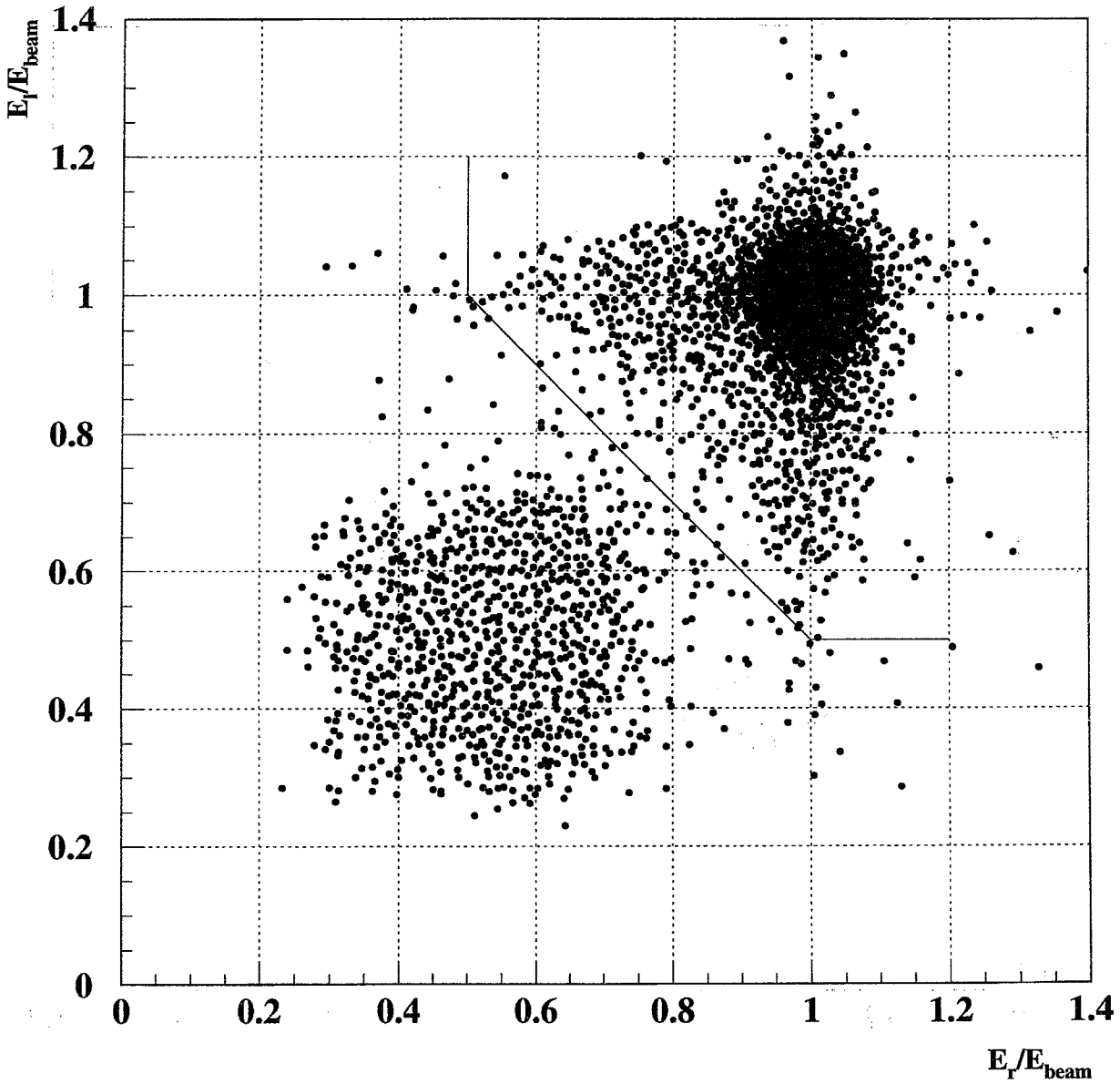


Figure 5.11: *Energy in the left calorimeter versus energy in the right. All cuts except the energy cuts have been applied. The energy cuts are indicated by the lines.*

Where $N_{SWitA}$, $N_{SWitR}$ and $N_{SWitL}$ are the numbers of events which satisfy each of the three selections and $\sigma_A, \sigma_R$ and $\sigma_L$ are the cross sections of the accepted Bhabha events for each selection.

The two luminosities have largely complementary sources of systematic errors with respect to their acceptance defining cuts. Because the SWitR and SWitL definition cuts allow a direct measurement of the bias in the coordinate, $L_{RL}$ is the favoured method of the luminosity

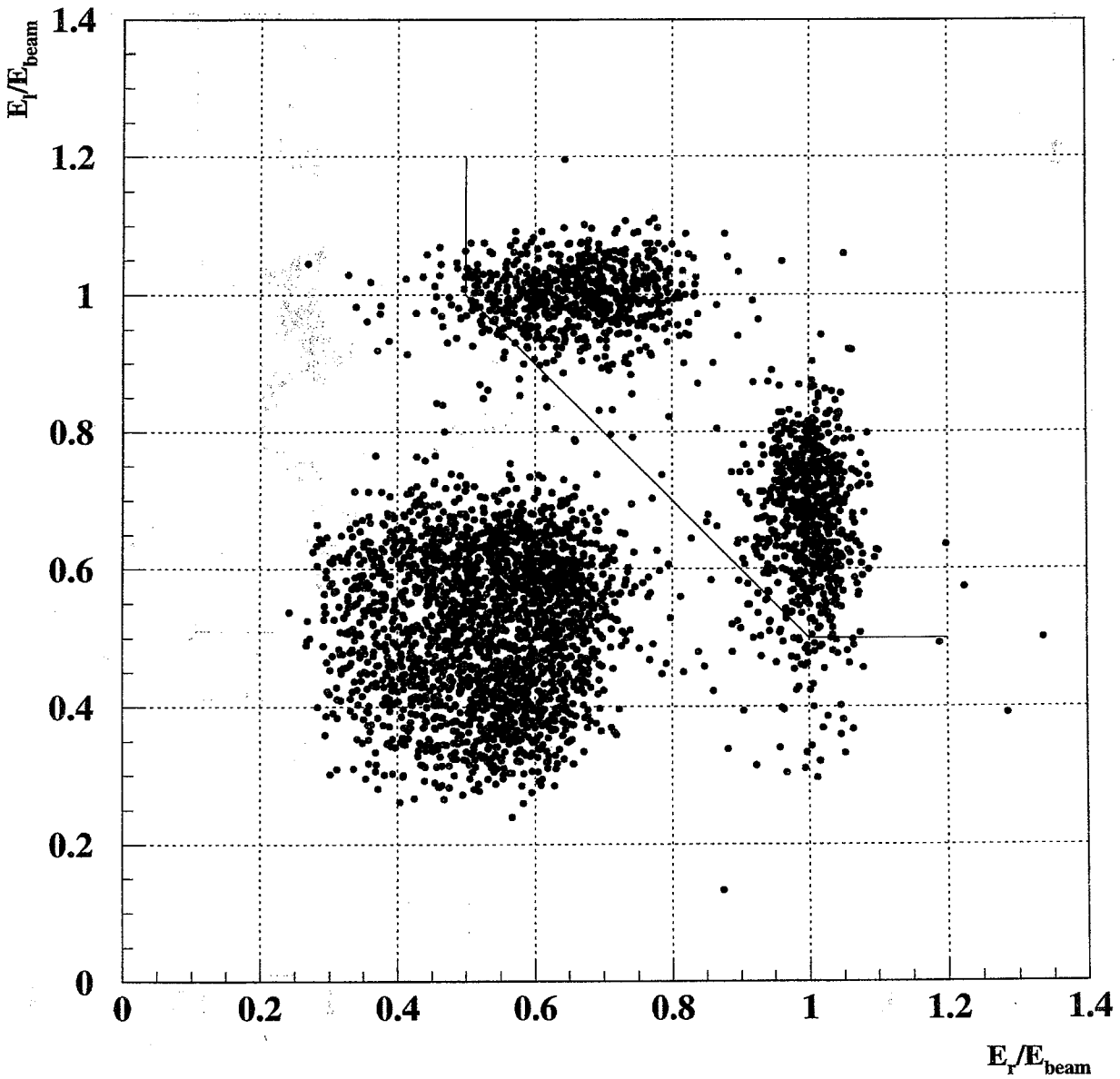


Figure 5.12: *Energy in the left calorimeter versus energy in the right for the events which fail the acollinearity cut.*

measurement and $L_A$ is used as a check that the effect of the beam parameters on the $L_{RL}$ results have been correctly understood and accounted for.

Effects of transverse and/or longitudinal beam spot offsets cancel almost exactly on an event by event basis in the quantity $R_A$. Therefore, the determination of $L_A$ is largely unaffected by such offsets. The effective cut boundary, however, is not centered with respect to the axis of either detector, but rather is centered with respect to the beam spot position. The presence

of acollinear events in the data means that the image of the effective cut boundary in each detector will be "fuzzy". This clearly complicates the understanding of how possible biases in the coordinate reconstruction will affect the cut on $R_A$. Placing a cut on either $R_R$ or $R_L$, on the other hand, ensures that the cut boundary is both uniquely defined and centered with respect to the corresponding detector. Thus, in principle, it is sufficient to understand the bias in the coordinate reconstruction about that unique boundary. The disadvantage of the SWitR and SWitL selections is that their acceptance depends to a significant extend on the geometry of the beam with respect to the detector. Although the strong dependence on the beam spot position on the individual $L_R$ and $L_L$ luminosities cancels to first order in their average $L_{LR}$, the $L_{LR}$ luminosity remains subject to second order corrections due to both longitudinal and transverse beam displacements to which the $L_A$ measurement is largely immune.

## 5.7 Systematic Errors of the Luminosity Measurement

The main sources for a systematic error of the luminosity determination are geometrical sources as discussed in chapter 5.2. The most important such source is the uncertainty in the acceptance defining radial position cut. Other geometrical errors arise from beam offsets and tilts.
Since a detailed energy parametrization of the detector response to electrons is used to determine the Bhabha cross section, uncertainties in this parametrization have to be examined.
It is also important that no clusters are lost due to trigger or clustering inefficiencies, or that accidental coincidences of off-momentum particles simulate a Bhabha event.
In the following the sensitivity of the luminosity measurement to the uncertainties listed above is discussed.

### 5.7.1 Errors in the Geometry of the SiW Detectors

The radial position of each silicon detector within the SiW calorimeter was systematically measured during assembly. The calorimeters each consist of two stacks of half rings, on which the silicon detectors are mounted. Within each stack, individual silicon detectors are placed with a rms scatter of better than 1.5 $\mu m$ with respect to the ideal semi-circles. The two calorimeter halves, however, are shifted against each other which causes, when brought together, a modulation of the radial positions with deviations from the average position of less than 20 $\mu m$. When integrated in $\phi$, the higher order corrections to the detector acceptance introduced by this structure is less than $10^{-6}$ so that only the average radial position of each layer of silicon detectors needs to be taken into account. The rms for the distributions of the average radial positions of the 19 layers in each calorimeter is 2.6 $\mu m$ for the right and 1.6 $\mu m$ for the left side. During the winter shut-down in 1994 the two calorimeters were partially disassembled and the positions for a subset of layers remeasured. The two sets of measurements differ by 2.2 $\mu m$ rms for each layer, and by 0.7 $\mu m$ in the mean.
These measurements all suffer from a common overall scale uncertainty of 6 $\mu m$. This is dominated by an uncertainty in the absolute calibration of the metrology instrument against a reference laser interferometer: $\pm 4$ $\mu m$, imperfections in the masks used in processing the silicon

wafers: $\pm 3\ \mu m$, and temperature variations during the metrology measurements: $\pm 2\ \mu m$.
The measurements discussed so far were made under reference conditions which were not identical to the operating conditions of the calorimeters. The effect of this was also measured with direct metrology. Under operating conditions (including the heat load of the front end electronics and the cooling system) the average radius of the silicon detectors changed by $-6 \pm 3\,\mu m$. Similarly, a $-3 \pm 6\,\mu m$ effect is found, when the calorimeters are moved from the horizontal reference position to the vertical operating position.
During operation the cooling system ensures an average temperature of $21.5 \pm 0.2°$ C. This results in a radial stability of about $0.2\ \mu m$ rms.
Taking all the sytematic uncertainties discussed so far into account the absolute average radial position of the silicon detectors in SiW is known to within $9\ \mu m$ under operating conditions, which corresponds to an uncertainty in the absolute luminosity of $\frac{\Delta L}{L} = 3.6 \cdot 10^{-4}$. After the data taking period of 1994 the calorimeters were again disassembled and the radial positions of the silicon detectors were remeasured. The average radial positions showed a common $5\ \mu m$ shift compared to the positions before the installation in 1993. This shift is not understood and an additional error of $\frac{\Delta L}{L} = 2.0 \cdot 10^{-4}$ due to the $5\ \mu m$ shift is assigned for the 1994 luminosity measurement.

The distance between the two calorimeters was also determined by direct metrology. For this purpose the end flanges of the OPAL beam pipe are used as a reference. The distance of the machined surfaces of the end flanges is known, including thermal expansion, to a precision of $\pm 100\ \mu m$. The position of each calorimeter was then measured and continously monitored during data taking. Due to the accurate knowledge of the internal dimensions of the SiW modules the half-distance of the reference planes of the two calorimeters was determined to be $2460.225 \pm 0.075$ mm in 1993. During 1993 the half-distance was stable throughout the year. In 1994 the pressure of the Central Detector was allowed to decrease slowly during the year. This caused the half-distance to gradually decrease by $250\ \mu m$ from the beginning to the end of data taking. Because of the permanent monitoring this effect could be accounted for and no additional error for 1994 is assigned and the same uncertainty on the absolute luminosity of 75 $\mu m$, which corresponds to an uncertainty on the absolute luminosity of $\frac{\Delta L}{L} = 6 \cdot 10^{-5}$, is used for 1993 and 1994.

The total error due to the knowledge of the geometry of the SiW calorimeters is $3.6 \cdot 10^{-4}$. This error is fully correlated between 1993 and 1994. As mentioned above, an additional uncorrelated error of $2.0 \cdot 10^{-4}$ is assigned to 1994.

### 5.7.2 Errors Due to the Radial Coordinate Reconstruction

The fine radial granularity of the SiW calorimeters allows a reconstruction of the radial coordinates of the incoming electrons which is both precise and essentially bias free, independent of the shower position. For the $L_{RL}$ luminosity the detailed characteristics of R away from the acceptance defining cuts are relatively unimportant. What is critical, however, is the residual bias in R where these cuts are made. This residual bias can be directly measured by comparing the value of R for electron showers which deposit equal energy in the pads directly above and below a radial pad boundary in a given layer. For such showers the true trajectory of the incident electron is offset from the actual pad boundary due to the non-Cartesian pad geometry.

Based on the data taken during a testbeam run in 1992, the bias is measured to $8 \pm 6$ $\mu m$ (see section 5.4). Therefore, radial pad boundaries provide well understood reference points at which it is possible to study the behaviour of R.
The anchoring procedure, described in detail in section 5.5, is performed using as reference the boundaries between radial pad rows 6 and 7 in the layers 4 to 8. The positions of these five boundaries projected to the layer 7 form a grid with $\approx 200$ $\mu m$ spacing which covers the region around the acceptance defining inner cut. Each of these constitute an anchor point which determines the bias in the coordinate R absolutely with an error of 6 $\mu m$ (the uncertainty of the testbeam measurement). Figure 5.13 shows the variation in each of the SWitR and SWitL luminosities when the acceptance defining inner radius cut is placed at each of the five anchor points of R. Also shown in figure 5.13 is the Monte Carlo prediction. As can be seen the Monte Carlo fails to exactly predict the effect on the right side. The largest discrepancy of 6 $\mu m$ is therefore used as the error due to the coordinate reconstruction. The difference between the right and the left side is due to the different amount of material in front of the two calorimeters, mainly due to the micro vertex cables which are just in front of the left side. Figure 5.13 is made for the 1994 data. The error of 6 $\mu m$ is as well used for the 1993 data, where the difference is not significant because of less statistics. Together with the uncertainty of the testbeam measurement of the bias at the pad boundary this results in an error of the luminosity of $\frac{\Delta L}{L} = 3.4 \cdot 10^{-4}$ which is taken to be fully correlated between 1993 and 1994. Additional uncorrelated statistical errors of $0.8 \cdot 10^{-4}$ and $0.5 \cdot 10^{-4}$ are assigned to 1993 and 1994, respectively.

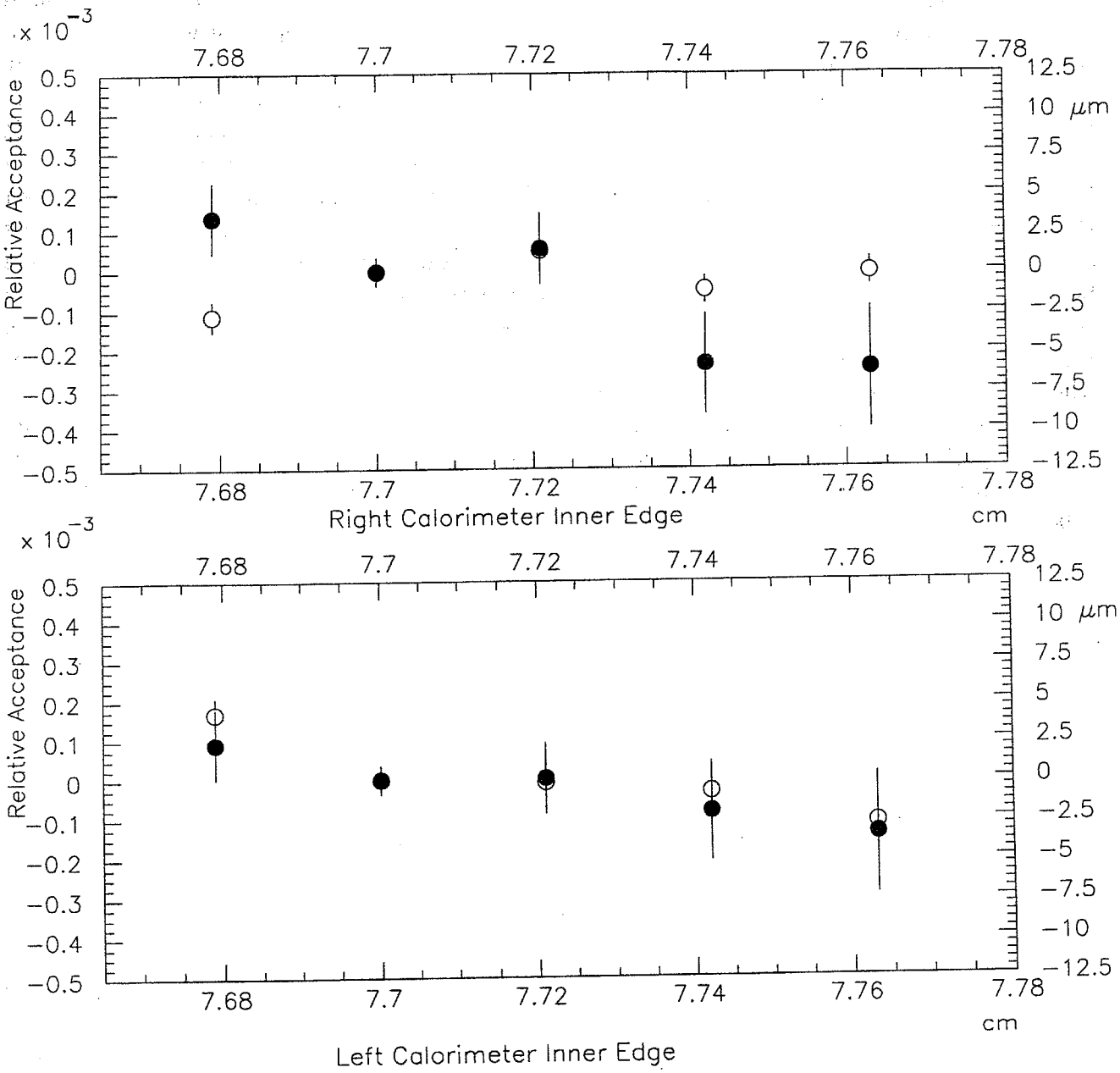


Figure 5.13: *Variation in the SWitR (upper plot) and SWitL (lower plot) luminosities as the acceptance defining inner acceptance cut is varied. The open circles show the prediction from the anchoring procedure and the solid circles show the difference between data and MC in the luminosity. The prediction from the anchoring procedure has been corrected for the variation of the luminosity due to different inner acceptance boundaries. The remaining differences are due to local offsets in the coordinate. The Monte Carlo has no local offsets. The difference in the luminosity between data and MC should therefore follow the prediction from the anchoring.*

### 5.7.3 Effect of the LEP Beam Parameters on the Luminosity Measurement

Changes in the beam parameters (offset and tilt of the beam) occur from fill to fill as well as within fills, and provide a potentially large source of systematic error for the luminosity measurement. These, however, are relatively simple geometric effects and the corrections can therefore be reliably calculated, as long as the beam parameters are known. Beam offsets, both transverse and longitudinal, are measured in the data for each fill by two essentially independent methods using the SiW detectors themselves. The change in acceptance due to the beam parameters is then calculated using Monte Carlo. One method to determine the beam offset is to use the variation of the observed Bhabha rate with $\phi$. Figure 5.14 shows the modulation in $\phi$ and the determined beam offset for a typical run. Since non-radiative Bhabhas all have their origin in the luminous region and are back-to-back it is possible to determine the beam offset as the point (x,y,z) in the SiW coordinate system which is closest to all lines which connect the hit in one calorimeter to the hit in the other calorimeter for a sample of collinear events. This is the other method for determining the beam offsets.

The luminosity measured is corrected for these beam movements, thus reducing substantially the systematics from this sources. A comparison of the two methods shows that the relevant beam parameters can be determined with an accuracy of $5 \cdot 10^{-5}$ on the absolute luminosity. The average values of the corrections for the $L_{RL}$ luminosity are listed in table 5.1. In 1994 the transverse beam offsets changed abruptely after about 1/5 of the data had been collected. The corrections are therefore calculated separately for the data taken before (1994 A) and after (1994 B) the shift. After the corrections are applied the $L_A$ and $L_{RL}$ luminosities show no evidence for systematic inconsistencies.

| $L_{RL}$ Acceptance corrections$\cdot 10^{-4}$ | 1993 | 1994 A | 1994 B | Av. 1994 |
|---|---|---|---|---|
| Definition cuts | $+7.0$ | $+13.4$ | $+6.0$ | $+7.3$ |
| Safety Zone cuts | $-0.9 \pm 0.2$ | $-1.1 \pm 0.3$ | $-0.4 \pm 0.2$ | $-0.5 \pm 0.2$ |
| Acoplanarity cut | $-1.1 \pm 0.2$ | $-1.6 \pm 0.2$ | $-0.8 \pm 0.1$ | $-0.9 \pm 0.1$ |
| Acollinearity cut | $-1.8 \pm 0.4$ | $-2.9 \pm 0.4$ | $-1.2 \pm 0.3$ | $-1.5 \pm 0.3$ |
| Overall change (MC) | $+3.1 \pm 0.5$ | $+7.8 \pm 0.5$ | $+3.6 \pm 0.4$ | $+4.4 \pm 0.4$ |

Table 5.1: *This table summarizes the results of the Monte Carlo calculation for the combined effect on the $L_{RL}$ acceptance introduced by both transverse and longitudinal beam spot offsets, equal to the measured mean values for the 1993 run and for the first and second parts of the 1994 run (A and B). The last column indicates the luminosity weighted average correction for the 1994 data set as a whole. The changes in acceptance for the definition cuts given in the table are the result of a high statistics Monte Carlo calculation which has a negligible statistical error.*

The luminosity determination is, although to a lesser degree, also sensitive to the divergence of the LEP beams and the size of the luminous region. These parameters are less well measured than the beam offsets. They have a similar effect on the acceptance as the beam offsets. The number of events passing the definition cuts is increased, whereas the number of events passing the isolation cuts is decreased. The size of the effect is determined with Monte Carlo. For reasonable variations in the beam spot dimensions, the overall change in the acceptance is less

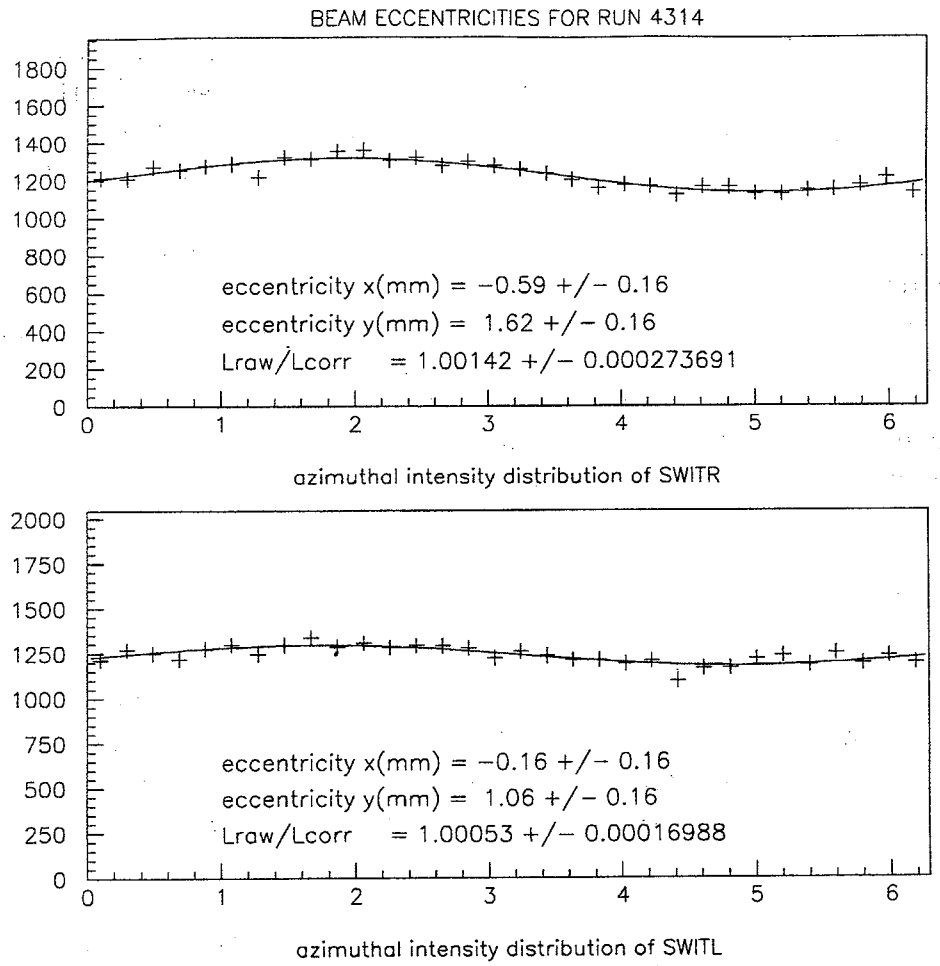


Figure 5.14: *Modulation of the Bhabha rate due to a beam offset.*

than $10^{-4}$. In estimating the systematic error 100% of the largest individual contribution is taken. This is $2.0 \cdot 10^{-4}$ due to the effect of the beam divergence on the definition cuts.

### 5.7.4 Errors Due to Uncertainties in the Energy Response

As mentioned in chapter 5.6 the acollinearity cut of $|R_R - R_L| < 25\ mm$ is introduced in order to minimize the sensitivity of the acceptance to details of the energy response of the calorimeters. For events which have lost energy due to a single initial state photon emitted along the beam pipe, transverse momentum conservation implies:

$$\frac{E_R}{E_L} = \frac{R_L}{R_R} \tag{5.11}$$

so that an acollinearity cut, for single radiative Bhabhas, effectively determines the minimum kinematically allowed cluster energy. The acollinearity cut raises this boundary from $0.49 \cdot E_{BEAM}$, given by the ratio of the inner to outer acceptance angles, to $0.75 \cdot E_{BEAM}$, safely above the explicit energy cuts. As a result of this, a change in the effective average gain of the calorimeters results in a change in the acceptance of

$$\frac{\Delta L}{L} \approx 0.015 \cdot \frac{\Delta E}{E}$$

for a range of less than a few percent in $\frac{\Delta E}{E}$. The coefficient in the expression above is derived from data by observing the change in the number of accepted events as the energy scale is varied.

Upstream material and shower leakage at the inner and outer edges significantly affects the energy response of the calorimeters. The upstream material has been kept to a minimum in the regions close to the inner and outer edges of the acceptance. The energy lost due to leakage and preshowering has been parametrized as a function of the polar angle and

$$F_{pre} = \frac{E_{pre}}{E_{main}}$$

where $E_{pre}$ is the energy deposited in the first four layers (0 to 3 $X_0$) and $E_{main}$ is the energy deposited in the remaining layers. The parametrization is obtained using collinear events which to a good approximation have beam energy.
In regions of clean acceptance the energy resolution is approximately

$$\frac{\Delta E}{E} = \frac{24\%}{\sqrt{E}}$$

As mentioned in chapter 5.2 no Monte Carlo detector simulation is used to determine the acceptance. The energy response of the detector is parametrized and to each event from the Bhabha event generator an energy according to this parametrization is assigned. The parametrization is shown in figure 5.15. Indicated are also the extreme limits of the non-Gaussian tails which are used to estimate a part of the systematic error. In the following the errors of the luminosity measurement due to uncertainties in the energy parametrization are discussed.

To check the extrapolation of the energy correction procedure to lower energies acollinear events are used. Events consistent with the beam energy on one side are selected and the energy on the other side is predicted using formula 5.11. The difference between the measured energy and the predicted energy is less than 1% at half the beam energy (where the acceptance cut on the energy is made). The difference in the acceptances obtained assuming a $\pm 1\%$ non-linearity at half the beam energy is used as an estimate of the related error. The energy resolution is assumed to scale with $1/\sqrt{E}$. As a systematic error due to this assumption the energy resolution is taken to be constant and the difference in the acceptance is calculated.

As a further check the average energy cut, $E_{average} = 0.75 \cdot E_{beam}$, $(E_R + E_L)/2 > E_{average}$, is varied from 0.7 to $0.8 \cdot E_{beam}$. The minimum energy cut, $E_{min} = 0.5 \cdot E_{beam}$, $E_{R,L} > E_{min}$, on the single sides is simulataneously changed such that it stays coincident with the average energy cut, i.e. $E_{min} = 2 \cdot E_{average} - E_{beam}$. The change in the luminosity is less than $10^{-4}$ for the variation of the average cut from 0.7 to $0.8 \cdot E_{beam}$.

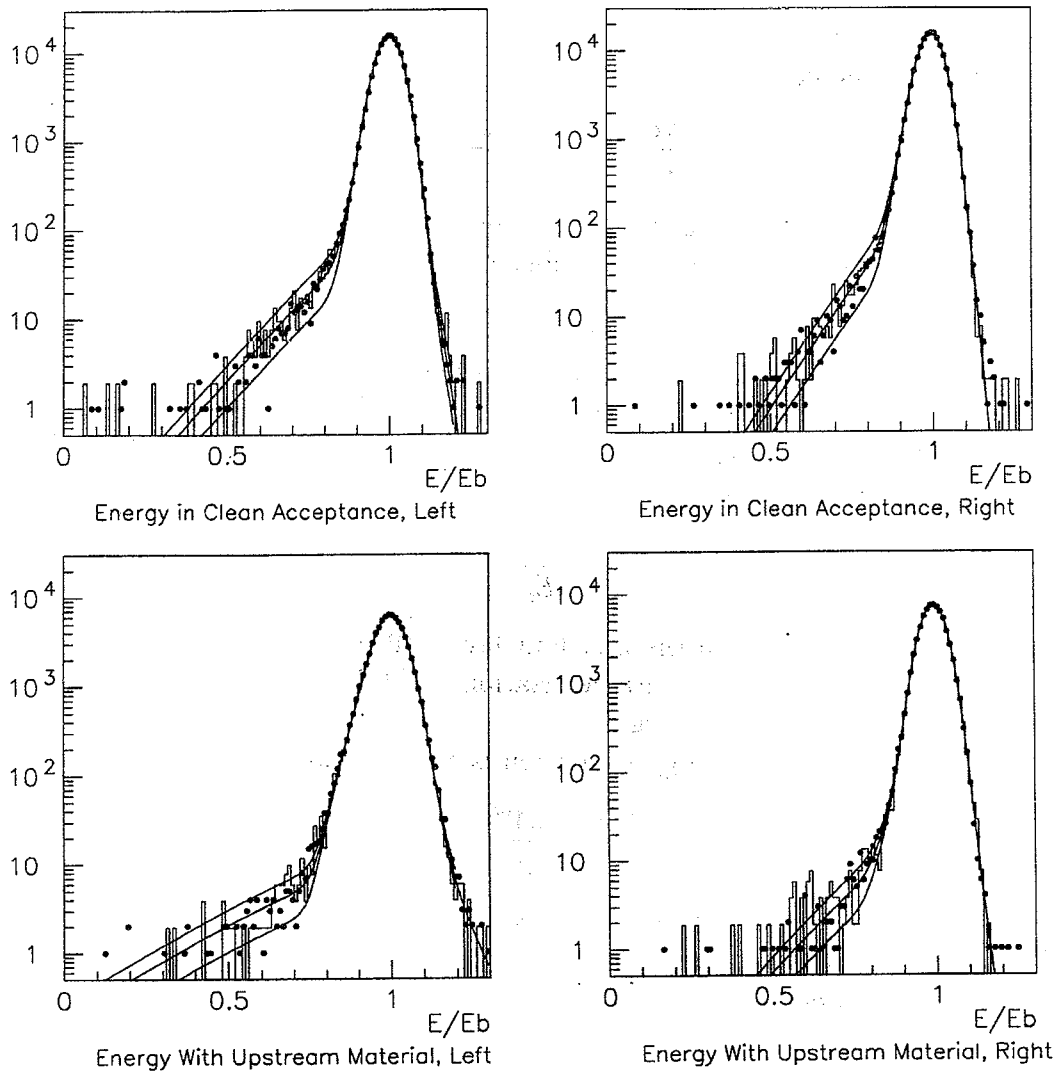


Figure 5.15: *Parametrization of the energy. The histogram is the energy distribution for data. The points is the energy distribution which is assigned to the four vectors from the Bhabha event generator. The lines show the energy parametrization.*

The total systematic uncertainty on the absolute luminosity due to uncertainties in the energy response is:

$$\frac{\Delta L}{L} = 3.4 \cdot 10^{-4}$$

The individual contributions to the systematic error from the energy selection cuts are listed in table 5.2. It can be seen, that the acollinearity cut substantially decreases the systematic error.

A comparison of the 1993 and 1994 data shows two measurable differences. The most noticeable is a change in the gain in the two calorimeters, by $-4.8 \cdot 10^{-3}$ and $-2.5 \cdot 10^{-3}$ on the right and left sides, respectively. This, however, changes the acceptance by only $5 \cdot 10^{-5}$. The

| Effect | systematic error $10^{-4}$ | |
|---|---|---|
| | With Acollinearity Cut | Without Acollinearity Cut |
| change in tail ±50% | 2.0 | 2.5 |
| scale Gaussian ±10% | 1.5 | 2.0 |
| non-linearity ±1% at $E = E_{beam}/2$ | 2.1 | 4.0 |
| low energy resolution | 1.0 | 1.0 |
| total | 3.4 | 5.2 |

Table 5.2: *Systematic errors of the energy selection cuts on the luminosity.*

other difference found is a slight change in the non-Gaussian tails, which is within the uncertainties assigned to the parametrization of the energy response for the 1993 data. Therefore, the acceptance calculation of 1993 is applied to the 1994 data and the same systematic error is assigned for the 1993 and 1994 data, fully correlated.

### 5.7.5 Cluster Finding Efficiency

The cluster finding efficiency is checked by comparing the sum of the energies of the reconstructed clusters per event triggered using a threshold of 15 GeV. The trigger efficiency for events with less than 10 GeV is 0. The existance of clusters with such little energy is therefore either a failure in the cluster finder or a sign for noise in the trigger.
For this analysis the $5 \cdot 10^6$ SWSEG triggered events from 1993 are used. Out of these events 201 events are found which have a reconstructed energy of less than 10 GeV. Most of these events have an energy deposit at the outer edge of the calorimeter where leakage significantly distorts the shower shape. These events are well outside the geometrical acceptance and therefore have no influence on the luminosity measurement. The number of events which are within the acceptance and which would have passed the energy cut if the clusters were properly reconstructed is 51. Since not all of them pass the acoplanarity and acollinearity cuts this number is an upper limit for failures in the cluster reconstruction. The upper limit for the effect of cluster reconstruction failures on the luminosity measurement therefore is $2.4 \cdot 10^{-5}$.

### 5.7.6 Trigger Efficiency

The SiW trigger is designed to be 100% efficient for events passing the selection cuts. The principle trigger, "SWSEG", is defined as

- SWSEG
  - energy cut $\quad MIN(E_R^{TSEG}, E_L^{TSEG}) > 18$ GeV
  - acoplanarity cut $\quad |\phi_R - \phi_L| < 500$ mrad

where the cut values shown correspond to a nominal efficiency of 100% and $E_{R,L}^{TSEG}$ are the energies summed over trigger segments (see chapter 4.5) in the right and left calorimeters, re-

spectively.

A second trigger ,"SWHILO", is also used. This allows to check the SWSEG trigger. The SWHILO trigger is defined as:

- SWHILO
  - high energy cut on one side $MAX(E_R^{TSUM}, E_L^{TSUM}) > 40$ GeV
  - low energy cut on the other side $MIN(E_R^{TSUM}, E_L^{TSUM}) > 10$ GeV

where the cut values again correspond to 100% nominal efficiency. $E_{R,L}^{TSUM}$ are the energies summed over the entire right or left calorimeter.
Since, for the SWHILO trigger, the energy is summed over the entire calorimeter the SWHILO trigger is more sensitive to coherent pedestal shifts than the SWSEG trigger, where the sensitivity is reduced by a factor of 8.

The main concern with respect to the trigger efficiency is that events with rather low energies deposited in the calorimeter would be accepted by the selection cuts after the potentially large corrections for leakage and preshowering. This, coupled with the fact that the trigger energy thresholds are fixed, rather than scaled to the beam energy, is a potential source of bias in the luminosity, determined at one energy point compared to another energy point.

To study the trigger efficency the SWHILO trigger has first been verified by using events which fall in the overlap region of SiW and FD. These events cause both SiW and FD to issue a trigger. Then events triggered by SWHILO were used to check the SWSEG trigger. Seven events out of $2.3 \cdot 10^6$ are found which are selected by one of the SWITA, SWITR or SWITL selections, but were triggered exclusively by SWHILO. Three of these events occured in fills taken at the peak energy point, and two at each of the off-peak energy points. The 7 events correspond to an uncertainty of $(3.0 \pm 1.2) \cdot 10^{-6}$ where the error is purely statistical. This error is used for both the 1993 and 1994 data taking periods.

### 5.7.7 Background

Background due to accidental coincidences of off-momentum beam particles directly effects the error on the luminosity. As a diagnostic tool to access accidental background a delayed coincidence trigger (SWSEGA) is set up. It imposes the SWSEG requirements on clusters from the current beam crossing (in-time) and clusters recorded 8 beam crossings earlier (out-of-time). The SWSEGA trigger, prescaled by 1/16, was active for the entire scan of 1993 and the 1994 data taking period.
The energy spectrum of the SWSEGA sample is identical to the low energy tail (the region which is dominated by accidentals) of the SWSEG sample after applying all the SWITA selection cuts besides the energy cut. Therefore, the SWSEGA sample reliably models the background and can, by applying the energy cuts, be used to extrapolate into the signal region. The following

level of accidental coincidence background is found in 1993:

| | |
|---|---|
| $SWITA$ | $(10.7 \pm 1.4) \cdot 10^{-5}$ |
| $SWITR$ | $(10.9 \pm 2.0) \cdot 10^{-5}$ |
| $SWITL$ | $(8.0 \pm 1.7) \cdot 10^{-5}$ |
| $1/2\ (SWITR + SWITL)$ | $(9.5 \pm 1.3) \cdot 10^{-5}$ |

The luminosity is corrected for this effect, an uncertainty due to accidental background of $1.3 \cdot 10^{-5}$ is assigned for 1993.

In 1994 an additional source of background is found, which appears to be due to a single off-momentum electron showering first in one calorimeter and then in the other. These events are not contained in the delayed coincidence triggers and produce a significant excess of background in the very low energy region of the spectrum. These electrons are characterized by highly anomalous longitudinal shower profiles in the calorimeters, consistent with the shower striking the rear of one calorimeter and the front of the other. Once these events are removed, the low energy tail is well reproduced by the delayed coincidence sample. An estimate of the remaining background results in $(1.4 \pm 0.3) \cdot 10^{-5}$. Since the background due to the single off-momentum electrons is not studied in more detail, an uncertainty of $1 \cdot 10^{-4}$ is assigned for the background in 1994, uncorrelated to 1993.

The effect of off-momentum particles overlapping true Bhabha events is examined in the following way. Clusters with an energy spectrum corresponding to that of the accidental SW-SEGA clusters are added to real clusters. This increased the number of accepted events by $5 \cdot 10^{-5}$. The resulting energy is usually larger than the beam energy. Therefore, an energy of more than the beam energy is a sign for an accidental overlap. The effect of the overlap background on the acoplanarity cut and the acceptance defining R cuts is measured by applying these cuts to a sample were either $E_R$ or $E_L$ is higher than the beam energy and comparing this sample to the standard sample. A loss in the acceptance due to the accidental overlap of $5 \cdot 10^{-5}$ for the acoplanarity cut and of $1.2 \cdot 10^{-6}$ for the acceptance defining cut on R is found. The difference due to the overlap background between the number of events coming into the selection (because of the energy cut) and the number of events rejected by the selection is negligible and an upper limit for this effect is $10^{-5}$.

As a result of these studies a total uncertainty of $1.3 \cdot 10^{-5}$ and $1.0 \cdot 10^{-4}$ due to accidental background is assigned in 1993 and 1994, respectively.

## 5.8 Theory Error

The determination of the cross section of accepted Bhabha events is based on the BHLUMI4.01 Monte Carlo event generator [21]. BHLUMI is a multiphoton exponentiated second order generator for small angle Bhabha events. It is currently the most precise Monte Carlo for small angle Bhabha scattering. According to [21] the total theoretical uncertainty of the luminosity calculation is $1.6 \cdot 10^{-3}$.

The matrix element used in the Monte Carlo program is based on a logarithmic expansion. The terms which are implemented are shown in figure 5.16. Here $L = ln(t/m_e^2)$ is the so-called

big-log in the leading logarithmic (LL) approximation where t is t-channel transfer (of order 1 GeV). The missing contributions to the cross section of the missing higher order terms, mainly from the $\mathcal{O}(\alpha^2 L)$ term, is expected to be small. To check the implementation of the matrix element in the Monte Carlo program the cross section of the Monte Carlo is compared to the analytic integration. The matrix element is, however, only integrable analytically for cut-offs in the energy of the emitted photons but not for the experimental cuts. The comparison of the integration and the Monte Carlo shows for this specific choice of cuts an agreement of $3 \cdot 10^{-4}$. It remains to be shown that the cross section determined from Monte Carlo and the direct analytical integration of the matrix element agrees for realistic experimental cuts (this, in principal, has to be verified for each choice of cuts individually). Since the analytic integration of the matrix element is not possible for experimental cuts, the authors of BHLUMI therefore compare BHLUMI with other Monte Carlo programs. This results in an estimate of 0.16% for the error of the determination of the cross section for the accepted Bhabha events.

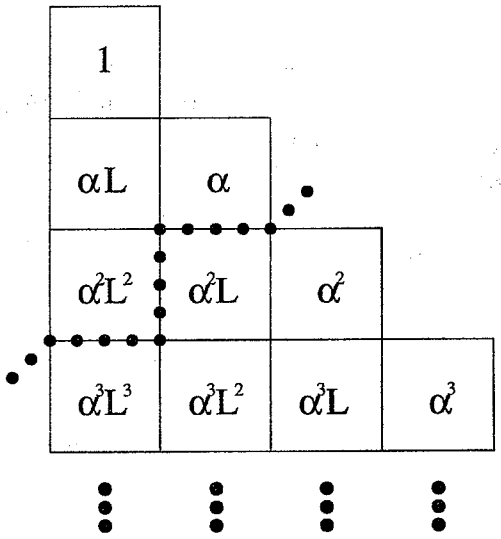


Figure 5.16: *QED perturbative leading and subleading corrections. Rows represent corrections in consecutive perturbation orders. The first row is the Born contribution. The first column represents leading logarithmic (LL) approximation and the second column depicts the next-to-leading (NLL) approximation. The terms above the dotted line are implemented in BHLUMI4.01.*

## 5.9 Summary of the Errors of the Luminosity Measurement

The main experimental errors are due to the metrology of the detector ($3.6 \cdot 10^{-4}$), due to biases in the coordinate reconstruction ($3.4 \cdot 10^{-4}$) and due to the parametrization of the energy response ($3.4 \cdot 10^{-4}$). The installation of the SiW-detector allowed to reduce the experimental systematic error of the luminosity measurement from $4.1 \cdot 10^{-3}$, measured with the old forward detector (FD), to $7.9 \cdot 10^{-4}$.

The contribution from theory to the luminosity determination is $16 \cdot 10^{-4}$. The luminosity

measurement is therefore limited by the theory error. The individual errors and corrections are listed in table 5.3.

| Effect on $L_{RL}$ | Correction $\times 10^{-4}$ | | Systematic $\times 10^{-4}$ | |
|---|---|---|---|---|
| | 1993 | 1994 | 1993 | 1994 |
| SiW radial dimensions ($\pm 9\mu$m) | — | — | $3.6 \oplus 0.0$ | $3.6 \oplus 2.0$ |
| Radial coordinate bias | — | — | $3.4 \oplus 0.8$ | $3.4 \oplus 0.5$ |
| Energy parametrization | $-7.3$ | $-7.3$ | $3.4 \oplus 0.3$ | $3.4 \oplus 0.3$ |
| Monte Carlo, statistics | — | — | $3.7 \oplus 0.0$ | $3.7 \oplus 0.0$ |
| Trigger inefficiency | — | — | $< 0.01$ | $< 0.01$ |
| Cluster finding efficiency | — | — | $0.2 \oplus 0.0$ | $0.2 \oplus 0.0$ |
| LEP Beam parameters (average) | $+3.1$ | $+4.4$ | $1.9 \oplus 0.5$ | $1.9 \oplus 0.4$ |
| Fluctuations in LEP beam parameters | — | — | $0.0 \oplus 0.5$ | $0.0 \oplus 0.5$ |
| Accidental coincidence background | $+1.0$ | $+0.1$ | $0.0 \oplus 0.1$ | $0.0 \oplus 1.0$ |
| Total experimental error | $-1.2$ | $-0.8$ | $7.3 \oplus 1.1$ | $7.3 \oplus 2.4$ |
| Theory error | - | - | $16 \oplus 0$ | $16 \oplus 0$ |

Table 5.3: *This Table summarizes the corrections applied and the corresponding experimental systematic uncertainties on the absolute $L_{RL}$ luminosity measurement. They are shown separately for the 1993 and 1994 measurements. The errors are decomposed into the components which are correlated amongst the 1993 and 1994 data sets, and those which are not.*

# Chapter 6

# The Event Selection

This chapter describes the selection of the different $Z^0$ decay channels. While the selection of $e^+e^- \rightarrow leptons$ is not the aim of this thesis, the selected lepton events are, however, used for the line shape fits described in chapter 8. Therefore, the selection of $e^+e^- \rightarrow leptons$ is described in here only very briefly.

The efficiencies are calculated with the JETSET Monte Carlo for the selection of multihadrons, BABAMC [18] for the selection of electron pairs, and KORALZ [19] for the selection of muon and tau pairs.

## 6.1 Multi Hadron Events

The process $e^+e^- \rightarrow hadrons$ typically has a high multiplicity and a high visible energy (see figure 6.1). The selection is therefore based on simple cuts on the measured multiplicity and energy. The selection is described in detail in chapter 7.

## 6.2 $e^+e^-$ Events

An $e^+e^-$ candidate event is shown in figure 6.2. These events usually have two tracks in the central detector (CJ). The energy of the electrons is completely absorbed in the electromagnetic calorimeter (ECAL) and there is no signal in the muon chambers.

An electron is identified by a high energy electromagnetic cluster associated to a charged track. Events are required to have two electron candidates with an acollinearity of less than 10°. Hadronic events are rejected by cuts on the number of ECAL clusters and charged tracks. A high visible energy is required to remove remaining background from $\tau$ pairs. The angular range is restricted to $|\cos\vartheta| < 0.7$ measured with the clusters in ECAL. The systematic errors at the different energy points are listed in table 6.1. The main systematic errors arrise from the cuts on $\cos\vartheta$ and the energy. The number of selected $e^+e^-$ events is 22468 in 1993 and 49799 in 1994.

| 1993 peak−2 | 1993 peak | 1993 peak+2 | 1994 |
|---|---|---|---|
| 0.34% | 0.23% | 0.35% | 0.24% |

Table 6.1: *Total systematic errors of the selection $e^+e^- \to e^+e^-$ at the different energy points in 1993 and 1994.*

## 6.3 $\mu^+\mu^-$ Events

Figure 6.3 shows an example of a $\mu^+\mu^-$ event. These events usually have two tracks in CJ, and only a small energy in ECAL as well as in the hadron calorimeter (HCAL). They usually have a signal in the muon chambers. The selection is described in detail in [28].

Candidate muon pairs are required to contain two tracks each having a momentum larger than 6 GeV, pointing to the interaction point and identified as a muon by one of the outer detectors (ECAL, HCAL or muon chambers). Multi hadron events are rejected by requiring that the event contains three or less charged tracks, after correcting for photon conversions and for tracks split by the reconstruction algorithm. Remaining $\tau$ pair and two photon background is rejected by requiring a visible energy, defined as the sum of the momentum of the two highest momentum tracks and the highest energy electromagnetic cluster, of at least $0.6 \cdot \sqrt{s}$. The angular acceptance cut is made at $|\cos\vartheta| < 0.95$. These criteria select 28119 events from the 1993 and 68539 events from the 1994 data. The systematic errors at the three 1993 energy points and the 1994 energy point are listed in table 6.2. The main contributions are from estimating the $\tau$ background and from track reconstruction problems close to the jet chamber sense wire planes. The error of 0.16% of the 1993 peak energy point is taken to be fully correlated between the 1993 energy points while the remainder is taken to be uncorrelated. The error of 0.15% of the 1994 energy point is taken to be fully correlated with the 1993 data.

| 1993 peak−2 | 1993 peak | 1993 peak+2 | 1994 |
|---|---|---|---|
| 0.26% | 0.16% | 0.22% | 0.15% |

Table 6.2: *Total systematic errors of the selection $e^+e^- \to \mu^+\mu^-$ at the different scan points.*

## 6.4 $\tau^+\tau^-$ Events

A $\tau^+\tau^-$ candidate event is shown in figure 6.4. The muon pair selection described above is used as a veto for the tau pair selection. Tau pair events are required to contain two narrow back-to-back low multiplicity jets identified using information from CJ and ECAL with an acollinearity of less than 15°. Time of flight measurements are used to reject cosmic ray events and the muon pair selection is used as a veto. The remaining background from multi hadron and two photon background is rejected using multiplicity cuts. The angular acceptance cut is made at $|\cos\vartheta| < 0.9$. The systematic errors at the different energy points are listed in table 6.3. The largest component comes from differences between data and Monte Carlo mainly in the track multiplicity and ECAL energy. A common systematic error of 0.43% (error of the 1993 peak energy point) is taken to be correlated between the 1993 energy points. The error of the 1994 data is 0.46%. The number of selected events is 24118 in 1993 and 56795 in 1994.

| 1993 peak−2 | 1993 peak | 1993 peak+2 | 1994 |
|---|---|---|---|
| 0.89% | 0.43% | 0.83% | 0.46% |

Table 6.3: *Total systematic errors of the selection* $e^+e^- \to \tau^+\tau^-$ *at the different energy points.*

The complementarity of the muon and tau pair selection leads to an anticorrelated error of 0.08% due to cross over events. This error is basically the uncertainty of the tau background in the muon selection.

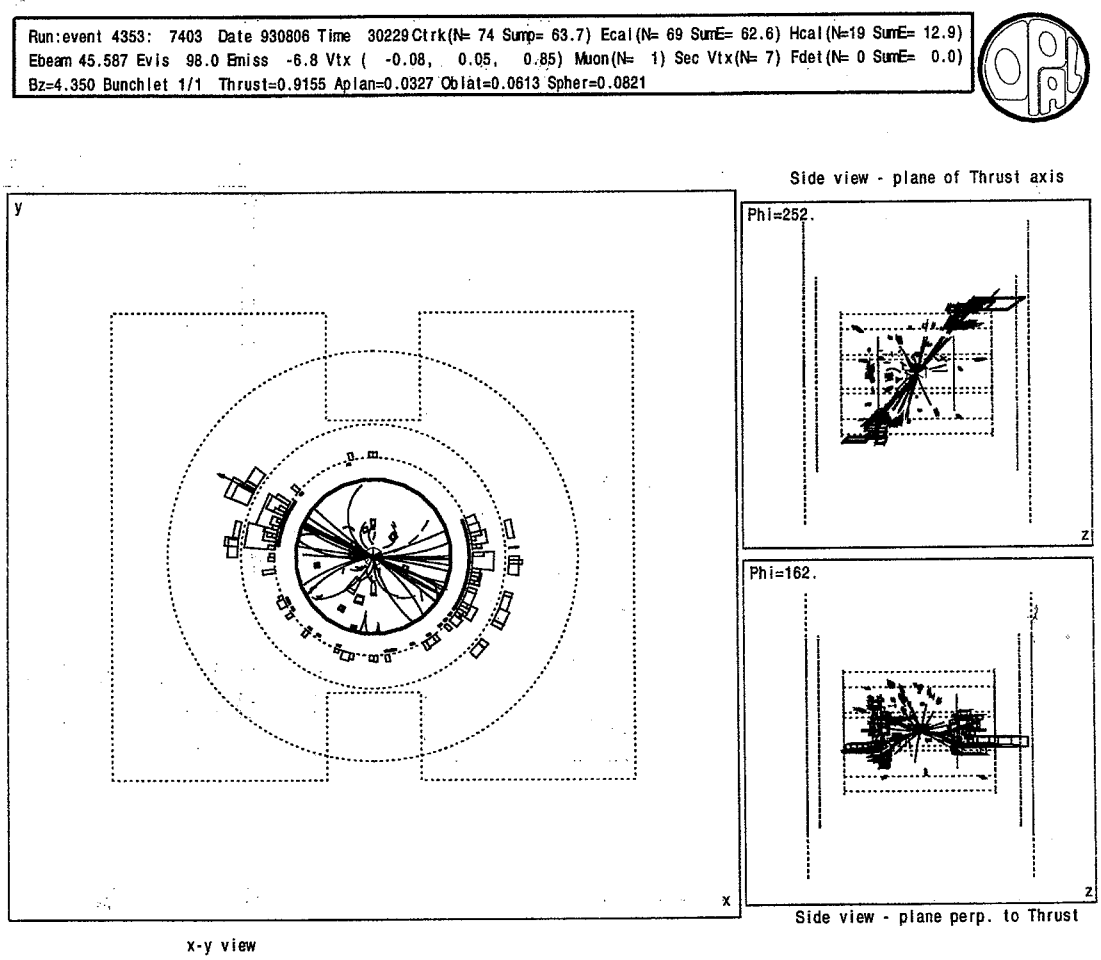


Figure 6.1: *A multi hadron candidate event. It has a high multiplicity and a high visible energy.*

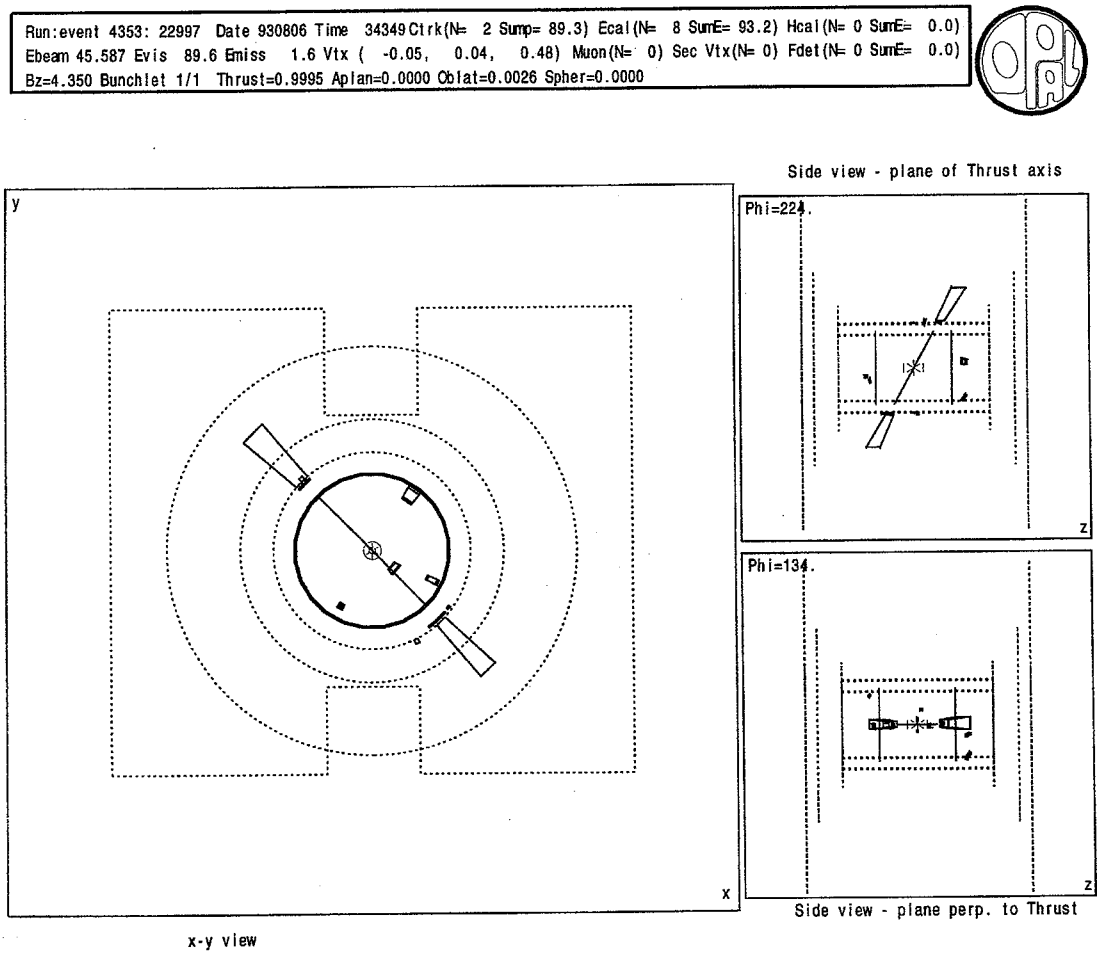


Figure 6.2: *A candidate event of the process* $e^+e^- \rightarrow e^+e^-$. *It has two tracks, each with an associated cluster in ECAL of almost the beam energy.*

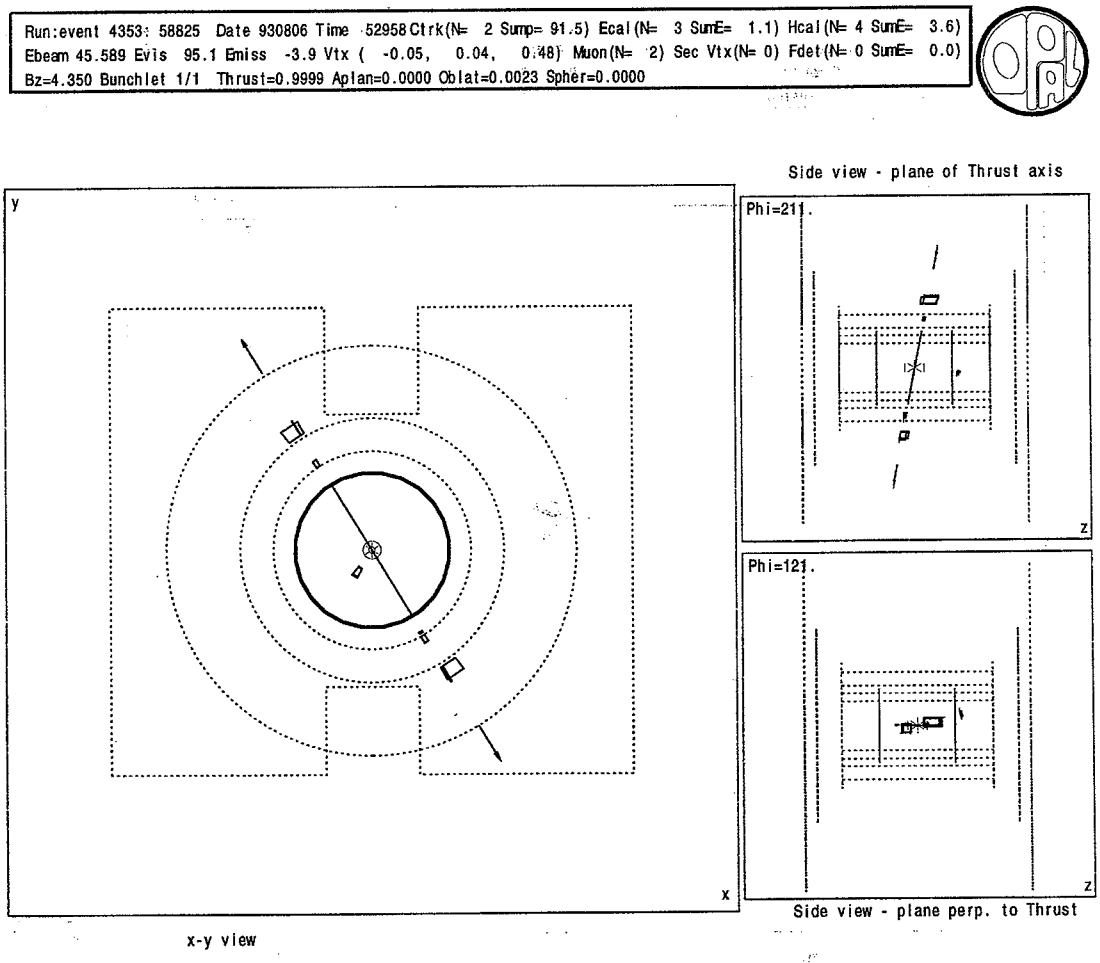


Figure 6.3: *A muon pair candidate event. It has two tracks and only little energy in ECAL and HCAL and has signals in the muon detectors.*

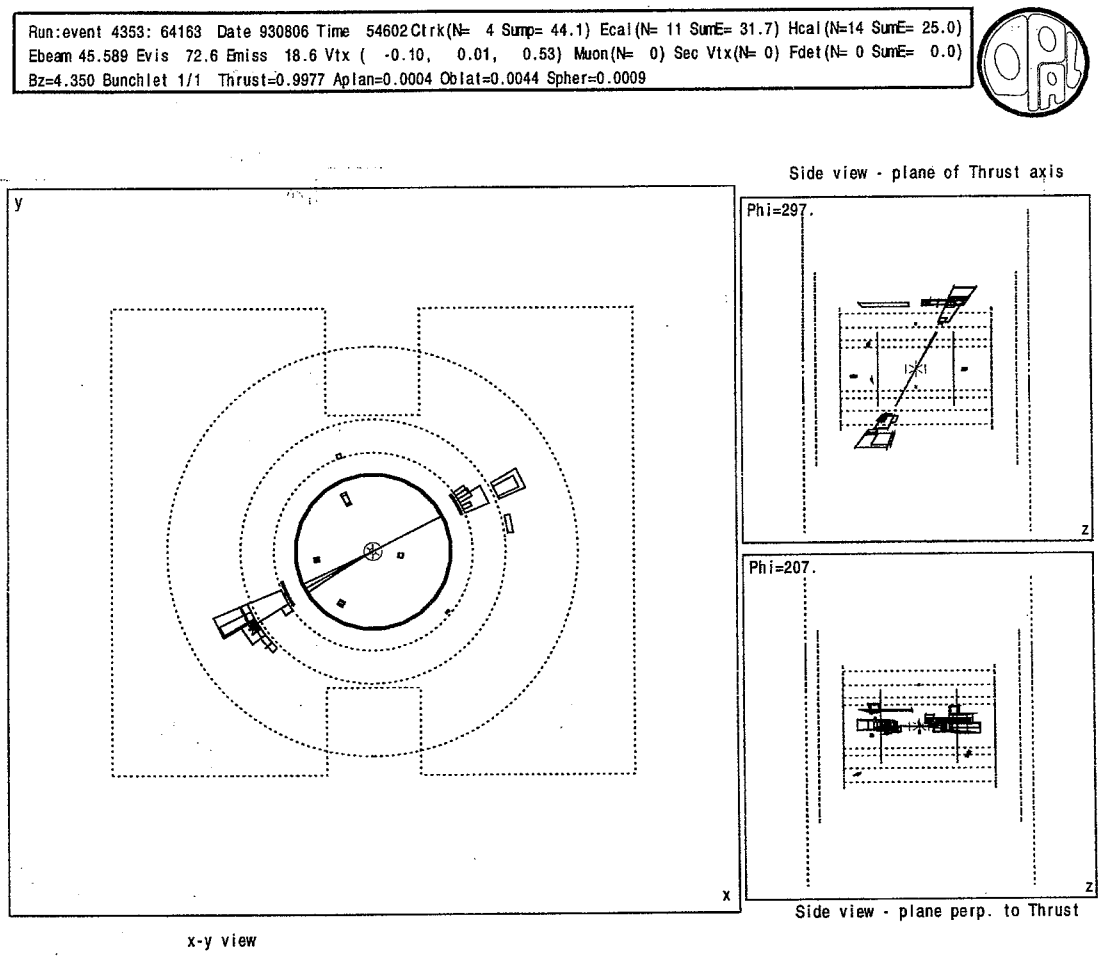


Figure 6.4: *A tau pair candidate event. It has two narrow back-to-back jets.*

# Chapter 7

# The Selection of Multi Hadronic Events

## 7.1 Introduction

This chapter describes the selection of multi hadronic events. The main task is the determination of the event selection efficiency and its systematic error. The selection efficiency is usually determined from Monte Carlo as $\epsilon = \frac{N_{sel}}{N_{all}}$, where $N_{sel}$ is the number of selected events and $N_{all}$ is the total number of events. After several years of running OPAL had two well established selections for multi hadronic events. One, the TKMH selection, was used until 1991 and the other selection, the HDMH selection, was used in 1992* and for the preliminary 1993 results. Rather than deriving a new selection, the aim of this analysis thus is to reduce the uncertainty on the number of events which are at the edge of, or lost by, the selection.

The TKMH selection has an efficiency of 98.5% with a systematic error of $4.0 \cdot 10^{-3}$. This systematic error was sufficient for the statistics available at that time. After accumulating more data the systematic error was no longer competitive to the statistical one and had to be reduced. This was achieved by introducing an additional detector component in the selection which partly closed geometrical gaps in the detector components used so far. The efficiency increased to 99.5% and the systematic error decreased to $2.0 \cdot 10^{-3}$.

After 1993, with event samples in the order of a few $10^6$ events and the improved luminosity measurement using the new SiW luminometer the systematic error of the HDMH selection was again too large. Therefore, the goal of this analysis was to reduce the systematic error by a factor of two to match the available statistics and the precision of the luminosity measurement.

The two main contributions to the systematic error of the HDMH selection (as well for the TKMH selection) come from the Monte Carlo simulation. One contribution is due to shortcomings in the detector simulation mostly the energy and multiplicity simulation of the electromagnetic calorimeter, especially the response to hadronic particles.
The other main contribution is due to uncertainties in the event generator. Phenomenological models are used for the Monte Carlo generation of hadronic events. These models depend on

*In 1992 a selection called TKMHL was used. It is with the exception of slightly different cuts identical to the HDMH selection.

parameters which control such quantities as the particle multiplicity of the events, the energy spectrum or the width of the jets (see chapter 3.4). The parameters are tuned to best represent the data. They have, however, a certain uncertainty which affects the selection efficiency. This uncertainty in the event generator is called fragmentation uncertainty.

To achieve a $1.0 \cdot 10^{-3}$ systematic error, initially, the strategy was to increase the efficiency by using additional detector components to further close the gaps in the geometrical coverage of the selection. An increased efficiency would automatically decrease the error of both, the fragmentation uncertainty and the detector simulation. Ideally, for an efficiency of 100% the detector simulation is no longer a reason of concern. However, simply increasing the geometrical acceptance of the hadron selection turned out to have other disadvantages as explained in appendix B.2. Therefore a different approach was pursued aiming at a selection largely independent on fragmentation details of the various models by constraining the number of lost events from the data themselves. This chapter first describes the event selection in 7.2 then the new analysis method in 7.3 and 7.4. Afterwards the systematic errors are discussed in 7.5.

## 7.2 Selection Cuts

The selection of multi hadronic events is conceptually easy since they have, compared to the other $Z^0$ decay channels, a high multiplicity and a high visible energy. The selection uses the central detector CJ, the electromagnetic calorimeter ECAL and the forward detector FD. It is based on simple cuts to discriminate against leptons and two photon events: on the total multiplicity (from CJ tracks, ECAL and FD clusters), the visible energy (from ECAL and FD clusters), the energy imbalance along the z-axis (from ECAL and FD clusters) and the sum of the invariant masses of the forward and backward hemispheres (calculated from CJ tracks, ECAL and FD clusters). The forward and backward hemispheres are defined with respect to the thrust axis[†] of the event.

Quality cuts are made to select good tracks and clusters. For CJ each track is required to have a $p_t$ of more than 150 MeV, the hit density has to be 50% of all geometrically possible hits, but at least 20 hits are required. The distance to the vertex has to be within 100 cm along the beam pipe and 2 cm in the perpendicular direction. ECAL clusters in the barrel (EB) are required to have a minimum energy of 100 MeV, clusters in the endcap (EE) have to consist of at least 2 ECAL blocks and have to have an energy of more than 200 MeV.

With the definitions :

$$E_{ECAL} = \sum_{cluster} E_{cluster}$$
$$PZ_{ECAL} = \sum_{cluster} E_{cluster} \cos(\vartheta_{cluster})$$

[†]The thrust axis is defined as the vector $\hat{n}$ which maximizes the quantity

$$thrust = \frac{\sum_i \mathbf{p_i} \cdot \hat{\mathbf{n}}}{\sum_i |\mathbf{p_i}|} .$$

For narrow, pencil like, events the thrust value is close to 1, for spherical events the thrust value is smaller approaching 0.5 for completely spherical events.

$$E_{FD} = \sum_{cluster} E_{cluster}$$
$$PZ_{FD} = \sum_{cluster} E_{cluster} \cos(\vartheta_{cluster})$$

the selection cuts are:

- $X_E^{vis} = (E_{ECAL} + \frac{1}{3}E_{FD})/\sqrt{s} > 0.1$
- $R_{bal} = |PZ_{ECAL} + PZ_{FD}|/(E_{ECAL} + E_{FD}) < 0.75$
- $InvMassSum = InvMass_F + InvMass_B > 4.5\ GcV$
- $N_{all} = N_{CJ} + N_{ECAL} + N_{FD} \geq 11$

Where $N_{CJ}$ is the total number of good CJ tracks in the event. Similarly, $N_{ECAL}$ and $N_{FD}$ are the total numbers of good ECAL and FD clusters. $E_{ECAL}$ is defined as the sum of the energies of all good ECAL clusters. $PZ_{ECAL}$ is the sum of the energies projected onto the z-axis (the direction along the beam pipe), $\vartheta$ is the cluster angle with respect to the z-axis. Corresponding expressions are used for FD.

Since for two photon events often one or both scattered electrons escape undetected along the beam pipe they usually have low visible energy. They also tend to be unbalanced since the two emitted photons usually have different energies. The event is therefore boosted in one direction. If one of the electrons hits the detector (mainly FD) the energy is also unbalanced since the electron leaves a lot of energy on this side. The cuts on the energy imbalance and the visible energy therefore discard mainly two photon events.
The main leptonic background comes from $\tau^+\tau^-$ events. They look like narrow two jet events. The event is devided into two hemispheres such that each hemisphere contains a jet. Each jet has a low invariant mass and the cut on the sum of the invariant masses of the forward and backward hemispheres therefore discards $\tau^+\tau^-$ events. The invariant masses in the two hemispheres are not physical quantities since they are calculated using all CJ tracks, ECAL and FD clusters. Charged particles with a track in CJ and a cluster in ECAL are therefore double counted.
The multiplicity cut discards $e^+e^-$ events. They can only pass the invariant mass cut if they are highly radiative. The $\mu^+\mu^-$ events are discarded by all the cuts mentioned above.

A comparison of data and Monte Carlo in the distributions of the cut variables is shown in figures 7.1-7.2. The agreement is good. Small discrepancies in the energy and multiplicity distributions can be observed.

The inefficiency due to each cut applied is shown in figure 7.3. The energy cut discards most of the events. Figure 7.4 shows $\cos(\theta_{thrust})$ for the lost events. As can be seen almost all lost events fall in the forward region ($|\cos(\vartheta)| > 0.9$) where CJ, ECAL and FD have holes in their coverage. The efficiency in the barrel region ($|\cos(\vartheta)| < 0.7$) is almost 100% and the overall efficiency is approximately 99.6%. Figure 7.5 shows the thrust distribution for all and for the lost events. The thrust value is a measure of the width of the jets. Figure 7.4 and 7.5 indicate that the lost events are mainly narrow two jet events which point in the forward direction.

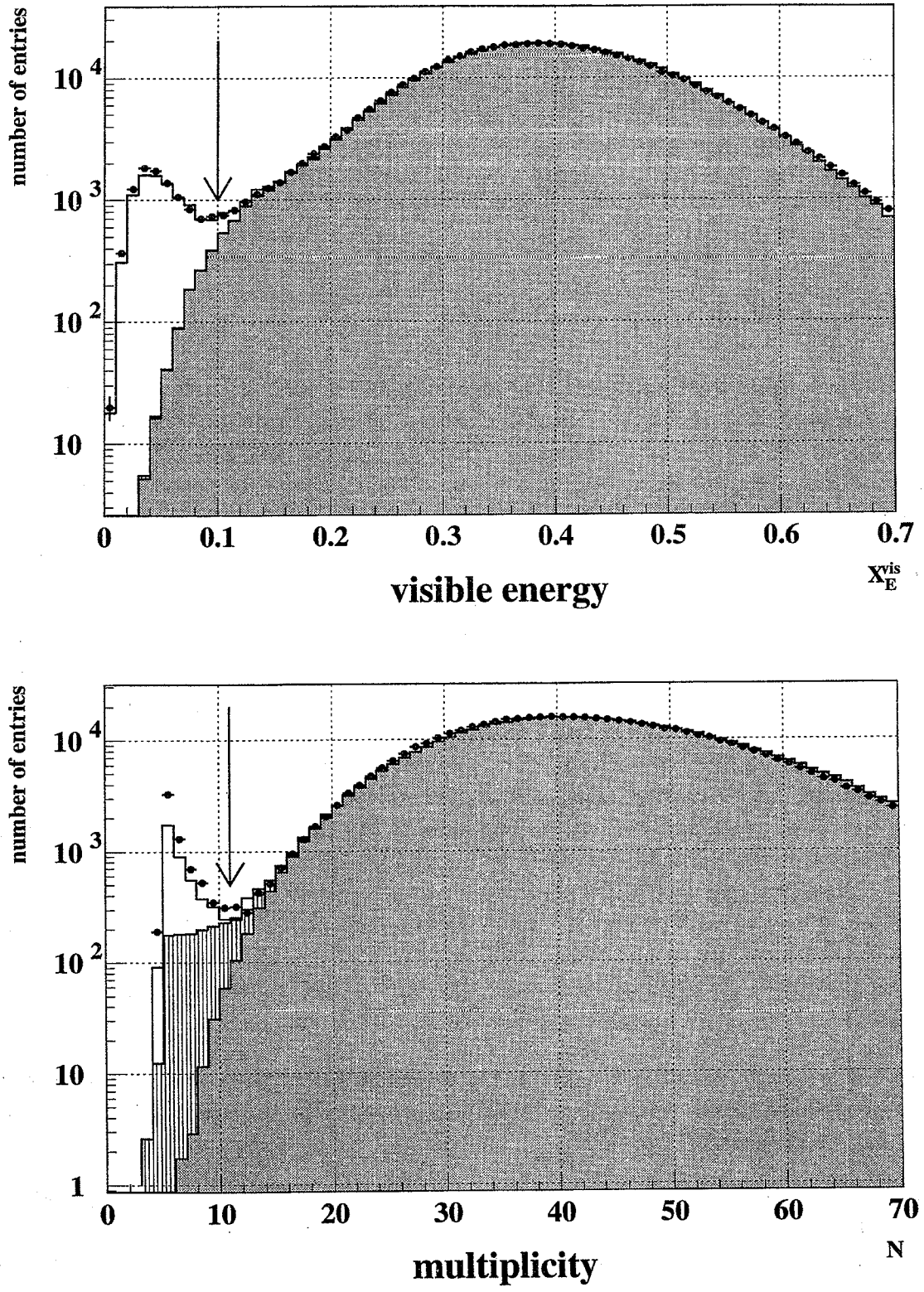


Figure 7.1: *Comparison of the visible energy and multiplicity distributions (as defined in the text) between data and Monte Carlo. The arrows indicate the positions of the cuts. The shaded histogram corresponds to multi hadron Monte Carlo, the hatched histogram represents $\tau\tau$ Monte Carlo and the open histogram shows the two photon background. The data are the points.*

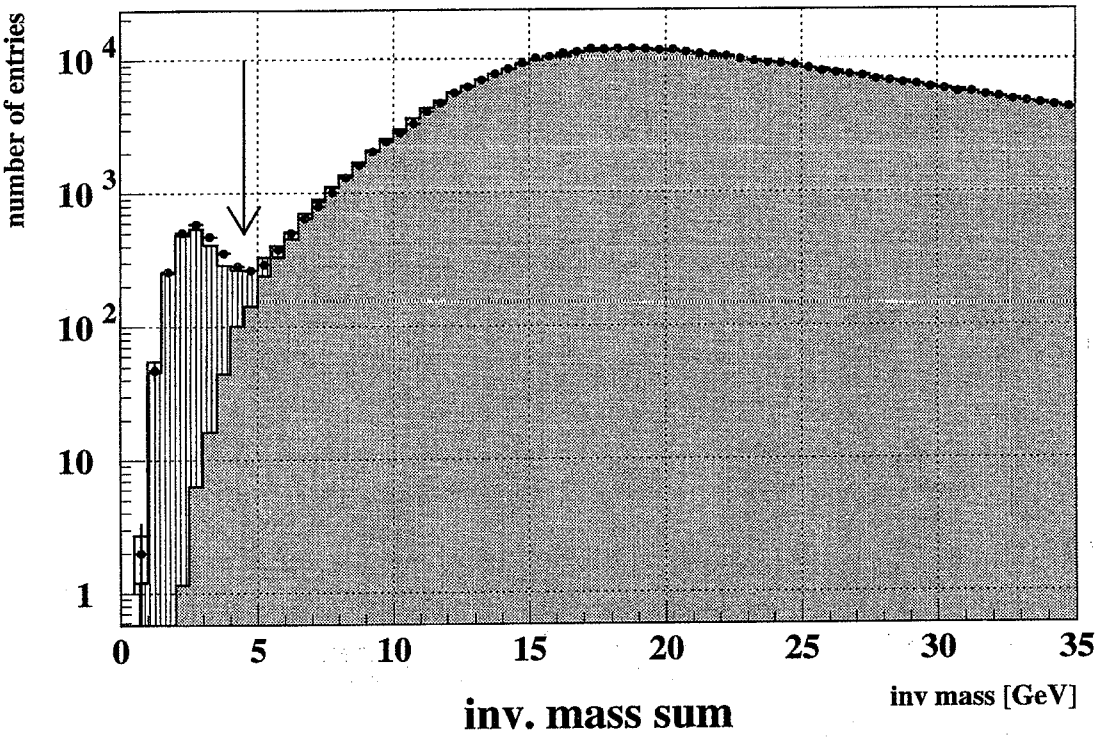


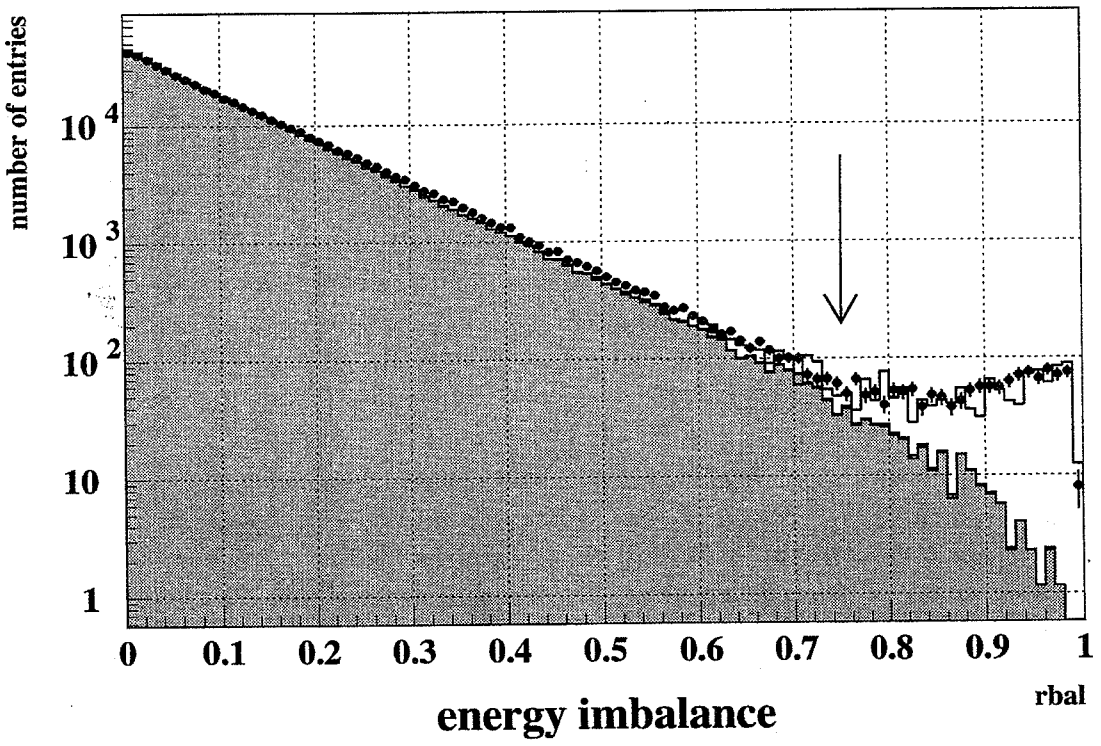


Figure 7.2: *Comparison of the sum of the invariant masses in the forward and backward hemispheres and energy balance distributions. The arrows indicate the position of the cuts (explanations as in figure 7.1).*

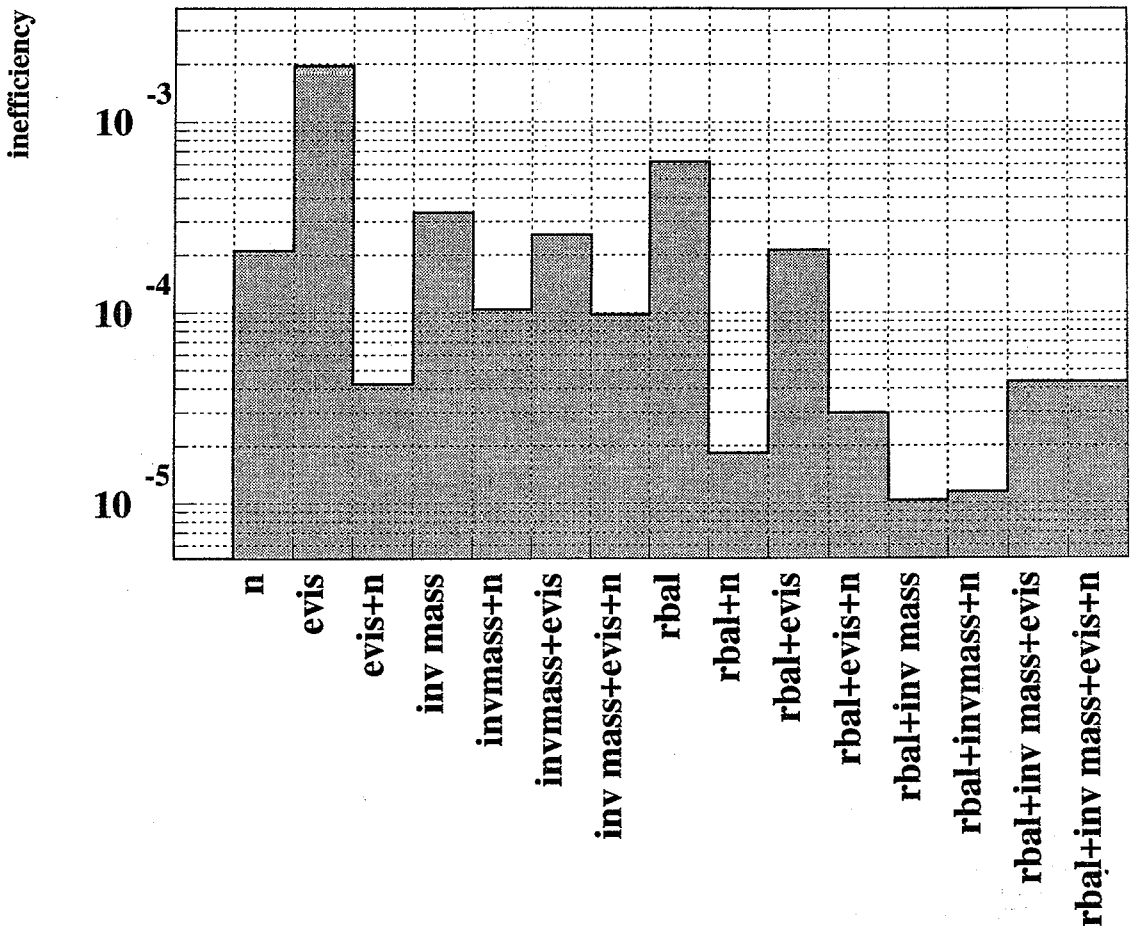


Figure 7.3: *Inefficiency due to each cut applied. The combinations of cuts are exclusive, for example an event which fails the multiplicity and visible energy cut counts to the evis+n bin and not to the n bin or evis bins. Note that the correlation between the cuts on energy and multiplicity is very small. The multiplicity cut discards less events than the other cuts. The cut on the visible energy is the hardest cut.*

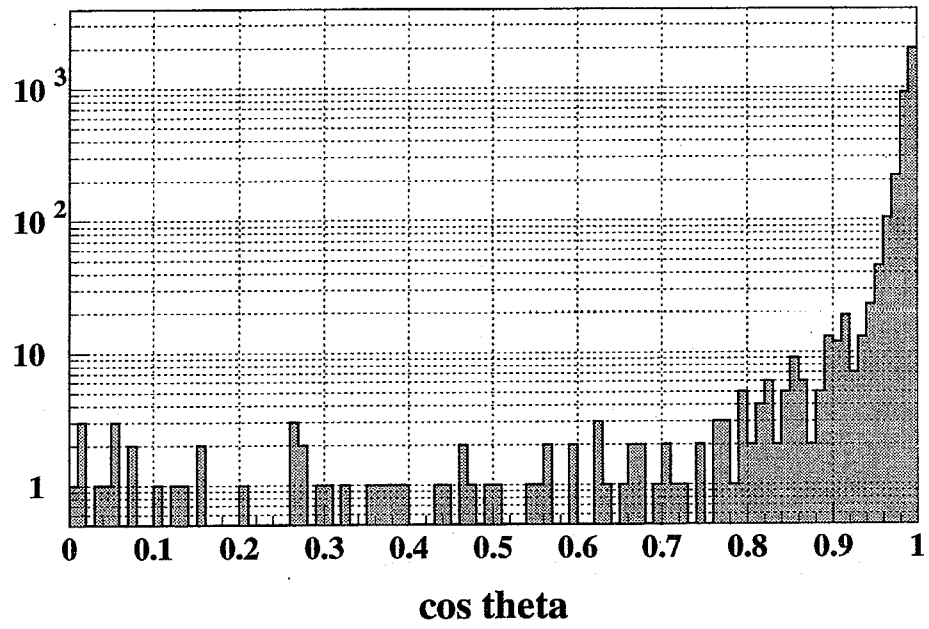


Figure 7.4: $|\cos(\vartheta_{thrust})|$ *of the events lost in the selection (MC). Almost all lost events lie in the forward region.*

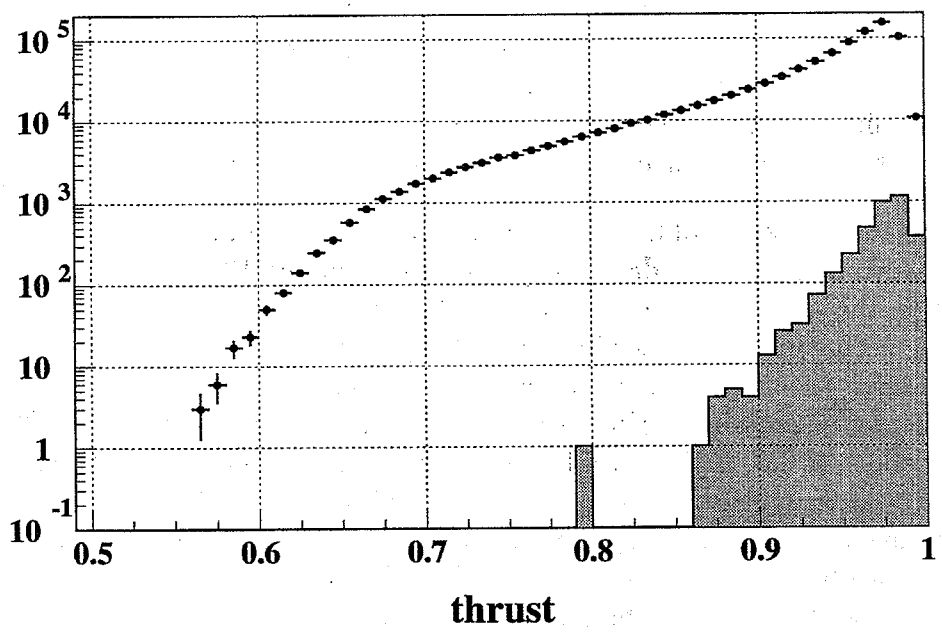


Figure 7.5: *Thrust of all events (points) and the lost events (histogram) for MC events. The lost events have mainly a high thrust value indicating that they are narrow two jet events.*

## 7.3 Analysis Strategy

The basis for the selection used in this analysis is the HDMH selection. The HDMH selection has, compared to this analysis, two additional cuts on the multiplicity of the forward and backward hemispheres. The reasons why the selection has been changed is described in appendix B.1. For the HDMH selection the main contributions to the systematic error are $12 \cdot 10^{-4}$ due to shortcomings in the detector simulation and $12 \cdot 10^{-4}$ due to fragmentation uncertainties.

The fragmentation uncertainty is largely due to different rates of narrow two jet events predicted by different event generators. Studies using the JETSET Monte Carlo and a fast smear mode detector simulation (see appendix) indicated that the acceptance calculation is most sensitive to changes in the parameter $Q_0$. The parameter $Q_0$ is the invariant mass cut-off below which partons do not radiate gluons. It mainly has an effect on the multiplicity of the events. Using the full GOPAL detector simulation and changing $Q_0$ from its standard value of 1.0 $GeV$ to 1.8 $GeV$ ($1\sigma$) resulted in a change of $10 \cdot 10^{-4}$ in the selection efficiency. Similarly the results obtained using the HERWIG Monte Carlo differed by $7 \cdot 10^{-4}$ from those using the standard JETSET Monte Carlo. As a result of this, an uncertainty of $12 \cdot 10^{-4}$ was assigned to the HDMH selection due to the modelling of fragmentation.

As mentioned in chapter 3.4, the fragmentation parameters are adjusted using global event shape distributions [17]. These distributions have a rather undefined sensitivity to the special topology of events which are lost in the selection (namely narrow two jet events). There might therefore be a difference in the number of these events between data and Monte Carlo. The analyses done so far never compared the number of these events between data and Monte Carlo. It was assumed that these events lie within the phase space explored by using different event generators and by varying the fragmentation parameters.

To reduce the fragmentation error in this analysis the rate of events susceptible to being lost through the acceptance holes in the forward region is determined directly from the data by simulating the acceptance holes in the barrel region. This method allows a fragmentation independent determination of the selection inefficiency. This strategy is described in chapter 7.4. It is the key for obtaining the reduced systematic error of the multihadron selection.

For the old analysis the effect of the differences between data and Monte Carlo was estimated in the following way: Compared to data the Monte Carlo for the 1991 detector setup showed a difference of 3% in the mean of the energy in the electromagnetic calorimeter and a difference of 7% in the mean multiplicity. Rescaling the energy (by 3%) and the multiplicity (by 7%) separately and adding the effects on the acceptance in quadrature resulted in an error of 0.1% for the 1991 detector simulation. Similarly had the differences between the 1990 data and Monte Carlo an effect of 0.07%. The 1991 Monte Carlo had a different treatment of hadronic interactions in the electromagnetic calorimeter compared to the 1990 Monte Carlo. Both errors added in quadrature were then used as the error due to the detector simulation.
This method has two big disadvantages. One is that the mean of the energy and multiplicity distribution is far away from the cut boundaries and the events which are at the cut boundary might have totaly different problems with the detector simulation. Deriving a scaling factor from the mean is therefore not useful. The other disadvantage is that the difference in the mean of the energy and multiplicity distributions could as well come from the event generator. The event generator could wrongly predict the energy spectrum and the multiplicity of the events

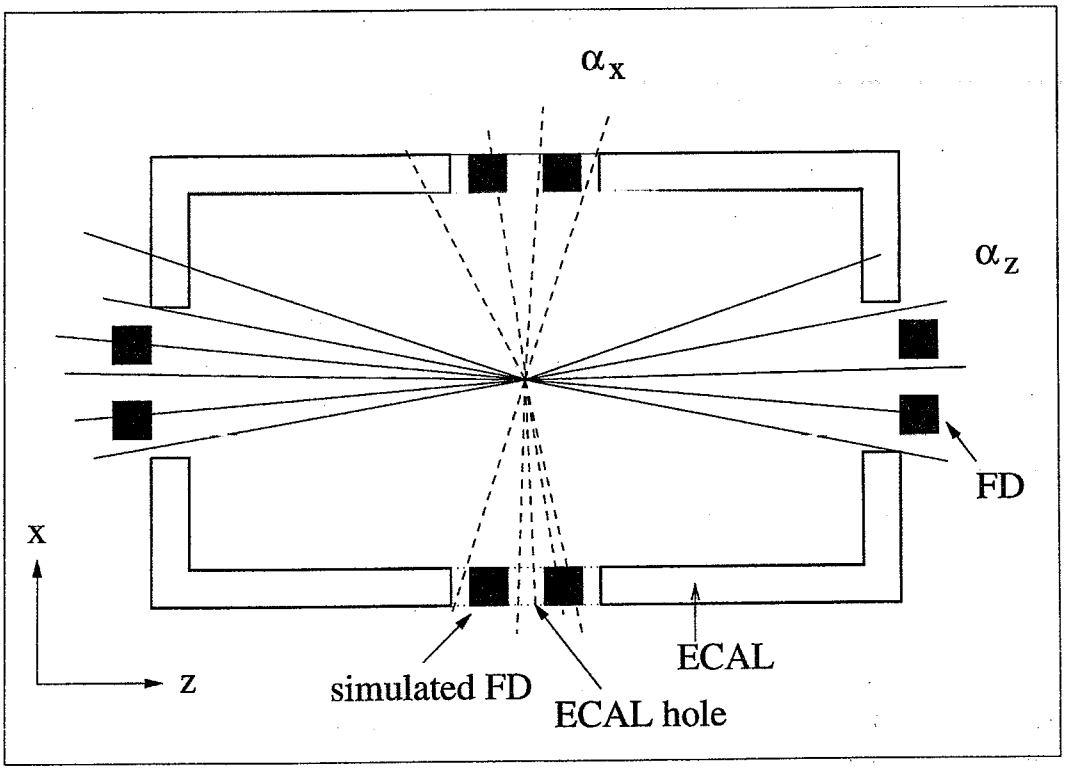


Figure 7.6: *Simulation of the forward acceptance holes in the barrel region.*

which would then have an effect on the measured energy and multiplicity in the Monte Carlo. The old procedure is therefore not well adopted to determine the error due to the detector simulation. It could have double counted contributions of the fragmentation uncertainties or even have completely underestimated the effect of possible differences in the detector simulation for the events close to the cut boundaries.
In this analysis the error of the detector simulation is estimated in a fragmentation independent way. This is described in section 7.5.2.

## 7.4 Measuring the Inefficiency with Data

The overall inefficiency of the event selection is approximately $4 \cdot 10^{-3}$, as determined using Monte Carlo. The inefficiency in the barrel region is less than $10^{-4}$ and almost all lost events fall in the forward region where CJ, ECAL and FD have holes in their coverage.

Events with a radiated initial state photon of more than 35 GeV make up $5.7 \cdot 10^{-4}$ of all events and only 3.6% of the lost events. Most of the lost events are lost for geometrical reasons. They are typically narrow two jet events which escape through the holes in the forward acceptance. Such events are, as already explained, not necessarily well described by the Monte Carlo. The new approach is to infer the rate of events which are lost through the forward hole by measuring the rate of events lost through an equivalent, artificially created, hole in the barrel region using data (see figure 7.6).

The response in the forward region and in particular the holes in the coverage of CJ, ECAL and FD are simulated in the barrel. The multihadron selection is applied to both data and MC and then the inefficiency $\alpha_x$ introduced by the simulated hole in the barrel is measured for events with $|\cos(\vartheta_{thrust})| > 0.87$ with respect to the x-axis. The inefficiencies $\alpha_x, \alpha_z$ are defined as the number of events which fail the selection expressed as a fraction of the number of events satisfying $|\cos(\vartheta_{thrust})| > 0.87$ with respect to the x- or z-axis.

In the absence of hard initial state photon radiation the event topologies for the events which are lost in the simulated hole and those lost in the forward direction are quite similar. It is therefore plausible that the ratio of the number of events lost in the forward hole to the number of events lost in the barrel hole should be independent of fragmentation parameters. Under this assumption a fragmentation independent estimate of the inefficiency of the event selection can be obtained by rescaling the inefficiency $\alpha_x$ measured in data by the ratio predicted by the MC. Algebraically the extrapolated overall inefficiency can be expressed as:

$$\alpha_{all_{data}} = \alpha_{z_{data}} \cdot g \qquad \text{with} \qquad \alpha_{z_{data}} = \alpha_{x_{data}} \cdot \frac{\alpha_{z_{MC}}}{\alpha_{x_{MC}}}$$

Here $g$ is a geometrical factor which extrapolates the inefficiency in the forward cone to the full angular acceptance. It is determined with the standard Monte Carlo $g = \frac{\alpha_{all_{MC}}}{\alpha_{z_{MC}}}$, where $\alpha_{all_{MC}}$ is the overall inefficiency determined using Monte Carlo.

Using the above method the rate of jets escaping through the forward acceptance holes is determined with data. The MC still has to predict the number of events which are lost due to hard initial state photon radiation. Their number can not be measured by this technique. These events are included in $\alpha_{all_{MC}}$ and the hole simulation procedure therefore does not change the Monte Carlo prediction.

### 7.4.1 The Simulation of the Forward Region in the Barrel

To the extend that the simulated holes in the barrel and the true acceptance holes in the forward direction are not identical, and also that the angular distribution of events in these regions are different, the Monte Carlo has to be used to extrapolate from the measured rate of events lost through the simulated barrel holes to the rate lost in the forward direction. It is therefore important to get a good simulation of the endcap response in the barrel to minimize the extrapolation required. To account for the different angular event distributions in the barrel and the endcap the events in the barrel are weighted to obey the $1 + \cos^2\vartheta$ distribution of the forward direction. Since the energy cut is the most important (it discardes most of the events) emphasis is put on the energy response of ECAL and FD. Less important is the multiplicity of CJ.

The simulated holes are cylindrically symmetric in the two hemispheres about the x-axis. The simulation for the three detectors used is done as follows:

**ECAL**: To simulate the hole in the forward region all clusters within a given radius around the x-axis are discarded. Since the EE (endcap ECAL) response is different from the EB (barrel ECAL) response two further effects also have to be corrected for: the energy response and the

two-cluster separation of EE.
The EB energy response is adjusted to reproduce the effective EE response as a function of energy and angle using energy correction functions. These functions correct the energy loss of electrons and photons in material in front of ECAL. The corrected energy is therefore uniform and does not depend on the amount of material in front of the detector. As the EB and EE energy correction functions are derived for electrons but most of the low energy clusters are from hadrons, the correction is applied for a fraction of clusters starting with 0% at 0.7 *GeV* linearly increasing to 100% at 7.0 *GeV*.
To correct for the worse two-cluster separation of EE compared to EB, clusters in EB which are closer than the minimal EE two-cluster separation are merged. Figure 7.8 shows the cluster energy distribution in the forward direction and the barrel region before all corrections, after merging, and after merging plus the energy correction. Figure 7.9 shows the event energy and multiplicity distributions before and after the corrections. The merging of clusters shifts the low energy peak of the cluster energy distribution slightly to higher energies and decreases the multiplicity. The energy correction affects mostly the high energy tail of the cluster energy distribution. Although the changes in the cluster energy distributions are rather small the effect of the corrections in the event energy and multiplicity distributions are large.
To study the sensitivity of the procedure to details of the hole simulation three different-sized cones are used. The sizes in $\cos(\vartheta)$ are 0.9772, 0.9805 and 0.9832. These sizes correspond to the center of the frontface of the innermost ECAL block, the inner edge and the middle of the lower side. For the plots the central cone is used (see figure 7.7).

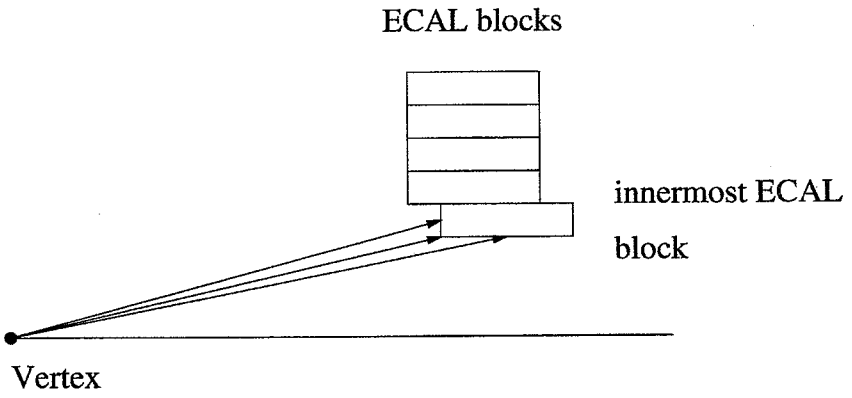


Figure 7.7: *The sizes of the three ECAL holes used.*

**FD**: EB clusters are used to simulate FD. All clusters above the energy cut-off of 2.0 GeV in the geometrical acceptance ($0.9892 < |\cos(\vartheta_x)| < 0.99933$) of FD are used. Figure 7.10 shows the event energy and multiplicity distributions of the simulated FD and the real FD. The simulation of FD works very well. There is just a slight disagreement in the high energy tail.

**CJ**: Since CJ is only used for the cuts on the multiplicity and the sum of the invariant masses of the forward and backward hemispheres, the hole simulation for CJ in the barrel is done in a rather simple way. Tracks within a circular cone of $|\cos(\vartheta_x)| > 0.96$ or with $p_{t_x}$ of less than 150.0 MeV (as in the forward direction) are rejected. Figure 7.11 shows the event multiplicity distribution. The endcap distribution is slightly shifted to higher multiplicities compared to the simulated endcap hole.

The detailed differences between the simulated barrel hole and the endcap region shown in figures 7.8-7.11 cause the cut variables to be different. The cut variables are shown in figure 7.12. The effect of the differences in the cut variables is estimated by shifting each cut variable with the hole simulation for events in the barrel region until the inefficiency due to the specific cut is almost the same as in the forward region. The difference in the extrapolated inefficiency between the shifted and not shifted distributions is taken as a systematic error. Details can be found in chapter 7.5.1.

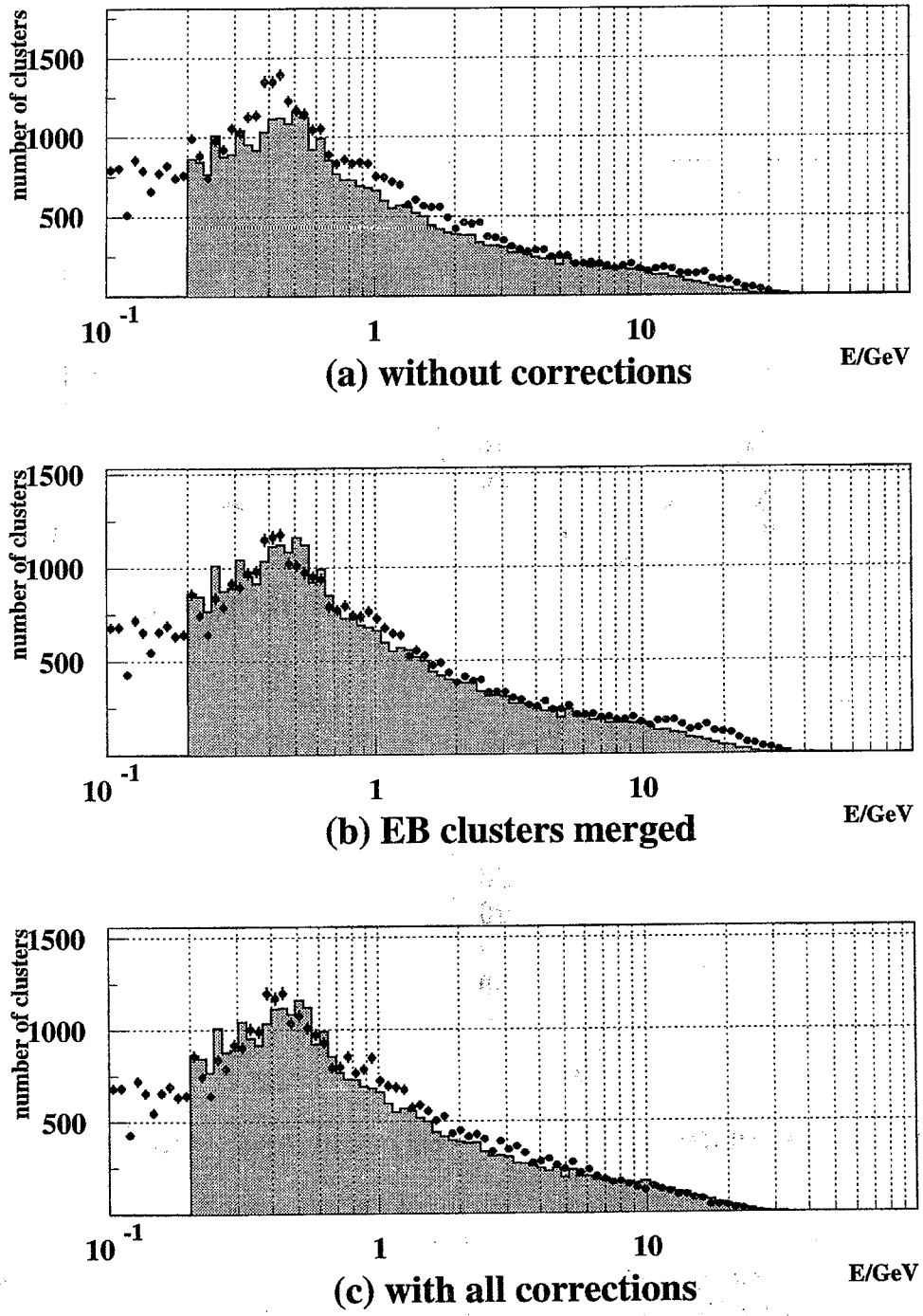


Figure 7.8: *(a) Cluster energy distribution for EE (histogram) and EB (points). (b) The same distribution as in (a) after merging the EB clusters. (c) The same distribution as in (a) after merging the EB clusters and correcting their energy.*

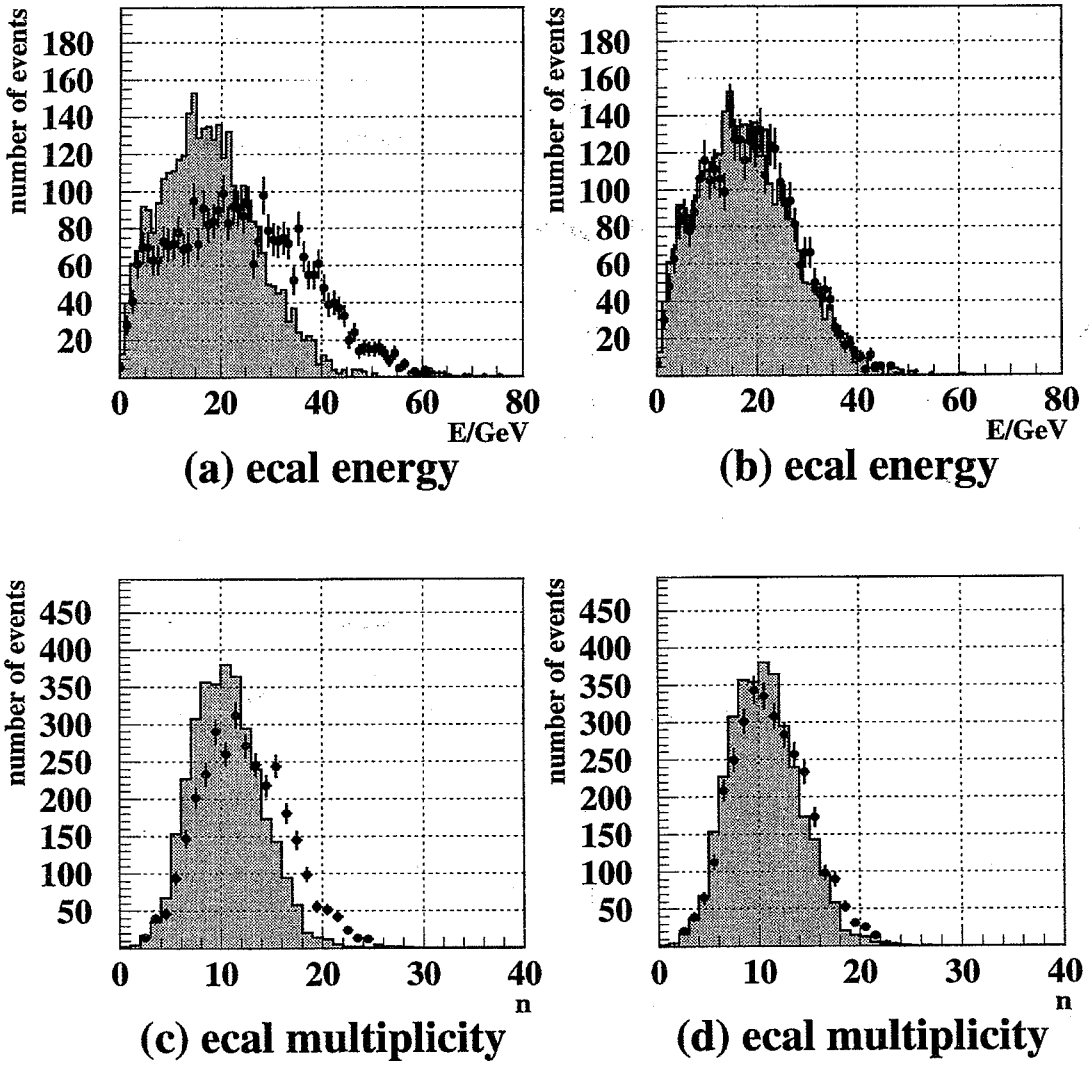


Figure 7.9: *(a) ECAL event energy distribution without corrections. The histogram is EE, the points EB. (b) ECAL event energy distribution with the corrections. (c) ECAL event multiplicity without corrections. (d) ECAL event multiplicity with the corrections.*

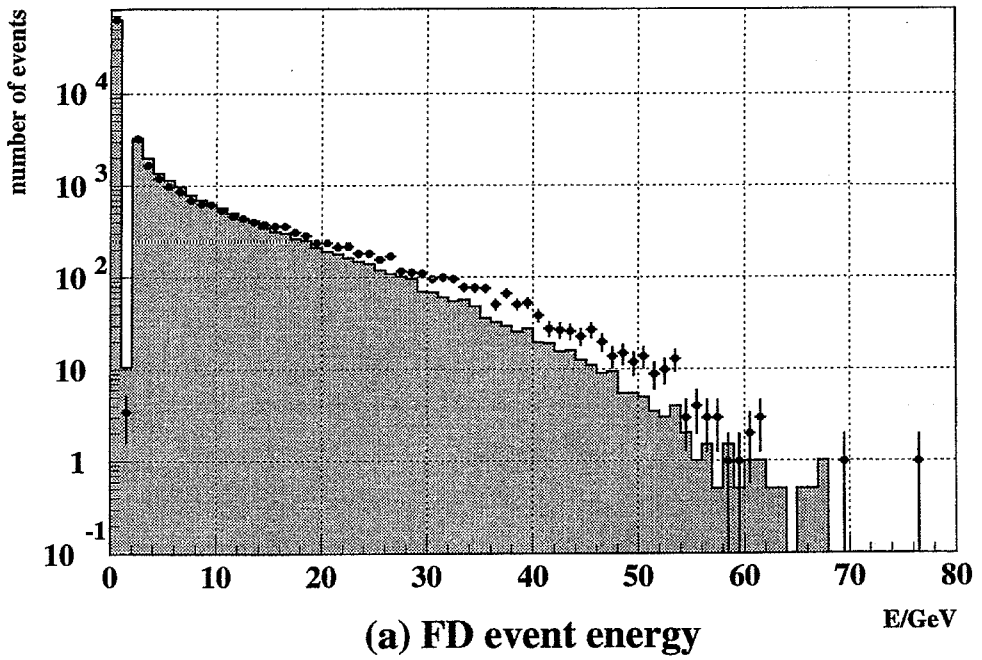


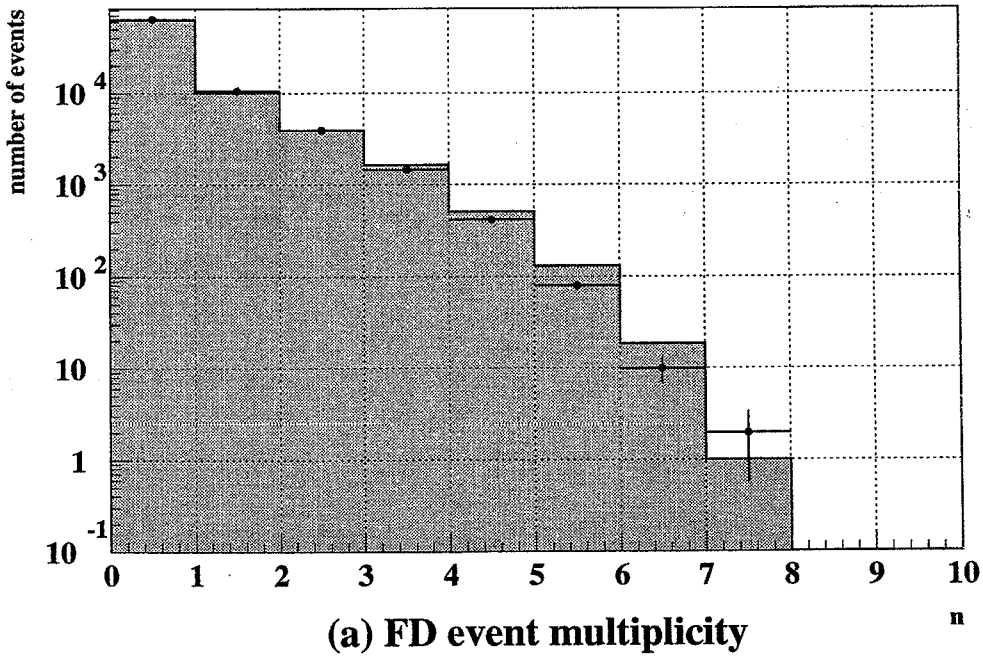


Figure 7.10: *(a) Comparison of the event energy distribution of the real FD (histogram) and the simulated FD (points). (b) Comparison of the event multiplicity distribution of the real FD (histogram) and the simulated FD (points).*

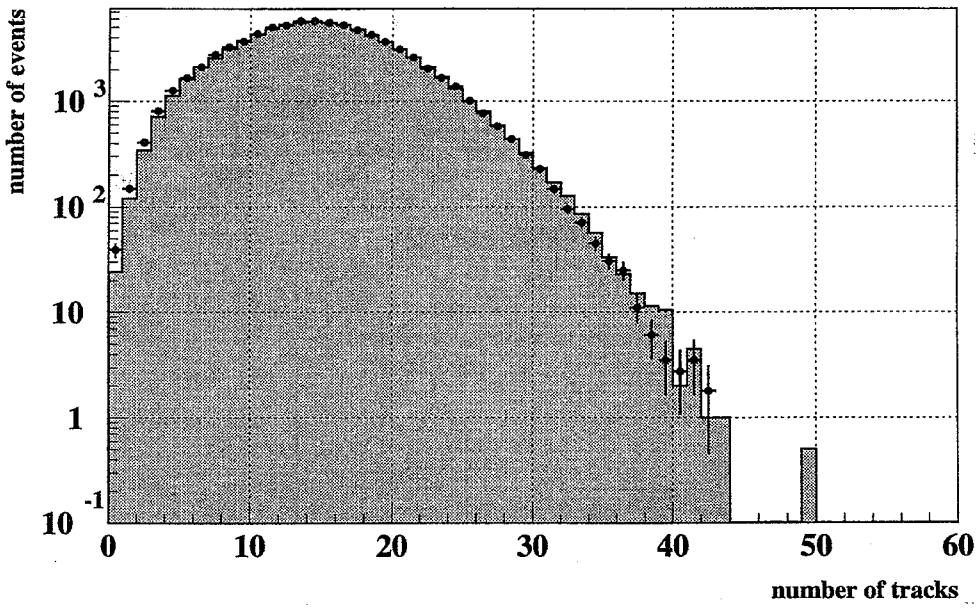


Figure 7.11: *CJ event multiplicity distribution for endcap (histogram) and simulated endcap region (points).*

### 7.4.2 Result of the Hole Simulation Procedure

The final efficiency of the selection determined with the hole procedure after correcting for the shifts in the energy and the multiplicity (see section 7.5.1) is $\epsilon = 99.562\%$. The determination of the efficiency using Monte Carlo events without the hole simulation is $\epsilon = 99.599\%$. Because this determination has an uncertainty due to fragmentation parameters of $12 \cdot 10^{-4}$ the efficiency determined with the new procedure is more reliable and has a smaler error (see below).

## 7.5 Systematic Errors of the Multihadron Selection

The hole simulation procedure allows a factorization of the systematic errors into components related to the simulated hole in the barrel region and those which are due to the determination of the inefficiency in the forward direction (which is, except for a geometrical factor, identical to the total inefficiency determined using Monte Carlo). The error due to the hole simulation procedure is described in the next section. This includes residual fragmentation uncertainties. Therefore, no additional fragmentation uncertainties have to be taken into account for the determination of the total efficiency (or the inefficiency in the forward direction). The only contributions to the error of the forward direction are due to the detector simulation described in section 7.5.2 and due to the background subtraction (section 7.5.3).

### 7.5.1 Systematic Errors of the Hole Simulation Procedure

There are different sources of systematic errors for the hole simulation procedure. The extrapolation required to translate the measured rate of events lost in the simulated barrel holes to the rate of events lost in the forward direction results in a residual fragmentation uncertainty. This has been checked in several ways. To see how critical the size of the artificially created hole is, three different sizes of ECAL holes have been used. The effect of the different detector response has been examined by scaling the cut variables of the barrel. Finally different event generators have been used for the acceptance calculation. The method relies on a high efficiency of the standard selection in the barrel, since the inefficiency of the standard selection in the barrel can not be measured. Any differences in the standard barrel efficiencies of different event generators have to be included in the systematic error.
Other sources of systematic errors are differences between the GOPAL detector simulation and the data in the barrel region, the $\tau$-background in the data and the cut in $\cos(\vartheta_{thrust_{x,z}})$. The error due to the barrel detector simulation is a new error which is introduced by the new method. For the standard efficiency determination differences between data and Monte Carlo in the barrel almost do not matter because the efficiency is nearly 100%. In the following a detailed description of the systematic errors is given.

The error due to detailed differences between the simulated barrel hole and the true response of the detector in the forward region is examined in two ways. A comparison of the cut variables in the forward region with the simulated hole in the barrel is shown in Figure 7.12 for the JETSET MC. There are clear differences. To study the effect of these differences each

variable is scaled, for events pointing in the barrel region, until the inefficiency due to this variable closely reproduces the inefficiency of the forward direction. Figure 7.12 also shows the scaled distributions compared to the unscaled distributions. The difference of $1.7 \cdot 10^{-4}$ in the extrapolated overall inefficiency calculated using the scaled and unscaled distributions is taken as the systematic error. An additional error is estimated by using the three different ECAL holes and taking the largest difference between them of $0.7 \cdot 10^{-4}$ in the overall inefficiency as an error.

A check of residual systematics due to fragmentation uncertainties is done by comparing the efficiency determined with the standard JETSET Monte Carlo to the efficiencies determined with different event generators. For this purpose a JETSET sample with a changed $Q_0$ ($Q_0$ changed by $2\sigma$ from 1.0 GeV to 2.6 GeV) and a HERWIG MC are used, both generated with full detector simulation. The $Q_0$ sample shows a difference of $1.5 \cdot 10^{-4}$ in the extrapolated overall inefficiency. The difference in the direct determination of the efficiencies would be $7 \cdot 10^{-4}$, which shows how well the method works. The HERWIG sample differed by $3.6 \cdot 10^{-4}$. As a further study, $\sigma_q$ and $\Lambda_{QCD}$ are changed in a fast treelevel based smear mode MC (see appendix B.3). These parameter are, as explained in section 3.4, the parameters to which the selection is most sensitive to. The differences observed are small and consistent with 0. The maximum difference found is $4.0 \cdot 10^{-4}$. The statistical uncertainty on these comparisons is of the order of $2.0 \cdot 10^{-4}$. Although the differences in the inefficiency are not very statistically significant the largest difference of $4.0 \cdot 10^{-4}$ is used as a systematic error due to leftover fragmentation dependencies.

To check the fragmentation dependence of the standard selection in the barrel region the same Monte Carlos as above are used. The inefficiency in the barrel region of the standard Monte Carlo is $7.4 \cdot 10^{-5}$ and is taken into account in the extrapolation to full acceptance. The largest difference in the barrel inefficiency with respect to the standard Monte Carlo is found for the sample with $Q_0 = 2.6$. The difference is $2.1 \cdot 10^{-4}$ and originates from the cut in the visible energy. Since this difference is not treated by the extrapolation and it can not be measured with data it has to be taken as an additional systematic error.

Figure 7.13 shows a comparison of the cut variables with the simulated barrel hole for the data and the JETSET MC. Small shifts between data and MC can be observed for the energy and multiplicity distributions. The shape is well simulated. The mean of the energy distribution of MC events with $|\cos(\vartheta_{thrust})| > 0.87$ (with respect to the x-axis) is shifted to larger energies by 1.6% compared to data. The mean of the multiplicity distribution is larger by 1.02 units. As explained in section 7.3 it is unclear if this difference is due to fragmentation uncertainties or detector simulation. What matters, however, is the difference between data and Monte Carlo for the narrow two jet events, i.e. the events which are lost through the acceptance holes. The events which are lost through the simulated acceptance holes show a difference of 3.5% in the mean of the energy and 0.36 units in the mean of the multiplicity (the MC is shifted towards larger values). The mean in the energy and multiplicity are determined without the hole simulation for events lost due to the hole simulation. After scaling the energy and multiplicity in the Monte Carlo such that the means of data and MC agree, the extrapolated overall efficiency differs by $3.9 \cdot 10^{-4}$ compared to the unscaled Monte Carlo. This difference is used as an estimate of the error due to the detector simulation. The rescaled Monte Carlo is used as reference.

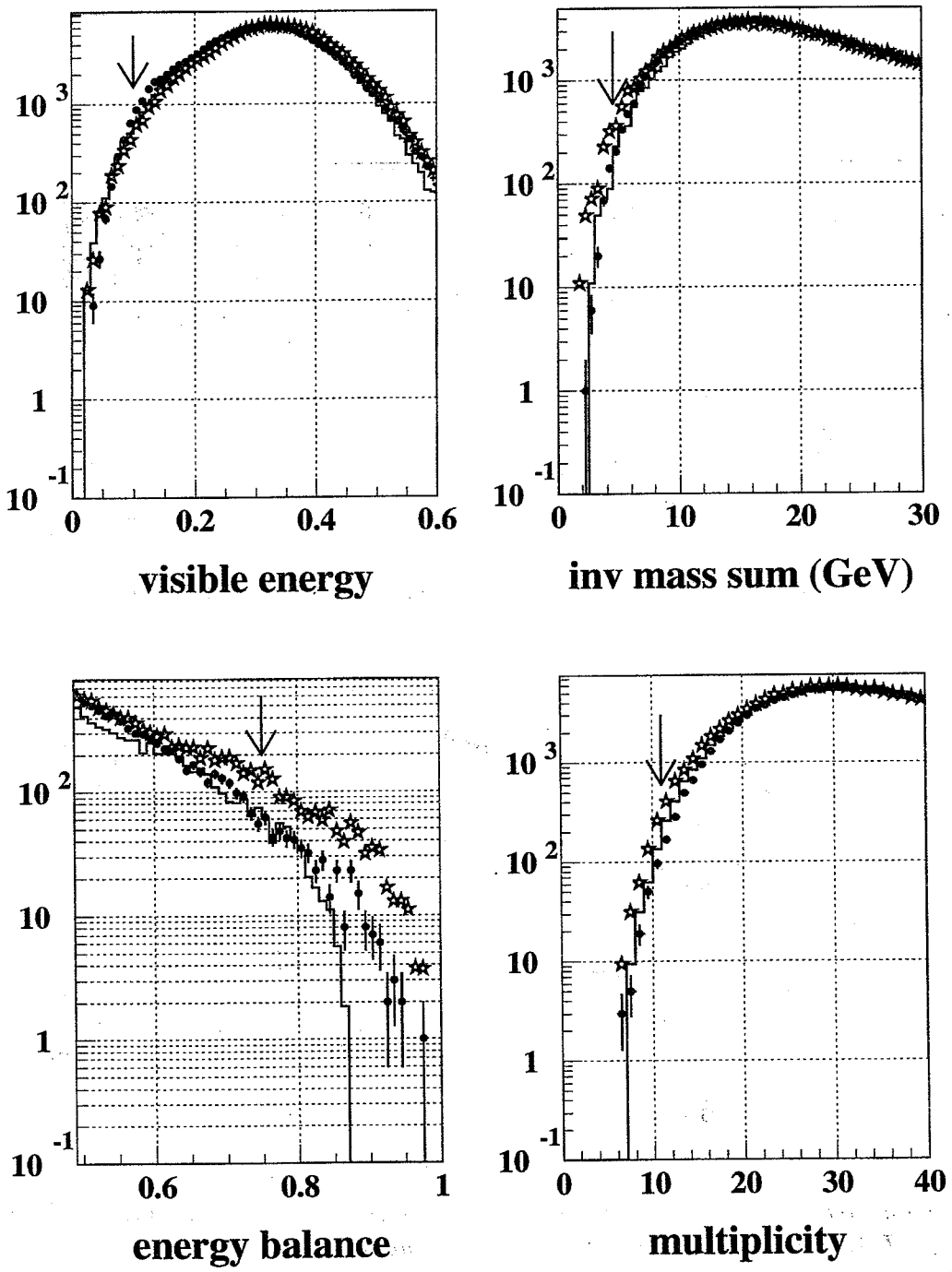


Figure 7.12: *A comparison of the cut variables in the forward region (points) with the simulated hole (stars) in the barrel for the JETSET MC. Also shown are the rescaled distributions (histogram) compared to the unscaled distributions. Events were required to satisfy the condition* $\cos(\vartheta_{thrust}) > 0.87$ *with respect to either the z- or x-axis.*

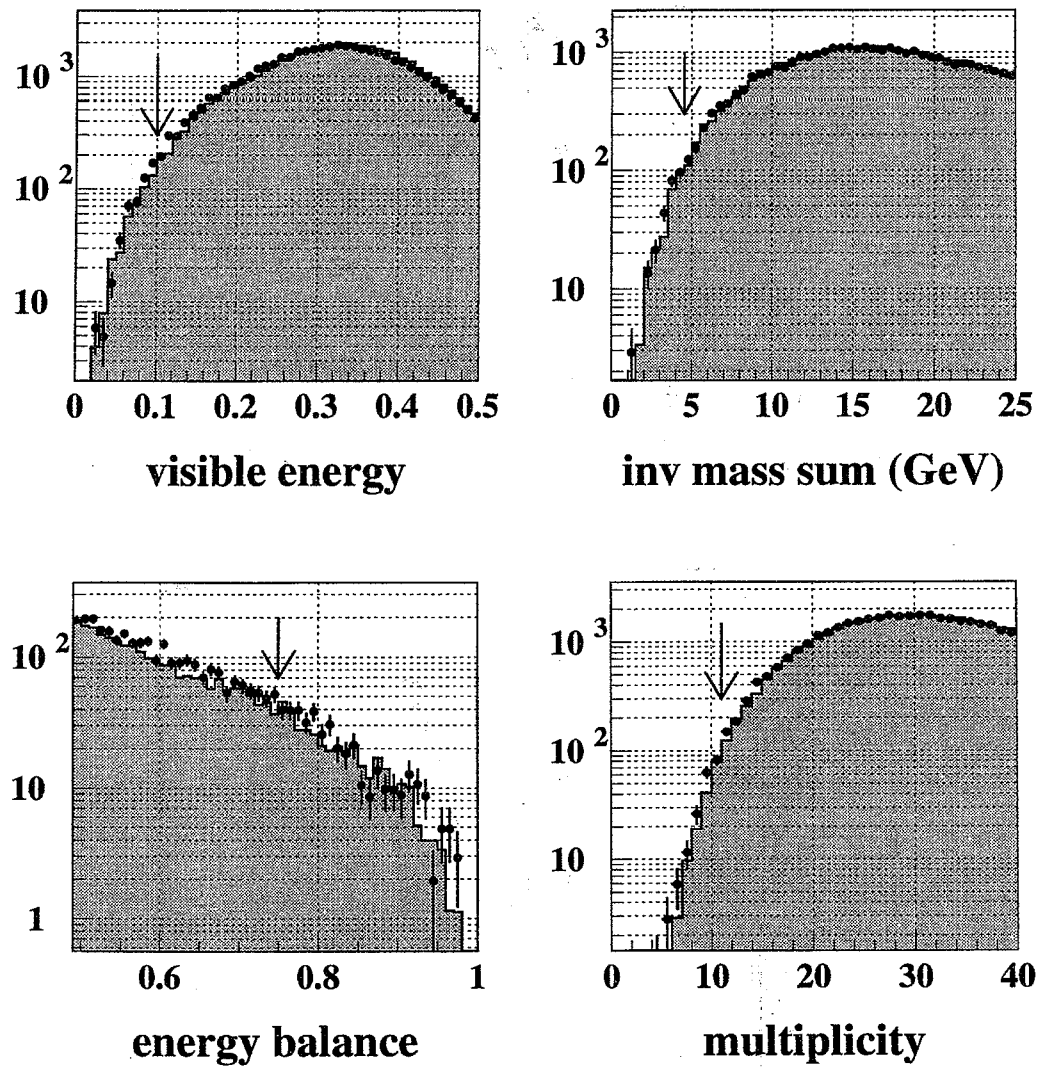


Figure 7.13: *Comparison of the cut variables with the simulated barrel hole for the data (points) and the JETSET MC (histogram). For these plots events are required to pass the standard MH selection with no barrel hole switched on. They are further required to satisfy the condition* $|\cos(\vartheta_{thrust})| > 0.87$ *with respect to the x-axis. The arrows indicate the cut values.*

To estimate the effect of the cut in $|\cos(\vartheta_{thrust})|$ on the extrapolation procedure the cut is changed to 0.90. The difference in the extrapolated inefficiency of $0.2 \cdot 10^{-4}$ is negligible.

The $\tau$ background is determined using MC and the number of $\tau's$ in the lost events of the data is subtracted. The uncertainty in this number is negligible.

All the errors are listed in Table 7.1 .

| | Uncertainty $\times 10^{-4}$ |
|---|---|
| Fragmentation: | |
| Residual Fragmentation | |
| Sensitivity | 1.0 |
| Barrel Inefficiency | 2.1 |
| Rescaling of | |
| Cut Variables | 1.7 |
| Comparison of the | |
| Cones | 0.7 |
| Detector simulation: | |
| 1993 MC | 4.0 |
| **overall** | **6.3** |

Table 7.1: *Systematic errors for the hole simulation procedure.*

### 7.5.2 Systematic Error of the Detector Simulation

The differences in the mean of the multiplicity distribution (data - Monte Carlo= -1.15) and the energy distribution ($\frac{data}{MonteCarlo} = 0.9815$) as mentioned in chapter 7.2 shows that the Monte Carlo simulation of multihadron events is not perfect and that there are uncertainties in the description of the multiplicity and energy. These uncertainties in the multiplicity and energy cause uncertainties in the determination of the selection efficiency.

It remains unclear if the difference between data and Monte Carlo is due to fragmentation (i.e. the event generator predicts the multiplicity and energy spectrum of the particles wrong) or due to the simulation of the detector response (i.e. the interaction of the particles with the detector is badly modelled). So far the data - Monte Carlo differences were completely attributed to the simulation of the detector response. The former procedure to account for the differences was to scale the energy and multiplicity of the Monte Carlo to assure that the mean of the multiplicity and energy distributions is the same in data and Monte Carlo. The difference of the selection efficiencies of the unscaled and rescaled Monte Carlo was used as an estimate of the systematic error due to the detector simulation. In the new analysis the uncertainty in the efficiency determination due to fragmentation is already accounted for by the systematic error of the hole simulation procedure. In order to avoid double counting it is important to determine the detector simulation uncertainties in a fragmentation independent way. Therefore, a new fragmentation independent method for determining the uncertainty of the selection efficiency due to the detector simulation is used in this analysis. It is described in detail in [30].

The main problem for the detector simulation is the simulation of the energy response of the electromagnetic calorimeter (ECAL), especially the response to hadrons. The energy response of ECAL is examined separately for hadronic and electromagnetic particles. According to the Monte Carlo 95% of the low momentum particles ($< 4$ GeV) are hadrons. A sample of isolated tracks in the central detector (CJ) is selected. These tracks are required to point to a cluster in ECAL and to have no other CJ track inside a cone of 0.6 rad around them. The energy response of ECAL as a function of the track momentum is measured with these isolated tracks in data and the extracted parametrization is applied to the Monte Carlo. The difference in the efficiency of the Monte Carlo with and without this procedure is used as a systematic error due to the response of ECAL to hadronic particles. This procedure is fragmentation independent because it does not depend on the underlying energy spectrum of the particles.

The response of ECAL to electromagnetic particles is studied using radiative Bhabhas. For single radiative Bhabha events the energy and position of the photon can, due to momentum conservation, be predicted after a measurement of the two electrons. A comparison of the predicted and measured energy of the photon gives a limit in the uncertainty of the reconstructed energy. An upper limit of 5% is obtained by this procedure. Scaling the measured energy by this 5% changes the selection efficiency by $2 \cdot 10^{-4}$.

An additional uncertainty is due to a calibration uncertainty of the innermost (closest to the beam pipe) ECAL blocks. Due to leakage these blocks can not be calibrated using Bhabha events. They have a common gain uncertainty of 10%. This correponds to an uncertainty in the efficiency of $3 \cdot 10^{-4}$ as determined by scaling the energy of the innermost blocks by 10%.

The error due to the uncertainty in the energy scale of the forward detector (FD) is estimated with the same method as the uncertainty of the ECAL response to electromagnetic particles, this results in an $3 \cdot 10^{-4}$ error.

The Monte Carlo simulation of the central detector (CJ) is rather well understood. Furthermore, uncertainties in CJ are, compared to the ECAL energy response, not important since CJ is only used for the multiplicity and the cut on the multiplicity is the least hard cut.

The systematic erros are listed in table 7.2.

| | Uncertainty $\times 10^{-4}$ |
|---|---|
| ECAL: | |
| Response to Hadrons | 3 |
| Response to electromagnetic Particles | 2 |
| Calibration of Inner Blocks | 3 |
| Calibration of FD | 3 |
| **overall** | **6** |

Table 7.2: *Systematic errors for the efficiency determination in the forward direction.*

### 7.5.3 Background

There are two contributions to the background, $\tau^+\tau^-$ and two photon events. The $\tau^+\tau^-$ background is determined using Monte Carlo. The selection is applied to 240000 $\tau^+\tau^-$ events generated with KORALZ. The selection efficiency is 2.98 $\pm$ 0.004%. Using the Standard Model value of $\frac{\Gamma_{\tau^+\tau^-}}{\Gamma_{had}} = 0.048$ this results in a background of $(1.43 \pm 0.002) \cdot 10^{-3}$.

Since two photon events have a low visible energy and/or a high energy imbalance a sample which is enriched with two photon events can be obtained by selecting events with a low visible energy $0.1 < X_E^{vis} < 0.18$. A complementary clean sample is obtained by requiring a high visible energy $X_E^{vis} > 0.18$ ($X_E^{vis}$ is defined as a fraction of the center of mass energy).
The cross section for two photon events does not show the resonant behaviour of the multi hadron events, at the different energy points, and can, for the purpose of this analysis, be approximated to be constant. The clean sample shows the behaviour of events coming from $Z^0$ decays (resonant behaviour). The background enriched sample therefore consists of two parts: the constant background and a fraction of multihadron events which shows the resonant behaviour at the different energy points.

$$\sigma_{back} = f \cdot \sigma_{clean} + \sigma_{twophoton}$$

By plotting the background enriched sample versus the clean sample for different energy points and fitting a straight line the two photon background $\sigma_{twophoton}$ can be obtained as the offset of the fit. To eliminate also the two photon contamination of events with $X_E^{vis} > 0.18$ a second background enriched sample is obtained by requiring a high energy imbalance $0.5 < R_{bal} < 0.75$ in addition to the high visible energy cut. By plotting the cross section of this second background enriched sample against the clean sample $R_{bal} < 0.5$ and $X_E^{vis} > 0.18$ a second contribution of the two photon background can be obtained. Figure 7.14a shows $\sigma_{back}$ versus $\sigma_{clean}$ for the low $X_E^{vis}$ sample and figure 7.14b for the high $X_E^{vis}$ sample with the energy imbalance cut. The two background contributions are 0.0416 $\pm$ 0.0083 nb for the low $X_E^{vis}$ sample and 0.0078 $\pm$ 0.0045 nb for the high energy imbalance sample. Added together this results in a background of 0.0494 $\pm$ 0.0094 nb.

The measured cross sections are corrected for the background by applying a correction factor. The correction factor for the two photon background and its error is calculated separately at the three energy points of 1993 since the absolute value of the two photon background is constant. For the three 1993 energy points (peak$-$2, peak and peak+2) the corection factors are: 0.9950 $\pm$ 0.0009, 0.9984 $\pm$ 0.0003 and 0.9964 $\pm$ 0.0007, respectively. For the 1994 energy point (on peak) the same correction factor as for the 1993 peak point is used. Since with the one energy point of 1994 no separate background determination is possible the uncertainty on the background is increased to 0.0005. The correction factor for the $\tau^+\tau^-$ background is 0.9986 $\pm$ 0.0003. This is assumed to be the same for all 1993 and 1994 energy points.

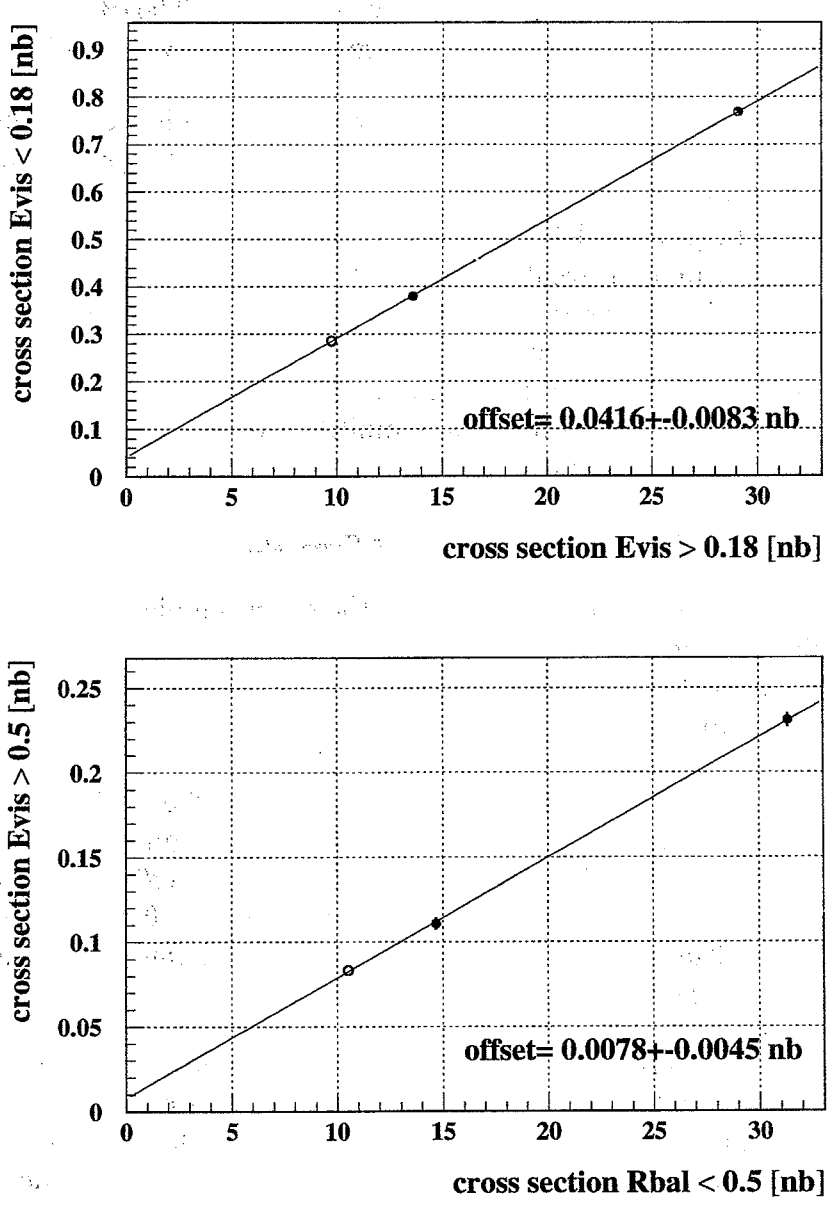


Figure 7.14: *Fit of the non resonant background for the sample with low visible energy (a) and for the sample with high energy imbalance (b). The three points correspond to the three 1993 energy points.*

### 7.5.4 Detector Stability and Calibration

The stability and the calibration of CJ and ECAL in the selection is checked on a run by run basis by using a multi hadron selection with each of these detectors alone and comparing the number of selected events with the number of events selected with the standard selection.

The CJ based selection is:

- $P_{CJ} = (\sum p_{CJ_i})/\sqrt{s} > 0.14$
- $R_{bal} = |\sum p_{CJ_i} \cdot \cos\vartheta_i|/\sum p_{CJ_i} < 0.7$
- $N_{CJ} \geq 5$

The sum of the momentum of all good tracks in CJ has to be larger than 14% of the center of mass energy, the momentum imbalance along the beam pipe has to be smaller than 0.7 and the number of good CJ tracks has to be at least 5.

The ECAL based selection is:

- $E_{ECAL} = (\sum E_{ECAL_i})/\sqrt{s} > 0.1$
- $R_{bal} = |\sum E_{ECAL_i} \cdot \cos\vartheta_i|/\sum E_{ECAL_i} < 0.65$
- $N_{ECAL} \geq 7$

The sum of the energies of all good ECAL clusters has to be larger than 10% of the center of mass energy, the energy imbalance has to be smaller than 0.65 and the number of good clusters has to be at least 7.

The upper plot in figure 7.15 shows the quantity $y_i$

$$y_i = \frac{N^{CJ}_{sel\ i} - N^{std}_{sel\ i}}{N^{std}_{sel\ i}}$$

where $N^{CJ}_{sel\ i}$ is the number of events in run i selected with the CJ based selection and $N^{std}_{sel\ i}$ is the number of events in run i selected with the standard selection. The error shown is the statistical error. The lower plot shows

$$\frac{y_i - \bar{y}}{\Delta y_i}$$

where $\bar{y}$ is the average of $y$ of all runs and $\Delta y$ is the statistical error of $y$ in run $i$. This distribution should be a gaussian peaked at 0 with a sigma of 1 if the deviations in $y$ from $\bar{y}$ are caused by statistical fluctuations. The expected distribution is also shown. No significant deviation from the expectation is observed.

Figure 7.16 shows the same plots for the ECAL based selection, with again no deviation from the expected shape.

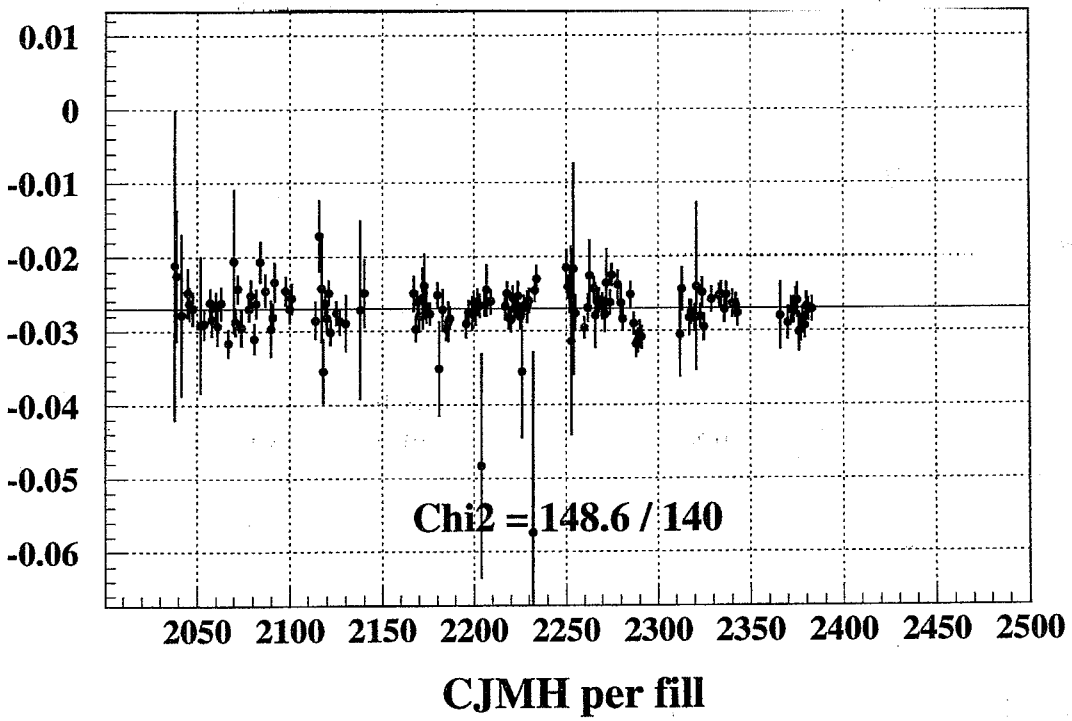


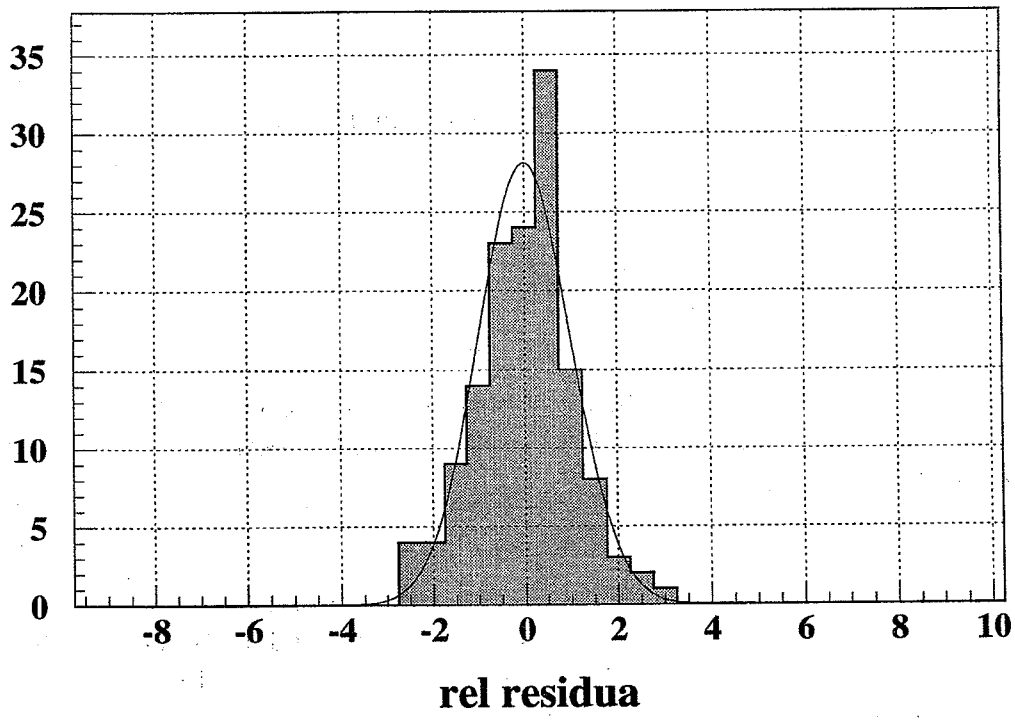


Figure 7.15: *Stability test for CJ. The ploted quantities are explained in the text.*

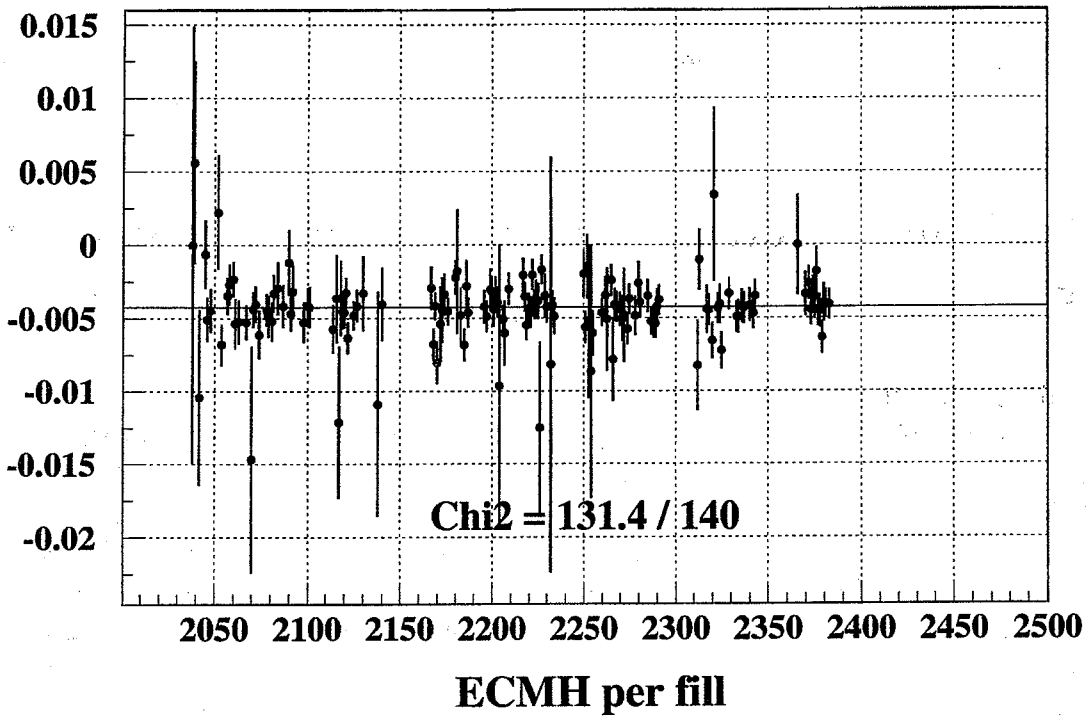


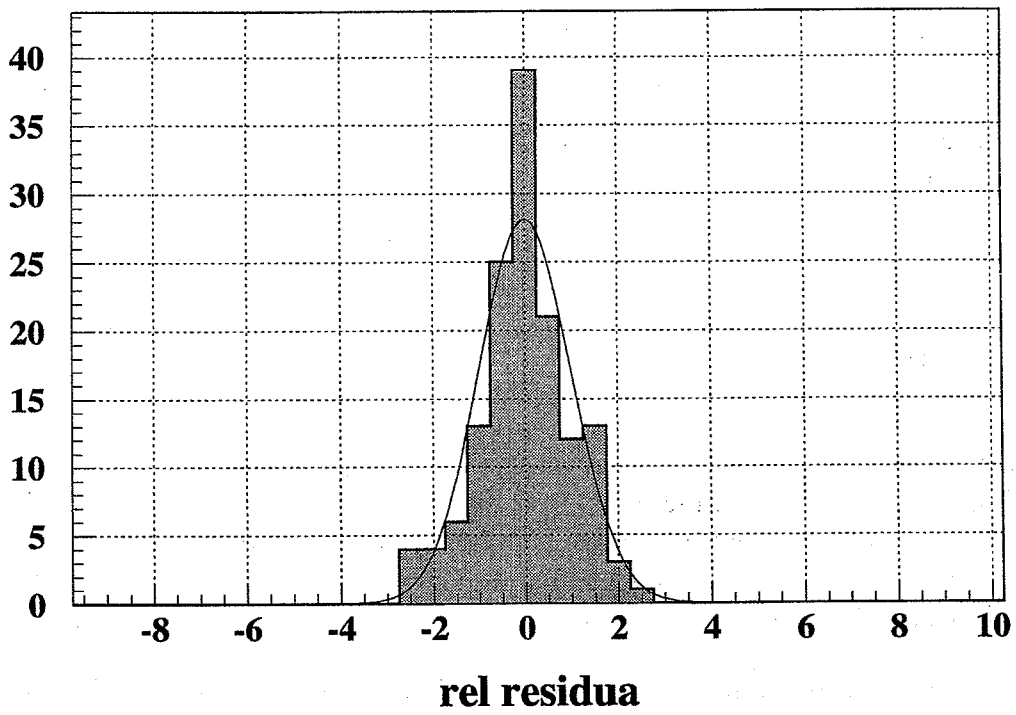


Figure 7.16: *Stability test for ECAL. The quantities are again explained in the text.*

Since the geometrical coverage of FD is too small to make an FD based selection the stability of FD is instead examined by looking at the number of events which were not selected if FD was not used in the selection. Here also no significant deviations are found.

Additional plots of the average energy of ECAL and FD are made for each run. In 1993 no deviations from the average energy are found. In 1994 some runs showed a miscalibration of the ECAL energy. From all these studies an upper limit of the sytematic error due to detector instabilities or miscalibrations of 0.05% and 0.07% for 1993 and 1994, respectively, are found.

## 7.6 Efficiency Determination at the Different Scan Points

For determining the efficiency at the different scan points Monte Carlo is used which is generated with a center of mass energy of the specific scan point. Table 7.3 shows the efficiencies determined at the three 1993 energy points. The selection efficiency differs at the three energy points. This effect is due to the emission of initial state photons, which is enhanced at the off-peak points. Since the emission of only one initial state photon is implemented in the Monte Carlo half the difference between the on-peak and off-peak efficiency is used as an estimate of the error due to missing higher order terms. This error of 0.05% is taken to be an additional uncorrelated error at the off-peak points. All other errors are fully correlated among the three energy points of 1993.

| | peak−2 | peak | peak+2 |
|---|---|---|---|
| c.m. energy (GeV) | 89.4525 | 91.2067 | 93.0359 |
| efficiency/% | 99.508 | 99.599 | 99.552 |

Table 7.3: *Efficiencies at the different energy points of the 1993 energy scan. In 1994 LEP was running at the peak energy.*

## 7.7 Summary

It has been shown that the error due to fragmentation uncertainties can be substantially reduced by simulating the forward acceptance holes in the barrel region, and measuring the rate of events lost due to the simulated acceptance holes from true data. The effect of the different detector response between the barrel and endcap region (which comes mainly from the different amount of material in front of the detector) is small.

The procedure leads to an inefficiency which is $3.7 \cdot 10^{-4}$ smaller than the determination using the standard JETSET Monte Carlo generator. The main sources of systematic uncertainties are the detector simulation, both in the barrel and in the endcap region, and residual fragmentation errors. For the off-peak points a large contribution to the systematic error is due to the background determination. The off-peak points also have an additional uncorrelated error due

to possible imperfections in the description of initial state photon radiation. All errors and correction factors are listed in table 7.4.

| | 93 peak | | 93 peak−2 | | 93 peak+2 | | 94 | |
|---|---|---|---|---|---|---|---|---|
| | $f$ | $\Delta f/f$ [%] | $f$ | $\Delta f/f$ [%] | $f$ | $\Delta f/f$ [%] | $f$ | $\Delta f/f$ [%] |
| Acceptance: | | | | | | | | |
| Detector Simulation | | | | | | | | |
| Standard | 1.0042 | 0.06 | 1.0051 | 0.06 | 1.0045 | 0.06 | 1.0042 | 0.06 |
| Barrel Hole | 1.0000 | 0.04 | 1.0000 | 0.04 | 1.0000 | 0.04 | 1.0000 | 0.04 |
| Fragmentation | 1.0004 | 0.05 | 1.0004 | 0.05 | 1.0004 | 0.05 | 1.0004 | 0.05 |
| Detector Stability/ Reconstruction | 1.0000 | 0.05 | 1.0000 | 0.05 | 1.0000 | 0.05 | 1.0000 | 0.07 |
| Background: | | | | | | | | |
| $e^+e^- \to \tau^+\tau^-$ | 0.9986 | 0.03 | 0.9986 | 0.03 | 0.9986 | 0.03 | 0.9986 | 0.03 |
| Non-resonant ($0.049 \pm 0.009$ nb) | 0.9984 | 0.03 | 0.9950 | 0.09 | 0.9964 | 0.07 | 0.9984 | 0.05 |
| **overall** | **1.0016** | **0.11** | **0.9991** | **0.14** | **0.9999** | **0.13** | **1.0016** | **0.13** |

Table 7.4: *Summary of the correction factors $f$ and systematic errors $\Delta f/f$ for the 1993 $e^+e^-$ → hadrons cross section at the different energy scan points and the 1994 cross section. The 1993 off-peak points have an additional uncorrelated error of* 0.05%.

# Chapter 8

# The Line Shape Fits

After the two components of the cross section measurement, the luminosity determination and the multi hadron selection, have been discussed in the last two chapters this chapter describes the determination of electroweak parameters from a fit to the data..

The electroweak parameters are determined by fitting the expected cross section at different centre of mass energies to the measured cross section. The expected cross section at any given energy point depends on several parameters which are the parameters of the fit. The most fundamental such parameter is $M_Z$. Section 8.1 gives simple lowest order predictions for the cross section. Also in this section is the description of the higher order corrections which have to be included to reach the experimental accuracy. In 8.2 and 8.3 we discuss the electroweak parameters and the software packages used to calculate the cross section. The discription of the fitting procedure can be found in section 8.4. Finally, the results are given in section 8.5.

## 8.1 Parametrization of the Cross Sections

### 8.1.1 Lowest Order Predictions

As described in chapter 2 the total cross section for the process $e^+e^- \to f\bar{f}$ $(f \neq e)$ in the vicinity of the $Z^0$-pole ($\sqrt{s} = M_Z$) is dominated by $Z^0$ exchange. At Born level the total cross section can be written as

$$\sigma(s) = \sigma^0_{f\bar{f}} \frac{s\Gamma_Z}{(s - M_Z)^2 + M_Z^2\Gamma_Z^2} +' \gamma Z' +' \gamma^{2'} \tag{8.1}$$

where $\sigma^0_{f\bar{f}}$ is the cross section at $\sqrt{s} = M_Z$, the so called "pole cross section". '$\gamma Z^0$' and '$\gamma^2$' represent small corrections ($\mathcal{O}(1\%)$) from the $\gamma Z$-interference and the pure photon exchange.

For the process $e^+e^- \to e^+e^-$ additional t-channel diagrams and s-t interference have to be taken into account (see chapter 2). After correcting the measured $e^+e^-$ cross section for these effects also $e^+e^- \to e^+e^-$ can be treated as given in equation 8.1. The correction is often

determined using the large angle Bhabha event generator ALIBABA [20]. The theoretical error on these corrections is 0.5%. Since the corrections are not implemented in the program library used for the calculation of the cross section, $e^+e^- \rightarrow e^+e^-$ events are not included in this analysis.

The pole cross section $\sigma^0_{f\bar{f}}$ can be expressed in terms of the partial widths $\Gamma_{e^+e^-}$ and $\Gamma_{f\bar{f}}$.

$$\sigma^0_{f\bar{f}} = \frac{12\pi}{M_Z^2} \frac{\Gamma_{e^+e^-}\Gamma_{f\bar{f}}}{\Gamma_Z^2} \tag{8.2}$$

In the Standard Model the partial widths are not free parameters but are expressed through the electroweak coupling constants:

$$\Gamma_{f\bar{f}} = \frac{G_F M_Z^3}{6\pi\sqrt{2}} \left[ \left(g_a^f\right)^2 + \left(g_v^f\right)^2 \right] \tag{8.3}$$

$g_a^f$ und $g_v^f$ are the vector and axial vector couplings. At tree level they can be written as

$$\begin{aligned} g_a^f &= I_f^3 \\ g_v^f &= I_f^3 + 2Q_f \sin^2\theta_W \end{aligned} \tag{8.4}$$

$I_f^3$ is the weak isospin of the fermion f and $\theta_W$ is the weak mixing angle.

Note, that in lowest order the process $e^+e^- \rightarrow f\bar{f}$ is completely determined by the parameters $\alpha$, $G_F$, and $M_Z$.

### 8.1.2 Radiative Corrections

The above relations have to be modified by radiative corrections. They can be devided into photonic corrections, non-photonic corrections and QCD corrections.

**photonic corrections:**
These corrections arise from diagrams with an additional photon added to the Born diagram (see figure 8.1).

The dominant contribution is due to the first diagram where a photon is radiated off the initial state, thus modifying the effective centre of mass energy. Figure 8.2 shows the hadronic cross section for the pure Born diagram without and with initial state radiation. The pole cross section of the $Z^0$ resonance is decreased by approximately 30% and the peak position is shifted by 150 MeV.

The photonic corrections are taken into account by convoluting the cross section with a radiator function which describes the probability for the effective centre of mass energy being reduced from $s$ to $s'$ due to photon radiation.

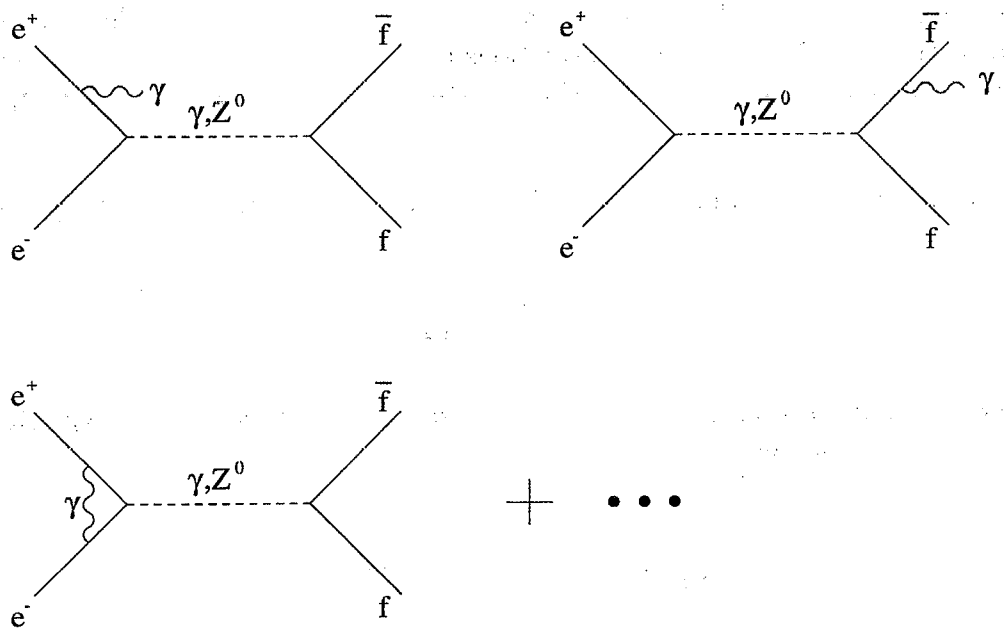


Figure 8.1: *Photonic corrections.*

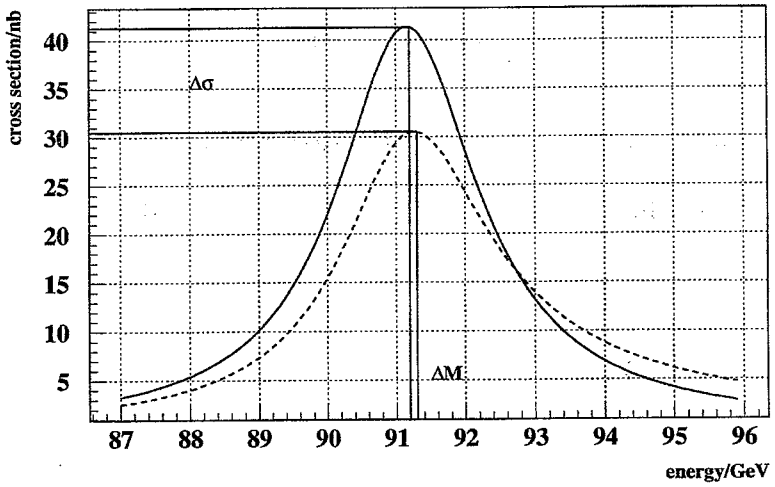


Figure 8.2: *Cross section without (solid line) and with initial state photon radiation.*

$$\sigma_{meas}(s) = \int_0^s \sigma(s')H(s,s')ds'$$

The radiator function H(s,s') can be calculated within the framework of QED and is known to a very high accuracy (better than 0.1%).

**non-photonic corrections:**
Non-photonic corrections arise from higher order diagrams without external photons, like those in figure 8.3.

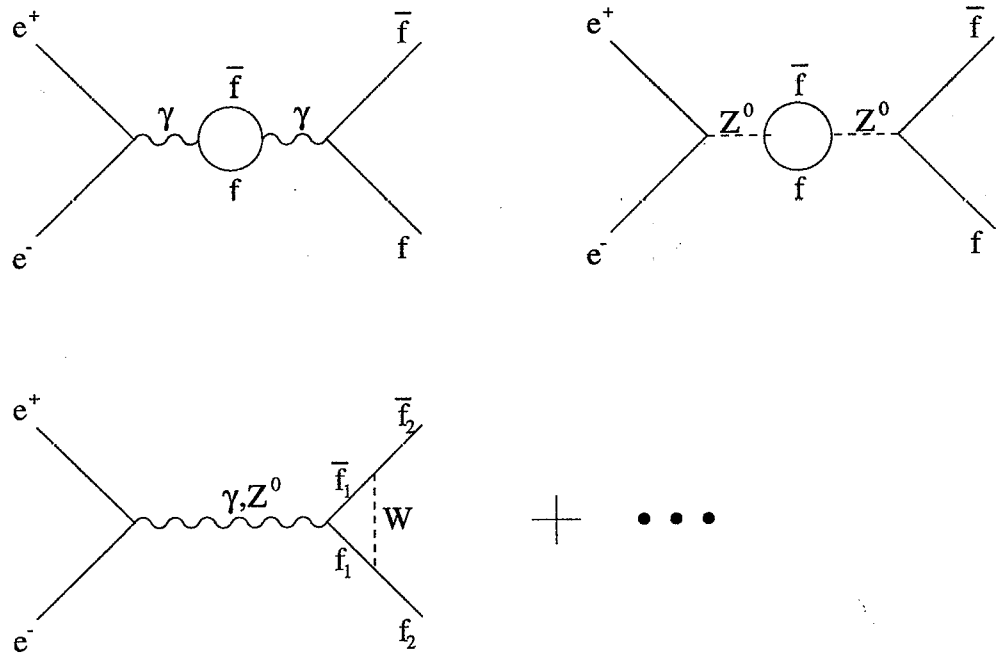


Figure 8.3: *Non-photonic corrections.*

A familiar example of non-photonic corrections is the vacuum polarisation of the photon, which leads to an s-dependent correction of the electromagnetic coupling constant $\alpha$.

$$\alpha = \alpha(s) = \frac{\alpha_0}{1 - \Delta\alpha}$$

Similar diagrams related to $Z^0$ exchange and diagrams involving heavy gauge bosons have to be taken into account as well. They modify the Born description of the hard scattering process which can be summarized to a very good approximation as follows.

- An s-dependent $Z^0$ total width, which can be approximated by

$$\Gamma_Z(s) = \frac{s}{M_Z^2} \cdot \Gamma_Z(M_Z^2) \ .$$

  In the following the abbreviation $\Gamma_Z \equiv \Gamma_Z(M_Z^2)$ will be used.

- The Standard Model vector and axial vector couplings, $g_v$ and $g_a$ are changed to effective couplings $\hat{g_v}$ and $\hat{g_a}$:

$$\begin{aligned} \hat{g_v} &= \sqrt{\rho} g_v \\ \hat{g_a} &= \sqrt{\rho} g_a 0 \end{aligned} \tag{8.5}$$

  where $g_v$ and $g_a$ are the coupling constants given by equation 8.4 and $\rho$ accounts for the non-photonic corrections. Writing $\rho = \frac{1}{1-\Delta\rho}$ the leading -$M_{top}$ and $M_{Higgs}$- dependent corrections are:

$$\begin{aligned} \Delta\rho_{top} &= \frac{3G_F}{8\pi^2\sqrt{2}} M_{top}^2 \\ \Delta\rho_{Higgs} &= \frac{-11 G_F M_Z^2 \sin^2\theta_W}{24\pi^2\sqrt{2}} ln\left(\frac{M_{Higgs}^2}{\cos^2\theta_W M_Z^2}\right) \end{aligned} \tag{8.6}$$

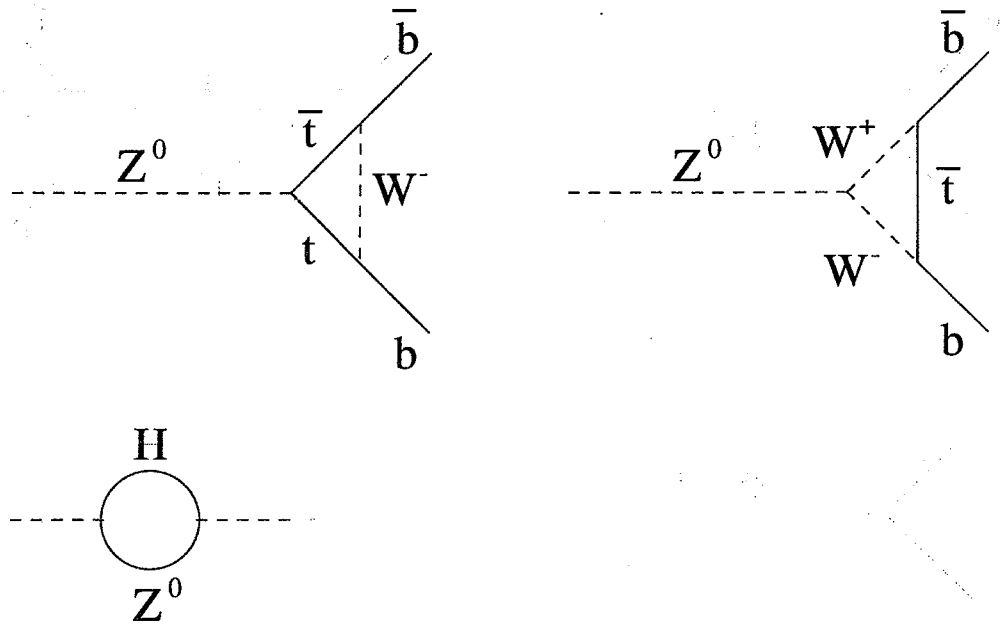


Figure 8.4: *Diagrams with large contributions to the $M_{top}$ and $M_{Higgs}$ dependent corrections.*

The largest contributions to $M_{top}$ and $M_{Higgs}$ dependent corrections arise from the diagrams in figure 8.4. The corrections depending on the light quarks or leptons arising from inner loops like in figure 8.3 are well defined because the effective masses of the light quarks and the lepton masses are known from low energy experiments to good accuracy.

These modifications retain the Born structure of the description and are known as Improved Born Approximation (IBA).

**QCD corrections:** QCD corrections account for gluon radiation off real and virtual quarks (see figure 8.5). They modify the $Z^0$ partial widths for decays into $q\bar{q}$-pairs.

$$\Gamma_{q\bar{q}} = \Gamma_{q\bar{q}}(1 + \delta_{QCD}) \tag{8.7}$$

The QCD corrections have been calculated to $\mathcal{O}(\alpha_s^3)$ [32]:

$$\delta_{QCD} = \frac{\alpha(M_Z^2)}{\pi} + 1.409\left(\frac{\alpha(M_Z^2)}{\pi}\right)^2 - 12.805\left(\frac{\alpha(M_Z^2)}{\pi}\right)^3 \tag{8.8}$$

Effects of quark masses are also included in the parametrizations.

Due to the higher order corrections a complete set of parameters is now $\alpha$, $\alpha_S$, $M_Z$, $M_{top}$, and $M_{Higgs}$.

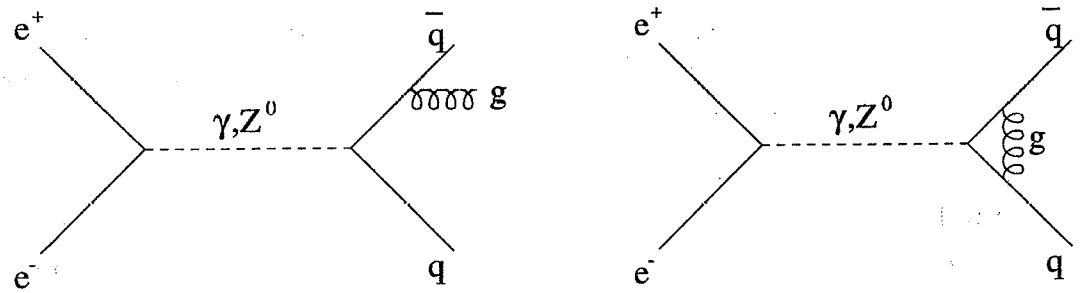


Figure 8.5: *QCD corrections.*

## 8.2 Electroweak Observables

One of the main goals of LEP is to measure $M_Z$ and $\Gamma_Z$ to high accuracy.

The importance of the $M_Z$ measurement lies in the fact that after $M_Z$ is determined, the mass of the top quark and the Higgs mass, are the only less well known parameters of the Standard Model. The other parameters, the fermion masses and the coupling constants, are known to a very high accuracy. Once $M_Z$ is measured everything else is fixed and can be predicted by the Standard Model. Single, Standard Model independent measurements like $\Gamma_Z$ or the partial widths then allow to independently test the Standard Model. Since $\Gamma_Z$ and the partial widths still depend, through radiative corrections, on less well known parameters like $M_{top}$ or $M_{Higgs}$ it is advantageous to measure quantities which have a reduced sensitivity to these two parameters.

A particularly interesting quantity is the ratio of the invisible width to the leptonic width $\frac{\Gamma_{inv}}{\Gamma_{lept}}$. In this ratio universal corrections cancel. It is therefore (almost) independent of $M_{top}$ and $M_{Higgs}$, and is uniquely predicted by the Standard Model. A measurement of $\frac{\Gamma_{inv}}{\Gamma_{lept}}$ significantly different from the Standard Model prediction would be a strong hint for "new physics".

$\frac{\Gamma_{inv}}{\Gamma_{lept}}$ can be calculated as

$$\frac{\Gamma_{inv}}{\Gamma_{lept}} = \frac{\Gamma_Z - \Gamma_{had} - 3\Gamma_{lept}}{\Gamma_{lept}} = \frac{\Gamma_Z}{\Gamma_{lept}} - \frac{\Gamma_{had}}{\Gamma_{lept}} - 3 \tag{8.9}$$

Using $\frac{\Gamma_Z}{\Gamma_{lept}} = \left(\frac{12\pi}{M_Z^2}\right)^{\frac{1}{2}} \cdot {\sigma^0_{lept}}^{-\frac{1}{2}}$ and $\frac{\Gamma_{had}}{\Gamma_{lept}} = R_{lept}$ , this results in

$$\frac{\Gamma_{inv}}{\Gamma_{lept}} = \left(\frac{12\pi}{M_Z^2}\right)^{\frac{1}{2}} \cdot {\sigma^0_{lept}}^{-\frac{1}{2}} - R_{lept} - 3 \tag{8.10}$$

A simple error calculation then gives

$$\Delta\left(\frac{\Gamma_{inv}}{\Gamma_{lept}}\right) = 21\frac{\Delta N_{had}}{N_{had}} \oplus 6\frac{\Delta N_{lept}}{N_{lept}} \oplus 15\frac{\Delta L}{L} \tag{8.11}$$

where the absolute error on $\frac{\Gamma_{inv}}{\Gamma_{lept}}$ is expressed in terms of the relative errors of the multihadron selection, the lepton selection and the luminosity measurement. The coefficients show that the

error of the luminosity measurement and the multihadron selection are the most important errors for the determination of $\frac{\Gamma_{inv}}{\Gamma_{lept}}$. For the leptons (especially for the $\mu's$) the statistical error is still larger than the experimental error.

Until 1993, before the installation of the SiW detector, the luminosity systematic error of 0.41% was the limiting factor for the determination of $\frac{\Gamma_{inv}}{\Gamma_{lept}}$. The systematic error for the multihadron selection was 0.2%. Assuming a systematic error of $10^{-3}$ for the luminosity measurement and the selection of multihadronic events and that the error for the lepton selection is limited by statistics one obtains for $10^6$ $Z^0$ decays:

$$\frac{\Delta L}{L} = 5 \cdot 10^{-3} \qquad \Delta\left(\frac{\Gamma_{inv}}{\Gamma_{lept}}\right) \approx 0.08 \qquad (1992)$$

$$\frac{\Delta L}{L} = 1 \cdot 10^{-3} \qquad \Delta\left(\frac{\Gamma_{inv}}{\Gamma_{lept}}\right) \approx 0.04 \qquad (1993)$$

The uncertainty on $\frac{\Gamma_{inv}}{\Gamma_{lept}}$ can be reduced by a factor of two with a luminosity measurement of $\frac{\Delta L}{L} = 1 \cdot 10^{-3}$. This was the motivation for the installation of the SiW detector and for this thesis.

Using the Standard Model prediction of $\frac{\Gamma_\nu}{\Gamma_{lept}}$=1.99194 it is possible to determine the number of neutrinos as

$$N_\nu = \frac{\left(\frac{\Gamma_{inv}}{\Gamma_{lept}}\right)_{measured}}{\left(\frac{\Gamma_\nu}{\Gamma_{lept}}\right)_{SM}} \qquad (8.12)$$

## 8.3 The Progam ZFITTER

The two most commonly used software packages for the calculation of the cross sections for the different $Z^0$ decay channels around the $Z^0$ pole are MIZA [35] and ZFITTER [34]. ZFITTER is used for this analysis. It includes all the corrections discussed in section 8.1. Photonic corrections are calculated in complete $\mathcal{O}(\alpha)$, including leading $\mathcal{O}(\alpha^2)$ contributions and soft photon exponentiation. For the non-photonic corrections full one-loop calculations with leading $\mathcal{O}(\alpha^2 M_{top}^4)$ and $\mathcal{O}(\alpha\alpha_s)$ are included. QCD corrections are calculated to $\mathcal{O}(\alpha^3)$ including $b\bar{b}$ mass effects.

Using the appropriate values for the effective couplings, $\hat{g}_a$ and $\hat{g}_v$, the differences between the improved Born approximation and the full Standard Model calculation are much smaller than the present experimental accuracy.

The improved Born approximation therefore allows two approaches to parametrize the cross sections:

- **Standard Model approach**
  This approach is based on the precise calculation of the radiative corrections within the

Standard Model, i.e. the effective couplings are used to predict the partial widths. This parametrization uses $M_Z, M_{top}, M_{Higgs}, \alpha$ and $\alpha_s$ as parameters for the calculation of the cross section.

- **model independent approach**
  The model independent approach is to directly use the partial widths without using their Standard Model predictions. Only the '$\gamma Z$' interference is fixed to its Standard Model value. This approach uses $M_Z, \Gamma_Z, \Gamma_{had}, \Gamma_{e^+e^-}, \Gamma_{\mu^+\mu^-}$ and $\Gamma_{\tau^+\tau^-}$ as parameters to calculate the cross section.

The two approaches are implemented in ZFITTER as two separate branches. The Standard Model branch is used to calculate the cross section at a given center of mass energy as a function of the parameters $M_Z, M_{top}, M_{Higgs}, \alpha$ and $\alpha_s$. The fit performed with this branch is called the Standard Model fit. The other branch calculates the cross section as a function of the parameters $M_Z, \Gamma_Z, \Gamma_{had}, \Gamma_{e^+e^-}, \Gamma_{\mu^+\mu^-}$ and $\Gamma_{\tau^+\tau^-}$. This branch is used for the model independent fit. The model independent branch is also used for a fit assuming lepton universality. Under the assumption of lepton universality the partial widths necessary for the fit can be calculated as:

$$\Gamma_{e^+e^-} = \Gamma_{lept} \qquad \Gamma_{\mu^+\mu^-} = \Gamma_{lept} \qquad \Gamma_{\tau^+\tau^-} = (1 - \delta_m)\,\Gamma_{lept} \tag{8.13}$$

where $\delta_m = 0.0023$ [33] represents a small correction for the mass of the $\tau$ lepton.

Since the correlation between the parameters is smaller, the parameters $M_Z$, $\Gamma_Z$, $\Gamma_{had}$, $\Gamma_{e^+e^-}$, $\Gamma_{\mu^+\mu^-}$ and $\Gamma_{\tau^+\tau^-}$ are usually replaced by $M_Z$, $\Gamma_Z$, $\sigma^0_{had}$, $R_{e^+e^-}$, $R_{\mu^+\mu^-}$ and $R_{\tau^+\tau^-}$ with:

$$R_{e^+e^-} = \frac{\Gamma_{had}}{\Gamma_{e^+e^-}} \qquad R_{\mu^+\mu^-} = \frac{\Gamma_{had}}{\Gamma_{\mu^+\mu^-}} \qquad R_{\tau^+\tau^-} = \frac{\Gamma_{had}}{\Gamma_{\tau^+\tau^-}} \tag{8.14}$$

This is the prefered parameter set of the LEP experiments.

The analysis strategy for the determination of the line shape parameters is to perform a model independent fit for the determination of $M_Z$, $\Gamma_Z$, $\sigma^0_{had}$ and $R_\mu$, $R_\tau$. A comparison of $R_\mu$ and $R_\tau$ allows to check lepton universality between $\mu$'s and $\tau$'s. A model independent fit assuming lepton universality is performed to determine $\frac{\Gamma_{inv.}}{\Gamma_{lept}}$ which is then compared to the Standard Model prediction. $\frac{\Gamma_{inv.}}{\Gamma_{lept}}$ is also used to determine the number of neutrino species. The Standard Model fit is used in order to determine $\alpha_S$ and an indirect value for $M_{top}$.

## 8.4 Fitting Procedure

For the line shape fits the measured cross sections at the different energy points for multi hadronic-, $\tau^+\tau^-$-, and $\mu^+\mu^-$-events are used as input and the predicted cross sections, as a function of the fit parameters, are calculated using ZFITTER. As explained in chapter 2 the electron channel is not used here.

To determine the fit parameters a simultaneous $\chi^2$ minimization for all channels at all energy points is done using the program MINUIT [36]. For the $\chi^2$ minimisation the full covariance matrix ($cov$) of the experimental and theoretical errors of the cross sections has to be used.

$$\chi^2 = \Delta\sigma \cdot cov \cdot \Delta\sigma^T$$

Where $\Delta\sigma = \sigma_{measured} - \sigma_{predicted}$.

### 8.4.1 Experimental Errors

The cross sections are determined using the relation

$$\sigma = \frac{N_{sel} - N_{back}}{\epsilon \cdot \int Ldt} \tag{8.15}$$

where $N_{sel}$ is the number of events passing the cuts, $\epsilon$ is the efficiency of the selection and $N_{back}$ is the number of background events in the data. $\int Ldt$ is the integrated luminosity.

The errors which mainly affect the cross section measurement are the error of the selection and the luminosity error. The error in the selection efficiency $\epsilon$ and in the background are combined to the systematic error of the selection $\Delta^{sel}_{sys}$. The statistical error of the selection is $\Delta^{sel}_{stat} = \sqrt{N_{sel}}$. For the luminosity there is the systematic error of the luminosity $\Delta^{lumi}_{sys}$, the theory error $\Delta^{lumi}_{theory}$ and the statistical error of the luminosity $\Delta^{lumi}_{stat}$.

The covariance matrix is calculated as $cov_{ij} = c \cdot \Delta_i \Delta_j$. c is the correlation coefficient and $\Delta_i$ is the error of the cross section at the energy point i. By deviding each error $\Delta_i$ into two contributions such that one part is fully correlated between energy point i and j and the other part is uncorrelated c is 1 for the correlated part and 0 for the uncorrelated part. All errors which are fully correlated between the energy points i and j are then added quadratically. A correlated contribution of the error between energy point i and j for the multi hadron selection, for example, is the systematic error of the selection. Contributions which are not correlated between the different energy points are the statistical errors of the selection and the luminosity measuremend and, if present, an additional uncorrelated systematic error, e.g. the additional uncertainty of the multi hadron selection at the 1993 off-peak energy points.

According to the correlation, the covariance matrix can best be devided into submatrices:

$$cov = \begin{pmatrix} \boxed{\text{had}} & \boxed{\text{had},\mu} & \boxed{\text{had},\tau} \\ \boxed{\text{had},\mu} & \boxed{\mu} & \boxed{\mu,\tau} \\ \boxed{\text{had},\tau} & \boxed{\mu,\tau} & \boxed{\tau} \end{pmatrix} = (cov^{nm}_{kl})$$

$(cov^{nm}_{kl})$ is a submatrix which describes the covariance between channel n at the energy point k and channel m at the energy point l. The channel n can either be hadrons, $\mu's$ or $\tau's$ and $k, l$ starts with 1 within each sub matrix for the first energy point of the year 1991 and goes up to

13 for the energy point of the year 1994. In the following the submatrices are described.

$cov_{kl}^{nn}$:

$cov_{kl}^{nn}$ gives the covariance of channel n between the energy points k and l. The diagonal elements $cov_{kk}^{nn}$ consist of all errors of channel n at the energy point k, i.e. the systematic error of the selection (the part which is correlated between different energy points and the uncorrelated part), the statistical error of the selection, the systematic luminosity error (correlated and uncorrelated part), the theoretical luminosity error and the statistical luminosity error.

$$cov_{kk}^{nn} = \Delta^2{}_{syscorr}^{sel} + \Delta^2{}_{sysuncor}^{sel} + \Delta^2{}_{stat}^{sel} + \Delta^2{}_{syscorr}^{lumi} + \Delta^2{}_{sysuncor}^{lumi} + \Delta^2{}_{theo}^{lumi} + \Delta^2{}_{stat}^{lumi}$$

with $\Delta\sigma$ in nanobarns.
For the off-diagonal elements there are just the errors which are correlated between the energy points k and l, i.e. the correlated part of the systematic error, the correlated part of the luminosity systematic error and the theoretical error of the luminosity.

$$cov_{kl}^{nn} = \Delta^2{}_{syscor}^{sel} + \Delta^2{}_{syscorr}^{lumi} + \Delta^2{}_{theo}^{lumi}$$

$cov_{k,l}^{n,m}$:

$cov_{kl}^{n,m}$ describes the covariance between channel n at the energy point k and channel m at the energy point l. The systematic error of the selection of hadrons and $\mu's$ is not correlated. The correlation between hadrons and $\tau's$ is very small and can be neglected. There is a small anti-correlation between the lepton channels due to crossover events (see chapter 6). The error which is fully correlated is the correlated part of the luminosity systematics (for the diagonal elements as well the uncorrelated part) and the luminosity theory error.

$$cov_{kl}^{had,lepton} = \Delta^2{}_{syscorr}^{lumi} + \delta_{k,l}\left(\Delta^2{}_{stat}^{lumi} + \Delta^2{}_{sysuncor}^{lumi}\right) + \Delta^2{}_{theo}^{lumi}$$

$$cov_{kl}^{\mu,\tau} = \Delta^2{}_{syscorr}^{lumi} + \delta_{k,l}\left(\Delta^2{}_{stat}^{lumi} + \Delta^2{}_{sysuncor}^{lumi}\right) + \Delta^2{}_{theo}^{lumi} - \Delta^2{}_{anti}^{\mu\tau}$$

Additional erros which have to be implemented are the LEP energy errors (see chapter 8.4.2).

The input data are the measured cross sections from 1991 to 1994. The data can be subdevided into two periods, before 1993 without the SiW-detector and without the hole simulation procedure for the multihadron selection and from 1993 onwards including the SiW detector and the hole simulation procedure. The errors on the cross sections are therefore fully correlated

between the years 1993 and 1994. The systematic errors of the selections are larger in 1991 and 1992 than in 1993 and 1994. The contribution of the systematic error of 1991/92 which is considered to be fully correlated with 1993/94 is assumed to be the 1993/94 systematic error. Table 8.1 lists the cross sections at the different energy points used for this analysis.

| Year | cm energy (GeV) | $\sigma_{had}$ (nb) | $\sigma_\mu$ (nb) | $\sigma_\tau$ (nb) |
|---|---|---|---|---|
| 1991 | 91.254 | $30.46 \pm 0.10$ | $1.490 \pm 0.018$ | $1.436 \pm 0.019$ |
| | 88.481 | $5.35 \pm 0.10$ | $0.233 \pm 0.020$ | $0.278 \pm 0.023$ |
| | 89.472 | $10.13 \pm 0.13$ | $0.519 \pm 0.027$ | $0.486 \pm 0.029$ |
| | 90.227 | $18.32 \pm 0.17$ | $0.912 \pm 0.035$ | $0.836 \pm 0.036$ |
| | 91.223 | $30.48 \pm 0.13$ | $1.491 \pm 0.023$ | $1.442 \pm 0.025$ |
| | 91.969 | $24.69 \pm 0.22$ | $1.249 \pm 0.042$ | $1.192 \pm 0.044$ |
| | 92.968 | $14.11 \pm 0.18$ | $0.686 \pm 0.035$ | $0.697 \pm 0.040$ |
| | 93.717 | $9.95 \pm 9.95$ | $0.481 \pm 0.024$ | $0.500 \pm 0.027$ |
| 1992 | 91.299 | $30.707 \pm 0.045$ | $1.4846 \pm 0.0083$ | $1.4786 \pm 0.0090$ |
| 1993 | 89.4525 | $10.0767 \pm 0.0365$ | $0.4991 \pm 0.0080$ | $0.5027 \pm 0.0094$ |
| | 91.2067 | $30.3561 \pm 0.0673$ | $1.4525 \pm 0.0132$ | $1.4825 \pm 0.0143$ |
| | 93.0359 | $13.8652 \pm 0.0427$ | $0.6703 \pm 0.0090$ | $0.6642 \pm 0.0107$ |
| 1994 | 91.2226 | $30.4336 \pm 0.0290$ | $1.4816 \pm 0.0057$ | $1.4581 \pm 0.0062$ |

Table 8.1: *This table lists the cross sections measured at the different energy points. The error of the cross section is the total uncorrelated error, i.e. the statistical and, possibly, an additional uncorrelated error.*

### 8.4.2 Uncertainties in the LEP Energy Scale

The LEP energy errors also have to be taken into account in the line shape fit. There are two different kind of errors. As explained in chapter 3.1.1 there is an error on the absolute energy scale. An other error is due to the energy spread. At each energy point the electrons are not monoenergetic, therefore the center of mass energy has a certain spread. In the following the treatment of the energy error and the energy spread is explained.

- **Uncertainty in the center of mass energy**
  The result of the energy calibration of LEP in 1993 and 1994 as explained in chapter 3.1.1 is the energy matrix shown in table 8.2 (see [23]). The energy error of 1994 is 4 MeV and assumed, according to [23], to be uncorrelated to 1993. The energy error matrix for 1991 and 1992 is obtained as in [24]. It is assumed to be uncorrelated to 1993/1994 data.

  The energy error matrix has to be converted to an error matrix in the cross section in order to be included in the fit. This is done using the covariance transformation law (see for example [37]).

  An uncertainty $\Delta E$ is equivalent to an uncertainty $\Delta\sigma$ in the cross section of

$$\Delta\sigma_i = \frac{d\sigma_i}{dE_i}\Delta E_i$$

| | Peak−2 | Peak | Peak+2 |
|---|---|---|---|
| Peak−2 | 4.32 | 1.34 | 1.33 |
| Peak | 1.34 | 29.5 | 1.41 |
| Peak+2 | 1.33 | 1.41 | 2.51 |

Table 8.2: *Energy error matrix for 1993 in $MeV^2$.*

The covariance matrix of the energy errors can be transformed to the cross section error matrix as:

$$\begin{aligned} cov_E(\sigma_i, \sigma_j) &= \sum_{k,l} \frac{d\sigma_i}{dE_k} \frac{d\sigma_j}{dE_l} cov(E_k, E_l) \\ &= \frac{d\sigma_i}{dE_i} \frac{d\sigma_j}{dE_j} cov(E_i, E_j) \end{aligned} \tag{8.16}$$

Here $i$, $j$, $k$ and $l$ are the different energy points. For the covariance between different decay channels due to the energy error one obtains

$$cov_E(\sigma_i^n, \sigma_j^m) = \frac{d\sigma_i^n}{dE_i} \frac{d\sigma_j^m}{dE_j} cov(E_i, E_j) \tag{8.17}$$

Where $i$ and $j$ describe the energy point and $n$ and $m$ describe the decay channel. After a first iteration of the fit with the covariance matrix from chapter 8.4.1 the derivatives $\frac{d\sigma^n}{dE_i}$ are calculated numerically and the resulting matrix $cov_E(\sigma_i^n, \sigma_j^m)$ is added to the corresponding matrix of the experimental error.

- **treatment of the energy spread**
  At each energy point i there is a certain spread in the center of mass energy of the events. The measured cross section is therefore not the cross section at a single energy point but the convolution of the cross section $\sigma(E)$ with the number of events $N(E)$:

$$\sigma_{measured} = \frac{\int \sigma(E) \cdot N(E)\, dE}{\int N(E)\, dE} \tag{8.18}$$

The energy spread $E_{spread}$ is assumed to be symmetric about the mean energy $E_i$, i.e. the center of mass energy of the energy point i, which is used for the fit. Expanding the cross section about the mean energy $E_i$ shows that the effect of the energy spread cancels to first order:

$$\sigma(E_i + \Delta E) = \sigma(E_i) + \frac{d\sigma}{dE_i}\Delta E + \frac{1}{2}\frac{d^2\sigma}{d^2E_i}\Delta E^2 + \cdots \tag{8.19}$$

because the number of events with an energy of $E_i + \Delta E$ is equal to the number of events with an energy of $E_i - \Delta E$.

The remaining second order effect on the cross section can be approximated by:

$$\Delta\sigma^n_{iEspread} = \frac{1}{2}\frac{d^2\sigma^n}{dE_i^2} \cdot E^2_{spread} \tag{8.20}$$

where $E_{spread}$ is the energy spread. The difference of this approximation to the calculation with the convolution is negligible.

After a first iteration of the fit $\frac{d^2\sigma^n}{dE_i^2}$ is calculated numerically for each channel n at the energy point i and the measured cross section of each channel is corrected:

$$\sigma^n_{icorrected} = \sigma^n_{imeasured} - \Delta\sigma^n_{iEspread} \tag{8.21}$$

The energy spread is determined from the longitudinal beam size [22]. It is $Espread = 55 \pm 5$ MeV in the years 1993 and 1994. The error on the energy spread is fully correlated between the different energy points and causes a correlated error in the cross section:

$$\Delta\left(\Delta\sigma^n_{iEspread}\right) = \frac{d^2\sigma^n}{dE_i^2} \cdot E_{spread}\Delta E_{spread} \tag{8.22}$$

This contribution is added to the covariance matrix of the experimental errors.

The fit is first performed without the energy errors and without correcting for the energy spread. Then the correction of the cross section for the energy spread is calculated and the energy errors and the error on the energy spread are converted to the covariance matrix $cov_E$ which is added to the covariance matrix of the experimental errors. Afterwards a second iteration of the fit is done. The result of the second iteration then constitutes the final result of the fit. The correction of the measured cross sections due to the energy spread changes $\Gamma_Z$ by 4.4 MeV. This is because the correction increases the cross section on peak and decreases the cross section values off-peak.

## 8.5 Results of the Fit

### 8.5.1 Model Independent Fit

For the model indepedent fit $M_Z$, $\Gamma_Z$, $\sigma^0_{had}$, $R_\mu$ and $R_\tau$ are used as fit parameters. This parameter set only suffers little from correlations and is therefore the preferred parameter set of the four LEP experiments. ZFITTER calculates the cross section as a function of $M_Z$, $\Gamma_Z$ and the partial widths $\Gamma_{had,ll}$. To obtain the partial widths from the LEP standard parameter set a parameter transformation is necessary. Using the relations from chapter 8.1 these transformations are :

$$\Gamma_\mu = \frac{M_Z^2\Gamma_Z^2}{12\pi} \cdot \frac{\sigma^0_{had}}{\Gamma_{ee}R_\mu} \tag{8.23}$$

$$\Gamma_\tau = \frac{M_Z^2\Gamma_Z^2}{12\pi} \cdot \frac{\sigma^0_{had}}{\Gamma_{ee}R_\tau} \tag{8.24}$$

$$\Gamma_{had} = R_\mu \cdot \Gamma_\mu = \frac{M_Z^2\Gamma_Z^2}{12\pi} \cdot \frac{\sigma^0_{had}}{\Gamma_{ee}} \tag{8.25}$$

$\Gamma_{ee}$ is fixed to a value of $\Gamma_{ee} = 83.77$ MeV. This is the preliminary OPAL result for a dataset up to 1994 [27].

Having verified that $R_\mu = R_\tau$ within errors it is possible to assume lepton universality. Assuming lepton universality the above transformations are:

$$\Gamma_{lept} = \frac{M_Z \Gamma_Z}{\sqrt{12\pi}} \cdot \left( \frac{\sigma^0_{had}}{R_{lept}} \right)^{\frac{1}{2}} \tag{8.26}$$

$$\Gamma_{ee} = \Gamma_{lept} \tag{8.27}$$

$$\Gamma_{\mu} = \Gamma_{lept} \tag{8.28}$$

$$\Gamma_{\tau} = (1 - \delta_m)\Gamma_{lept} \tag{8.29}$$

$$\Gamma_{had} = R_{lept} \cdot \Gamma_{lept} = \frac{M_Z \Gamma_Z}{\sqrt{12\pi}} \cdot \left( \sigma^0_{had} R_{lept} \right)^{\frac{1}{2}} \tag{8.30}$$

Figures 8.6-8.8 show the measured cross sections and the shape of the fitted cross section as a function of the energy for hadrons, $\mu$'s and $\tau$'s. Data and fit agree well. The results of the two fits (with and without lepton universality) are shown in table 8.3.

The results obtained with the fit performed in this analysis have been compared to the official OPAL results. There is excellent agreement, the discrepancy usually is $< 1/10$ of the parameter error. The largest discrepancy (1.8 MeV) is in the measurement of $M_Z$. It has been seen that 1 MeV is due to the electron channel which is included in the official OPAL fit but not in this analysis. A further difference is that the official analysis also includes the data from the 1990 running. Identical results can therefore not be expected.

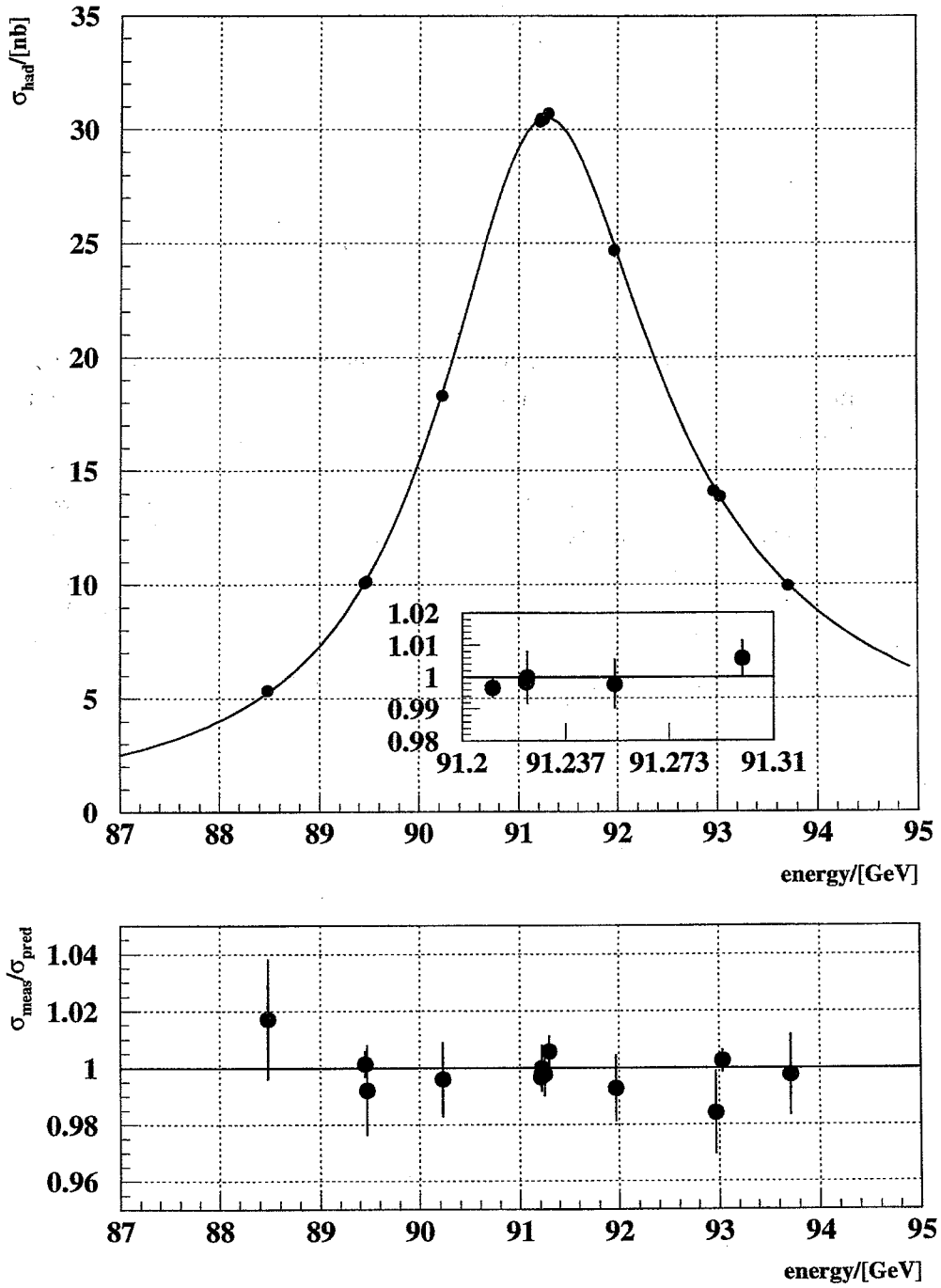


Figure 8.6: *Line shape fit using $e^+e^- \rightarrow$ hadrons. The upper figure shows the measured hadronic cross sections at the different energy points and the fitted cross section. The lower figure shows the measured cross section devided by the fitted cross section at the different energy points. The small inset in the upper figure shows the same ratio for the points at the peak energy between 91.2 and 91.3 GeV.*

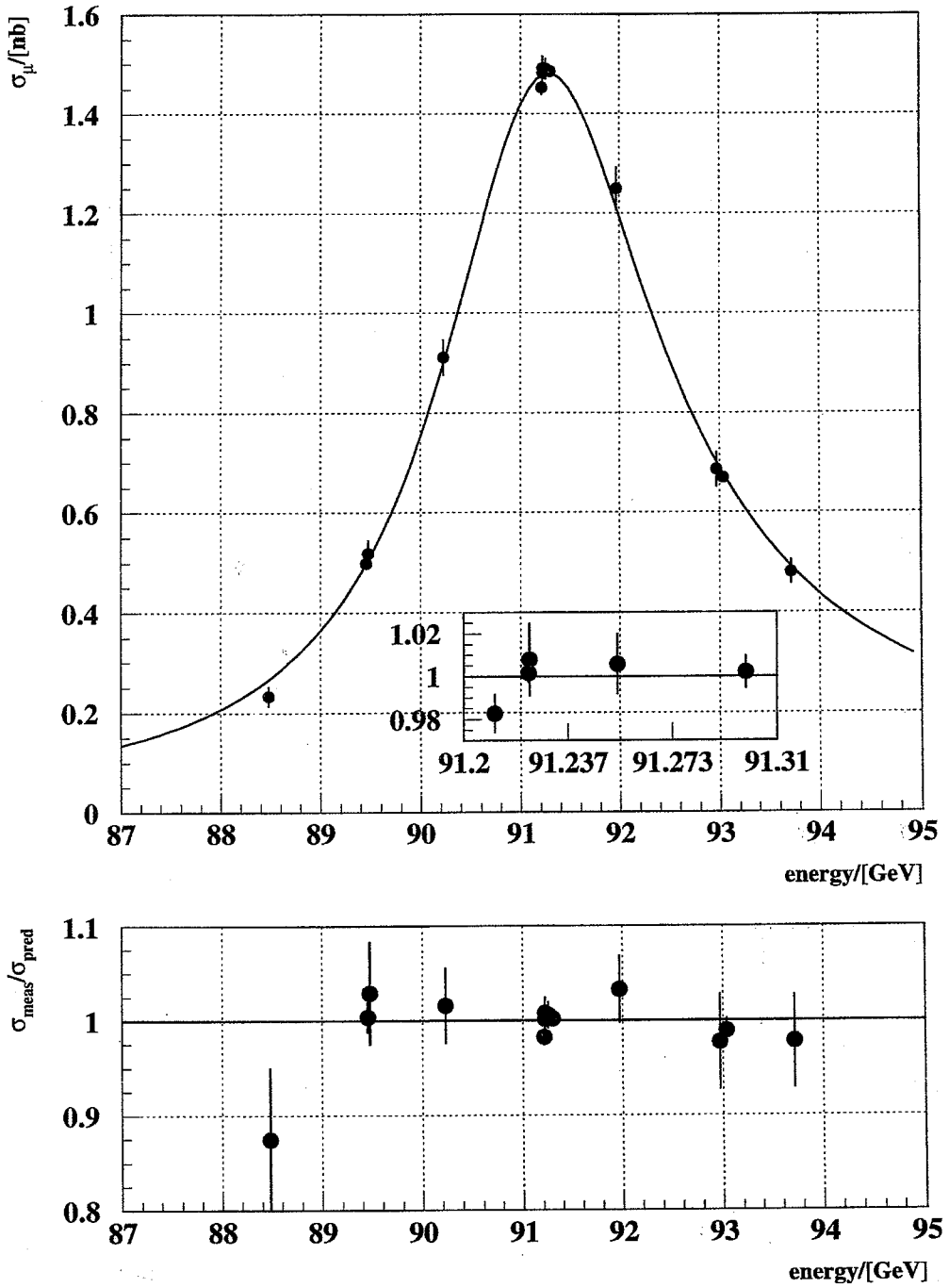


Figure 8.7: *Line shape fit using $e^+e^- \rightarrow \mu^+\mu^-$. The upper figure shows the measured cross sections at the different energy points and the fitted cross section. The lower figure shows the measured cross section devided by the fitted cross section at the different energy points. The small inset in the upper figure shows the same ratio for the points at the peak energy between 91.2 and 91.3 GeV.*

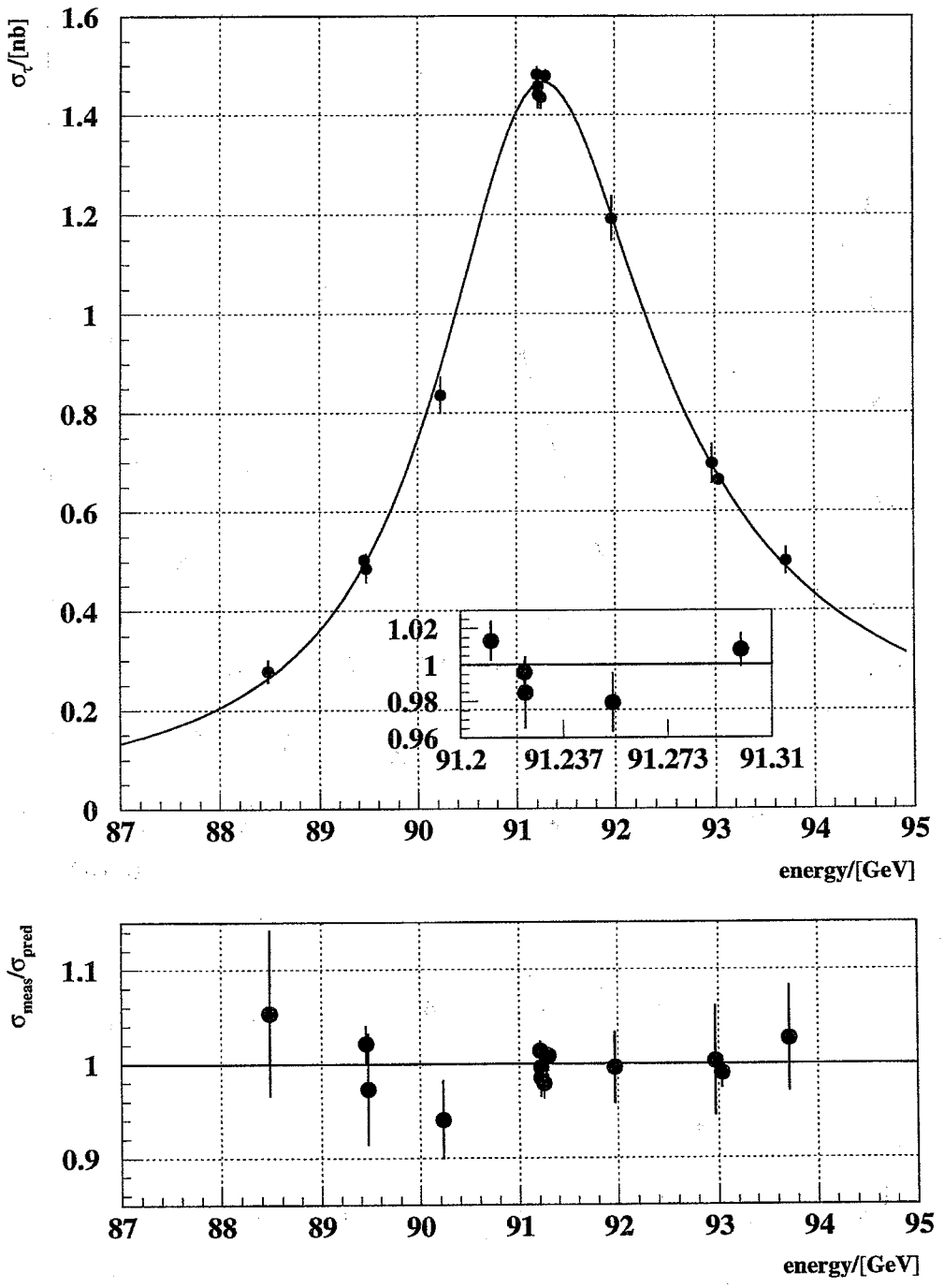


Figure 8.8: *Line shape fit using $e^+e^- \rightarrow \tau^+\tau^-$. The upper figure shows the measured cross sections at the different energy points and the fitted cross section. The lower figure shows the measured cross section devided by the fitted cross section at the different energy points. The small inset in the upper figure shows the same ratio for the points at the peak energy between 91.2 and 91.3 GeV.*

| | without lepton universality | with lepton universality |
|---|---|---|
| $M_Z$ | $91.1870 \pm 0.0036$ GeV | $91.1868 \pm 0.0032$ GeV |
| $\Gamma_Z$ | $2.4957 \pm 0.0051$ GeV | $2.4955 \pm 0.0051$ GeV |
| $\sigma^0_{had}$ | $41.47 \pm 0.10$ nb | $41.47 \pm 0.10$ nb |
| $R_\mu$ | $20.78 \pm 0.07$ | - |
| $R_\tau$ | $21.00 \pm 0.11$ | - |
| $R_{lept}$ | - | $20.838 \pm 0.057$ |
| $\chi^2$/p.d.o.f. | 26.9/34 | 28.2/35 |

Table 8.3: *Results of the fit to the cross sections.*

Using relations 8.23-8.29 it is possible to calculate the partial widths listed in table 8.4. The errors are calculated using the full error matrix of the fit parameters.

| | without lepton universality | with lepton universality |
|---|---|---|
| $\Gamma_{had}$ | $1.746 \pm 0.042$ GeV | $1.746 \pm 0.049$ GeV |
| $\Gamma_\mu$ | $84.02 \pm 0.31$ MeV | - |
| $\Gamma_\tau$ | $83.15 \pm 0.46$ MeV | - |
| $\Gamma_{lept}$ | - | $83.79 \pm 0.19$ MeV |

Table 8.4: *Partial widths.*

The partial widths allow a model independent determination of the $Z^0$ invisible width, $\Gamma_{inv}$:

$$\Gamma_{inv} = \Gamma_Z - \Gamma_{had} - (3 - \delta_m)\Gamma_{lept} \tag{8.31}$$

$$\Gamma_{inv} = 498.4 \pm 4.1 \quad \text{MeV}$$

$\frac{\Gamma_{inv}}{\Gamma_{lept}}$ can be calculated using the result of the fit assuming lepton universality:

$$\frac{\Gamma_{inv}}{\Gamma_{lept}} = \frac{12\pi R_{lept}}{M_Z^2 \sigma^0_{had}} - R_{lept} - (3 - \delta_m) \tag{8.32}$$

This results in:

$$\frac{\Gamma_{inv}}{\Gamma_{lept}} = 5.948 \pm 0.044$$

As mentioned earlier universal corrections depending on $M_{top}$ and $M_{Higgs}$ cancel almost completley in the ratio $\frac{\Gamma_{inv}}{\Gamma_{lept}}$ thus allowing a precise test of the Standard Model. A comparison with the Standard Model prediction is shown in figure 8.9. There is good agreement between the measurement and the Standard Model. Note, that $\frac{\Gamma_{inv}}{\Gamma_{lept}}$ as determined with equation 8.32 does not depend on $\Gamma_Z$. It is determined by the hadronic pole cross section and $R_{lept}$.

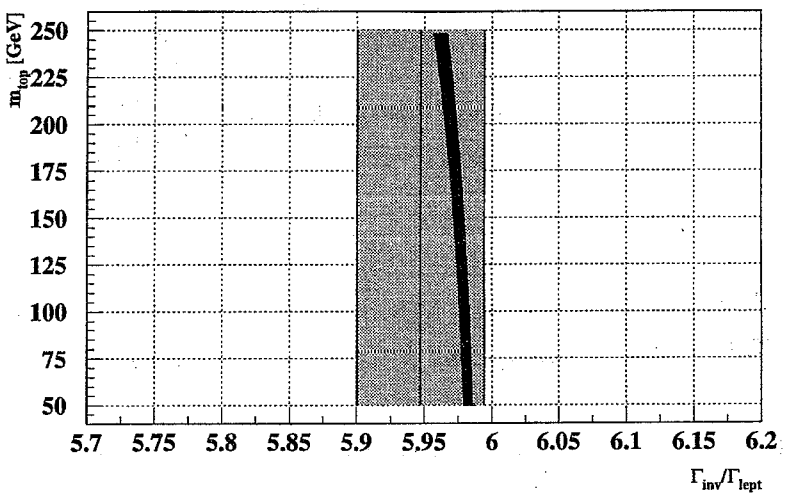


Figure 8.9: *Comparison of the measured* $\frac{\Gamma_{inv}}{\Gamma_{lept}}$ *and the prediction from the Standard Model. The shaded region is the range allowed by the measurement (central value* $\pm$ *one standard deviation). The thick solid line is the Standard Model prediction as a function of* $m_{top}$ *for a range of* 50 *GeV*$< m_{Higgs} <$ 1000 *GeV and 0.126*$< \alpha_S <$*0.138.*

Comparing to the Standard Model prediction for $\frac{\Gamma_\nu}{\Gamma_{lept}}$ the number $N_\nu$ of neutrino types is derived:

$$N_\nu = 2.986 \pm 0.023^{+0.005}_{-0.006}$$

The first error is the experimental error and the second one accounts for varying $M_{top}$ from 50 GeV to 300 GeV and $M_{Higgs}$ from 50 GeV to 1000 GeV.

### 8.5.2 Standard Model Fit

The parameters for the Standard Model fit are $M_z$, $M_{top}$, $M_{Higgs}$ and $\alpha_s$. $\alpha_{QED}$ is fixed to a value of $\alpha_{QED}(M_Z^2) = \frac{1}{128.896}$ [31]. For the fit $M_H$ is fixed to a value of 300 GeV. The results of this fit are shown in table 8.5. The top mass is in good agreement with the direct measurements of $M_{top} = 176 \pm 8$ (stat) $\pm$ 10 (sys) from CDF [38] and $M_{top} = 199^{+19}_{-21}$ (stat) $\pm$ 22 (sys) from D0 [39].

| | |
|---|---|
| $M_Z$ | $91.1868 \pm 0.0032$ GeV |
| $M_{top}$ | $170 \pm 21$ GeV |
| $\alpha_s$ | $0.133 \pm 0.006$ MeV |
| $\chi^2$/p.d.o.f. | 28.6/36 |

Table 8.5: *Results of the Standard Model fit. Changing* $M_H$ *to 1000 GeV increases the value of* $M_{top}$ *to 185 GeV and* $\alpha_s$ *to 0.136. The value of* $M_Z$ *and the errors remain unchanged.*

# Chapter 9

# Summary and Conclusion

The main aim of LEP is to measure the mass and the width of the $Z^0$ boson with high accuracy. $M_Z$ is a fundametal parameter of the Standard Model. After a measurement of $M_Z$ the Standard Model predicts quantities like the $Z^0$ partial widths. The motivation for a precise $M_Z$ determination is therefore twofold: on the one hand it is a fundamental parameter of the Standard Model on the other hand it is a prerequisite for tests of the Standard Model.

In this thesis a precision measurement of the hadronic cross section is performed. The measured hadronic cross sections, together with the cross sections of the processes $e^+e^- \rightarrow \mu^+\mu^-$ and $e^+e^- \rightarrow \tau^+\tau^-$, are used to determine the mass and the width of the $Z^0$ boson. The partial widths are used for a precision test of the Standard Model using $\frac{\Gamma_{inv}}{\Gamma_{lept}}$. Also determined is $\alpha_s$ and an indirect limit for the mass of the top quark.

The total experimental systematic error of the hadronic cross section is reduced from 0.46% to 0.14%. This is mainly possible because of the new SiW luminosity detector. The luminosity monitor allowed to reduce the luminosity systematic experimental error from 0.41% to 0.079%. The measurement of the hadronic cross section in this analysis is characterized by reducing the dependence on Monte Carlo as much as possible. For the luminosity determination only the event generator is used which is needed in order to obtain the cross section of the accepted Bhabha events. No detector simulation is used. The main problems of the luminosity measurement the knowledge of the detector geometry and the coordinate reconstruction are under very good control. The main contributions to the luminosity systematic error are the detector geometry, the coordinate reconstruction and the energy parametrization.
For the multihadron selection Monte Carlo events are only used to extrapolate from the number of events lost in the simulated hole measured with data to the number of events lost in the real physical acceptance holes. This procedure allows an almost fragmentation independent determination of the selection efficiency. New methods are also used to obtain a fragmentation independent comparison of the detector response between data and Monte Carlo. The error of the multihadron selection is reduced by approximately a factor of 2 to 0.11%. The two main contributions are the detector simulation and fragmentation uncertainties.
The cross section measurement is now limited by the theory error of the luminosity of $1.6 \cdot 10^{-3}$.

The measured values for the mass and the width of the $Z^0$ boson are:

$$M_Z = 91.1870 \pm 0.0036\,\text{GeV}$$
$$\Gamma_Z = 2.4957 \pm 0.0055\,\text{GeV}$$

The improved calibration of the LEP energy in the 1993 energy scan allows a reduction of the error of $M_Z$ from 7 MeV to 3.6 MeV [23]. The contribution of the energy calibration error to the error on $M_Z$ and $\Gamma_Z$ is listed in table 9.1.

| | 1992 | | 1994 | |
|---|---|---|---|---|
| | overall | energy calibration | overall | energy calibration |
| $\Delta M_Z$ | 7 | 6 | 3.6 | 1.4 |
| $\Delta\Gamma_Z$ | 11 | 4 | 5.5 | 1.5 |

Table 9.1: *Total error and error due to the LEP energy calibration on $M_Z$ and $\Gamma_Z$. Both errors are in MeV.*

For the determination of $M_Z$ only the energy calibration error and the statistical errors are important. The effect of the systematic experimental error of the cross section measurement is negligible since common systematic errors only have an effect on the absolute value of the cross section which is not important for the $M_Z$ determination. The contribution of the energy calibration to the error on $\Gamma_Z$ is 1.5 MeV. The error on $\Gamma_Z$ due to the error on the energy spread is 1 MeV. Other contributions to the error are the statistical errors and systematic experimental errors of the cross section measurement. The measurement of $\Gamma_Z$ can still be improved with more off-peak statistics. The 1995 energy scan is therefore intended to reduce the error of $\Gamma_Z$.

The error of $\frac{\Gamma_{inv}}{\Gamma_{lept}}$ is reduced by a factor of two compared to the 1992 values. The measured value of $\frac{\Gamma_{inv}}{\Gamma_{lept}}$ is in good agreement with the Standard Model prediction. The number of neutrino families is determined to be $N_\nu = 2.986 \pm 0.023^{+0.005}_{-0.006}$. The indirect limits for the top mass, $M_{top} = 170 \pm 21$ GeV, is also in good agreement with the direct measurement from CDF and D0. The measurement of the strong coupling constant results in $\alpha_s = 0.133 \pm 0.006$.

# Appendix A

# Details of the Luminosity Measurement

## A.1 Geometrical Errors of the Luminosity Measurement

All formulae given in chapter 5.2 depend on the differential cross section

$$\frac{d\sigma}{d\cos\vartheta} = \frac{32\pi\alpha^2}{s} \cdot \frac{1}{\sin^4\vartheta} \tag{A.1}$$

which is calculated using only the t-channel diagram. Using

$$d\cos\vartheta = d\vartheta \sin\vartheta \qquad \text{and} \qquad k = \frac{32\pi\alpha^2}{s} \tag{A.2}$$

this transforms to

$$\frac{d\sigma}{d\vartheta} = k \cdot \frac{1}{\sin^3\vartheta} \; . \tag{A.3}$$

With the geometry shown in figure A.1 one obtains

$$\sin\vartheta = \frac{r}{\sqrt{r^2+z^2}} \qquad \text{and} \qquad \vartheta = atan\frac{r}{z}$$

and

$$\frac{d\vartheta}{dr} = \frac{1}{z} \cdot \frac{1}{1+\left(\frac{r}{z}\right)^2} = \frac{z}{z^2+r^2} \; . \tag{A.4}$$

This results in

$$\begin{aligned} \frac{d\sigma}{dr} &= \frac{d\sigma}{d\vartheta}\frac{d\vartheta}{dr} = k\frac{(r^2+z^2)^{\frac{3}{2}}}{r^3}\frac{z}{z^2+r^2} \\ &= k\frac{z}{r^3}\sqrt{r^2+z^2} \; . \end{aligned} \tag{A.5}$$

For the cross section of the acceptance region one obtains

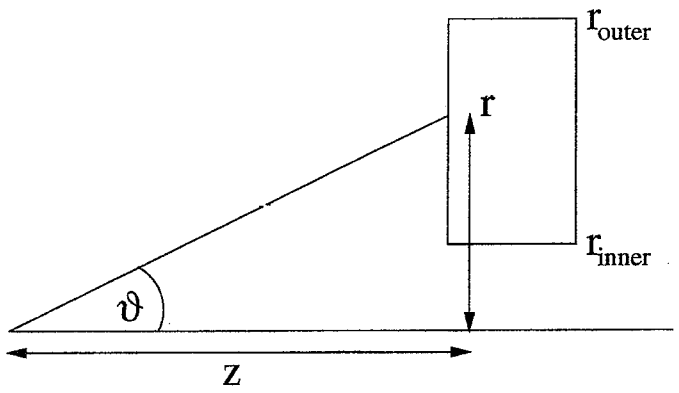


Figure A.1: *Definition of the geometry.*

$$\begin{aligned}\sigma &= \int_{r_{inner}}^{r_{outer}} \frac{d\sigma}{dr} dr = kz \int_{r_{inner}}^{r_{outer}} \frac{\sqrt{r^2+z^2}}{r^3} dr \\ &= kz \left[ \underbrace{-\frac{\sqrt{r^2+z^2}}{2r^2}}_{a} \underbrace{-\frac{1}{2z} ln \frac{z+\sqrt{r^2+z^2}}{r}}_{b} \right]_{r_{inner}}^{r_{outer}} \end{aligned} \tag{A.6}$$

and since $a \gg b$

$$\begin{aligned}\sigma &\approx kz \left( \frac{\sqrt{r_{inner}^2+z^2}}{2r_{inner}^2} - \frac{\sqrt{r_{outer}^2+z^2}}{2r_{outer}^2} \right) \\ &= \frac{kz}{2r_{inner}^2 r_{outer}^2} \left( r_{outer}^2 \sqrt{r_{inner}^2+z^2} - r_{inner}^2 \sqrt{r_{outer}^2+z^2} \right) \\ &= \frac{kz^2}{2r_{inner}^2 r_{outer}^2} \left( r_{outer}^2 \sqrt{1+\frac{r_{inner}^2}{z^2}} - r_{inner}^2 \sqrt{1+\frac{r_{outer}^2}{z^2}} \right) . \end{aligned} \tag{A.7}$$

Using $\sqrt{1+x} \approx 1+\frac{1}{2}x$ this results in

$$\begin{aligned}\sigma &\approx \frac{kz^2}{2r_{inner}^2 r_{outer}^2} \left( r_{outer}^2 \left( 1+\frac{1}{2}\frac{r_{inner}^2}{z^2} \right) - r_{inner}^2 \left( 1+\frac{1}{2}\frac{r_{outer}^2}{z^2} \right) \right) \\ &= \frac{kz^2}{2r_{inner}^2 r_{outer}^2} \left( r_{outer}^2 - r_{inner}^2 \right) . \end{aligned} \tag{A.8}$$

**Uncertainty in the inner edge of the acceptance region**

According to formula A.5 an uncertainty $\Delta r_{inner}$ of the inner acceptance cut is equivalent to an uncertainty in the cross section of

$$\Delta\sigma = \Delta r_{inner} k \frac{z}{r_{inner}^3} \sqrt{r_{inner}^2 + z^2} \tag{A.9}$$

The uncertainty in the luminosity measurement thus is

$$\begin{aligned} \frac{\Delta L}{L} &= \frac{\Delta\sigma}{\sigma} = \Delta r_{inner} k \frac{z}{r_{inner}^3} \sqrt{r_{inner}^2 + z^2} \cdot \frac{2 r_{inner}^2 r_{outer}^2}{k z^2} \frac{1}{r_{outer}^2 - r_{inner}^2} \\ &= \frac{2\Delta r_{inner}}{r_{inner} z} \frac{r_{outer}^2}{r_{outer}^2 - r_{inner}^2} \cdot z \underbrace{\left(1 + \frac{1}{2}\frac{r_{inner}^2}{z^2}\right)}_{\approx 1} \\ &\approx \frac{2\Delta r_{inner}}{r_{inner}} \frac{1}{1 - \frac{r_{inner}^2}{r_{outer}^2}} . \end{aligned} \tag{A.10}$$

**Uncertainty in the outer edge of the acceptance region**

An uncertainty $\Delta r_{outer}$ of the outer acceptance cut is equivalent to an uncertainty of the cross section

$$\Delta\sigma = \Delta r_{outer} k \frac{z}{r_{outer}^3} \sqrt{r_{outer}^2 + z^2} \tag{A.11}$$

and

$$\begin{aligned} \frac{\Delta L}{L} &= \Delta r_{outer} k \frac{z}{r_{outer}^3} \sqrt{r_{outer}^2 + z^2} \cdot \frac{2 r_{inner}^2 r_{outer}^2}{k z^2} \frac{1}{r_{outer}^2 - r_{inner}^2} \\ &\approx \frac{2\Delta r_{outer}}{r_{outer}} \frac{r_{inner}^2}{r_{outer}^2 - r_{inner}^2} = \frac{2\Delta r_{outer}}{r_{outer}} \frac{1}{\frac{r_{outer}^2}{r_{inner}^2} - 1} . \end{aligned} \tag{A.12}$$

**Uncertainty in the distance of the two detectors**

To calculate the effect of an uncertainty $\Delta z$ in the half-distance $z$ of the two detectors formula A.8 is used

$$\frac{d\sigma}{dz} = \frac{2kz}{2 r_{inner}^2 r_{outer}^2} \left(r_{outer}^2 - r_{inner}^2\right) . \tag{A.13}$$

This results in

$$\frac{\Delta L}{L} = 2\frac{\Delta z}{z} . \tag{A.14}$$

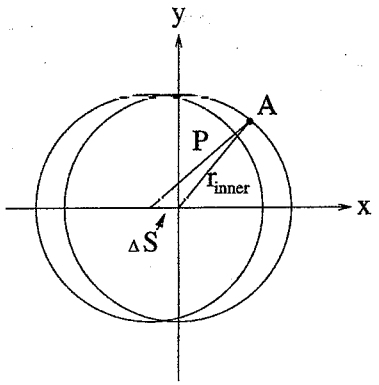


Figure A.2: *Shift of one detector.*

**Shift of one detector**

To calculate the effect of a shift $\Delta S$ of one detector perpendicular to the beam axis the change in the acceptance can be calculated neglecting the outer edge. The difference in the cross section can therefore be calculated from A.7

$$\sigma \approx \frac{kz}{2}\frac{\sqrt{r_{inner}^2 + z^2}}{r_{inner}^2} \; . \tag{A.15}$$

In the shifted detector frame the radius of the point P can be calculated as

$$\left(\vec{P} - \Delta\vec{S}\right)^2 = \vec{r}_{inner}^{\,2} \tag{A.16}$$

$$P^2 - 2P\Delta S\cos\varphi + \Delta S^2 = r_{inner}^2 \tag{A.17}$$

and

$$P = \Delta S\cos\varphi + \sqrt{r_{inner}^2 - \Delta S^2\sin^2\varphi} \; . \tag{A.18}$$

Using

$$\sigma_1 = \frac{kz}{2}\frac{\sqrt{r_{inner}^2 + z^2}}{r_{inner}^2} \tag{A.19}$$

for the cross section of the unshifted detector and

$$\sigma_2 = \frac{kz}{2}\frac{\sqrt{P^2 + z^2}}{P^2} \approx \frac{kz}{2}\frac{\sqrt{r_{inner}^2 + z^2}}{P^2} \tag{A.20}$$

for the cross section of the shifted detector the difference in the two cross sections can be calculated as

$$\Delta\sigma = \frac{1}{2\pi}\int_0^{2\pi} (\sigma_1 - \sigma_2)\, d\varphi \; . \tag{A.21}$$

In order to integrate $\sigma_2$ over $\varphi$, $\sigma_2$ is expanded in a Taylor series. With

$$f(\Delta S) = \frac{1}{P^2} \qquad \text{and} \qquad P = \Delta S\cos\varphi + \sqrt{r_{inner}^2 - \Delta S^2\sin^2\varphi} \tag{A.22}$$

the necessary derivatives are:

$$\left.\frac{df}{\Delta S}\right|_{\Delta S=0} = \frac{-2\cos\varphi}{r_{inner}^3} \tag{A.23}$$

and

$$\left.\frac{d^2f}{d\Delta S^2}\right|_{\Delta S=0} = \frac{1}{r_{inner}^4}\left(6\cos^2\varphi + 2\sin^2\varphi\right) \tag{A.24}$$

With

$$f(0) = \frac{1}{r_{inner}^2} \,. \tag{A.25}$$

$\Delta\sigma$ can be calculated as

$$\begin{aligned}
\Delta\sigma &= |\sigma_1 - \sigma_2| \\
&= \left| \frac{kz}{2}\sqrt{r_{inner}^2 + z^2} \right. \\
&\quad \left. \cdot\frac{1}{2\pi}\int_0^{2\pi} d\varphi \left[\frac{1}{r_{inner}^2} - \left(\frac{1}{r_{inner}^2} - \frac{2\cos\varphi}{r_{inner}^3}\Delta S + \frac{1}{2r_{inner}^4}\left(6\cos^2\varphi + 2\sin^2\varphi\right)\Delta S^2\right)\right]\right| \\
&= \frac{kz}{2}\sqrt{r_{inner}^2 + z^2} \cdot \frac{1}{2\pi}\left[\frac{1}{r_{inner}^4}\left(\frac{3}{2}\varphi + \frac{1}{2}\varphi\right)\Delta S^2\right]_0^{2\pi} \\
&= kz\frac{\sqrt{r_{inner}^2 + z^2}}{r_{inner}^2} \cdot \frac{\Delta S^2}{r_{inner}^2}
\end{aligned} \tag{A.26}$$

and

$$\frac{\Delta\sigma}{\sigma} = 2\left(\frac{\Delta S}{r_{inner}}\right)^2 \,. \tag{A.27}$$

## A.2 Details of the Coordinate Reconstruction

The coordinate reconstruction of SiW is a combination of two separate coordinate reconstruction schemes. Both obey the symmetry of the SiW detector as discussed in section 5.5 and both use the pulse heights of three pads as input. One method which is used to calculate the apparent width $W^0$ of the shower is based on a fit of a gaussian to the pulse heights of the three pads. Then the width $W^0$ is used as additional input parameter for the linearization of the second coordinate reconstruction method. This second coordinate reconstruction is used for determining the coordinate R of the luminosity measurement.

### A.2.1 Determination of the Apparent Width $W^0$

A simple gaussian of the form

$$f(r) = \frac{a}{\sqrt{2\pi}}\, e^{-\frac{(r-r_0)^2}{2\sigma^2}}$$

is used to get the radial coordinate $r_0$ and the width $\sigma$ of the shower. The pad with the highest pulse height and its two neighbours in R sumed over two pads in $\phi$ are used. The fit

of f(r) to the pulse heights is well determined and the parameters can be directly calculated without performing the fit. Using

$$\begin{aligned} f(-2.5) &= E_3 \\ f(0) &= E_2 \\ f(+2.5) &= E_1 \end{aligned}$$

results in

$$r_0 = -\frac{1}{5}\sigma^2 ln\left(\frac{E_3}{E_1}\right) \tag{A.28}$$

and

$$\sigma = \sqrt{\frac{-6.25}{ln\frac{E_3 \cdot E_1}{E_2 \cdot E_2}}} \tag{A.29}$$

It turns out that $\sigma$ as a function of $r_0$ can be described by a parabola and the offset $P^0$ of the parabola is a measure for the apparent width $W^0$ of the shower.

$$P^0 = \sigma - a_1 r_0 - a_2 r_0^2 \tag{A.30}$$

a1 and a2 are the parameters of the parabola. The mean of $P^0$ is a linear function of $X_0$, the amount of material in radiation lengths in front of the shower. The apparent width $W^0$ is then calculated as

$$W^0 = a_3 + a_4 P^0 \tag{A.31}$$

### A.2.2 Linearization of the Coordinate Reconstruction

As described in section 5.5 the reconstruction of the R-coordinate is based on the symmetric function

$$Y^0 = \frac{E_1 - E_3}{2E_2 - E_1 - E_3} \tag{A.32}$$

A function which can be used to describe the variable $Y^0$ is

$$Y^0 = F(R) = D_0 + \frac{A}{(R_0 - R)^B} \tag{A.33}$$

$R_0$ can be fixed to 1.1 and the conditions

$Y^0 = F(R) = 0$ for R=0 (pad center) and
$Y^0 = F(R) = 1$ for R=1 (pad boundary)

give relations to determine A and $D_0$. The radius $R_{pad}$ in a given pad can be calculated as

$$R_{pad} = R_0 - \left(\frac{A}{Y^0 - D_0}\right)^{\frac{1}{B}}$$

B is a function of the width $W^0$ of the shower:

$$B = a_5 W^0 e^{-a_6 W^0}$$

All parameters $a_i$ are determined directly from data. $R_{pad}$ in each layer is the radius which is then combined to the radius $\bar{R}$ as described in section 5.5.

## A.3 Determination of the Lateral Shower Profile

The reconstruction of the radial coordinate R is based, as discussed in section 5.5, on the testbeam measurement of the shift $\Delta s$ due to the r - $\phi$ geometry of the detector. The error of the measurement directly translates to the systematic error of the luminosity measurement. It is therefore important to have a second independent determination of the shift. The shift, however, is a purely geometrical effect. Once the radial energy distribution of the electromagnetic showers is known the shift can be calculated.
This chapter describes the determination of the lateral shower profile of electromagnetic showers in the SiW detector. The shower profile is determined using the same testbeam data as used for the direct measurement of the shift described in section 5.4.

### A.3.1 Parametrization of the Lateral Shower Profile

The energy density within the electromagnetic shower is parametrized as:

$$f(d) = \sum_{i=1}^{3} a_i e^{-t_i d} \tag{A.34}$$

where $d$ is the distance to the shower center defined as the extrapolated position of the electron. This extrapolation is done using the microstrip detectors and delay wire chambers of the testbeam setup (see section 5.4). Other parametrizations have also been tried. The sum of the three exponentials gives the best parametrization in terms of the $\chi^2$ of the fit performed to determine the parameters.

### A.3.2 Determination of the Parameters

As input parameters the pulse heights of the pads 3 to 18 sumed of the two $\phi$-segments of a detector and the coordinate P(x,y) of the shower center are used (see figure A.3). The

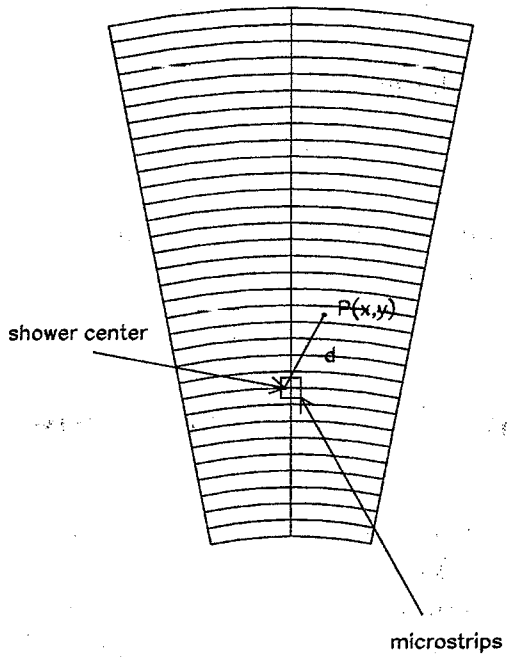


Figure A.3: *Definition of the variables used for the fit. The area covered by the microstrip detectors is indicated by the box.*

parameters $a_i$ and $t_i$ are determined in a fit to 1000 events. The expected pulse height $ph_j^{pred}$ of pad j as a function of the parameters can be calculated as

$$ph_j^{pred} = \int_{r_j}^{r_{j+1}} \int_{-\varphi_0}^{+\varphi_0} \sum_{i=1}^{3} a_i e^{-t_i d(\varphi,R)} d\varphi dR \tag{A.35}$$

where $\varphi_0 = 11.25°$ is half the width of a silicon detector and $d$ is the distance to the shower center (see again figure A.3)

$$d(\varphi, R) = \sqrt{(x - R\sin\varphi)^2 + (y - R\cos\varphi)^2} \tag{A.36}$$

The integration is done numerically. Since just 64 channels of the microstrip detectors in the testbeam were read out the covered area was about 3×3 mm$^2$ placed at the pad boundary between pad 9 and 10.

The fit is performed by minimizing

$$\chi^2 = \sum_{i=1}^{1000} \Delta ph_i \, cov_i^{-1} \, \Delta ph_i^T \tag{A.37}$$

where $(\Delta ph_i)_j = ph_{i,j} - ph_{i,j}^{pred}$, ie. $ph_{i,j}$ specifies the measured pulse height of pad j in event i and $ph_{i,j}^{pred}$ is the predicted pulse height for pad j and the shower center of event i. The covariance matrix cov describes the fluctuations and correlations of the showers. It is not known a priori but has to be calculated. Since both the pulse heights and the correlation depend due to the lateral shower profile on the position of the shower center within a pad, cov is calculated in 100 $\mu m$ bins of R:

$$(cov_{kl})_i = \sum_j \left(ph_{jk} - \overline{ph}_k\right)\left(ph_{jl} - \overline{ph}_l\right) \tag{A.38}$$

where the sum extends of all events with a shower center in the bin i. $\overline{ph}_k$ is the average pulse height in pad k of these events and $ph_{jk}$ is again the pulse height of pad k in the event j. The minimisation is performed using MINUIT. A first fit showed that the parameters $t_i$ are very similar in all layers. They are therefore fixed to minimizes the correlation between the parameters and the fit is repeated. The result for the fit parameters is listed in table A.1 for the layers which were equipped in the testbeam.

| | $4X_0$ | $6X_0$ | $8X_0$ |
|---|---|---|---|
| $a_1$ | 106.22 | 108.52 | 69.54 |
| $a_2$ | 10.07 | 16.54 | 17.53 |
| $a_3$ | 0.56 | 1.58 | 2.29 |

Table A.1: *Parameters determined by the fit. The parameters $t_1$, $t_2$ and $t_3$ are fixed to the values 2.4, 0.65 and 0.22, respectively.*

Figure A.4 shows the lateral shower profile $f(d)$ and figure A.5 shows the energy content within a distance r from the shower center. The radius which contains 90% of the energy, the Moliere Radius, is 8.87 mm, 11.71 mm and 13.27 mm after $4X_0$,$6X_0$ and $8X_0$, respectively.

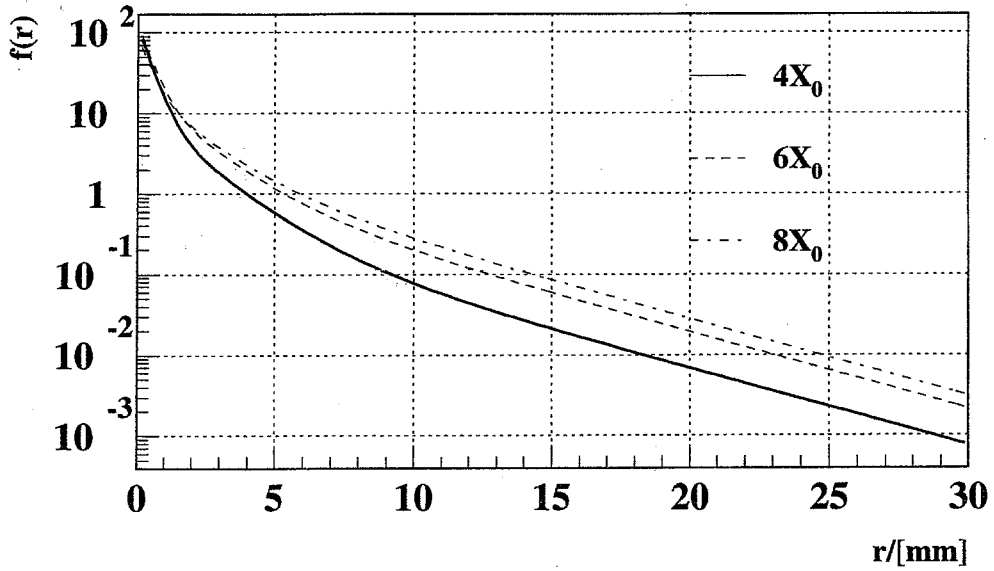


Figure A.4: *Lateral shower profiles for the three layers.*

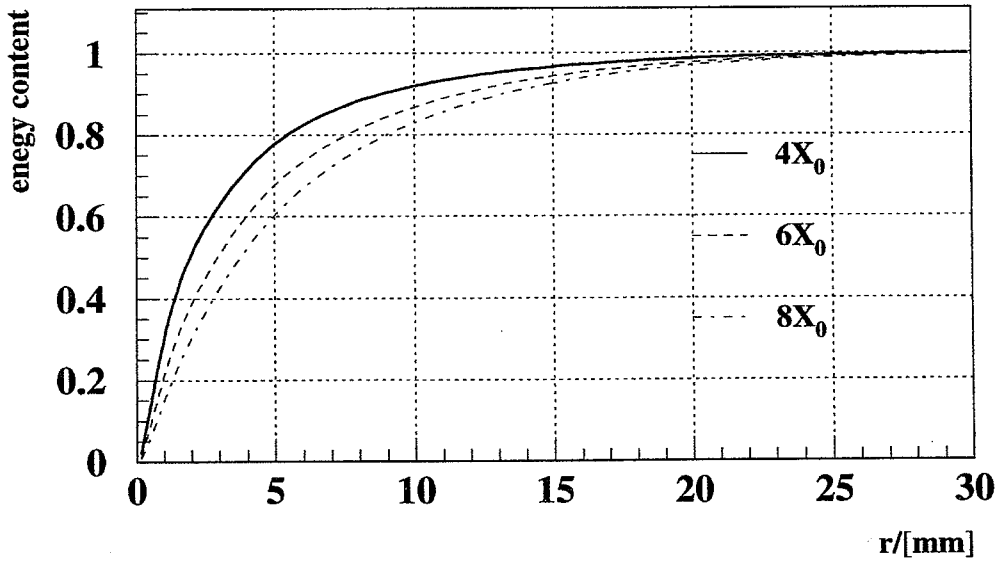


Figure A.5: *Energy contained within a distance r of the shower center.*

### A.3.3 Determination of the Shift with the Lateral Shower Profile

The shift $\Delta s$ is defined as $\Delta s = R_{pad}^{true} - R_{50}$, where $R_{pad}^{true}$ is the real physical position of the pad boundary and $R_{50}$ is the radius at which the shower deposits an equal amount of energy in the pads (summed over the two $\phi$-segments) above and below the pad boundary. For the determination of $R_{50}$ the shower center P(x,y) is placed at the pad boundary at $\varphi = 0°$ and succesively moved towards smaller radii until the calculated pulse height of the pads above and below the pad boundary is equal. The pulse height of the pads are calculated using formular A.35. The numerical precision of this determination is less than 1 $\mu m$. Table A.2 shows the determined shifts for $4\,X_0$,$6\,X_0$ and $8\,X_0$. This has to be compared to the $8 \pm 6$ $\mu m$ of the direct testbeam measurement.

| | shift $\Delta s/\mu m$ |
|---|---|
| $4\,X_0$ | 6 |
| $6\,X_0$ | 9 |
| $8\,X_0$ | 12 |

Table A.2: *Calculated shifts.*

The systematic error of the determination of the shift with the lateral shower profile is small $\mathcal{O}(2\,\mu m)$. The reason why this determination can not be used instead of the direct measurement is because this measurement describes the shift of the average shower whereas the direct measurement describes the average shift of showers which is what is needed for the coordinate reconstruction. But since both measurements agree and have largely complementary sources of systematic errors the determination of the shift with the lateral shower profile gives confident that the direct testbeam measurement is correct. This is very important since the entire luminosity measurement relies on the determination of the shift.

Furthermore allows the determination of the shift with the lateral shower profile to extrapolate the shift from the positon where it was measured to other positions in R and $\phi$. The testbeam measurement of the shift is made at the pad boundary between pad 9 and 10 whereas the inner acceptance cut is made at the pad boundary between pad 6 and 7. Since the shift depends on the curvature of the pad boundary with respect to the shower width the shift is different at the pad boundary 6/7 compared to 9/10. The shift is also different for the pad boundary 26/27 (where the outer acceptance cut is made). Table A.3 shows the calculated shifts at the different relevant positions (inner and outer acceptance boundary).

| pad boundary | $\Delta s$ after $4\,X_0$ | $\Delta s$ after $6\,X_0$ | $\Delta s$ after $8\,X_0$ |
|---|---|---|---|
| 6/7 | 6.0 | 8.7 | 12.3 |
| 26/27 | 3.7 | 5.2 | 7.3 |

Table A.3: *Calculated shifts at the pads where the inner and outer acceptance cuts are made.*

# Appendix B

# Details of the Multihadron Selection

This appendix describes some more historic details of the development of the selection of multihadronic events. These details are not necessary for understanding the selection method used in this analysis.

## B.1 Modification of the HDMH Selection

The HDMH selection is the basis for the selection used in this analysis. Compared to the selection used here, the HDMH selection has two addidtional cuts on the multiplicity of the forward and backward hemispheres.

- $N_F = N_{F_{CJ}} + N_{F_{ECAL}} + N_{F_{FD}} \geq 4$
- $N_B = N_{B_{CJ}} + N_{B_{ECAL}} + N_{B_{FD}} \geq 3$

Monte Carlo studies have shown that the sensitivity of the HDMH selection to fragmentation uncertainties and hard initial state photon radiation can be reduced without significantly increasing the background if the cuts on the forward and backward multiplicities are dropped.

To study fragmentation uncertainties 100000 events generated with JETSET and a changed value of $Q_0$ ($Q_0$ changed from 1.0 $GeV$ to 2.6 $GeV$) and an event axis of $|\cos(\vartheta_{thrust_{x,z}})| > 0.87$ with respect to the x- or z-axis are passed through the full detector simulation. Figure B.2 shows $\cos(\vartheta_{thrust})$ for the lost events of the standard Monte Carlo and the changed $Q_0$ sample. Figure B.3 shows the number of lost events for the different cut variables for events which point in the barrel. Most of the events are lost due to the cut on forward or backward multiplicity. $Q_0$ is the invariant mass cut-off parameter below which partons do not radiate gluons. Increasing $Q_0$ changes the particle multiplicity and the energy spectrum. Since the cuts on the forward and backward multiplicity are the hardest multiplicity cuts of the HDMH selection (as can be seen in figure B.1) the sensitivity to changes in the multiplicity in the Monte Carlo is much reduced without these two cuts. This also has a positive effect on the detector simulation

uncertainty since the selection is less sensitive to differences in the multiplicity between data and Monte Carlo.

Events with hard initial state photon radiation tend to be unbalanced. They are similar to two photon events but often do not get discarded by the cut on the visible energy or energy imbalance. Figure B.4 shows the initial state photon energy spectrum for all events and for the lost events. The lost events fall into two classes. They either have low initial state photon energy and are lost for geometrical reasons or are lost because of high energy radiation. Figure B.5 shows the number of lost events for each cut for events with more than 35 $GeV$ initial state photon energy. It can be clearly seen that most of the events with hard initial state photon radiation are discarded due to the cuts in the forward or backward multiplicity.
Since the initial state photon energy varies slightly with the center of mass energy the selection efficiency varies as well. Not applying these two cuts makes the selection less dependent on the centre of mass energy.

The background is not significantly increased if the cuts in forward and backward multiplicity are dropped. The $\tau$ background is increased from $11 \cdot 10^{-4}$ to $14 \cdot 10^{-4}$. The uncertainty on the $\tau$ background stays unchanged. The two photon background is not affected. The selection efficiency is increased from 99.5% to 99.6%.

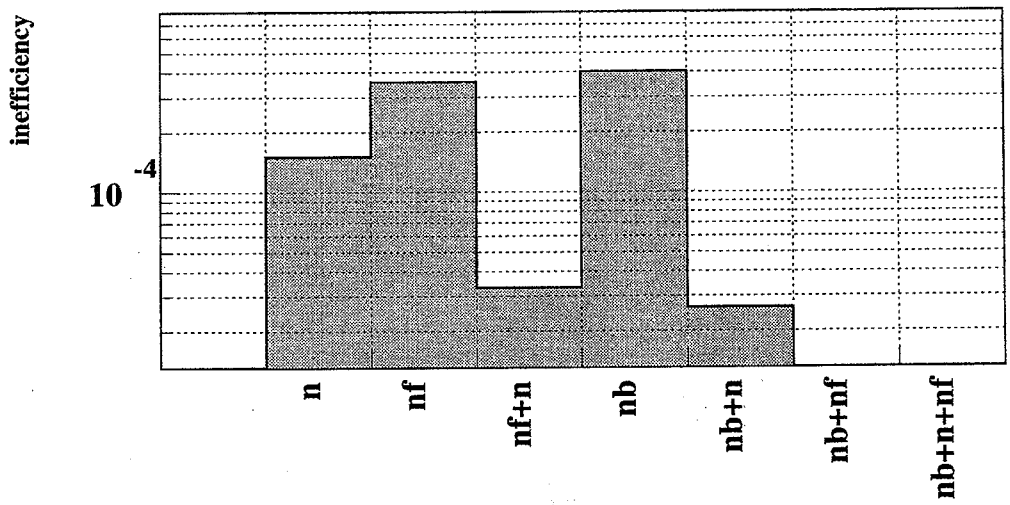


Figure B.1: *The inefficiency of the HDMH selection due to the multiplicity cuts. The cuts on the forward and backward multiplicity are the hardest multiplicity cuts.*

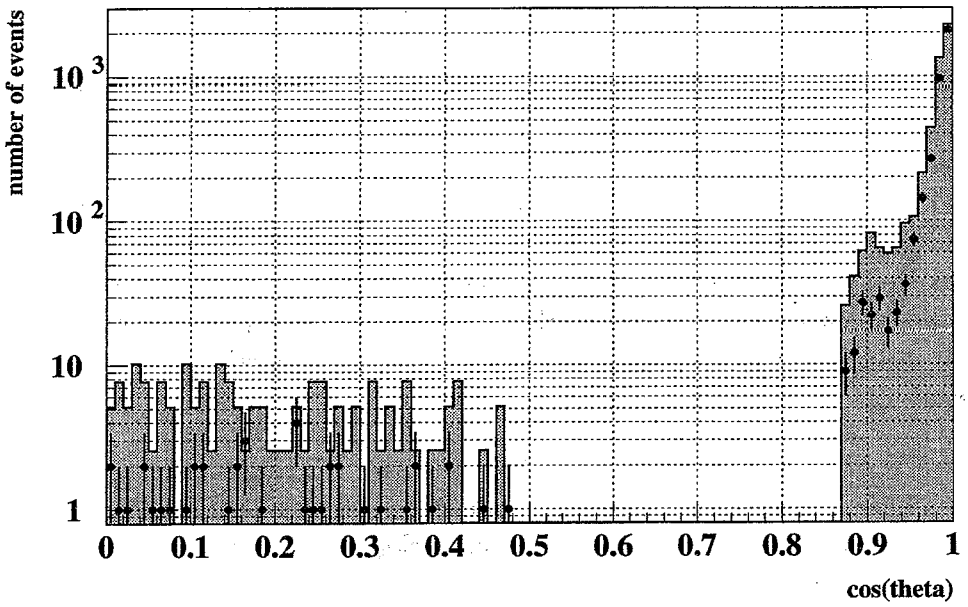


Figure B.2: $|\cos(\vartheta_{thrust_z})|$ *for the events which are lost for the sample with a* $Q_0$ *of 1.0 GeV (points) and for the sample with a* $Q_0$ *of 2.6 GeV (histogram).*

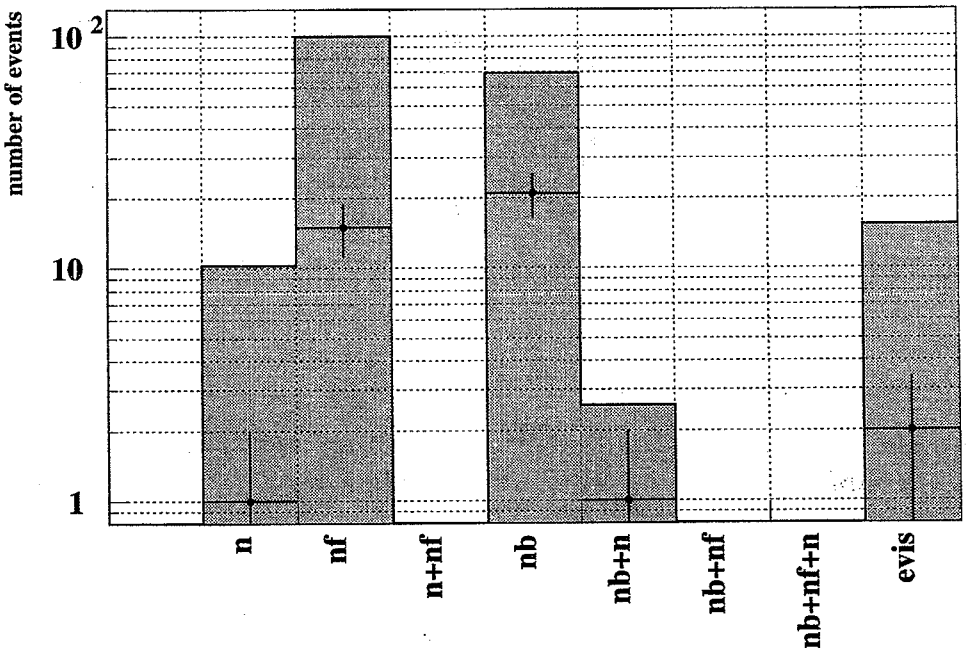


Figure B.3: *Cuts of lost events pointing in the barrel region. The points are for the standard sample* ($Q_0 = 1.0$ *GeV) and the histogram for the* $Q_0 = 2.6$ *GeV sample.*

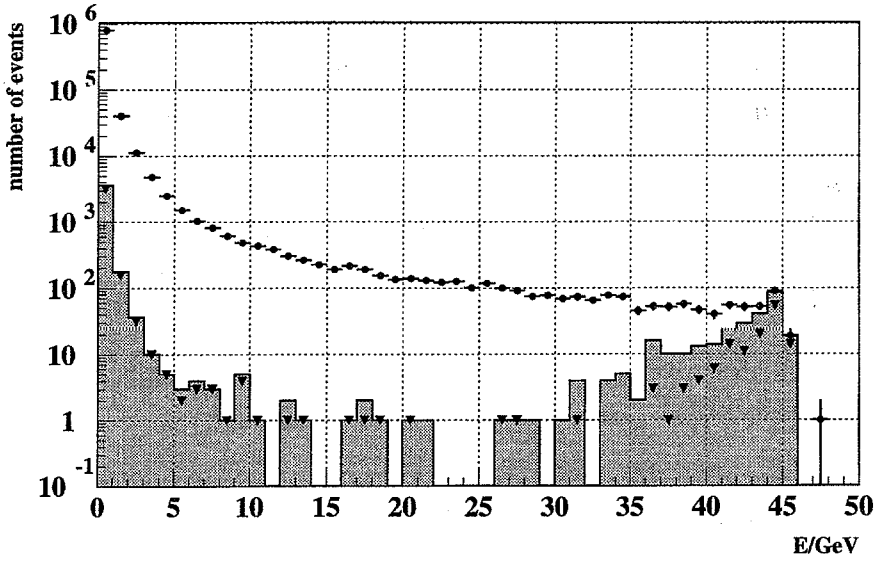


Figure B.4: *Initial state photon energy spectrum of all events (points) and the lost events (histogram). The triangles show the number of lost events after dropping the cuts in the forward and backward multiplicity.*

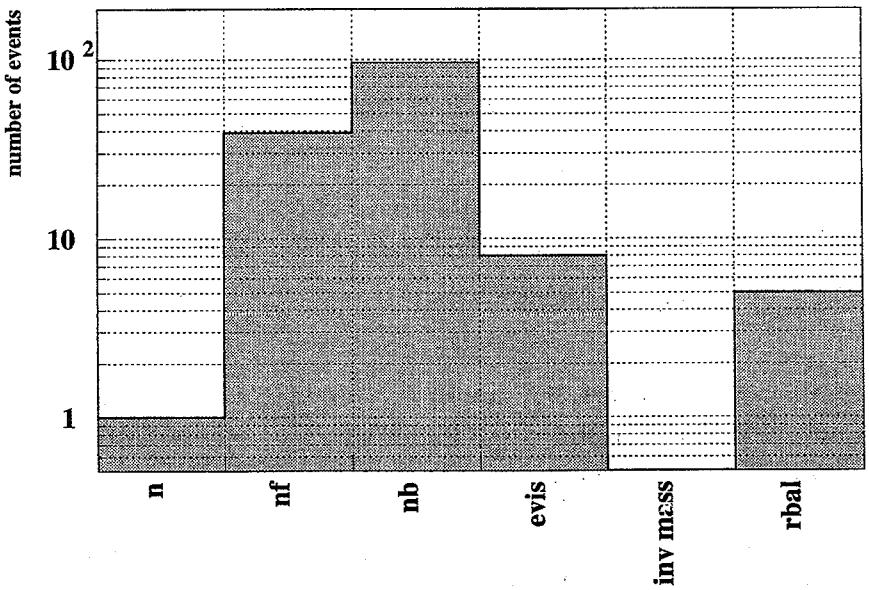


Figure B.5: *Cuts of the events which are lost exclusively due to the specific cut and have a radiated initial state photon with an energy of more than 35 GeV. Most of the events which are discarded due to a single cut are discarded due to the cuts on the multiplicity in the forward and backward hemispheres.*

## B.2 Studies to Increase the Efficiency of the Multi Hadron Selection

Multi hadron events which escape undedected are lost due to the holes in ECAL, CJ and FD in the forward region. The new SiW-detector (SiW) may offer the possibility to increase the acceptance and to reduce the systematic error. The geometrical holes in the coverage of ECAL and FD are a gap between ECAL and FD at $0.98 < \cos\vartheta < 0.9928$ and the hole in the center of FD at $\cos\vartheta < 0.9989$. The SiW detector covers a region from 0.9984 to 0.9997. Another possibility to increase the acceptance is to make use of the hadron calorimeter poletip HP. It covers a region up to 0.99 in $\cos\vartheta$ and almost closes the gap between ECAL and FD.

This section describes studies done to increase the efficiency by using the SiW detector or HP in the multihadron selection.

**Using SiW in the multihadron selection**
Most of the particles in multihadronic events are pions which usually leave along their trajectory a signal of a minimum ionizing particle. Occasionally they have a hadronic interaction in the SiW detector and are absorped. The trace of the minimum ionizing signal along the trajectory of the pion is not found by the clustering algorithm which looks for three dimensional connected group of pads in the detector. Therefore a track finding algorithm was written which searches for a number of pads above a certain energy threshold aligned in a line. The detection probability for pions above 5 GeV using both, the clusters and the tracks found, is about 94%.

The SiW calorimeter is implemented in the multi hadron selection using all clusters and tracks in the same way as FD.

- $X_E^{vis} = \left(E_{ECAL} + \frac{1}{3}(E_{FD} + E_{SiW})\right)/\sqrt{s} > 0.1$
- $R_{bal} = (PZ_{ECAL} + PZ_{FD} + PZ_{SiW})/(E_{ECAL} + E_{FD} + E_{SiW}) < 0.75$
- $N_{all} = N_{CJ} + N_{ECAL} + N_{FD} + N_{SiW} \geq 11$
- $N_F = N_{F_{CJ}} + N_{F_{ECAL}} + N_{F_{FD}} + N_{F_{SiW}} \geq 4$
- $N_B = N_{B_{CJ}} + N_{B_{ECAL}} + N_{B_{FD}} + N_{B_{SiW}} \geq 3$

where $N_{SiW}$ is the number of all clusters and tracks in SiW. $E_{SiW}$ is the sum of the cluster and track energies. This increases the efficiency from 99.52% to 99.60 % as determined with Monte Carlo. Figure B.6 shows the total energy deposited in the SiW detectors for multi hadron events which are selected without SiW. As can be seen data and Monte Carlo disagree because of the off-momentum particles entering SiW. These off-momentum particles overlap good multi hadronic events in data and can discard events due to the energy imbalance cut. This effect more than cancels the gain due to the increased acceptance.

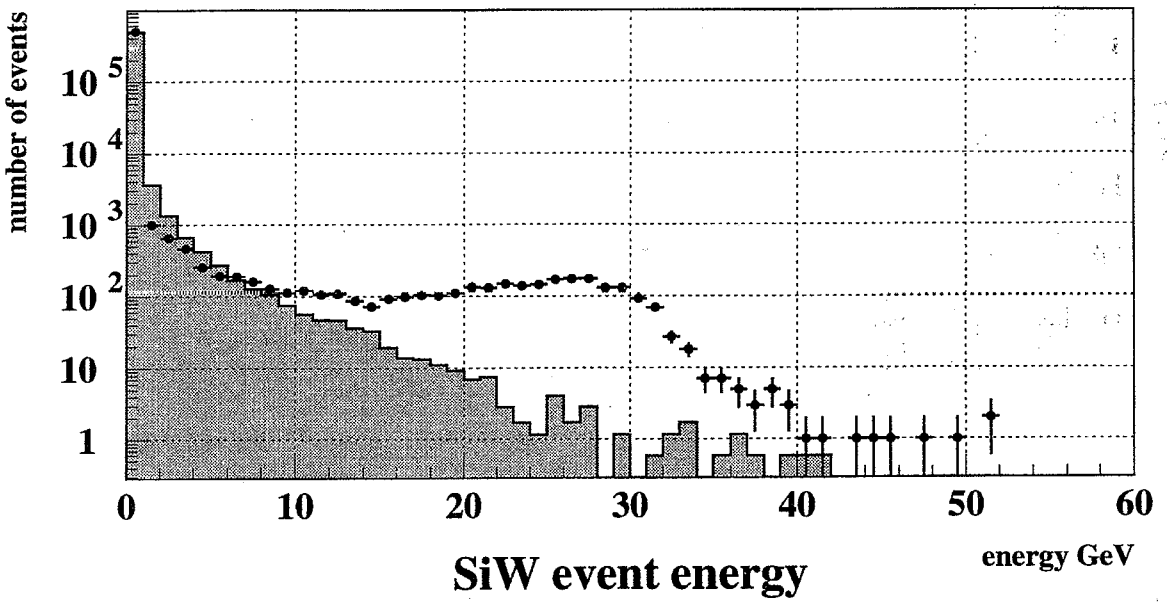


Figure B.6: *Distribution of the total energy in SiW for multi hadron events selected without SiW.*

**Using HP in the multihadron selection**

Another possibility to increase the efficiency is to make use of the hadron poletip calorimeter, HP. HP partly covers the gap between ECAL and FD and provides additional energy information in the endcap region where the EE energy is small because of material in front of ECAL. HP is used in the following way:

- $X_E^{vis} = (E_{ECAL} + \frac{1}{3}(E_{FD} + E_{HP})/\sqrt{s} > 0.1$
- $R_{bal} = (PZ_{ECAL} + PZ_{FD} + PZ_{HP})/(E_{ECAL} + E_{FD} + E_{HP}) < 0.75$
- $N_{all} = N_{CJ} + N_{ECAL} + N_{FD} + N_{HP} \geq 11$
- $N_F = N_{F_{CJ}} + N_{F_{ECAL}} + N_{F_{FD}} + N_{F_{HP}} \geq 4$
- $N_B = N_{B_{CJ}} + N_{B_{ECAL}} + N_{B_{FD}} + N_{B_{HP}} \geq 3$

Where $N_{HP}$ is the total number of HP clusters, and $E_{HP}$ is the sum of the energy of all HP clusters. $PZ_{HP}$ is defined according to $PZ_{ECAL}$.

The increased acceptance including HP is 99.75%. This would be a substantial gain in the detection efficiency but a comparison of data and Monte Carlo (see figure B.7) shows that HP is rather poorly modelled in the Monte Carlo. After empirically correcting for the not completly understood differences in the energy distribution between data and Monte Carlo the efficiency

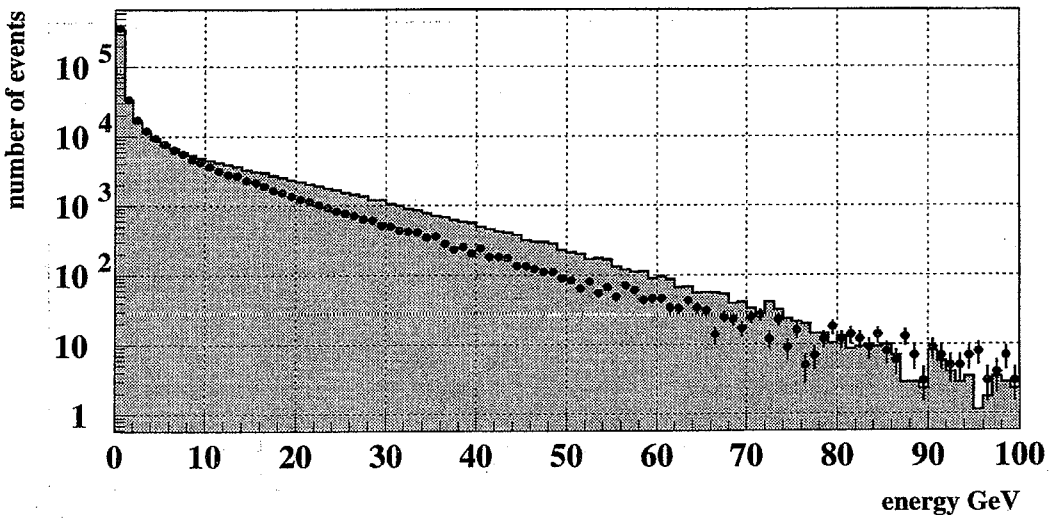


Figure B.7: *Distribution of the total energy in HP for multi hadron events selected without HP.*

decreases to 99.67%. The difference of $8 \cdot 10^{-4}$ to the uncorrected value of 99.75% serves as an estimate of the additional error due to the HP detector simulation. This is considered to be too large to be useful. For this reason HP is not used in the selection of multihadronic events.

## B.3 The Fast Smear Mode Monte Carlo

A fast smear mode Monte Carlo was developed as a flexible tool for making tests on a large number of generated multi hadron events very quickly. Information from the full GOPAL detector simulation of already generated events is combined with generator-level information to give a theta-, momentum-, and particle-dependent parameterization of the GOPAL simulated response of ECAL to generator-level particles.

The procedure used can be summarized as follows:
About 600000 events simulated with the full Gopal Monte Carlo (the standard multihadron Monte Carlo) passing the multi hadron selection cuts are chosen. The detector is divided into 2 sections, $|\cos(\theta)| < 0.75$ and $|\cos(\theta)| > 0.75$. Histograms corresponding to the two sections are filled depending on whether the cluster is in EB or EE. The particle type of each cluster is labelled as hadronic, electromagnetic, or muonic depending on which kind of stable generator-level particle contributes more than 50 % of the cluster's energy according to the Monte Carlo. Then the deposited energy versus ingoing momentum is entered into a two-dimensional histogram depending on the particle type and the cluster's $\theta$. These histograms are used to model the ECAL response in the fast smear mode Monte Carlo. Energy is assigned to each particle using the corresponding histogram as a random distribution. Clusters resulting from particles which are closer than 0.9985 in EB and 0.9965 in EE are merged.

The CJ response is assigned directly from the momentum of charged stable generator-level particles. All charged tree-level particles within $|\cos(\vartheta)| < 0.96$ and a $p_t$ of more than 150 MeV are used.

Since there is no tree-level information available for FD clusters, the FD response is modelled using the same procedure as for the ECAL response. The GOPAL simulated energy response of EB is used as input. The geometrical acceptance is $0.98998 < \cos(\theta) < 0.99928$. Clusters which are closer than 1.0472 rad in $\phi$ are merged and the clusters are required to have a energy of more than 2.0 GeV (the energy cut-off of FD).

Figures B.9-B.8 compare energy and multiplicity distributions between the full GOPAL simulation and the fast smear mode Monte Carlo. The distributions of ECAL and FD look quite good. The smear mode MC CJ multiplicity distribution is shifted towards smaller values compared to GOPAL. This might be due to missing conversions in the smear mode MC. The difference in the multiplicity has however only a minor effect since the cut on the multiplicity is the least hard cut.

To study the residual sensitivity of the acceptance calculation procedure discussed in section 7 to changes in the fragmentation parameters several parameters are changed by $1\sigma$ [17] and the acceptance of the selection is recalculated. Table B.1 shows the difference in the selection efficiency for the different sets of fragmentation parameters. For each set 100000 events are generated with the fast smear mode MC. The standard parameter set is : $Q_0 = 1.0\ GeV$, $\sigma_q = 0.36$ and $\Lambda_{QCD} = 0.31$. It can be seen that the largest change in the efficiency for the standard efficiency calculation is for the change in $Q_0$. The hole procedure leads to a reduced sensitivity. The largest difference is $4.0 \cdot 10^{-4}$.

| Changed parameter: | $Q_0 = 1.8\ GeV$ | $\sigma_q = 0.31$ | $\sigma_q = 0.39$ | $\Lambda_{QCD} = 0.30$ | $\Lambda_{QCD} = 0.3$ |
|---|---|---|---|---|---|
| Change in direct efficiency | $11.0 \cdot 10^{-4}$ | $-1.1 \cdot 10^{-4}$ | $1.4 \cdot^{-4}$ | $3.9 \cdot 10^{-4}$ | $-0.6 \cdot 10^{-4}$ |
| Change in extr. efficiency | $0.67 \cdot 10^{-4}$ | $1.6 \cdot 10^{-4}$ | $3.6 \cdot 10^{-4}$ | $0.92 \cdot 10^{-4}$ | $4.0 \cdot 10^{-4}$ |

Table B.1: *Effect of the changed fragmentation parameters on the selection efficiency. The statistical error in the difference is about* $2.5 \cdot 10^{-4}$.

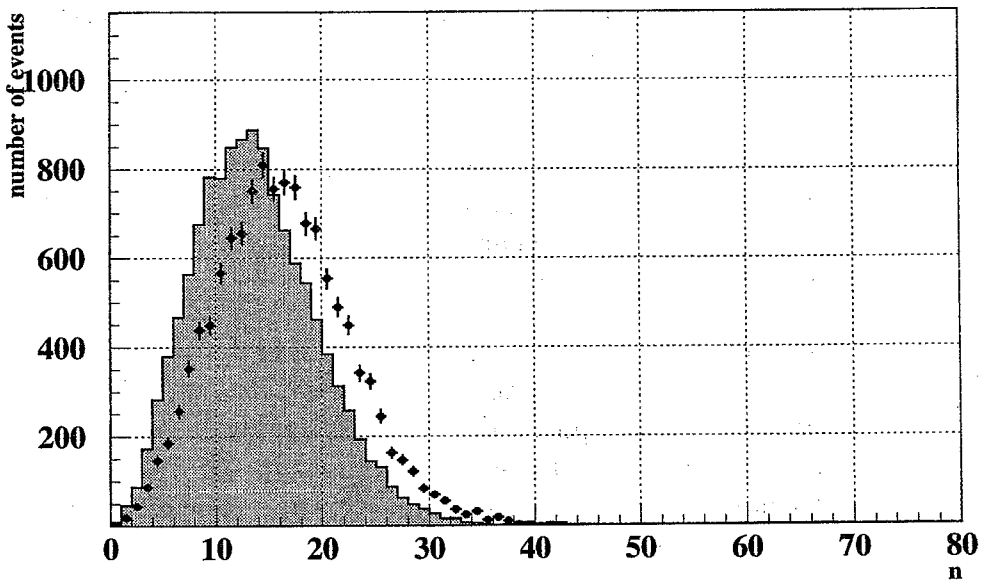


Figure B.8: *Comparison of the total CJ multiplicity distributions for the smearmode MC (histogram) and the full GOPAL simulation (points). The events were required to satisfy the condition* $\cos(\vartheta_{thrust}) > 0.90$ *with respect to the z-axis.*

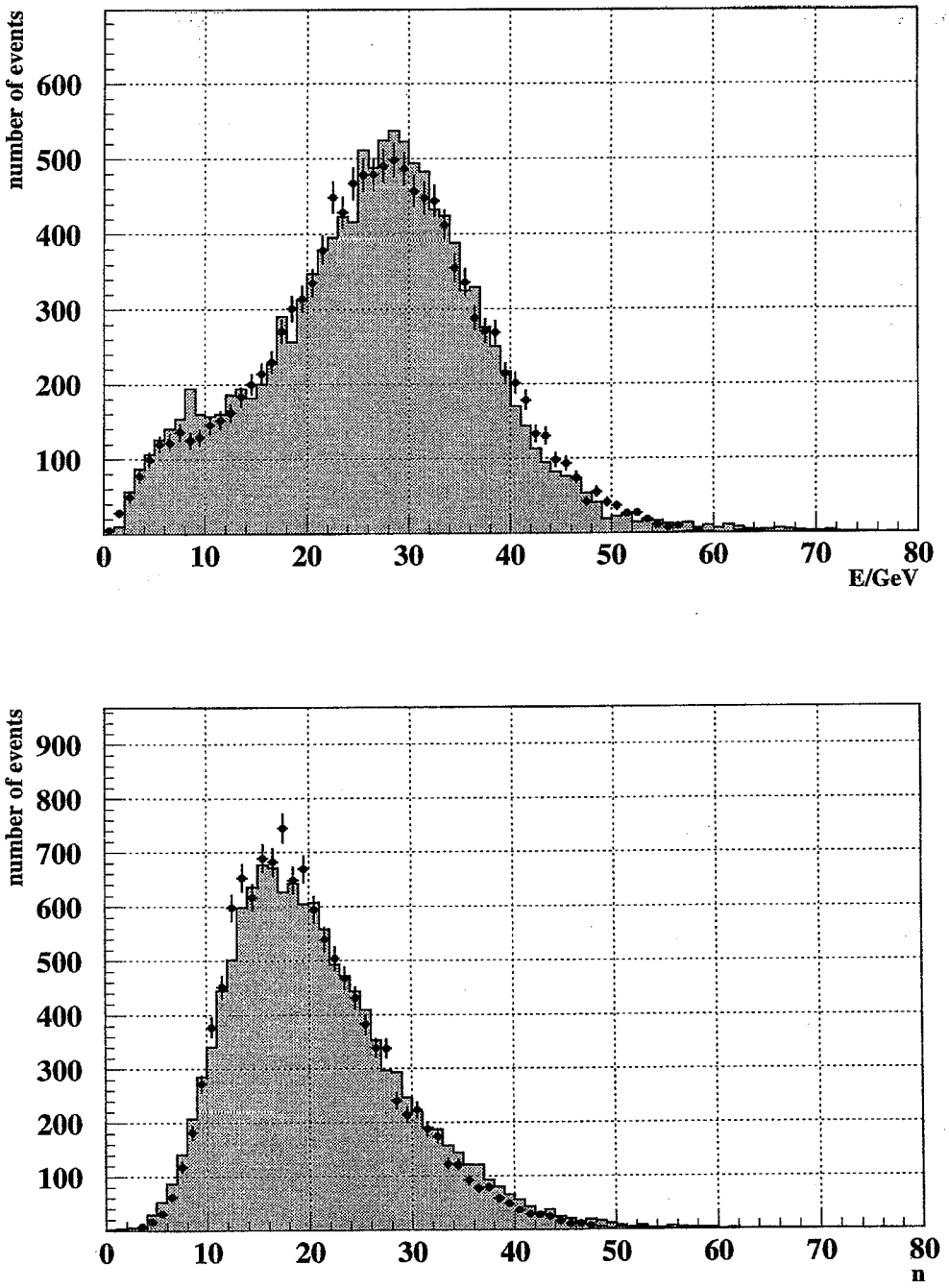


Figure B.9: *Comparison of the ECAL total visible energy and multiplicity distributions for the smearmode MC (histogram) and the full GOPAL simulation (points). The events were required to satisfy the condition* $\cos(\vartheta_{thrust}) > 0.90$ *with respect to the z-axis.*

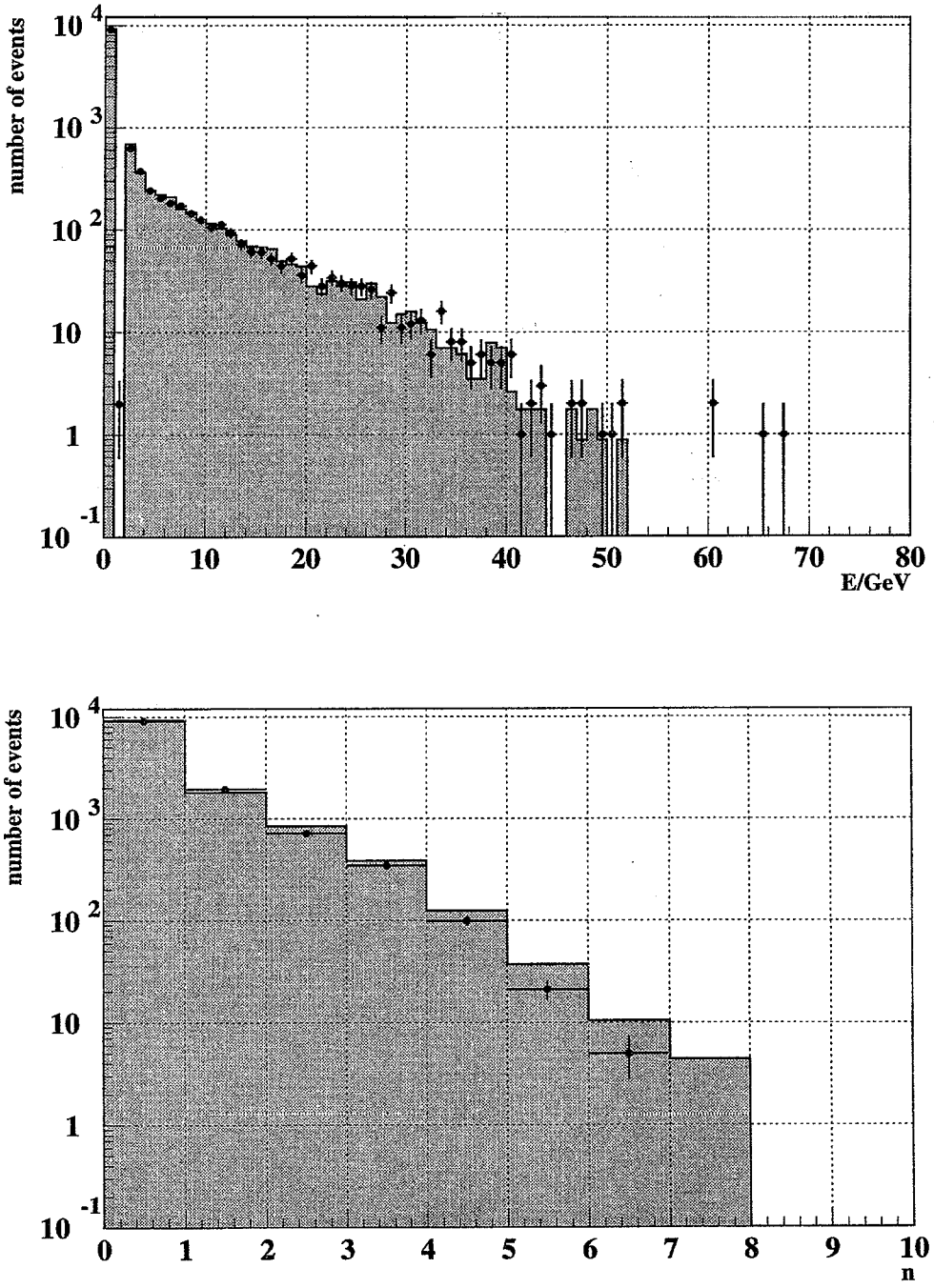


Figure B.10: *Comparison of the FD total visible energy and multiplicity distributions for the smearmode MC (histogram) and the full GOPAL simulation (points). The events were required to satisfy the condition* $\cos(\vartheta_{thrust}) > 0.90$ *with respect to the z-axis.*

# Bibliography


[1] Introduction to elementary particles; D. Griffiths; J.W & Sons.

[2] The OPAL Detector at LEP, K. Ahmet et al.; Nucl. Inst. Meth. A305 (1991) 275.

[3] The Detector Simulation Program for the OPAL Experiment at LEP; J. Allison et. al.; Nucl. Inst. Meth. A317 (1992) 103.

[4] GEANT; R. Brun et. al.; CERN DD/EE/84-1.

[5] F.A. Berends et al., *Z Physics at LEP1*, CERN 89-08, ed. G. Altarelli et al., Vol. 1 (1989) 89.

[6] M. Consoli and W. Hollik, *Z Physics at LEP1*, CERN 89-08, ed. G. Altarelli et al., Vol. 1 (1989) 7.

[7] M. Caffo and E. Remiddi, *Z Physics at LEP1*, CERN 89-08, ed. G. Altarelli et al., Vol. 1 (1989) 171.

[8] Precission Measurement of the Neutral Current from Hadron and Lepton Production at LEP, CERN-PPE/93-03; Zeit. f. Physik C58 (1993) 219-237.

[9] Improved Measurement of the Neutral Current from Hadron and Lepton Production at LEP; CERN-PPE/93-146; Zeit. f. Physik C61 (1994) 19 - 34.

[10] A measurement of $\sigma_T$ $(e^+e^- \rightarrow hadrons)$ for cm energies between 12 GeV and 36.7 GeV, Phys. Lett 113B (1982) 499.

[11] Low Noise Analog CMOS Signal Processor with a Large Dynamic Range for Silicon Calorimeters; E. Beuville et al, Nucl. Phys. B, 23A (1991) 198.

[12] AMPLEX, a Low Noise Low Power Analog CMOS Signal Processor for Multielement Silicon Particle Detectors; E. Beuville et al., Nucl. Inst. and Meth. A288 (1990) 157.

[13] Testbeam Results using the OPAL Silicon-Tungsten Calorimeter Prototype; SiW-Group, OPAL TN178.

[14] Large Acceptance Multihadron Selection; G. Duckeck, OPAL TN086.

[15] JETSET, Version 7.3; T. Sjöstrand, Comp. Phys. Comm. **39** (1986) 347; T. Sjöstrand and M. Bengtsson, Comp. Phys. Comm. **43** (1987) 367; T. Sjöstrand, CERN-TH/6488/92.

[16] G. Marchesini et al., Comp. Phys. Comm. **67** (1992) 465.

[17] A Measurement of Global Event Shape Distributions in the Hadronic Decay of the Z0; Opal Collaboration, M.Z. Akrawy et al. , Z. Phys. C47 (1990) 505.

[18] M. Böhm, A. Denner and W. Hollik, Nucl. Phys **B304** (1988) 687;
F.A. Berends, R. Kleiss and W. Hollik, Nucl. Phys. **B304** (1988) 712.

[19] S. Jadach et al., Comp. Phys Comm. 66 (1991) 276.

[20] W. Beenakker et al., Nucl. Phys. B349 (1991) 323.

[21] Higher-Order Radiative Corrections to Bhabha Scattering at Low Angles: YFS Monte Carlo Approach,
S. Jadach et al., CERN-TH 7452/94.

[22] Determination of the LEP energy spread from the longitudinal beam size in OPAL in 1993; D. Strom OPAL TN-264.

[23] The Energy Calibration of LEP in the 1993 Energy Scan, CERN-PPE/95-10.

[24] Measurement of the mass of the Z boson and the energy calibration of LEP,
CERN-PPE/93-53;
CERN-SL/93-17 (16th March 1993);
Physics Lett. B307 (1993) 187-193.

[25] Polarization Results and Future Perspectives, CERN SL/93-19.

[26] The Photon Energy Resolution in the Lead Glass Calorimeter, Peter Mättig, TN-324.

[27] A Preliminary Update of the $Z^0$ Line Shape and Lepton Asymmetry Measurements with the 1993 and 1994 Data, PN-166.

[28] A Detailed Description of the 1991 Muon Analysis, OPAL TN 109.

[29] A fragmentation independent determination of the inefficiency of the multi hadronic event selection, B. Schmitt, OPAL TN in preparation.

[30] A fragmentation independent determination of the uncertainty in the detector simulation, P. Hart, OPAL TN in preparation.

[31] Hadronic contributions to (g-2) of leptons and to the effective fine structure constant $\alpha(M_Z^2)$; S. Eichelmann and F. Jegerlehner, PSI-PR-95-1, BUDKERINP 95-5, January 1995.

[32] S.G. Goriskny, A.L. Kataev and S.A. Lorin, Phys. Lett. B259 (1991) 144;
L.R. Surguladdze and M.A. Samuel, Phys. Rev 66 (1991) 560.

[33] M. Consoli and W. Hollik, *Z Physics at LEP1*, CERN 89-08,
ed. G. Altarelli et al., Vol. 1 (1989) 7.

[34] ZFITTER an Analytical Program for Fermion Pair Production in $e^+e^-$ Anihilation; D. Bardin et al., CERN-TH 6443/92.

[35] Fortran program MIZA; M. Martinez et al., Z. Phys. C49 (1991) 645.

[36] MINUIT-longwriteup; F. James, M. Roos, CERN Program Library D506.

[37] Statistics, R.J. Barlow; J. Wiley and Sons.

[38] Observation of Top Quark Production in $p\bar{p}$ collisions;
CDF Collaboration, F. Abe et al.,FERMILAB-PUB-95/022-E.

[39] Observation of Top Quark;
D0 Collaboration, S. Albachi et al.,FERMILAB-PUB-95/028-E.

[40] A Combination of Preliminary LEP Electroweak Results for the 1995 Winter Conferences;
LEP Electroweal Working Group; internal note LEPEWWG/95-01.

## Here I would like to thank

Prof. N. Wermes for supervising this thesis, for the freedom I had with the analysis and the possibility to stay almost all the time at CERN,

all the people from the SiW group for the fun it was to build the SiW detector,

Marcello and Dick for all the things I learned from them,

the Chicago group for letting me be the $4^{th}$ on the list of the "top disk space users" of their cluster and all the nice dinners I had with them,

Phil and Günter for the discussions not only about the multi hadron selection,

all the people at the institute in Bonn, I very much enjoyed the time with them,

Ute for reading the first copy of my thesis and a lot more,

my parents for their continuous support during all these years,

Christiane for her understanding,

and all the others I did not mention.